

Structural transformations in complex perovskite-type relaxor and relaxor-based ferroelectrics at high pressures and temperatures

Dissertation

vorgelegt von: Naëmi Waesermann

aus: Hamburg

Zur Erlangung des Doktorgrades der Naturwissenschaften im
Fachbereich Geowissenschaften der Universität Hamburg

Erstgutachter: Dr. habil. Borianna Mihaylova

Zweitgutachter: Prof. Dr. Ulrich Bismayer

Hamburg, 2012

STRUCTURAL TRANSFORMATIONS IN COMPLEX PEROVSKITE-TYPE RELAXOR AND
RELAXOR-BASED FERROELECTRICS AT HIGH PRESSURES AND TEMPERATURES

Als Dissertation angenommen vom Fachbereich Geowissenschaften der
Universität Hamburg

auf Grund der Gutachten von Dr. habil. Boriana Mihaylova
Prof. Dr. Ulrich Bismayer

Hamburg, den 30. Mai 2012

Prof. Dr. Oßenbrügge
Dekan
Fachbereich Geowissenschaften

Abstract

Perovskite-type (ABO_3) relaxor ferroelectric crystals have perhaps the most simplest and at the same time the most puzzling structure. Relaxor ferroelectrics are a special type of ferroelectrics possessing remarkably high dielectric permittivity, electrostrictive coefficients, and electrooptical constants related to the complex nanoscale structure of this type of materials. These properties open a wide field of applications. Thus, it is of great significance to understand the atomistic mechanism that tailors the desired properties. Pb-based B-site complex perovskite-type materials commonly show relaxor behavior, which has been attributed to the existence of dynamic polar nanoregions, associated with local electric and/or elastic fields triggered by substitutional disorder. Recently long-range anti-ferrodistortive order has been detected at pressures up to 10 GPa, which at ambient conditions coexists with the polar order on the mesoscopic scale. This may also be an important factor for the outstanding relaxor properties.

The objective of this study was to analyze in detail the role of the coexisting polar and anti-ferrodistortive coupling for the development of the relaxor state. For this purpose first the pressure-induced structural changes up to 30 GPa in pure and doped $\text{PbSc}_{1/2}\text{Ta}_{1/2}\text{O}_3$ (PST) and $\text{PbSc}_{1/2}\text{Nb}_{1/2}\text{O}_3$ (PSN) were studied by complementary Raman spectroscopy and XRD, in order to determine whether or not the anti-ferrodistortive order persists at high pressure up to 30 GPa. Next, to gain further insights into the competitive behavior between the mesoscopic polar and anti-ferrodistortive order in-situ high-temperature high-pressure Raman spectroscopy at temperatures above the Curie temperature has been applied, at which relaxors are in ergodic state. Finally, the knowledge obtained from the structural investigations of relaxors was applied to study the ferroelectric structure of the solid solution $(1-x)\text{PbZn}_{1/3}\text{Nb}_{2/3}\text{O}_3-x\text{PbTiO}_3$ with $x = 0.1$ by combined Raman scattering and x-ray diffraction (XRD) at ambient pressure and different temperatures from 800–100 K as well as at ambient temperature and different pressures up to 18 GPa. The study intended to elucidate the origin of the giant piezoelectric effect close to the morphotropic phase boundary of this system.

The complementary XRD and Raman scattering analysis on pure PST and PSN up to 30 GPa revealed that Pb-based relaxors exhibit four characteristic pressures:

(i) an intermediate pressure p^*_1 at which the off-centered Pb and B-cations in PNRs decouple while local anti-polar order of Pb cations as well as quasi-dynamical long-range order of anti-phase BO_6 tilts is developed;

(ii) a critical pressure p_{C1} at which a continuous phase transition from relaxor-cubic to non-polar rhombohedral symmetry occurs, which is associated with anti-phase $a^-a^-a^-$ tilt order;

(iii) a second intermediate pressure p^*_2 at which the octahedral tilts around the three cubic axis become unequal from each other;

(iv) a second critical pressure p_{C2} at which a transition to a non-polar monoclinic or triclinic phase occurs, involving long-range ordering of anti-phase tilts with unequal magnitudes ($a^-b^-b^-$) or long-range order of mixed BO_6 tilts ($a^+b^-b^-$) accompanied by long-range anti-polar Pb^{2+} order.

Doping on the A or B site changes the critical pressures. The enhancement of compositional disorder on the B site shifts p_{C2} to higher pressures, while the change in p_{C1} depends on the local structural distortions in the vicinity of the doping element. Homovalent substitution of Pb^{2+} with cations having a larger ionic radius (Ba^{2+}) induces local elastic fields and thus considerably shifts p_{C1} and p_{C2} to higher pressures and suppresses the development of long-range anti-polar Pb^{2+} ordering. Lowering the tolerance factor by A-site doping favors the BO_6 tilting and thus reduces p_{C1} and p_{C2} . However, in the case of heterovalent substitution of Pb^{2+} (La^{3+}) the local B-site cation polar shifts persist to higher pressures due to the chemically-induced local electric fields, and thus the variation of the dopant concentration can tune the ratio between polar and anti-ferrodistortive order on the mesoscopic scale in order to vary the relaxor properties.

The in-situ high-pressure high-temperature Raman scattering data allowed me to construct a pT-phase diagram for Pb-based relaxors, which unambiguously confirms the coexistence of mesoscopic polar and anti-ferrodistortive order in perovskite-type relaxors and the proposed ferroelectric nature of the relaxor state. Using temperature and pressure as two separate tuning mechanisms, one can select a structural state with a certain degree of polar order (by changing temperature) or of anti-ferrodistortive order (by applying pressure). At elevated temperatures the first pressure-induced phase transition drops to lower pressures as the polar coupling is suppressed, which in turn facilitates the development of the mesoscopic anti-ferrodistortive order existing at ambient pressure into a long-range ordered anti-ferrodistortive state at high pressure.

Raman spectroscopy at different temperatures on 0.9PZN-0.1PT shows that there are two different intrinsic cubic states of Pb ions in regions with a local chemical order of the type $\text{Pb}(\text{B}^{2+}_{2/3}\text{B}^{5+}_{1/3})_{1/2}\text{B}^{5+}_{1/2}\text{O}_3$: (i) less abundant Pb1 ions surrounded by Nb^{5+} and (ii) more abundant Pb2 ions surrounded by both Zn^{2+} and Nb^{5+} . The temperature dependence of the Raman spectra of PZN-0.1PT indicates that off-centered Pb2 ions induce coherent polar shifts of ferroelectrically active B-cations, which in turn leads to the off-centering of Pb1 ions. Also, Raman data suggest the predominance of monoclinic-type ferroelectric domains over tetragonal-type domains in the room temperature structure of as-synthesized (unpoled) crystals. At room temperature and high pressures PZN-0.1PT undergoes several structural transitions. Near 1 GPa the preexisting multiphase (monoclinic + tetragonal) multidomain state changes to another, most probably, single-phase multidomain state. Near 2 GPa the system reaches a cubic relaxor state, in which the polar order exists only on the mesoscopic scale, as polar nanoregions. At 5.9 GPa PZN-0.1PT undergoes a reversible pressure-induced phase transition from a cubic to an anti-ferrodistortive phase comprising long-range ordered antiphase octahedral tilts, similar to

all other Pb-based relaxors. In the low-pressure range up to 1 GPa twinning is strongly enhanced, while the ferroic deviation of the atomic structure is reduced. This region coincides with the pressure range where the piezoelectric and electrochemical coefficients are decreased. Thus, the large shear piezoelectric and electromechanical responses are related with the intrinsic structural complexity on the local scale, rather than with the domain texture. Low levels of Ru doping on the B-site ($\text{Ru}/(\text{Zn}+\text{Nb}+\text{Ti}) \sim 0.002$) enlarges the temperature range where the tetragonal state is preferred at ambient pressures, but has a negligible effect on pressure.

The results of this study indicate the coexistence of polar and anti-ferrodistortive order on the mesoscopic scale as well as the doubling of the perovskite unit cell, which is typical of all Pb-based relaxors and relaxor-based solid solutions. The findings imply that the structure of the dynamic polar nanoregions is ferrielectric rather than ferroelectric in nature. Hence, the structure of polar nanoregions can be chemically tailored by tuning the polar as well as the anti-ferrodistortive coupling.

Contents

1	Introduction	1
1.1	Ferroelectricity	1
1.2	The perovskite structure type	3
1.3	Relaxor ferroelectrics	6
1.3.1	Models concerning the origin of the relaxor properties	7
1.3.2	Temperature-induced transformations	8
1.3.3	Pressure-induced transformations	10
1.4	Model compounds	12
1.4.1	PbSc _{1/2} Ta _{1/2} O ₃ (PST) and PbSc _{1/2} Nb _{1/2} O ₃ (PSN) as model compounds	12
1.4.2	A- and B-site doped PST and PSN	16
1.4.3	Solid solutions with giant piezoelectric effect	18
2	Objectives	20
3	Methods	21
3.1	Raman spectroscopy	21
3.1.1	A short history	21
3.1.2	The Raman scattering effect	21
3.1.3	Phonon modes	25
3.1.4	Converting energy units	28
3.1.5	Group-theory analysis and Raman peak assignment for Pb-based perovskite-type relaxors	29
3.1.6	The Raman spectrometer available at the Institute of Mineralogy and Petrology	32
3.2	X-ray diffraction	32
3.2.1	Principles of diffraction	32
3.2.2	Diffuse x-ray scattering in Pb-based relaxors	35
3.3	The diamond-anvil-cell technique	36
3.3.1	Diamond anvils	36
3.3.2	Gaskets	40
3.3.3	Pressure-transmitting media	41
3.3.4	Measuring pressure	43

4	Experimental conditions used in this study	46
4.1	Different types of DACs used	46
4.2	Raman spectroscopy	46
4.2.1	Temperature-dependent measurements at ambient pressure	46
4.2.2	Pressure-dependent measurements at ambient temperature	46
4.2.3	In-situ high temperature high pressure dependent measurements .	47
4.3	X-ray diffraction	48
4.3.1	Temperature-dependent measurements at ambient pressure	48
4.3.2	Pressure-dependent measurements at ambient temperature	48
5	Results and Discussion	49
5.1	Pressure-induced structural changes at room temperature up to 30 GPa . .	49
5.1.1	Pure PST	49
5.1.2	Pure PSN	56
5.1.3	A- and B-site doped PST and PSN	60
5.2	The high-pressure structural state of relaxors at elevated temperatures . .	70
5.3	Structural changes in relaxor-based solid solutions with giant piezoelectric effect	76
5.3.1	Temperature-driven structural transformations at ambient pressure	76
5.3.2	Pressure-driven structural transformations at room temperature .	93
6	Conclusions	108
6.1	Structural changes in Pb-based relaxors under pressure	108
6.2	The evolution of Pb-based relaxors under elevated temperatures and pressures	109
6.3	Structural changes in the solid solution PZN-0.1PT	112
6.3.1	Temperature-induced structural changes	112
6.3.2	Pressure-induced structural changes	112
6.3.3	A note about the structure-property relation in $\text{PbB}'_{1/3}\text{B}''_{2/3}\text{O}_3$ - PbTiO_3 binary systems	113
6.4	A plausible structural state of Pb-based B-site complex perovskite-type relaxors	114
	Bibliography	116
A	High-temperature high-pressure DAC easyLab Diacell® μScopeDAC-HT(G)	i
B	Alignment of the diamond anvils	vi
C	Manual for the spark eroder available at the Institute of Mineralogy and Petrol- ogy	viii

1 Introduction

1.1 Ferroelectricity

Ferroelectric materials show spontaneous polarization which can be reversed by an external electric field. This effect has first been found in Rochelle salt (also known as Seingette salt) in 1921 by Valasek (Valasek, 1921) and was first named Seignette electricity. Only when switchable spontaneous polarization was discovered in perovskite-type materials (e.g. BaTiO_3) the analogy with ferromagnetism was realized and the effect was named ferroelectricity.

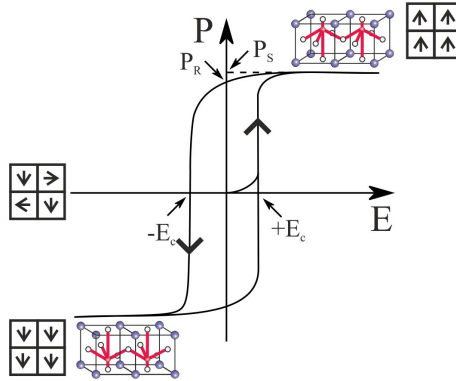


Figure 1.1: Hysteresis of the polarization P versus the external electric field E , E_C , P_R , and P_S denote coercive field, remanent polarization, and saturation polarization, respectively.

The field dynamic of the polarization follows a hysteresis loop (Figure 1.1). If an increasing direct electric field (E) is applied, the net polarization switches quite instantly once a certain electric field strength ($+E_C$) is reached resulting in the saturation polarization (P_S). Further increase in the electric field strength only leads to negligible further increase of the polarization. If the external electric field is removed, some of the domains remain aligned, thus the net polarization drops to the remanent polarization (P_R), hence the crystal cannot be completely depolarized. The polarization will switch back to its previous value at a certain negative electric field strength ($-E_C$) completing the hysteresis loop. The external field needed to change the polarization to zero is called coercive field (E_C). This hysteresis of the polarization (P) against the electric field strength (E) is the so-called ferroelectric effect.

Ferroelectricity is only possible in crystals with polar axis. From the 32 point groups 11 have a center of symmetry and thus possess no polar properties. Of the resulting 21 non-centrosymmetric point groups all but one (cubic 432) exhibit electrical polarity when

1 Introduction

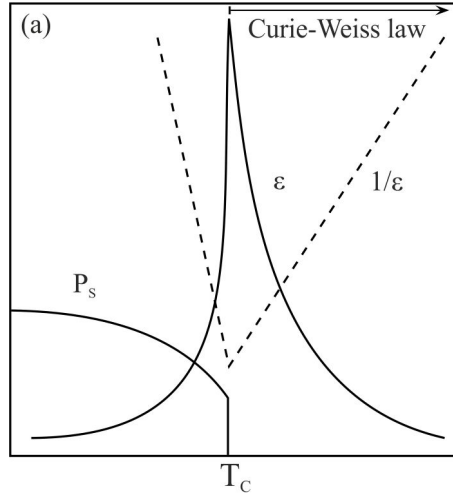


Figure 1.2: Temperature dependence of the spontaneous polarization P_s and the dielectric permittivity ϵ . After Hirota *et al.* (2006)

subjected to stress thus they are piezoelectric. Ten of these (1, 2, m, mm2, 3, 3m, 4, 4mm, 6, 6mm) have a unique polar axis (rotational axis with no mirror plane perpendicular to this axis) and thus are the so called polar point groups. These polar point groups show spontaneous polarization if subjected to a thermal treatment (pyroelectricity) or a reversible electric polarization (ferroelectricity), if subjected to an electric field below the Curie temperature T_C (Figure 1.2).

Due to the lowering of the structural symmetry at T_C from the higher symmetric paraelectric prototype structure, ferroelectric domains are formed in two or more directions. The shift of cations and anions against each other induces dipole moments in the structure (see the insets in Figure 1.1). Depending on the pattern of aligned domains there are four different types of ferroelectricity: (i) dipoles of the same magnitude are aligned in the same direction (ferroelectric); (ii) dipoles of the same magnitude are aligned in opposite directions (anti-ferroelectric); another possible configuration is: dipoles of larger magnitude are alternating with dipoles of smaller magnitude in the same directions ; and (iii) dipoles of larger magnitude are alternating with dipoles of smaller magnitude in opposite directions (ferrielectric).

The polarization is most easily switched just below T_C where the distortion from the unpoled paraelectric (PE) phase is still very small. Immediately below T_C the material spontaneously distorts to a polarized state which is associated with a maximum of the dielectric permittivity ϵ at the temperature T_m . Above T_C the temperature dependence of ϵ follows the Curie-Weiss law:

$$\epsilon = \frac{C}{T - T_{CW}}$$

where C is the Curie constant, T is the temperature in Kelvin and T_{CW} is the Curie-Weiss temperature, which coincides with the phase transition temperature T_C for second-order phase transitions.

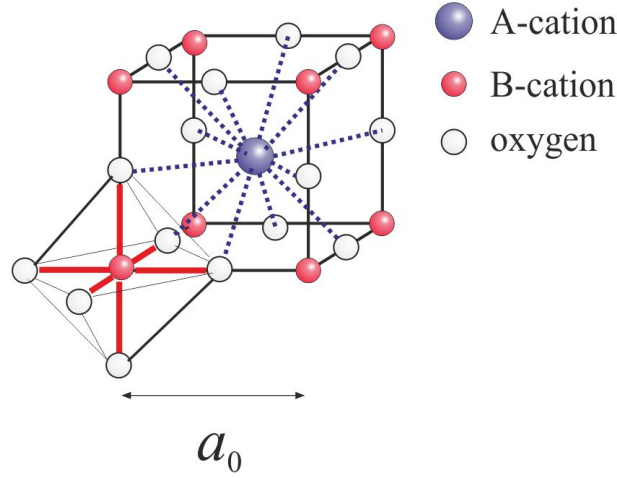


Figure 1.3: The ideal perovskite structure with the BO₆ octahedra located at the cube corners and the A-cation in the center of the cube.

1.2 The perovskite structure type

Perhaps the simplest and most studied structure type of ferroelectric crystal is the perovskite structure ABO₃ (Figure 1.3). The perovskite structure is named after the mineral perovskite CaTiO₃ which was discovered in the Ural mountains, Russia, in 1839.

The ideal perovskite is the primitive cubic $Pm\bar{3}m$ structure where A, B, and O atoms occupying the (1a), (1b), and (3c) Wyckoff positions respectively, which has first been published in 1946 by H. D. Megaw (Megaw, 1946). In this structure (Figure 1.3) BO₆ octahedra are located at the cube corners forming a corner-sharing array while the A-cation is located at the center of the cube coordinated to the 12 oxygen atoms (or other anions) located at the midpoint of each cubic edge. In ferroelectric perovskites the B-site is generally occupied by 4+ and 5+ transition metal elements (*d*-ions). These *d*-ions are highly polarisable "active" ions promoting ferroelectricity as they are close to the electronic "crossover" points where different types of atomic orbitals are comparable in energy and where hybrid bond formation is prevalent. The B-cations form BO₆⁸⁻ octahedra with the oxygen anions. If these octahedra are distorted to lower symmetry they form dipoles promoting spontaneous polarization. If the A-site is occupied by elements showing affinity to form stereochemically active electronic lone pairs, like Pb²⁺ and Bi³⁺ having two electrons outside a closed shell in an asymmetric hybrid orbital, this is another active participant in the spontaneous polarization.

Megaw (1946) showed that the ideal perovskite structure ($Pm\bar{3}m$) does not apply to all perovskite type materials. In general, the deformation of the perovskite structure from ideal consists of two types: (i) the unit cell changes its shape by altering either the lengths of the unit-cell edges or the axial angles; and (ii) the atomic positions of some or all atoms are slightly altered which lowers the symmetry as the atoms are located in special positions in the ideal perovskite structure. This lowering of symmetry results

1 Introduction

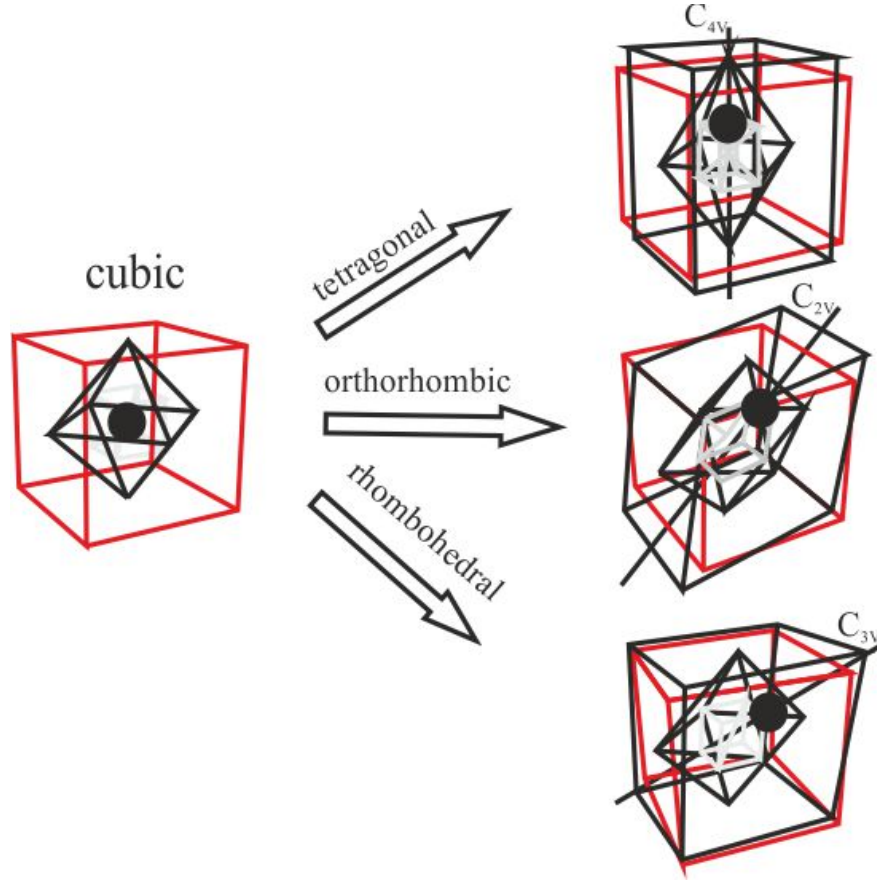


Figure 1.4: The distortion of the ideal cubic perovskite structure along [100] tetragonal, [110] orthorhombic, [111] rhombohedral. The displacive soft mode induced distortions with off-center B-cations (black dot). The distorted unit cells are shown by the solid black lines, while the undistorted cubic cell is shown in red (dotted line); the oxygen octahedra is shown in gray. Modified after Blinc (2011).

in a tetragonal, orthorhombic or rhombohedral distortion (Figure 1.4) of the ideal cubic perovskite structure which is referred to as pseudo-cubic as the distortion from cubic is very small. These distortions of the perovskite structure can basically be generated in three ways: (i) if the A-cation is too small for the large 12-fold site, the BO_6 octahedra will tilt relative to one another to reduce the size of the AO_{12} cavity; if (ii) the B-cation is too small for the octahedral site, the cation moves off-center within the octahedron; (iii) the A-O and /or B-O bond have a pronounced covalence which results in a distortion of the AO_{12} cubeoctahedron or BO_6 octahedron itself.

Goldschmidt (1927) showed that the stability of the perovskite structure depends on the ionic radii and is relatively independent of the valency. This is described by the tolerance factor t :

$$t = \frac{R_A + R_O}{\sqrt{2}(R_B + R_O)}$$

1 Introduction

Table 1.1: Glazer notation of the tilt systems and the resulting space groups that may occur in real crystals

Tilt system	Space group
$a^0a^0a^0$	$Pm\bar{3}m$
$a^-a^-a^-$	$R\bar{3}c$
$a^0a^0c^-$	$I4/mcm$
$a^0a^0c^+$	$P4/mbm$
$a^0b^-b^-$	$Imma$
$a^-b^+a^-$	$Pnma$
$a^+a^+a^+$	$Im\bar{3}$
$a^0b^-c^+$	$Cmcm$
$a^0b^+b^+$	$I4/mmm$
$a^+a^+b^-$	$P4_2/nmc$
$a^-a^-c^-$	$C2/c$
$a^0b^-c^-$	$C2/m$
$a^-b^-c^-$	$P\bar{1}$
$a^+b^-c^-$	$P2_1/m$
$a^+b^+c^+$	$Immm$

where R_A , R_B , R_O are the ionic radii of the ions A, B, and O. Goldschmidt showed empirically that a material preserves the perovskite structure type as long as t is between 0.78 and 1.05. If $t = 1$ the size of the A- and B-site cations perfectly matches the space provided by the oxygens or other anions. Lower values of t indicate smaller A-site cations which favors tilting of the BO_6 octahedra.

Glazer (1972) introduced a standard notation to describe octahedral tilt distortions in perovskites. The notation describes the tilt system by rotations of BO_6 octahedra about the three axes (x , y , z) of the aristotype cubic unit cell. The letters in the Glazer notation indicate the magnitude of the rotation about a given axis, a different letters a, b, and c imply non-equal tilts about the x , y , and z axes. A superscript is used to denote the phase of the octahedral tilting in adjacent layers. A positive superscript indicates that the neighboring octahedra tilt from the adjacent layers are in the same direction (in-phase) and a negative superscript implies the tilts of neighboring octahedra are in the opposite direction (out of phase). The superscript 0 signifies no tilting about the corresponding axis. The tilting of the octahedra reduces the symmetry of the undistorted perovskite tilt system $a^0a^0a^0$. Glazer derived 23 different tilt systems, but only 15 may occur in real crystals, each with a different space group.

1.3 Relaxor ferroelectrics

Relaxor ferroelectrics (relaxors) are a special type of ferroelectrics which have been extensively investigated over the past 50 years (Bhalla *et al.*, 2000) with the aim of tailoring their physical properties. At the beginning relaxors have also been called dirty ferroelectrics as they exhibit a diffuse frequency-dependent phase transition over a temperature range. The broad and frequency dispersive behavior of the dielectric permittivity (ϵ) at T_m distinguishes relaxors from normal ferroelectrics (see Figure 1.5). Relaxors can be separated

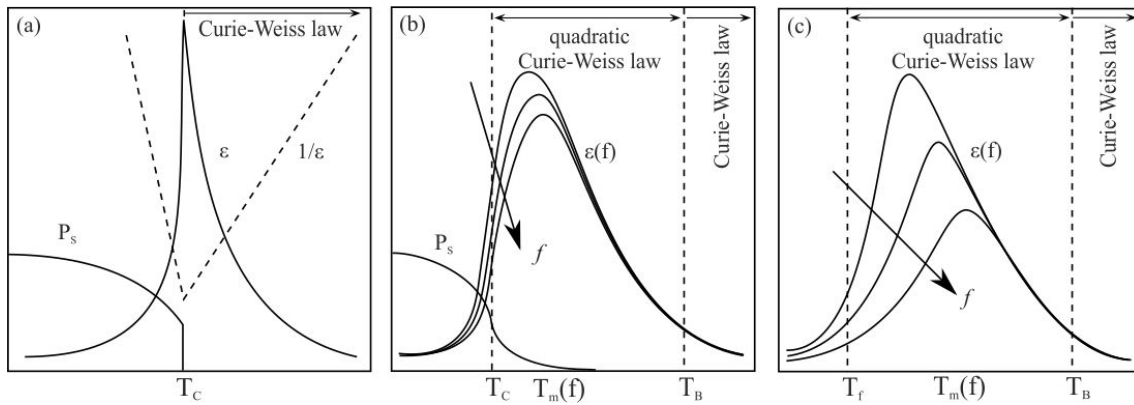


Figure 1.5: Behavior of the dielectric permittivity ϵ with respect to the different characteristic temperatures T_B , T_m , T_C , and T_f : in normal ferroelectrics (a), relaxors with a phase transition to ferroelectric (b), and canonical relaxors (c). After Hirota *et al.* (2006)

into two groups: (i) such that develop long-range ferroelectric order at T_C (Figure 1.5b), and (ii) canonical relaxors (Figure 1.5c) which do not show a macroscopic phase transition, therefore remain isotropic, i.e., the polar-nano regions (PNR) or domains freeze at T_f resulting in a change of the translational symmetry.

For relaxors the temperature dependence of ϵ only follows the linear Curie-Weiss law only at temperatures above T_B . The characteristic temperature T_B , has been defined on the basis of optical experiments (Burns & Dacol, 1983) to be the temperature at which polar nanoregions nucleate. Between T_m and T_C $\epsilon(T)$ can be approximated by a quadratic relation (Bokov & Ye, 2006):

$$\epsilon - 1 = \chi = \frac{C'}{(T - T'_{CW})^2}$$

Other distinct features in relaxors are the slim hysteresis loop near T_C with large saturation polarization (P_S) and small remanent polarization (P_R), exceptionally large electrostrictive coefficients, and large electrooptical constants (Setter & Cross, 1980). Those physical properties open a wide field of applications for relaxor material, for example as capacitors, actuators and micro-positioners, as well as for data storage, shutters or optical modulators (Ye, 1998; Scott, 2007; Cross, 2008). Different models have been proposed to explain the origin of the relaxor properties (see next Section 1.3.1).

1.3.1 Models concerning the origin of the relaxor properties

One of the first models to explain the relaxor properties was proposed by Smolenskii and Isupov (Smolenskii *et al.*, 1961; Isupov *et al.*, 1989). They explained the diffuseness in the transition temperature by the chemical inhomogeneity on the microscopic scale due to compositional fluctuations and impurities on the B-site (Setter & Cross, 1980). Thus, the chemically different nano-regions give rise to different local Curie temperatures, which results in a broad dielectric permittivity over a mean Curie temperature at approximately T_m . However, the structural atomic variation alone cannot explain the frequency dispersion of $\varepsilon(T)$ in the vicinity of T_m .

Burns & Dacol (1983) showed that local polarizations or polar nanoregions (PNRs) appear at a dipole temperature T_d (also referred to as the Burns temperature T_B), which is several hundred Kelvins above T_m . The presence of PNRs between T_B and T_m was also supported by the non-linear behavior of the thermal strain and the thermal expansion coefficient attributed to the electrostrictive effect which have not only been observed in disordered perovskite but also in highly ordered perovskites like PST. Also the deviation from the linear Curie-Weiss law suggests the presence of PNRs above T_m .

Cross (1987) proposed a superparaelectric model in analogy to the superparamagnetic state, in which spin clusters establish an anisotropic energy to remain stable against thermal motion. The random interactions between magnetic-spin or electric-dipole clusters gives rise to electric or magnetic relaxation which exhibits a freezing temperature. In relaxors these clusters are PNRs. The PNRs are able to switch between the equivalent orientation states according to the symmetry of the local polar phase. Above T_m the PNRs are considered to be dynamically distorted along the possible polar directions.

This model has been extended by Bokov (1997) and is known as the *dipolar glass model*. It proposes that above T_m dynamic PNRs or nano domains are embedded in the paraelectric (cubic) matrix which results in local elastic and electric fields increasing the total energy of the system. The dynamic nature of the PNRs explains the frequency dispersion of $\varepsilon(T)$. The disadvantage of this model is that it cannot commonly describe the crossover from relaxor to ferroelectric state under an external electric field.

A second concept is the quenched-random-field approach based on the theoretical work of Imry & Ma (1975) proposed by Westphal, Kleemann and Glinchuck (Kleemann, 1993). They suggest that the existence of stabilized size-restricted nano-regions is due to the interplay between the surface energy of domain walls and the bulk energy of domains in the presence of arbitrary weak random fields induced by compositional fluctuations. In this model the crystal is represented by low-symmetry nano-domains separated by domain walls with a thickness approaching the linear size of the nano-domains. In such systems with a continuous change of the order parameter, a second-order phase transition should be suppressed by quenched random local fields conjugated to the order parameter.

1 Introduction

Below the Curie temperature the system brakes into small-size domains, similar to the concept of PNRs, instead of forming a long-range ordered state.

Glinchuk & Farhi (1996) proposed a random field theory based on electrostatic interactions where the transition is regarded as an order-disorder phase transition. Thus at high temperatures the crystal is represented by a system of random reorientable dipoles embedded in a highly polarisable matrix similar to the concept of the dipolar glass model. In contrast to the dipolar glass model, the dipole-dipole interactions are not direct but indirect via the matrix leading to uniformly directed local fields and thus to ferroelectric ordering at low temperatures. Additional sources of random local electric fields are considered to explain the absence of macroscopic ferroelectric ordering coming from quenched compositional reorder or shifts of non-ferroactive ions from special positions. This model explains the relaxor behavior in chemically ordered materials such as $\text{Cd}_2\text{Nb}_2\text{O}_7$ (Samara *et al.*, 2006).

The existence of PNRs has been experimentally proven most prominently by the observation of diffuse x-ray and neutron scattering. The diffuse scattering is related to the intermediate-range correlation of polar atomic displacements with a correlation length insufficient to generate Bragg peaks. Pb-based relaxor ferroelectrics shows a very specific "butterfly" shape of the diffuse scattering for $h00$ reflection and an ellipsoid shape for $hk0$ reflections. Three dimensional mapping (Xu *et al.*, 2004) of x-ray diffuse scattering (XDS) showed that the diffuse scattering consists of $\langle 110 \rangle^*$ -type intensity rods with different distributions for each type of reflection. Thus, PNRs have a correlation along the cubic $\{110\}$ planes. Xu *et al.* (2004) suggested that the polarization of PNRs within the cubic $\langle 110 \rangle$ direction, i.e., along a direction different from the direction of the macroscopic polarization which is along the cubic $\langle 111 \rangle$ direction. However, neutron elastic scattering showed that the local polarization of PNRs indeed along the cubic $\langle 111 \rangle$ direction ((La-Orauttapong *et al.*, 2003)), although PNRs may be elongated or flattened along different directions.

1.3.2 Temperature-induced transformations

Under temperature decrease the evolution of the PNRs can be seen by a sequence of characteristic temperatures (Figure 1.6). As mentioned above, the temperature at which individual atomic shifts couple to form dynamic PNRs has first been described by Burns (Burns & Dacol, 1983). They observed a derivation of the temperature-dependence of the refractive index from a linear dependence which indicates the so called Burns temperature (T_B) where the PNRs nucleate. Above T_B the crystal is in a paraelectric state, below T_B the crystal enters the so called ergodic relaxor state, i.e., PNRs with randomly distributed directions of dipole moments appear within the paraelectric matrix but the average structure does not show a preferred polarization. This change can also be seen by the deviation of $\varepsilon(T)$ from the linear Curie-Weiss law (Samara, 2003). The Burns temperature is seen by Raman spectroscopy by the softening of the anomalous signal related to the cubic

1 Introduction

F_{2g} mode near 55 cm^{-1} generated by Pb-localized phonons in parallel polarized spectra (Mihailova *et al.*, 2005).

On further temperature decrease the PNRs couple due to their electric field at T^* to form larger clusters and slow down their flipping dynamics (La-Orautapong *et al.*, 2001; Svitelskiy *et al.*, 2003; Toulouse *et al.*, 2005; Mihailova *et al.*, 2008b; Dkhil *et al.*, 2009). T^* can be seen by acoustic emission (Dul'kin *et al.*, 2006), the deviation from linear in the pseudo-cubic cell parameters (Dkhil *et al.*, 2009) as well as by the kink in the FWHM in the anomalous Raman scattering arising from the B-site localized mode near 240 cm^{-1} associated with the cubic F_{1u} (Mihailova *et al.*, 2008b).

In the case of canonical relaxors, the temperature of the maximum of the dielectric permittivity T_m is reached before PNRs to freeze (Dul'kin *et al.*, 2010a). At T_f the system transforms into a non-ergodic relaxor state. On the mesoscopic scale the atomic structure deviates from cubic but the average crystal structure remains cubic. The non-ergodic state can be irreversibly transformed into a ferroelectric state by a sufficient external electric field. There are however relaxors which undergo a phase transition at $T_C < T_m$ to a long-range ordered ferroelectric state. However, the long-range ordered ferroelectric state does not show complete ferroelectric ordering as traces of the PNRs are still detectable at temperatures well below T_C (Xu, 2010) and abundant paraelectric (cubic) regions may still be present (Maier *et al.*, 2009). This indicates that there may be two types of coexisting length scales of polar order at low temperatures: ferroelectric domains as well as PNRs, which leads to a much more flexible and heterogeneous structure.

The phase transition temperature (T_C) can be determined by diffraction via the splitting of the cubic peaks at the appearance of a new phase. Using Raman spectroscopy the phase transition can be seen because of the lowering of the symmetry from cubic to rhombohedral which, similar to diffraction, results in new Raman scattering peaks and splitting of the existing peaks. The existence of long-range-ordered ferroelectric domains

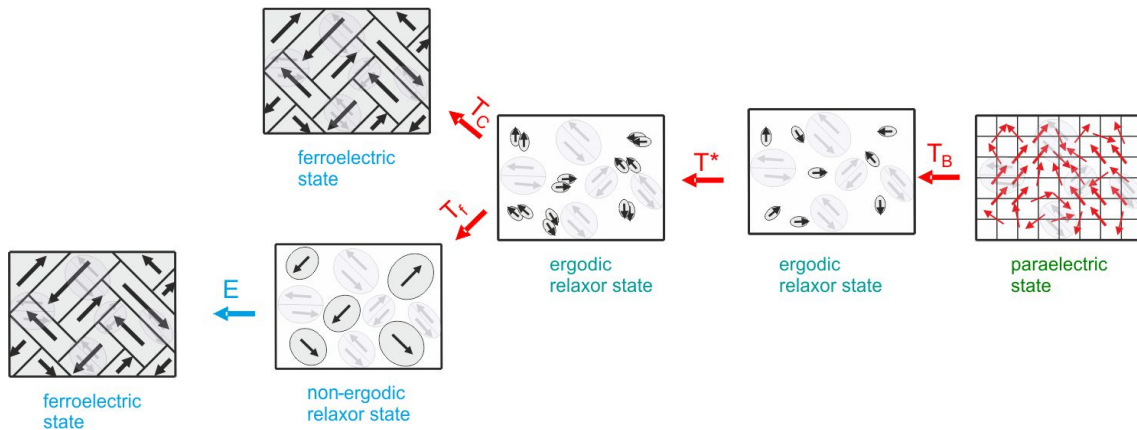


Figure 1.6: Evolution of PNRs upon temperature decrease.

1 Introduction

can be distinguished from the presence of PNRs via the observed depolarization ratio of Raman spectra collected from single crystals.

While nowadays the scientific community generally agrees on the existence of PNRs the primary reason for their existence is still under discussion. The actual intrinsic mechanism behind the relaxor properties (see Section 1.3.1) is still unclear as well as whether intrinsic local electric or elastic fields associated with chemical inhomogeneities are responsible for the relaxor structural state at low temperature. Doping with different elements can help to elucidate the influence of local charge imbalance and local strains. In the case of Pb-based relaxors it is also important to understand in which extent the disturbance of the system of lone pair electrons on the A-site affects the polar ordering.

To induce local elastic fields Pb-based perovskite-type relaxors are doped with cations of larger ionic radius on the A-site than Pb^{2+} such as Ba^{2+} . It has been shown by Maier *et al.* (2009) that doping with Ba^{2+} suppresses the ferroelectric long-range order and enhances the non-ergodic relaxor state, so to say it makes the structure more relaxor-like. If the tolerance factor is lowered due to A-site substitution with a dopant that has a smaller ionic radius than Pb^{2+} as in the case of Sr^{2+} or La^{3+} the structure itself favors anti-phase tilting and in appropriate depend concentrations can lead to incommensurate octahedral ferroelectric ordering at low temperatures (Maier *et al.*, 2011c) (see Section 1.2), which is also developed under pressure (see Section 1.3.3). Via doping with Bi^{3+} a local electric field is induced by the additional electron in the outermost shell without destroying the system of Pb lone-pairs. Bi^{3+} substitution, having nearly the same ionic radius as Pb^{2+} and active electron lone-pairs, leads to larger ferroic domains at low temperatures due to the formation of coherent ferroic atomic shifts governed by the lone-pair electron system. A-site substitution with Ba^{2+} , Sr^{2+} or La^{3+} on the other hand destroys the coherence length of the Pb^{2+} electron lone-pairs which disturbs the dynamical coupling between off-centered Pb and B-site cations (Maier *et al.*, 2011c).

1.3.3 Pressure-induced transformations

The application of pressure as a much stronger thermodynamic driving force has shown to enhance different ferroic structural species than the temperature decrease. Using dielectric permittivity measurements at moderate pressures up to 2 GPa Samara & Venturini (2006) showed a crossover from a ferroelectric to a relaxor state for various Pb-based perovskite-type compounds. The authors concluded that the relaxor state is favored at moderate pressures and assumed that at high pressures the paraelectric state should be dominant. The suppression of the PNRs under high pressure which has indeed been observed by single-crystal x-ray diffraction with synchrotron radiation (Chaabane *et al.*, 2003; Kreisel *et al.*, 2003; Ahart *et al.*, 2005; Janolin *et al.*, 2006; Mihailova *et al.*, 2008a; Welsch *et al.*, 2009b; Maier *et al.*, 2010a), indicating that the high-pressure phase of Pb-based perovskite-type materials does not correspond to a relaxor ergodic or non-ergodic state. However,

1 Introduction

synchrotron x-ray diffraction analysis revealed that the relaxor state does not transform into paraelectric either. High-pressure studies on relaxors have shown that pressure triggers a sequence of structural changes (Figure 1.7). A continuous phase transition from a relaxor cubic state to a non-polar rhombohedral phase has been detected associated with the development of anti-phase octahedral tilting $a^-a^-a^-$ (Glazer's notations (Glazer, 1972)) leading to anti-ferrodistortive order. The critical pressure is best determined by the kink in the pressure dependence of the bulk modulus obtained from x-ray diffraction.

The pressure-induced phase transition can also be seen by Raman spectroscopy via the appearance of a soft mode or by a maximum in the FWHM of the Pb-localized mode near 50 cm^{-1} (Mihailova *et al.*, 2008a; Welsch *et al.*, 2009b, 2011; Mihailova *et al.*, 2011). Above the phase-transition pressure p_C the Raman peaks associated with PNRs are strongly suppressed but the Raman scattering is inconsistent with the cubic symmetry of the paraelectric phase and clearly differs from the Raman scattering of the low-temperature ferroelectric state. This is in agreement with the cubic to non-polar rhombohedral phase transition, indicating that pressure enhances anti-ferrodistortive order while temperature decrease favors polar order. Raman spectroscopy also reveals that the local distributions associated with the mesoscopic polar order are heavily suppressed, when approaching the pressure-induced phase transition (Mihailova *et al.*, 2008a; Welsch *et al.*, 2009b; Maier *et al.*, 2010a,b).

As described in Section 1.3.2 inducing local elastic or electric fields via doping helps to get further insights into the structural transformations. It has been shown that A-site substitution with larger ionic radius, inducing local elastic fields, such as Ba^{2+} smears out the pressure-induced phase transition and hampers the development of the high pressure structural state (Welsch *et al.*, 2009a; Maier *et al.*, 2010b; Mihailova *et al.*, 2011). The disturbance of the Pb^{2+} lone-pair electrons, which is vital for the formation of ferroic long-range order, also hampers the pressure induced phase transition. The substitution with Bi^{3+} for Pb^{2+} , inducing local electric fields in the structure, enhances the fraction of material that undergoes a phase transition (Welsch *et al.*, 2009a; Maier *et al.*, 2010b; Mihailova *et al.*, 2011). The presence of active lone-pair electrons enhances the fraction of ferroic long-range ordered domains despite the charge imbalance, while the electric field induces additional nucleation of non-cubic structural species which also favors the overall ferroic ordering.

Still there are only very few publications on Pb-based relaxors above 10 GPa (Kornev *et al.*, 2005; Janolin *et al.*, 2006, 2008) though a sequence of structural transformations is

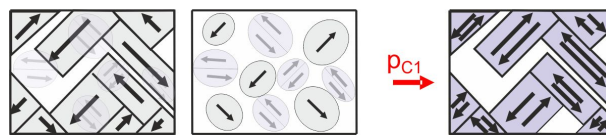


Figure 1.7: Pressure evolution: Pressure suppresses the polar order in favor of ferroic order.

1 Introduction

suggested under high pressure (Janolin *et al.*, 2006). Therefore the model compounds PST and PSN have been investigated up to 30 GPa to verify the occurrence of further phase transitions above the continuous phase transition involving long-range BO_6 anti-phase tilting. A-site doped PST and PSN was investigated to see the effect of induced electric- and elastic fields on the structural transformations up to 30 GPa. By doping the model compounds on the B-site with cations having a smaller ionic radius such as La and Sr, the effect of a smaller tolerance factor on the structural transformations up to 30 GPa was investigated as well as the effect of the solid-solution of both model compounds.

1.4 Model compounds

1.4.1 $\text{PbSc}_{1/2}\text{Ta}_{1/2}\text{O}_3$ (PST) and $\text{PbSc}_{1/2}\text{Nb}_{1/2}\text{O}_3$ (PSN) as model compounds

As the perovskite structure is quite flexible in occupying different A- and B-cations due to the large range of variation of the tolerance factor (see Section 1.2) B-site complex Pb-based perovskite ($\text{PbB}'_{1-x}\text{B}''_x\text{O}_3$) structures generally have mixed B-cations in fixed ratios to average the valence of 4+ on the B site. $\text{PbSc}_{1/2}\text{Ta}_{1/2}\text{O}_3$ (PST) and $\text{PbSc}_{1/2}\text{Nb}_{1/2}\text{O}_3$ (PSN) have proven to be valuable model compounds as due to the same ionic radii ($r_{\text{Ta}} = r_{\text{Sc}} = 0.64 \text{ \AA}$) of Ta^{5+} and Nb^{5+} in six fold coordination (Shannon, 1976) both PST and PSN have the same tolerance factor ($t = 0.977$) and they exhibit the maximum of the dielectric permittivity near room temperature.

In the model compounds PSN and PST the B site is occupied by Sc^{3+} and Nb^{5+} or Ta^{5+} . To achieve an average valence of 4+ on the B site the ratio between the two B-cations has to be 1:1. This stoichiometrically matches the ideal 1:1 B-site chemical order consisting of alternating B^{3+} and B^{5+} cations along the cubic $\langle 100 \rangle$ direction. Chemically B-site disordered perovskites have $Pm\bar{3}m$ symmetry in the paraelectric phase, while B-site ordering leads to the doubling of the perovskite structure and thus to a space group $Fm\bar{3}m$ (see Figure 1.8).

The degree of chemical B-site order can be determined using powder or single crystal XRD data: (i) by using the Bragg reflection intensities from powder XRD patterns as ratios of Q (Stenger & Burggraaf, 1980):

$$S = \frac{Q_{\text{experimental}}}{Q_{\text{theoretical}}}$$

with

$$Q = \frac{I_{(111)}}{I_{(200)}}$$

with respect to $Fm\bar{3}m$; (ii) from the site occupation factors (SOFs) of the (4a) or (4b) Wykoff positions in $Fm\bar{3}m$:

$$S = \frac{\text{SOF}(\text{B}^{3+}) - \text{SOF}(\text{B}^{5+})}{\text{SOF}(\text{B}^{3+}) + \text{SOF}(\text{B}^{5+})}$$

1 Introduction

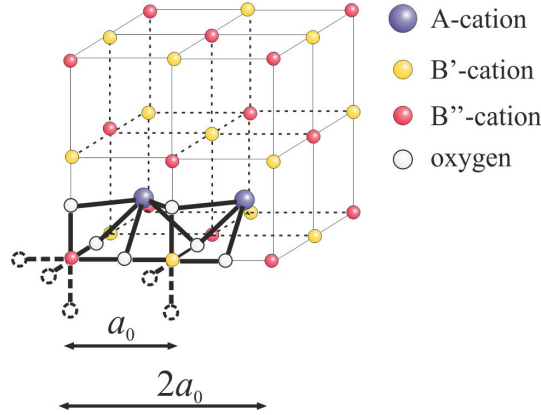


Figure 1.8: The perovskite structure with two different B-site cations B' and B'' exhibiting 1:1 order and thus leading to the doubling of the perovskite structure to $Fm\bar{3}m$. The unit-cell of the single perovskite structure $Pm\bar{3}m$ is marked with a_0 the one for $Fm\bar{3}m$ with $2a_0$.

using single crystal synchrotron data.

We used synthetic crystals grown by the high-temperature growth method Mihailova *et al.* (2007). The chemical B-site order is very low in PST $S_{\text{PST}} = 0.13$ derived from powder XRD (Mihailova *et al.*, 2008b) and $S_{\text{PST}} = 0.08$ derived from structure refinements to single-crystal synchrotron XRD data, while for PSN the chemical B-site order is below the detection limit of powder XRD and on the limit of sensitivity of single-crystal synchrotron XRD (Mihailova *et al.*, 2008a; Maier *et al.*, 2010a). This, and the absence of superlattice Bragg reflections, indicates that our PSN predominately stays in the single perovskite structure. On the length scale of Raman spectroscopy, however, all relaxors show chemical B-site ordering on the local scale and can only be interpreted in the doubled perovskite structure (Mihailova *et al.*, 2002; Welsch *et al.*, 2011).

The para-to-ferroelectric phase transition is associated with a lowering of the cubic symmetry to rhombohedral in the case of PST and PSN. Thus if the structure is chemically B-site disordered, the para-to-ferroelectric phase transition consists of $Pm\bar{3}m$ to $R\bar{3}m$ and in the case of B-site order from $Fm\bar{3}m$ to $R3$. The phase transition observed in PSN was determined as going from $Pm\bar{3}m$ $R\bar{3}m$, whereas for PST a transition from $Pm\bar{3}m$ to $R\bar{3}m$ or from $Fm\bar{3}m$ to $R3$ (depending on the degree of chemical order) has been detected (Perrin *et al.*, 2000; Woodward & Baba-Kishi, 2002). To determine the phase transition of PSN, neutron powder diffraction was used as the rhombohedral distortion was not resolved by XRD (Perrin *et al.*, 2000). In the case of B-site ordering a doubling of the perovskite structure ($Fm\bar{3}m$) is observed in the paraelectric phase by the appearance of superlattice Bragg reflections in single crystal XRD which not occurs for disordered perovskites ($Pm\bar{3}m$).

1 Introduction

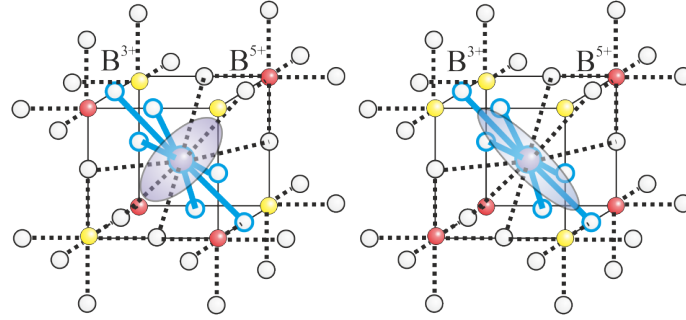


Figure 1.9: Schematic sketch of $\text{PbB}^{3+}_{1/2}\text{B}^{5+}_{1/2}\text{O}_3$ with local chemical 1:1 B-site order on the left and disorder on the right. The ellipses represent the anisotropic displacement of Pb^{2+} cations after Maier *et al.* (2011a).

Under temperature decrease both PST and PSN show the characteristic temperatures described in Section 1.3.2 due to the evolution of PNRs. The critical pressure (p_C) from the cubic to non-polar rhombohedral phase is associated with $a^-a^-a^-$ tilts and is preceded by an intermediate pressure at which the PNRs are suppressed in favor of ferroic order (see Section 1.3.3). As can be seen in Table 1.2 all characteristic temperatures and pressures are lower for PST than for PSN. Neutron powder diffraction has shown that above the intermediate pressure the anisotropic displacement ellipsoids of Pb are elongated along the cubic body diagonal for PST, while they are shaped like a flattened disk parallel to the cubic $\{111\}$ plane for PSN, see Figure 1.9 (Maier *et al.*, 2011a).

1 Introduction

Table 1.2: Sample characterization of PST and PSN

	PST	PSN	Reference
Chemical formula	$\text{PbSc}_{0.5}\text{Ta}_{0.5}\text{O}_3$	$\text{PbSc}_{0.5}\text{Nb}_{0.5}\text{O}_3$	Shannon (1976)
Ionic radius	$r_{\text{Ta}} = 0.64 \text{ \AA}$	$r_{\text{Nb}} = 0.64 \text{ \AA}$	
Tolerance factor	$t = 0.977$	$t = 0.977$	
Atomic mass of B"	180.95 u	92.91 u	
B"-O force constant	230 Nm^{-1}	210 Nm^{-1}	
	204 Nm^{-1}	188 Nm^{-1}	Repelin <i>et al.</i> (1999) ¹
Chemical 1:1 B-site order ²	$S = 0.13$	below detection limit	Mihailova <i>et al.</i> (2011)
Mean size of chemically ordered domains ³	6.4 nm	n.a.	Mihailova <i>et al.</i> (2011)
T_B	700 K	750 K	Mihailova <i>et al.</i> (2008b); Maier <i>et al.</i> (2009)
T^*	450 K	550 K	Mihailova <i>et al.</i> (2008b); Maier <i>et al.</i> (2009)
T_C	270 K	368–378 K ⁴	Mihailova <i>et al.</i> (2008b); Perrin <i>et al.</i> (2000)
p_C	1.9 GPa	4.1 GPa	Mihailova <i>et al.</i> (2008a); Maier <i>et al.</i> (2010a)

^aforce constants determined for LiTaO_3 and LiNbO_3 ; note that the relative difference in the force constants is the nearly same as that for PST and PSN (Mihailova *et al.*, 2002)

^bdetermined from the intensity ratio of the 111 and 200 Bragg peaks (Miller indices in $Fm\bar{3}m$) in the powder diffraction pattern, following Stenger & Burggraaf (1980)

^cFrom the Scherrer equation applied to the 111 diffraction peak in the powder XRD pattern

^dOur in-house powder XRD data did not reveal deviation from cubic metric down to 10 K; Bragg peaks consistent with polar rhombohedral structure were detected at 150 K by single-crystal XRD with synchrotron radiation (Maier *et al.*, 2009)

1.4.2 A- and B-site doped PST and PSN

Doping the model compounds PST and PSN has three major effects: (i) it can increase or decrease the tolerance factor; (ii) it may induce local electric field in the case of heterovalent substitution or local elastic field if the ionic radius of the substituting cation is larger than the ionic radius of the corresponding host cation; (iii) if the dopant has an isotropic outermost electron shell it disturbs the system of Pb^{2+} electron lone pairs; and (iv) it may effect the degree of B-site chemical ordering. Doping with Ba^{2+} on the A-site induces local elastic-stress as the ionic radius of Ba^{2+} (1.61 Å) is larger than the ionic radius of Pb^{2+} (1.49 Å). Also, Ba^{2+} disturbs the array of the Pb^{2+} electron lone pair as Ba^{2+} has an isotropic outermost electron shell. Thus doping with Ba^{2+} suppresses the development of ferroelectric long-range order on cooling (Cross, 1987; Bokov & Ye, 2006; Xu, 2010) and hinders the development of anti-ferrodistortive order under pressure (Maier *et al.*, 2010a, 2011a).

Doping with La^{3+} induces a local electric field due to the valence difference and thus may induce Pb vacancies which can effect the B-site stoichiometry in mixed B-cations systems. As in the case of Ba^{2+} , La^{3+} has an isotope outer most electron shell and thus disturbs the system of electron lone pairs associated with A-site Pb^{2+} . Due to the smaller ionic radius of La^{3+} (1.36 Å) the tolerance factor is reduced (see Table 1.3) which favors the development of BO_6 tilting. Sr^{2+} on the other hand does not induce any charge imbalance but it also lowers the tolerance factor ($r_{\text{Sr}^{2+}}$ 1.44 Å) and disturbs the Pb lone pairs.

Adding a third cation to the B-site induces additional chemical disorder. Doping PST with Nb^{5+} affects the B^{5+} -cation mass and the B^{5+} -O interactions without any change in the tolerance factor. Substituting the B-cation with Sn^{4+} in PST affects both Sc^{3+} and Ta^{5+} to keep the overall charge balance. In this case the tolerance factor is not effected as the ionic radius of Sn^{4+} (0.69 Å) is the average of the ionic radii of Sc^{3+} and Ta^{5+} (see Table 1.2).

Table 1.3: Sample characterization of standard A- and B-site doped PST and PSN

	Chemical formula	Tolerance factor	Unit cell parameter ¹ [Å]	Chemical B-site order: degree ²	domain size ³
PBST	$\text{Pb}_{0.78}\text{Ba}_{0.22}\text{Sc}_{0.50}\text{Ta}_{0.50}\text{O}_3$	0.985	8.265	0.11	32.8
PLST	$\text{Pb}_{0.86}\text{La}_{0.08}\square_{0.06}\text{Sc}_{0.53}\text{Ta}_{0.47}\text{O}_3$	0.971 ⁴ , 0.942 ⁵	8.128	~0.05	45.5
PLSN	$\text{Pb}_{0.70}\text{La}_{0.23}\square_{0.07}\text{Sc}_{0.62}\text{Nb}_{0.38}\text{O}_3$	0.961 ⁴ , 0.926 ⁵	4.060		
PSSN	$\text{Pb}_{0.62}\text{Sr}_{0.34}\square_{0.04}\text{Sc}_{0.51}\text{Nb}_{0.49}\text{O}_3$	0.971	4.065		
PSTN	$\text{PbSc}_{0.5}\text{Ta}_{0.36}\text{Nb}_{0.14}\text{O}_3$	0.977	4.079	0.09	4.6
PSTS	$\text{Pb}_{0.97}\square_{0.03}\text{Sc}_{0.40}\text{Ta}_{0.38}\text{Sn}_{0.22}\text{O}_3$	0.977	4.073		

¹From powder XRD at ambient conditions.

²Determined from the intensity ratio of the 111 and 200 Bragg peaks in the powder XRD pattern, according to Stenger & Burggraaf (1980). For the doped compounds the actual values may slightly deviate because of the difference in the atomic form factors between the host and dopant element on the corresponding crystallographic position.

³Mean size calculated from the FWHM of the 111 Bragg peak, using the Scherrer equation.

⁴Without taking into account the vacancies (Maier *et al.*, 2011c).

⁵Taking into account the vacancies (Maier *et al.*, 2011c).

1.4.3 Solid solutions with giant piezoelectric effect

Perovskite-type solid solutions such as $(1-x)\text{PbZn}_{1/3}\text{Nb}_{2/3}\text{O}_3$ - $x\text{PbTiO}_3$ (PZN- x PT) and $(1-x)\text{PbMg}_{1/3}\text{Nb}_{2/3}\text{O}_3$ - $x\text{PbTiO}_3$ (PMN- x PT) have been extensively studied during the past decade because of their excellent piezoelectric and dielectric properties (Chang *et al.*, 2008). The piezoelectric and dielectric responses of PZN- x PT are largest close to the morphotropic phase boundary (MPB) (Mulvihill *et al.*, 1996; Park & Shrout, 1997), which corresponds to $x \sim 0.08 - 0.10$ (La-Orautapong *et al.*, 2002). In the ferroelectric state, compositions with $x < 0.08$ show rhombohedral symmetry whereas those with $x > 0.10$ have tetragonal symmetry. The structural state at the MPB is still controversial. Based on synchrotron x-ray diffraction (XRD) analysis on poled samples it has been proposed that the polarization path between the rhombohedral and tetragonal phases is realized via an intermediate monoclinic phase (Noheda *et al.*, 2001), similar to other ferroelectric solid solutions (Guo *et al.*, 2000; Vanderbilt & Cohen, 2001). Further XRD studies on poled PZN- x PT single crystals revealed the existence of an orthorhombic phase in a narrow x -range with near-vertical boundaries on both sides (La-Orautapong *et al.*, 2003) (see Figure 1.10). The orthorhombic phase has the space group $Amm2$ with the net polarization P being along the cubic $[011]$ direction, which is the limiting case of the monoclinic phase Pm , also called the M_C phase (Vanderbilt & Cohen, 2001), with P along the cubic $[0vw]$ direction. Neutron diffraction on unpoled crystals showed that at the MPB an orthorhombic or monoclinic phase may exist along with a tetragonal phase (Uesu *et al.*, 2002). On the other hand, piezoresponse force microscopy studies give evidence for the coexistence of domains with various symmetries, including a possible combination of rhombohedral and tetragonal symmetries (Madeswaran *et al.*, 2005; Scholz *et al.*, 2009).

The single components of PZN- x PT are quite different in their structural behavior, leading to a very complex local structure of the mixed compound. PT is a normal ferroelectric undergoing a cubic-to-tetragonal phase transition at the Curie temperature T_C , whilst PZN is a relaxor ferroelectric (or relaxor) undergoing a sequence of phase transformations from a cubic to a rhombohedral phase with a few intermediate states consisting of polar nanoregions dispersed into a non-polar matrix (La-Orautapong *et al.*, 2003; Jeong & Lee, 2006). In addition, PZN possesses a strong chemical inhomogeneity due to the occupation of the B-site by two- and five-valent cations. This leads to a frustration between charge neutrality and lattice strain which on the local scale results in the formation of chemically 1:1 B-site ordered nanoregions of type $A(\text{B}^{2+}_{2/3}\text{B}^{5+}_{1/3})_{1/2}\text{B}^{5+}_{1/2}\text{O}_3$ (Yan & Pennycook, 1998). The structure of PZN- x PT is even more puzzling because above the critical temperature PNRs are formed (as in the case of relaxors) and at $T < T_C$ the PNRs persist, coexisting with the complex pattern of ferroelectric domains with established long-range order. Neutron elastic diffuse scattering revealed that the internal structure of PNRs is independent of x and is most probably of the rhombohedral-type, but the growth direction of PNRs changes

1 Introduction

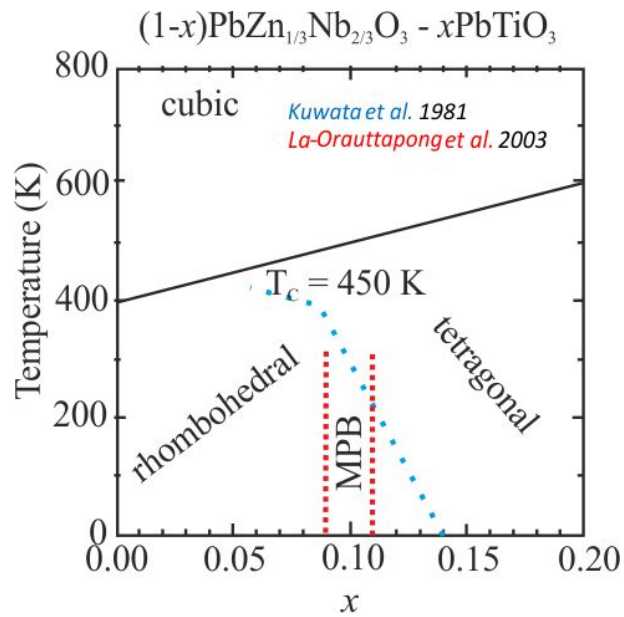


Figure 1.10: Phase diagram of $(1-x)\text{PZN}-x\text{PT}$ showing the x range for the rhombohedral and tetragonal structure (Kuwata *et al.*, 1981) as well as the range of the morphotropic phase boundary (La-Orauttapong *et al.*, 2003). The phase transition temperature at ambient pressure for 0.9PZN-0.1PT is $\sim 450 \text{ K}$.

from the cubic $\langle 111 \rangle$ to approximately $\langle 001 \rangle$ direction when x increases from 0 to 0.09 (La-Orauttapong *et al.*, 2003).

2 Objectives

"Science isn't about why,
it's about why not"
-Cave Johnson-

The aim of this study is threefold: First studies in this work concerned the pressure-induced structural changes up to 30 GPa in pure and doped PST and PSN were studied by complementary Raman and XRD, in order to check whether or not the anti-ferrodistortive order is enhanced at very high pressure and to better understand the effect of chemical variations on the structure. All compounds studied here have previously been analyzed at different temperatures ranging from 100–800 K by XRD and Raman spectroscopy as well as in the "low"-pressure regime below 10 GPa by single-crystal in-house and synchrotron XRD, neutron powder diffraction, Raman spectroscopy (see Section 1.4.1).

Second to gain further insights into the competitive behavior between polar and anti-ferrodistortive order in situ high-temperature high-pressure Raman spectroscopy at temperatures above the critical temperature in the ergodic relaxor state $T_C < T_1 < T^*$ and $T^* < T_2 < T_C$ was applied.

Third, the ferroelectric structure of the solid-solution $(1-x)\text{PbZn}_{1/3}\text{Nb}_{2/3}\text{O}_3-x\text{PbTiO}_3$ was studied by combined Raman scattering and XRD at ambient pressure and different temperatures from 800–100 K as well as at ambient temperature and different pressures up to 18 GPa to elucidate the origin of the giant piezoelectric effect for x close to the morphotropic phase boundary.

3 Methods

3.1 Raman spectroscopy

3.1.1 A short history

In 1923 A. Smekal predicted the inelastic scattering of light by assuming that light has a quantum structure. He showed that scattered monochromatic light would consist of its original wavelength as well as of higher and lower wavelengths (Smekal, 1923). On February 28th 1928 C. V. Raman and K. S. Krishnan first observed this wavelength shift using the sun as a light source (which was later replaced by a mercury lamp) recording the scattering of benzene (Raman & Krishnan, 1928). At the same time G. Landsberg and L. Mandelstam observed inelastic light scattering from a quartz crystal and explained the observed wavelength-shifted spectra by correlated atomic vibrations(vibrational modes) interacting with light (Landsberg & Mandelstam, 1928). However, the credit as well as the Nobel price in 1930 went to C. V. Raman for his work on the scattering of light and the phenomenon was named after him.

White light is a mixture of electromagnetic waves in the range of ca. 400–700 nm (Figure 3.1). The electromagnetic wave can be described as consisting of electric- and magnetic fields oscillating perpendicular to each other and perpendicular to the direction of propagation (Figure 3.2).

3.1.2 The Raman scattering effect

The terms light, electromagnetic wave and radiation all refer to propagation of electromagnetic energy. The characteristic parameters for each electromagnetic wave are: (i) frequency (f) measured in (Hz); (ii) wavelength (λ) measured in units of length usually μm , nm or \AA ; and (iii) energy (E) measured in electronvolts (eV). The shortest distance between two successive points oscillating in phase is the wavelength (λ) which is defined as (Figure 3.2):

$$f = \frac{1}{\tau}$$

with

$$\lambda = \frac{c}{f}$$

where c is the light velocity f is the number of oscillations per second and τ is the period of oscillation. According to the wave-particle dualism, light can be also regarded as a beam

3 Methods

of quasi particles with zero mass in rest, carrying a quantum of light energy. A quantum of light called a photon has a quasi-momentum \mathbf{p} of:

$$\mathbf{p} = \frac{h\nu}{c} \mathbf{e} = \hbar \mathbf{k}$$

and an energy of:

$$E = \hbar \omega$$

where h is the Planck's constant and $\hbar = \frac{h}{2\pi}$, \mathbf{k} is the wavevector with a magnitude of $\frac{2\pi}{\lambda}$ which describes the direction of the wave propagation \mathbf{e} (\mathbf{e} being the unity vector), and ω is the angular frequency ($2\pi f$). On the other hand, the motion of each particle with non-zero mass (m) and momentum $p = \frac{mv}{v}$ (with m being the mass of the particle and v its velocity) can be expressed according to quantum mechanics by the *de Broglie* wave having a de Broglie wavelength:

$$\lambda = \frac{h}{p} = \frac{2\pi\hbar}{\sqrt{2m_0E_{kin}}}$$

where E_{kin} is the kinetic energy and m_0 the reduced mass.

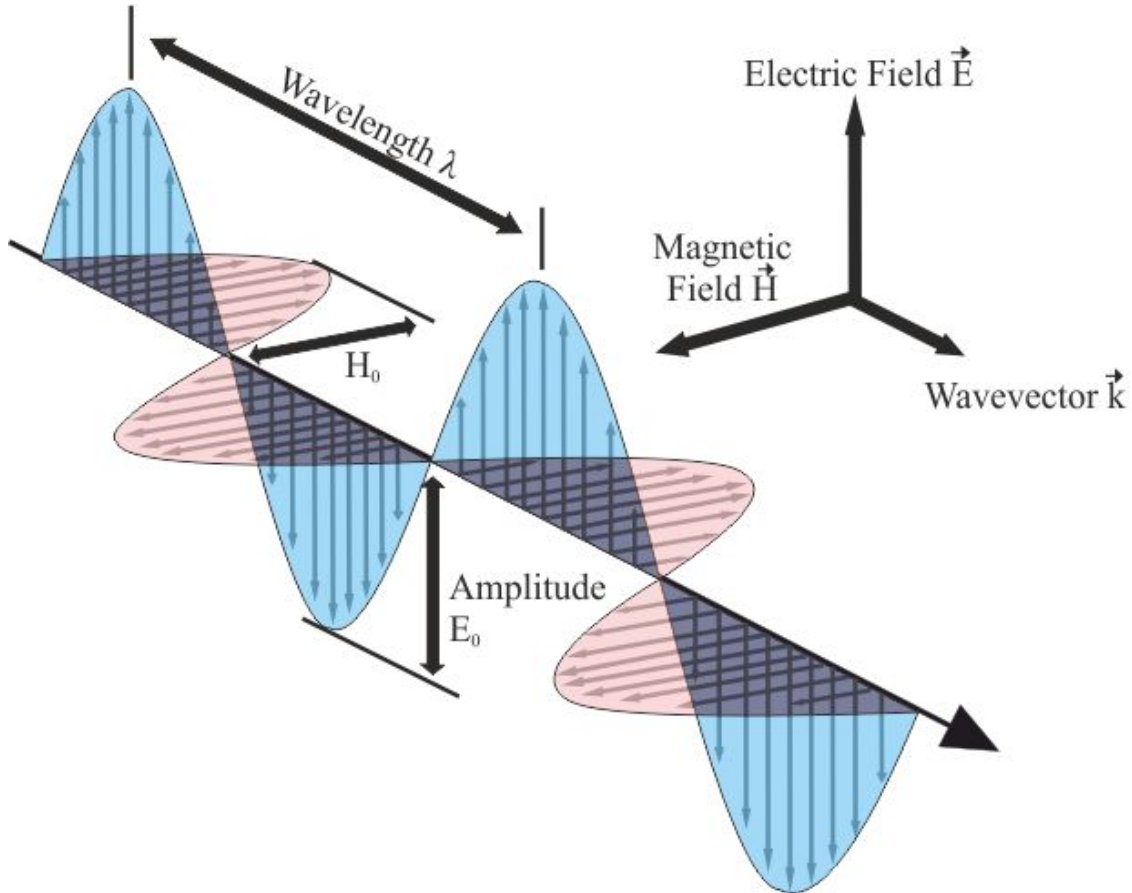


Figure 3.1: Electromagnetic spectrum indicating the different spectroscopic methods to the frequency regions and the associated quantum transitions after Geiger (2004).

3 Methods

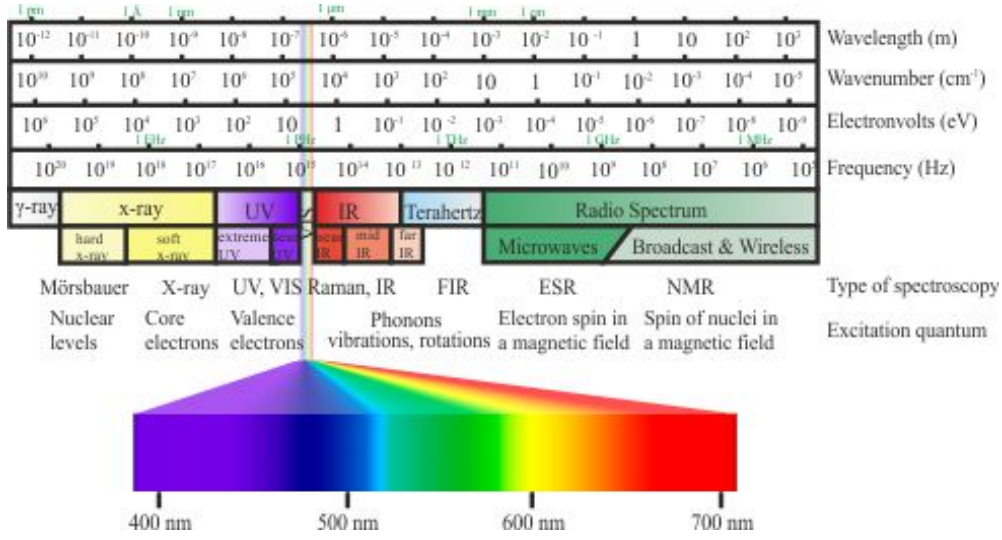


Figure 3.2: Schematic sketch of an electromagnetic wave. The magnetic field (red) and electric field (blue) are perpendicular to each other and perpendicular to the direction of propagation. The wavelength λ is the distance between to equal points; the amplitude is the maximum magnitude of the oscillating parameter.

The correlated motion of two coupled atoms can be described by a harmonic oscillator. The exact frequency is governed by the interatomic force constant K and the reduced mass m of the participating atoms. In the case of a monoatomic chain composed of identical atoms:

$$\omega = \sqrt{\frac{K}{m}}.$$

Atoms in a crystal are strongly coupled and thus correlated motions around the equilibrium positions of the crystal obey symmetric restrictions. The number of possible vibrations within a crystal having N atoms in the primitive unit cell vibrating in 3D-space can be replaced by a system of $3N$ normal phonon modes. The phonon modes represent quanta of vibrational energy in the crystal and are similar to photons as they are characterized by frequency and wavevector of the corresponding normal elastic waves. If there are more than one atoms in the primitive unit cell ($N > 1$) from those $3N$ normal elastic waves three are acoustic and $3N - 3$ are optical phonon modes. While the acoustic displacement involved in phonon modes are in-phase, the atoms in optical phonon modes vibrate out-of-phase and thus induce dipole moments which can interact with the electric field of light. The optical and acoustic phonon modes can be further differentiated into longitudinal and transversal. Longitudinal modes show an atomic displacement, i.e., polarization of the elastic wave parallel to the wave propagation while transverse modes show a perpendicular displacement with respect to the wave propagation. If the photon energy is close to the phonon energy, the interaction between those two can lead to absorption of the photon, which is the case of IR absorption spectroscopy (see Figure 3.1). An excitation of phonon by absorption is not possible in the near-IR, visible and near-UV

3 Methods

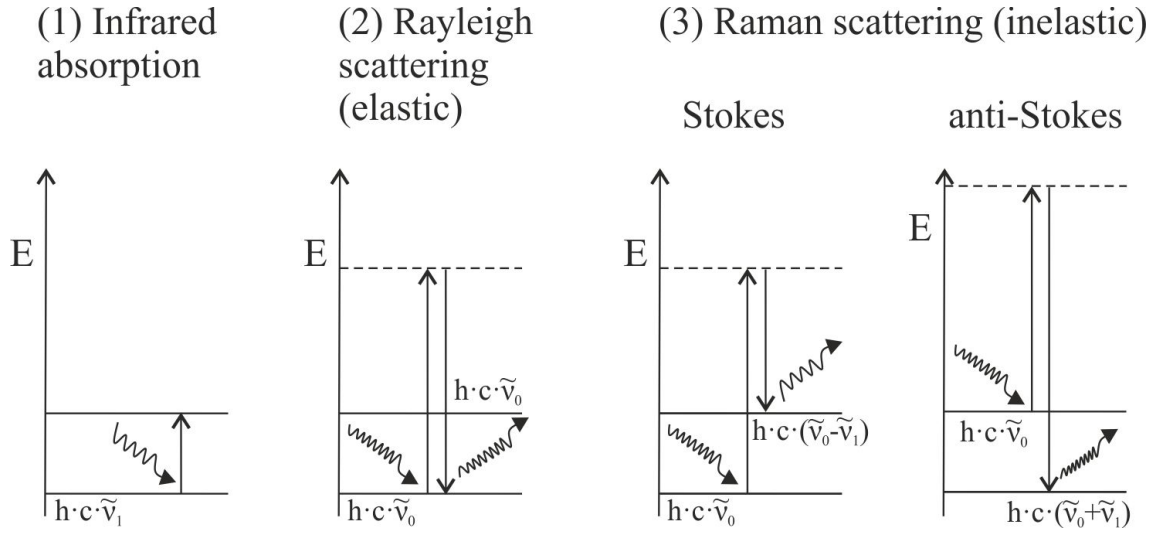


Figure 3.3: Schematic sketch of photon interactions with matter: (1) Infrared absorption, the photon energy corresponds to the energy difference between two allowed vibrational states. (2) Rayleigh scattering, excitation to a virtual electronic state (dashed line) from which the system recovers immediately. The incident and the scattered light have the same energy. (3) Raman scattering, the vibrational state after the photon-phonon interaction is either higher or lower than the initial state. The scattered phonon energy is decreased (Stokes) or increased (anti-Stokes) with respect to the initial photon energy, after Nasdala *et al.* (2004).

range due to substantial frequency differences. However, the electric field of the incident light can interact with the electron cloud around the vibrating atomic nuclei, leading to scattering processes.

If an initial photon excites the phonon to a "virtual" non-stationary energy level and the emitted photon returns from the intermediate transition to lower levels having the same energy and frequency as the initial photon, the scattering process is elastic and it is called Rayleigh scattering (Figure 3.3). This is the dominant scattering effect. However, a small fraction of the emitted photons ($\sim 10^{-5}$ times lesser than elastically scattered) show an energy shift to lower or higher wavelength. This process of inelastic scattering where the energy of the initial photon is not conserved during its return from the vibrating atoms is called Stokes and anti-Stokes scattering respectively (Figure 3.3). Inelastic light scattering by optical phonon modes is called Raman effect. Due to the differences in the wavevectors, only phonons in the vicinity of the Brillouin-zone center (the Γ point, with phonon wavenumber $\bar{q} = 0$) can scatter photons. During the Stokes inelastic light scattering process, the phonon is excited from the ground state to a virtual energy state and then relaxes back to an energy level higher than the initial ground state. In the case of anti-Stokes scattering it is vice versa: the initial energy state has an energy higher than the energy of the ground state and the phonon relaxes back to the lowest-energy ground state. Since the population fraction of the ground state is commonly higher than that of

3 Methods

the excited states, the probability of Stokes scattering is higher than the probability of anti-Stokes scattering. Thus, in Raman spectroscopy experiments usually only the Stokes scattering is recorded, because the Stokes peak intensity is higher than the anti-Stokes peak intensity. However, the population of phonon states and consequently the Stokes and anti-Stokes intensities depend on the temperature. This dependence is described by the Boltzmann distribution:

$$\frac{N_1}{N_0} = \frac{g_1}{g_0} e^{-\frac{\Delta E}{k_B T}}$$

with $\frac{N_1}{N_0}$ being the fractional number of particles occupying a set of states i possessing the energy E_i , k_B is the Boltzmann constant, g is the degeneracy and T is temperature. The intensity of the Raman spectra is due to the probability of Stokes and anti-Stokes scattering to occur which can be derived from the Boltzmann distribution. From this it follows that the Raman intensity of Stokes and anti-Stokes scattering is dependent on temperature and the intensity ratio of Stokes and anti-Stokes can therefore be used for temperature estimated.

$$\frac{I_{AS}}{I_S} = e^{-\frac{\hbar\omega}{kT}}$$

3.1.3 Phonon modes

The number and type of expected phonon modes for a crystal can be calculated by group theory analysis, if the space-group symmetry and the occupied Wyckoff positions are known. For these calculations the Bilbao Server offers a tool called SAM (Kroumova *et al.*, 2003) which gives the expected phonon modes for a given point group and selected Wyckoff positions. In addition this tool provides information about the type of vibration with respect to the corresponding symmetry elements as well as the polarisability of the expected phonon modes and whether the modes are IR- and/or Raman-active.

In literature, phonon modes are addressed to in several ways. Group theory analysis, which refers to phonon modes as irreducible representations, often uses the so called Mulliken symbols (see Table 3.1). Here the capital letters gives information about the degeneration, i.e., if two different vibrations have the same frequency thus being equal in phonon energy, while the subscripts g and u describe whether the modes are symmetric (g) and anti-symmetric (u) with respect to the center of inversion. The subscripts 1 and 2 denote whether the mode is symmetric or anti-symmetric upon rotation about the center of the atom, while the superscript ' and " denote whether the mode is symmetric or anti-symmetric with respect to a mirror plane horizontal to the principal rotational axis.

Another common nomenclature is the Miller-Love notation, which is often used in solid-state spectroscopy. This notation uses capital letters giving the points in the Brillouin zone and labels the modes from the highest symmetry mode ($i=1$) to the lowest ($i=n$) (X_i). In molecular spectroscopy two types of ν -nomenclature are commonly used: (i) ν_i numbers

3 Methods

the vibrations from the highest symmetry mode ($i=1$) to the lowest ($i=n$) to avoid the need to specify symmetry details; (ii) Greek letters symbolize the different types of vibrational movements, subscripts indicate whether the movement is symmetric (s) or anti-symmetric (a or as) (see Table 3.2).

Infrared (IR) and Raman spectroscopy both measure the vibrational energies but modes active in IR and Raman spectroscopy obey different selection rules. The IR-activity of a vibrational mode is related to an induced dipole moment due to the off set of the center of gravity of positively charged ions and negatively charged ions during the oscillation, whereas the Raman-activity is related to the change of the electronic shell induced by the oscillation of the nuclei, i.e., for a vibrational mode to be Raman-active there must be a change in the polarization α (see Figure 3.4). The governing equation using classical theory of light scattering describes the induced dipole moment (μ_{ind}):

$$\mu_{ind} = \alpha_0 \varepsilon_0 \cos(2\pi\nu_0 t) + \frac{1}{2} \left(\frac{\delta\alpha}{\delta q} \right)_0 \Delta q \varepsilon_0 (\cos[2\pi(\nu_0 + \nu_R)t] + \cos[\nu_0 - \nu_R]t)$$

were α_0 is the equilibrium polarisability, ε_0 the equilibrium amplitude of the radiation, ν_0 the frequency of the incident light, t the time, Δq the change in a normal coordinate of a vibration and $\left(\frac{\delta\alpha}{\delta q} \right)_0$ the change in polarisability with respect to a change in a normal coordinate. The first term of the equation describes the elastic Rayleigh scattering and the second and third terms describe the anti-Stokes and Stokes scattering. Thus for Raman scattering to occur the polarisability must change during a normal vibration of the mode to be Raman active.

$$\left(\frac{\delta\alpha}{\delta q} \right)_0 \neq 0.$$

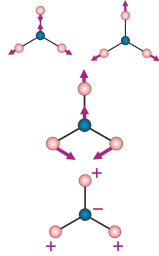
Due to anisotropic properties of crystals the lattice waves have directional properties. The Raman scattering intensities depend on the orientation of the crystallographic axis with respect to the direction and polarization of both the incident and scattered light. The orientation of a single crystal in Raman spectroscopy is generally specified by the Porto notation (Damen *et al.*, 1966). The three axis of the coordinate laboratory system x , y , z do not necessary coincide with the crystallographic axis of the crystal structure. In Porto's notation the first symbol gives the direction of the incident and the last symbol the

Table 3.1: Irreducible representations of phonon modes

Mode designation	Description
A	non-degenerated (single) symmetric mode, with respect to the principle rotation axis n
B	non-degenerated (single) anti-symmetric mode, with respect to the principle rotation axis n
E	doubly degenerated only in uniaxial and cubic crystals
F or T	triply degenerated (occurs only in lattices with cubic symmetry)

3 Methods

Table 3.2: Basic types of vibrations and their description using Greek symbols

Symbol	Description	Carbon group XY_3 -type
ν	commonly two-particle vibration changing mainly the bonds (stretching)	
δ	three-particle vibration within the plane of the bond angle (bending)	
π	membrane-type vibrational mode leading to non-coplanarity of the atoms involved	
ρ ω, τ	rocking wagging and twisting of CH_2 -type organic molecules	

direction of the scattered beam with respect to the laboratory coordinate system directions. The symbols in parentheses specify the polarization directions of the incident (first symbol) and the scattered (second symbol) light. Thus they identify the particular element of the Raman tensor which causes the observed Raman scattering.

3 Methods

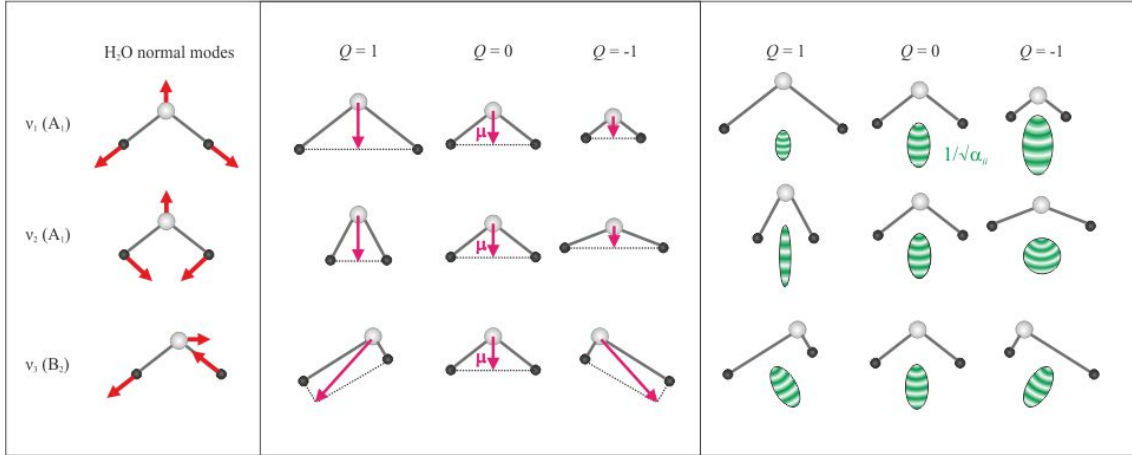


Figure 3.4: Schematic stretching and bending of a two atomic molecule H₂O (first column). A phonon mode is IR active if the vibration causes a change in the dipole moment ($\Delta\mu \neq 0$) (second column) and Raman active if the vibrations causes a change in the polarizability ellipsoid (third column) (pictures taken from B. Mihailova lecture 9 and 10 "Beugung und Spektroskopie" 2011 Universität Hamburg).

3.1.4 Converting energy units

Raman spectra are generally plotted as the Raman intensity vs. energy. The traditional units for the x-axis are "wavenumbers of shift from the exciting wavelength" the so-called Raman shift. Wavenumber ($\bar{\nu}$) is the reciprocal wavelength (λ)

$$\bar{\nu} = \frac{1}{\lambda} = \frac{f}{c}$$

where the wavelength (λ) is generally expressed in cm, f is the frequency and c is the speed of light. The Raman shift on a given vibration is a measure of energy of those vibrations. As such it is independent of the excitation wavelength used. To convert between the different energy units (cm^{-1} , nm, eV) which are used in spectroscopy the following equation for energy (E) using the Planck's constant (h):

$$E = hc\bar{\nu} = \hbar ck = hf$$

where k is the angular wavenumber ($\frac{2\pi}{\lambda}$) and f is the frequency. Using this equation it follows that the relation

$$c = \frac{f}{k}$$

gives the conversion from Hz to cm^{-1} and

$$k \cdot \lambda = 1$$

gives the conversion from cm^{-1} to nm.

3.1.5 Group-theory analysis and Raman peak assignment for Pb-based perovskite-type relaxors

As described in section 1.2 the ideal perovskite structure is $Pm\bar{3}m$ though if two B-site cations are present chemical 1:1 ordering of the structure can lead to a doubling of the unit cell and results in face-centered cubic symmetry $Fm\bar{3}m$. For such symmetries and the occupied Wyckoff positions in the perovskite structure the corresponding phonon modes at the Γ point of the Brillouin-zone are given in Table 3.3. The letters R, IR, and I stand for Raman-active, IR-active and inactive, respectively.

Table 3.3: Wyckoff positions and corresponding phonon modes

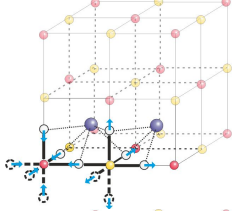
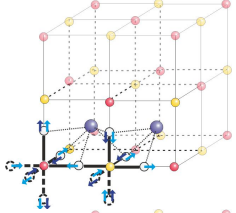
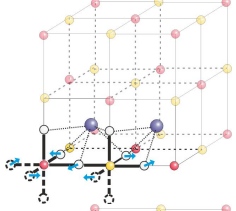
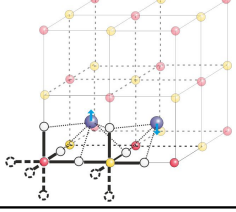
Atoms	Wyckoff position, $Pm\bar{3}m$	Phonon mode, $Pm\bar{3}m$	
		acoustic	optic
A	1a	F_{1u}	
B	1b		F_{1u} (IR)
O	3c		$2F_{1u}$ (IR) + F_{2u} (I)
Atoms	Wyckoff position, $Fm\bar{3}m$	Phonon mode, $Fm\bar{3}m$	
		acoustic	optic
A	8c	F_{1u}	F_{2g} (R)
B'	4a		F_{1u} (IR)
B''	4b		F_{1u} (IR)
O	24e		A_{1g} (R) + E_g (R) + $2F_{1u}$ (IR) +
			F_{1g} (I) + F_{2g} (R) + F_{2u} (I)

The F_{1u} irreducible representation associated to A-site cations was assigned to the acoustic vibration because Pb is the heaviest element in the structure, i.e., it should generate low-wavenumber vibrations. Symmetry analysis cannot distinguish between IR active and acoustic modes and therefore this distinction has to be made on the basis of physics. As there are always 3 acoustic modes and the wavevector should be small the heaviest atom is the most likely to generate this mode. Though only a small degree of chemical B-site ordering or none has been detected in our model compounds (see Table 1.2) previous analysis (see Section 1.3) have shown that the spectra should be interpreted in terms of doubled perovskite structure. Therefore, on the local scale B-site chemical ordering is always present, which is typical of all Pb-based relaxors with mixed B-site cations. Through the difference in the masses of Ta^{5+} and Nb^{5+} , Ta being heavier than Nb, as well as the selection rules and polarizability tensors for the cubic $Fm\bar{3}m$ it is possible to assign the four allowed Raman-active modes ($A_{1g} + E_g + 2 F_{2g}$) to the Raman spectra (Mihailova *et al.*, 2002). The assignment of the allowed Raman active modes is given in Table 3.4.

It is widely believed that PNRs have a fluctuation time of 10^{-7} to 10^{-6} s which makes them appear static to Raman spectroscopy, which is sensitive to dynamic phenomena with

3 Methods

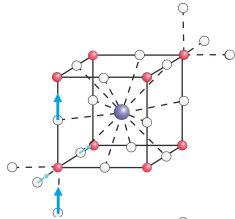
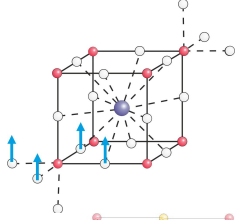
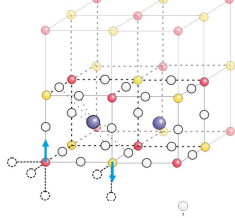
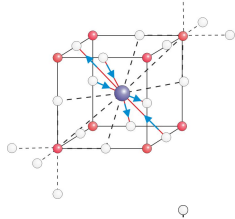
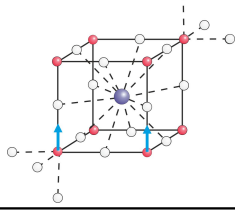
Table 3.4: Mode assignment for the symmetry-allowed Raman active modes in $Fm\bar{3}m$

Mode	Approximate wavenumber	Phonon vibration	
A_{1g}	820 cm^{-1}	symmetric BO_6 stretching	
E_g	800 cm^{-1}	symmetric B-O stretching	
F_{2g}	550 cm^{-1}	O-B-O symmetrical bending	
F_{2g}	50 cm^{-1}	Pb vibrations	

lifetimes larger than the period of phonon oscillations, which is $\sim 10^{-12}$ s. Thus it is not unexpected to see a contribution of the PNRs in the Raman spectra as this is sensitive to intermediate- and short range order. Those Raman bands that could not be assigned to the expected Raman-active modes are caused by the local distortions in the structure by the PNRs and can thus be related to the infrared and in-active modes of $Fm\bar{3}m$ ($4 F_{1u} + F_{1g} + F_{2u}$) (see Table 3.5). The F_{1u} mode related to the A-cation is an acoustic mode.

3 Methods

Table 3.5: Cubic phonon modes, which generate peaks in the Raman spectra of relaxors due to the local structural disturbance associated with PNRs. After Welsch *et al.* (2011)

Mode	Approximate wavenumber	Phonon vibration	
F_{1u}	700, 590 cm^{-1}	anti-symmetric BO_6 stretching	
F_{1u}	430 cm^{-1}	anti-symmetric BO_6 bending	
F_{1u}	240 cm^{-1}	B-site cation vibrations, this mode exists only in $Fm\bar{3}m$	
F_{2u}	350, 300 cm^{-1}	Pb-O bond stretching within the $\{111\}$ plane can be considered as BO_6 tilting	
F_{1u}	$\sim 140 \text{ cm}^{-1}$	Pb- BO_3 translation	

3.1.6 The Raman spectrometer available at the Institute of Mineralogy and Petrology

We are using a Horiba Jobin-Yvon T64000 triple-grating spectrometer equipped with an Olympus BH41 microscope operatin in subtractive and additive mode (see Figure 3.5). In subtractive regime we can achieve a spectral resolution of 2 cm^{-1} and measure the Raman shift down 15 cm^{-1} if visible lasers are used, which is extremely important for studying phase transitions. At the same time, if necessary the spectral resolution can be substantially increased by using the additive mode.

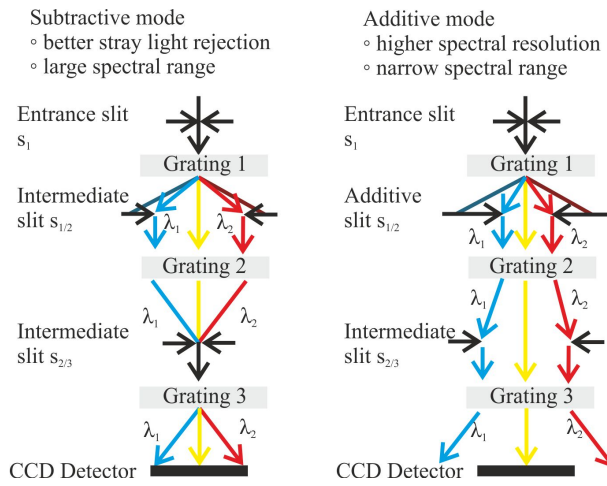


Figure 3.5: Schematic sketch of the additive and subtractive mode for triple monochromators. After Adar *et al.* (2003).

3.2 X-ray diffraction

Diffraction experiments are based on the scattering effect of an incident x-ray beam by a crystalline material. According to different techniques the scattered beam can be described as a function of the scattering angle, wavelength, or energy.

3.2.1 Principles of diffraction

X-rays have a wavelength of $0.01\text{--}10\text{ nm}$ which is within the same order of magnitude as the unit-cell parameters of crystalline materials. Such periodically arranged atoms, or rather their electron clouds, can interact with an electromagnetic wave by elastic scattering, leading to constructive and destructive superposition of the scattered wave. The constructive scattering in a certain direction is described by the Bragg's law:

$$2d_{hkl} \sin \theta = n\lambda$$

3 Methods

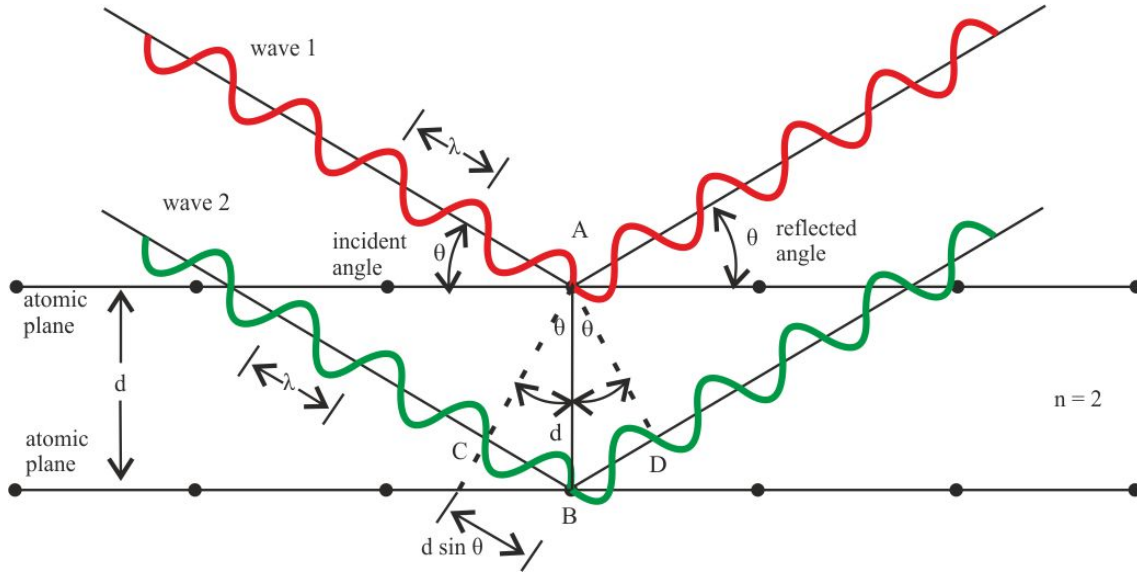


Figure 3.6: Schematic stretching of Bragg's law which can be derived from the triangle ABC.

where d is the spacing between atomic or diffracting layers and hkl are the Miller indices (see Figure 3.7), θ is the incident angle, n is the order of scattering, and λ is the wavelength. Thus diffraction experiment can be carried out either by using a fixed wavelength and changing the scattering angle or by having a fixed angle and using polychromatic light.

While the Bragg equation describes the scattering from the geometric point of view, the conditions for constructive interference are also described by the Laue equations:

$$a(\cos \varphi_a - \cos \varphi_{a0}) = h\lambda$$

$$b(\cos \varphi_b - \cos \varphi_{b0}) = k\lambda$$

$$c(\cos \varphi_c - \cos \varphi_{c0}) = l\lambda$$

with φ_{a0} , φ_{b0} , and φ_{c0} being the angle of the incident beam and φ_a , φ_b , and φ_c the angle of the propagating wave respectively, h , k , l being integers. Thus diffraction occurs in three dimensions if all three Laue equations are satisfied for each direction in space.

Using Miller indices each diffraction peak (also called Bragg peak or reflection) can be represented as a vector hkl defined in the reciprocal space lattice. Miller indices can also be used to describe layers, plans and directions which is indicated by different kinds of brackets (see Table 3.6). The distinction between the different meanings is indicated by brackets as shown in Table 3.6. If the indicated direction or plane is in the reciprocal space this is indicated by an asterisk (*). Any such integer triple in the reciprocal space can be

3 Methods

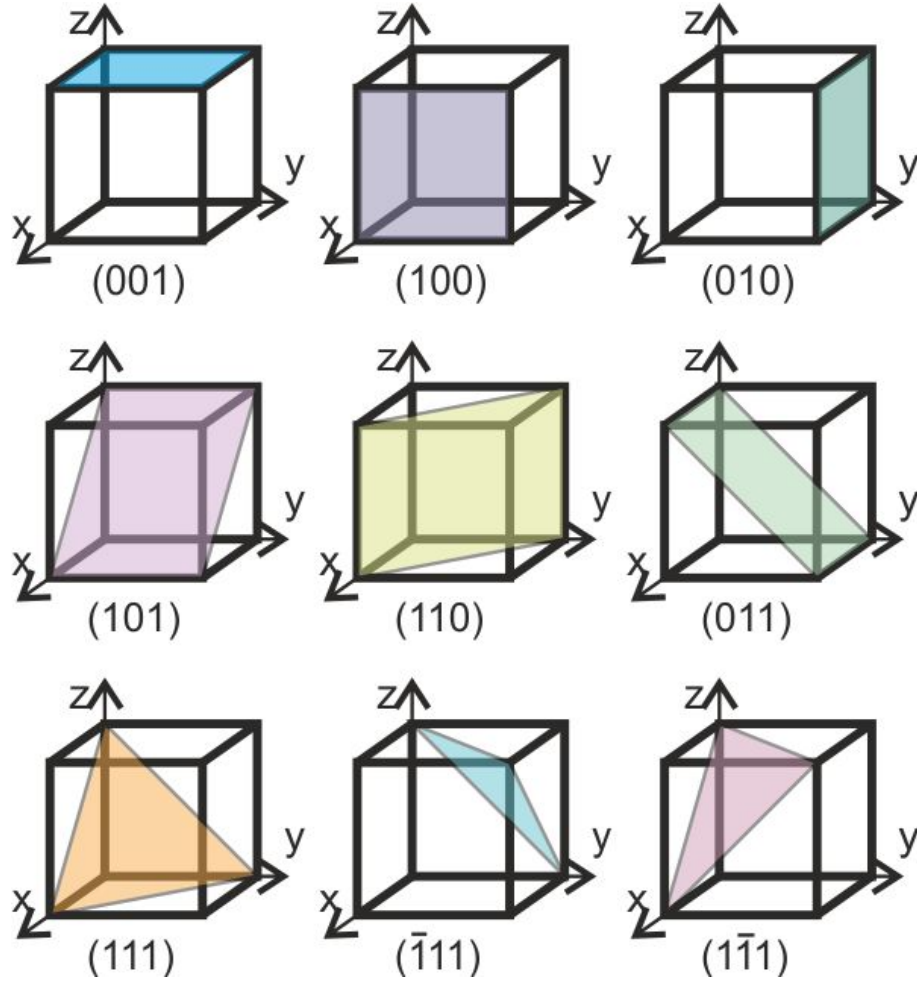


Figure 3.7: Miller indices indicating the plane perpendicular to the vector given for the cubic structure.

assigned to a d -spacing if the unit cell parameters are known. For the cubic system with $a = b = c$ and $\alpha = \beta = \gamma = 90^\circ$ the d -spacing can be determined as follows:

$$\frac{1}{d_{hkl}^2} = \frac{h^2 + k^2 + l^2}{a^2}$$

Both single crystals and powders are studied by x-ray diffraction. The use of powders has the advantage that several different lattice planes simultaneously satisfy Bragg's law at a given scattering angle. Single-crystal XRD has the advantage of giving very precise information of the atomic structure, while unit-cell parameters are better determined by powder XRD. If synchrotron radiation is used, single-crystal diffraction is able to resolve weak diffuse scattering from PNRs as well as weak reflections arising from chemical B-site ordering.

Table 3.6: The meaning of different brackets and symbols in diffractometry

Symbol	Description
$[\]$	specific crystallographic direction
$\langle \rangle$	all symmetrically equivalent crystallographic directions
$()$	a specific crystallographic plane
$\{ \}$	all symmetrically equivalent crystallographic planes
*	belonging to reciprocal space

3.2.2 Diffuse x-ray scattering in Pb-based relaxors

As x-ray diffraction is sensitive not only to the periodic long-range atomic order, but also to structural inhomogeneities on the mesoscopic scale as extended defects or domain walls do not generate Bragg peaks. However, they produce diffuse scattering of characteristic shapes. The existence of PNRs possessing a ferroelectric order on the intermediate scale is unique for relaxors and relaxor-based systems. Since PNRs are local ferroic inhomogeneities in the average structure, the observation of x-ray diffuse scattering is a direct indicator of their presence (Welberry & Goossens, 2008; Pasciak *et al.*, 2007) (see Section 1.3.1).

3.3 The diamond-anvil-cell technique

There are many different types of diamond anvil cells (DACs) and nearly every laboratory dedicated explicitly to high-pressure experiments has its own specifications depending on the experiment and experimental conditions. Due to the simplicity of the original design the general setup for all DAC has not changed during the years. Two opposing diamonds compress a gasket which holds the pressure chamber. Using a pressure-transmitting medium, the applied force is transformed into hydrostatic pressure (see Figure 3.8).

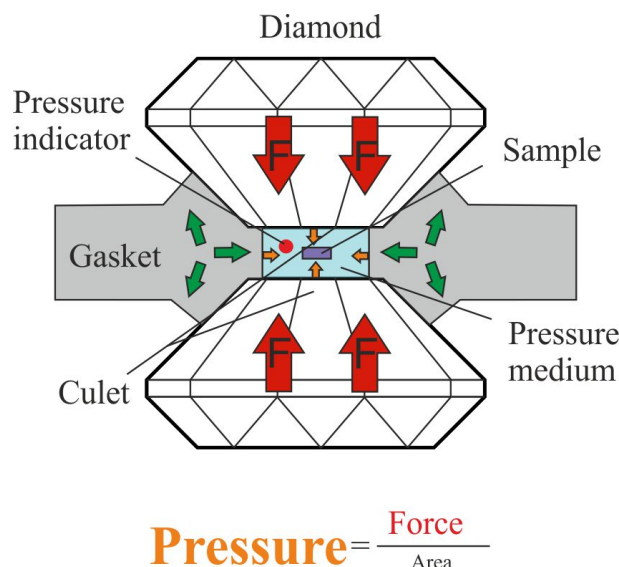


Figure 3.8: Schematic sketch of a diamond anvil cell.

As pressure (p) is defined by force (F) per area (A) a relatively small force on a small area leads to a high pressure. The SI unit for pressure is *pascal* while it is also common to use *bar*. They can be recalculated as follows:

$$\begin{aligned} 1 \text{ bar} &= 0.1 \text{ MPa} \\ 1 \text{ kbar} &= 100 \text{ MPa} = 0.1 \text{ GPa} \\ 10 \text{ kbar} &= 1000 \text{ MPa} = 1 \text{ GPa} \end{aligned}$$

Depending on the setup (diamond size and culet diameter, gasket material, pressure medium) DACs can reach pressures up to the *megabar*-range ($\sim 100 \text{ GPa}$) which is estimated to be the pressure of the lower mantle.

3.3.1 Diamond anvils

Diamond is used for anvils for two reasons (i) diamond is the hardest single crystal and (ii) diamond is transparent for electromagnetic radiation in the x-ray to infrared range. For different types of experiments different types of diamonds are available with different cuts and purity. The cut of the diamond has strong impact on the opening angle of the cell which is of high importance for methods like XRD and Brillouin spectroscopy.

3 Methods

Diamond is classified into two major groups depending on the quality and nature of the impurities (see Table 3.7). As can be seen from Table 3.7 impurities can be detected by IR spectroscopy. The diamond anvil best suited for Raman spectroscopy is of the IIa type and does not absorb in the UV and IR region but this type is quite expensive due to its rarity. Therefore diamonds of Ia type are also used for Raman spectroscopy but they should have low fluorescence. In addition to the caused optical effects, by impurities also influence the mechanical properties of the diamonds.

The maximum pressure a diamond anvil can withstand in an experiment is related to the diameter of the culet (working area). Generally it can be said that the smaller the culet the higher the pressure which can be reached but it also depends on the purity of the diamond. Though IIa diamonds are the hardest they are also brittle while diamonds of the Ia type are more resistant to plastic deformations giving additional security to the experiment (Eremets, 1996). The maximum pressure (p_{max}) is limited by the culet diameter (d). This limit is not well defined but can be estimated as follows (Dunstan & Spain, 1989)

$$p_{max}(GPa) = \frac{12.5}{d^2(mm)}.$$

The anvil shape and cut appear not to be too critical for pressures up to ~ 30 GPa. Most diamonds on the market are shaped in the modern brilliant cut (see Figure 3.9) which is composed of the best possible angles to enhance the brilliance, i.e., the amount of white light reflected from the diamond facets and the fire i.e., flashes of spectral color. This cut is slightly modified for high-pressure experiments in such a way that the culet diameter is enlarged. At higher pressures large elastic strains are known to occur, in particular on the anvil tips causing considerable elastic deformation (Merkel *et al.*, 1999). The Dukker and Boehler-Almax (see Figure 3.9) diamond cut has a larger table diameter at the same weight as the brilliant cut as well as increased anvil angles and waist. A further modification is the so called beveling (see Figure 3.10) which adds up to four additional facets to the culet. This allows the stress supporting the diamonds by the gasket to be optimized and thus the diamonds to withstand pressures in the megabar range.

As a hard monocrystalline material diamond is very strong in compression in certain directions. The DAC is thus designed to load the diamonds by straight-line movements along the z-axis. Any other movement is likely to break a diamond. Thus it is very important to have the diamonds aligned perfectly to each other. The diamonds should be aligned in such a way that they do not have an off-set and are parallel to each other (see Appendix B).

3 Methods

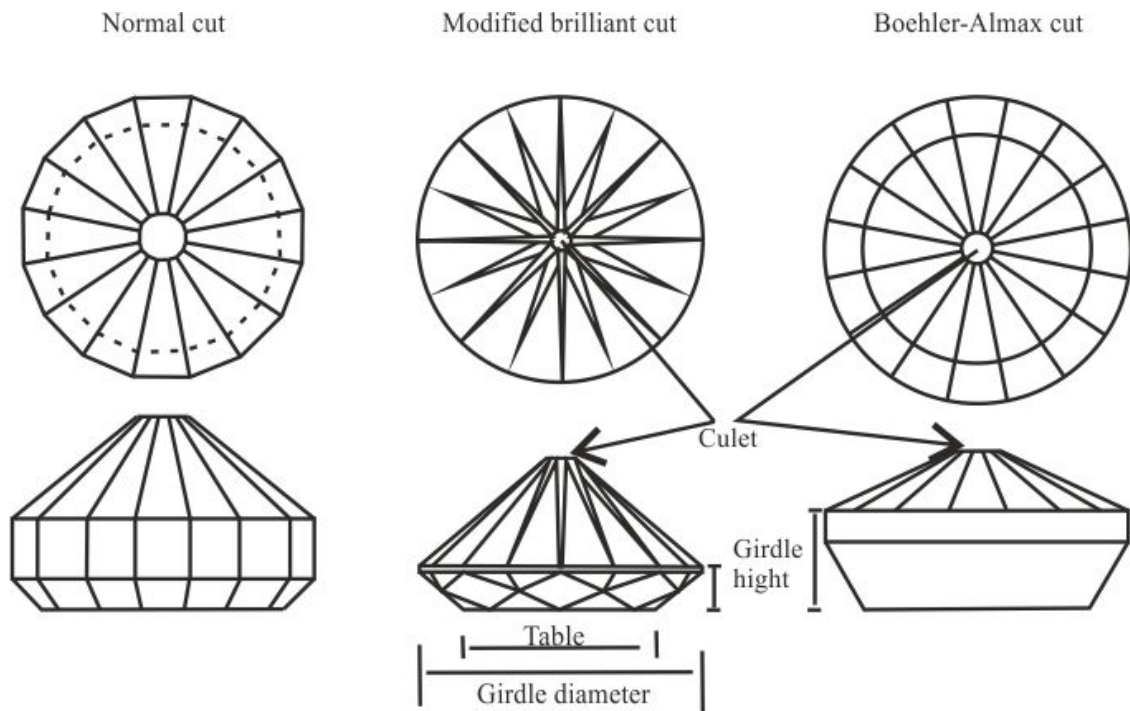


Figure 3.9: Schematic sketch of different diamond cuts.

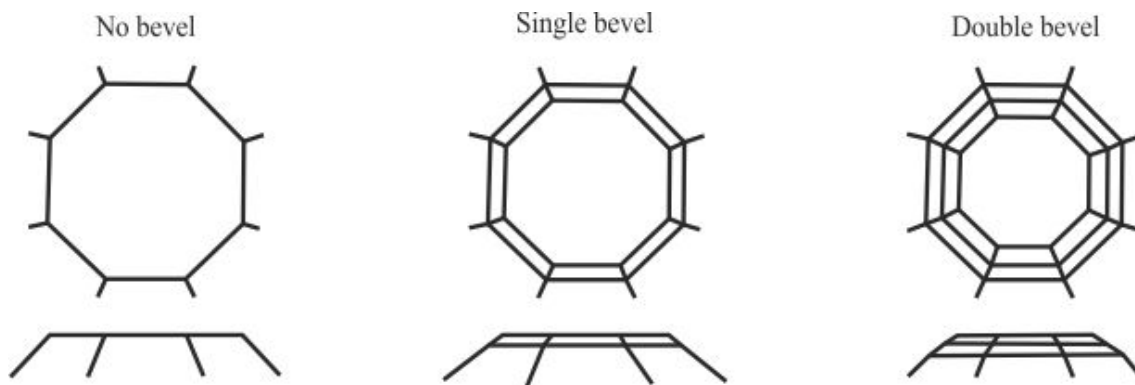


Figure 3.10: Schematic sketch of beveled culets.

Table 3.7: Classification of diamonds and their characteristics

	Type I (containing N)		Type II (without N)	
Diamond type	Ia	Ib	IIa	IIb
Natural occurrence	98%	0.1%	1.8%	0.1%
Defects	aggregated N impurities (A, B and N3 nitrogen centers)	isolated single N impurities (C-nitrogen center)	no impurities	Boron impurities
Color	colorless to yellow, brown, pink, orange, green, violet	yellow to brown	colorless, brown, pink, green	blue to gray
Absorption properties	absorption from 320 nm, short-wavelength UV absorbing	absorption from 320 nm, short-wavelength UV absorbing	absorption from 220 nm, short-wavelength UV transparent	
FTIR indicators	1282, 1175 cm ⁻¹	1344, 1130 cm ⁻¹	no detectable impurities	2803, 2458 cm ⁻¹
UV fluorescence long-wave	inert, blue, yellow, orange	inert to weak orange	inert, blue or orange	inert to weak blue
UV fluorescence short-wave	inert, blue, yellow, orange	inert to weak orange	inert, blue or orange	inert to weak blue or yellow

3.3.2 Gaskets

The two opposing diamonds are separated from getting into direct contact by a thin foil, the so-called gasket. Besides being a safe guard for the diamonds to avoid direct contact, the gasket also holds the actual pressure chamber in which the experiment is conducted. Gaskets are pre-indented before loading the sample, i.e., a deep imprint of the diamonds is produced in the gasket by compressing it between the anvils (Figure 3.11). The gasket should be pre-indented in such a way that further thinning during the pressure run is minimum, only the amount of thinning required to pressurize the compressible pressure transmitting media by inward extrusion (Spain & Dunstan, 1989). Thus, the force used for the indentation should approximately be near the same as the force needed for the target pressure or at least 50% of the target pressure. Still the indentation of the gasket should not exceed 70 % of the initial gasket thickness. Experimentally estimated indentation thickness are listed in Table 3.8. The purpose of this treatment is twofold (i) the gasket is stain-hardened by indentation and (ii) a bulge of metal develops on the outside of the anvil. This metal bulge supports the anvil at high pressures.

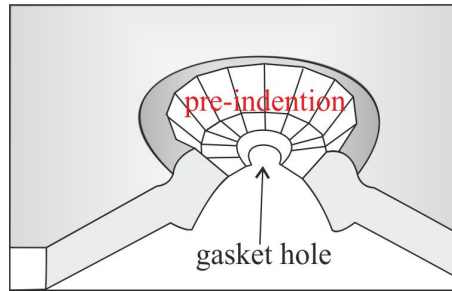


Figure 3.11: Schematic sketch of an indented gasket. The pre-indentation has been performed by a beveled diamond with an additional facet at the culet.

Table 3.8: Intention thickness and pressure from experimental experience

indentation thickness	Maximum pressure
50–60 μm	< 20 GPa
40–45 μm	50 GPa
25–30 μm	100 GPa

Gaskets are usually made of stainless steel. For experiments at elevated temperatures and pressures rhenium and occasionally iridium gasket are in use. Beryllium gaskets are sometimes used for XRD experiments if the x-ray beam is required to pass through the gasket. The actual pressure chamber is drilled into the gasket using either a mechanical micro-drill, a spark eroder (see Appendix C) or a laser. This gasket hole should be of smaller than $\frac{1}{3}$ of the indented area. The sample size should be proportional to the

3 Methods

gasket hole. The maximum experimental pressure and the dimensions of the sample are inversely proportional as the higher the pressure the thinner the sample. Usually the sample thickness should be around 60% of the indented gasket thickness.

3.3.3 Pressure-transmitting media

The pressure medium transforms the uniaxial stress which is applied to the diamonds into pressure onto the sample. The aim is to have hydrostatic conditions within the sample chamber thus depending on the experiment different pressure media are used which can be either solid, liquid or gaseous. Besides the hydrostatic limit, it is important to select a pressure medium which is inert to the sample, i.e., no reaction should occur between the pressure medium and any other substance within the pressure chamber (sample or pressure calibrant) or the gasket itself.

The most frequently used pressure medium is the alcohol mixture methanol:ethanol in the ratio 4:1. This mixture remains hydrostatic up to 9.8 GPa (Angel *et al.*, 2007) at room temperature. If this mixture is diluted with water to a methanol:ethanol:water mixture with the ratios 16:3:1 hydrostaticity is expanded to 10.5 GPa. The latter mixture is a little easier to handle while loading the cell as it does not evaporate so quickly as the pure alcohol mixture.

For high pressures up to the megabar range the best available pressure transmitting media is He, which allows for quasi-hydrostatic conditions up to 70 GPa according to (Klotz *et al.*, 2009). Helium is hydrostatic up to 30 GPa (Takemura & Dewaele, 2008) but remains quasi-hydrostatic up to the megabar range. For pressures above 10 GPa Ne is also a good choice as it allows for hydrostatic conditions up to 15 GPa (Klotz *et al.*, 2009). Ar which has been used for experiments up to 70 GPa has been recently shown to have hydrostatic conditions only up to 1.9 GPa (Angel *et al.*, 2007).

The use of a gas as a pressure transmitting medium requires special devices to load the gas into the DAC. There are two gas loading principles (i) cryogenic gas loading and (ii) loading pre-compressed gas using an autoclave. The cryogenic gas loading works via liquification of the gas which is then introduced into the sample chamber with a half closed DAC in an isolated container. During this procedure the whole DAC is plunged into the liquified gas and closed therein. Thus the diamonds are exposed to very low temperatures which may cause brittle failure of the anvils. Loading pre-compressed gas at room temperature requires a specific set-up which is able to pre-pressurize the selected gas, pump it into an autoclave which contains the DAC and close the DAC within the autoclave to keep the gas inside the gasket hole. As gas loading is such a complicated process not all DAC designs are suitable for this procedure. Especially for the pre-compressed gas loading the devices are normally made to fit one specific type of DAC.

For heated experiments a liquid pressure medium is not suitable thus if gas loading cannot be used a solid pressure medium is chosen. Alkali halides (NaCl, KBr, KI, CsI) are

3 Methods

Table 3.9: Hydrostatic limits of selected pressure transmitting media after Angel *et al.* (2007) and Klotz *et al.* (2009)

Pressure transmitting medium	Hydrostatic limit
Silicone oil	0.9 GPa
Glycerol	1.4 GPa
Argon	1.9 GPa
4:1 methanol:ethanol	9.8 GPa
16:3:1 methanol:ethanol:water	10.4 GPa
Helium	70 GPa

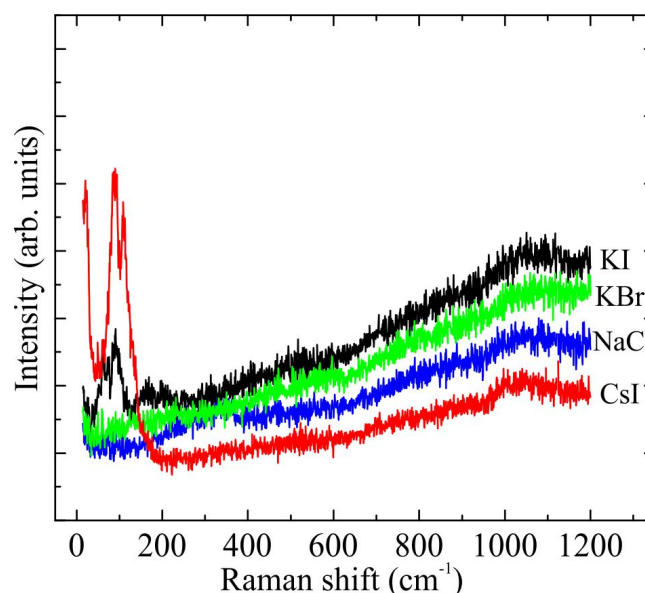


Figure 3.12: Raman spectra of different alkali halides which were tested for the use as a pressure-transmitting medium for Raman spectroscopy. NaCl is the best choice because it has no Raman peaks and the lowest background and no peaks.

well suited for this purpose, but in some cases they react with the sample. Additionally, their high background fluorescence at high pressure often interferes with Raman measurements. For Raman spectroscopy it is also necessary to select a solid pressure medium which does not have any Raman signals which is the case for the NaCl-structural type in which most alkali halides crystallize (CsI crystallizes in $Pm\bar{3}m$). From the spectra shown in Figure 3.12 it is obvious that NaCl is the best choice as it shows no Raman activity and has the lowest background. For preparation NaCl has to be grained to a fine powder and dried at 500 °C for 24 hours before it can be loaded in the cell.

3.3.4 Measuring pressure

Different methods can be used to determine the pressure in the DAC. The ruby luminescence method is most commonly used. The accuracy of this pressure scale has been tested by many methods, e.g., Zha *et al.* (2000) using simultaneous XRD and Brillouin measurement on MgO up to 55 GPa.

Ruby is a red variety of corundum ($\alpha\text{-Al}_2\text{O}_3$) containing between 0.3–0.5 wt % Cr^{3+} substituting for Al^{3+} . As the Cr^{3+} ion is slightly larger than the Al^{3+} ion (0.64 vs. 0.57 Å) the incorporation of Cr causes a small expansion of the host lattice. This expansion causes a small elastic strain in the structure and leads to an off-centred displacement of the Cr^{3+} ions along the c-axis without breaking the 3-fold rotational symmetry around the c-axis. Under laser excitation a strong doublet can be observed due to the photoluminescence. Due to the splitting of the $\text{Cr}^{3+} 3d^3$ into three T_{2g} and two E_g orbitals there is a spin-allowed U and Y band absorption which causes the red color of ruby. The photon-induced excitation of the U and Y bands in combination with phonon-assisted relaxation leads to the population of the excited 2E state. Characteristic R1 R2 doublet is observed at 694.2 nm (R1) and 692.8 nm (R2). Under pressure the R-lines shift with a linear pressure dependence under hydrostatic conditions up to the megabar range. Thus the pressure can be determined from the wavelength of the R1 line according to recalibrated pressure scale by Mao *et al.* (1986):

$$p = 1904 \left[\left(\frac{\lambda(p)}{\lambda_0} \right)^B - 1 \right] \cdot \frac{1}{B}$$

where λ_0 is the wavelength of R1 at ambient conditions and $\lambda(p)$ the wavelength at the pressure p and B is an empirically determined coefficient $B = 7.655$ for quasi-hydrostatic conditions. The frequencies of the R-lines show a small increase with Cr concentration thus for calculating the pressure from the shift in the R1 line it is important to know the exact frequency at ambient conditions.

The disadvantage of the ruby luminescence method is the shift of the R-lines with temperature $\Delta\lambda \approx 6.2 \times 10^{-3} \frac{\text{nm}}{\text{K}}$ (Barnett *et al.*, 1973). Other material which show a pressure shift in their luminescence but no significant shift with temperature are Sm^{2+} doped compounds such as $\text{SrB}_4\text{O}_7\text{:Sm}$ (SBO:Sm) (Datchi *et al.*, 2007). SBO:Sm shows a single luminescence line at 685.14 nm (at room conditions) which is well separated from the neighboring lines. The luminescence of the ${}^5D_0 - {}^7F_0$ (referred to as the 0-0 line) transition was calibrated up to the megabar range by Datchi *et al.* (1997). The advantages over the ruby luminescence method are: (i) the single character of the line is retained up to the megabar range (ii) the small band width increases very slowly with temperature and pressure (iii) the fluorescence background remains flat at high pressures (iv) the pressure response is within uncertainties independent of the magnitude of non-hydrostaticity. A disadvantage is that SBO:Sm may react with chemically active pressure transmitting media

3 Methods

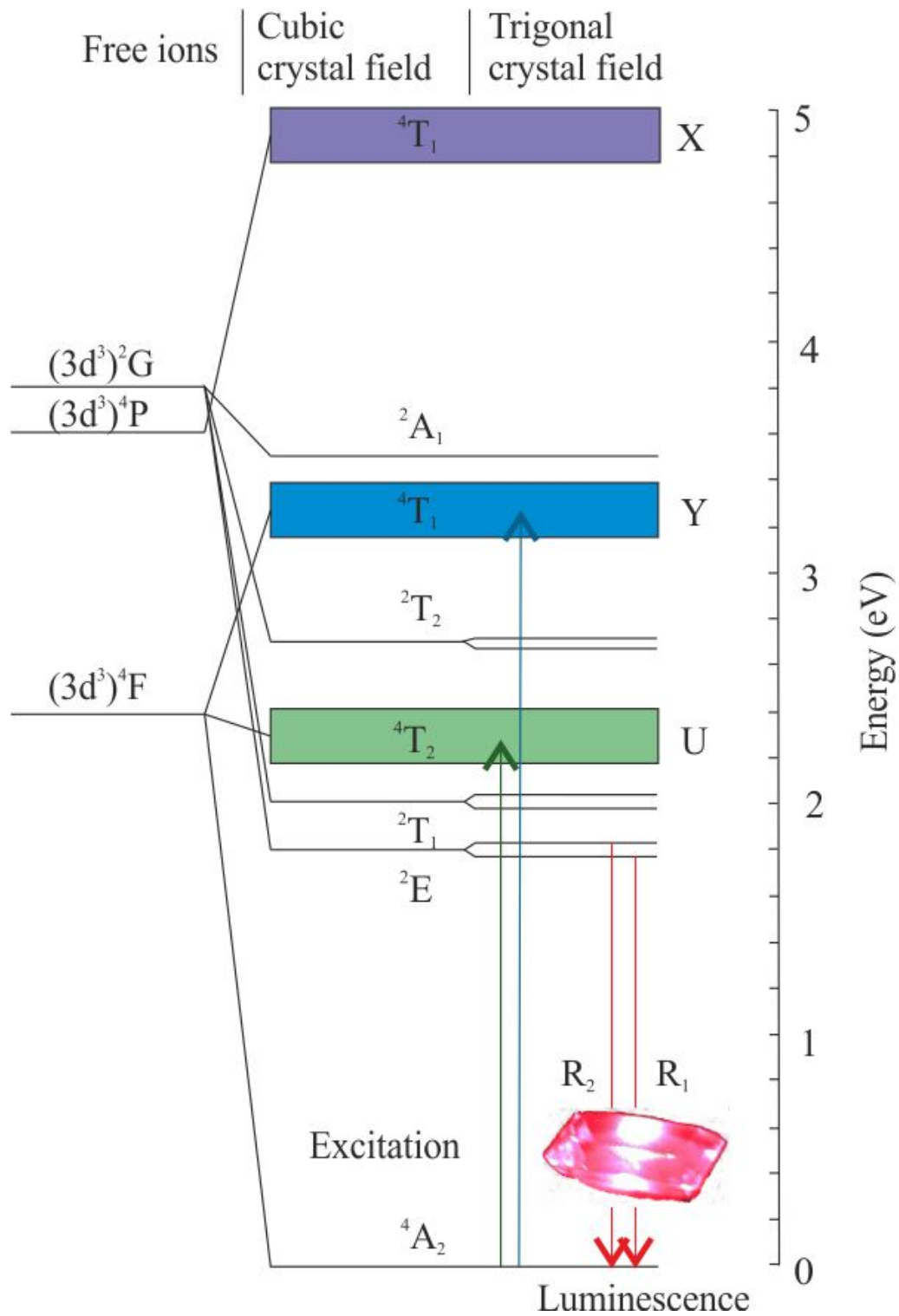


Figure 3.13: Excited states of Cr^{3+} (Syassen, 2008) showing the splitting of the $3d^3$ orbital, the absorption bands and the R1 and R2 luminescence lines of ruby. The small picture in the upper left corner shows the luminescence of a ruby crystal irradiated by a 514.5 nm laser.

3 Methods

like water at 650 K and 8.5 GPa (Datchi *et al.*, 2000). The pressure scale for SBO:Sm can be expresses as follows:

$$p = A\Delta\lambda_{0-0} \frac{1 + B\Delta\lambda_{0-0}}{1 + C\Delta\lambda_{0-0}}$$

with $A = 4.032$, $B = 9.29 \times 10^{-3}$ and $C = 2.23 \times 10^{-2}$ if the pressure scale is compared with the calibration of Mao 1986 (Datchi *et al.*, 1997) the values for comparison with other pressure scales can be found in Datchi *et al.* (2007). The temperature shift between 296–900 K with respect to the wavelength can be expressed as follows:

$$\Delta\lambda_{0-0}(T) = -8.7(12) \times 10^{-5} \Delta T + 4.62(60) \times 10^{-6} \Delta T^2 - 2.38(70) \times 10^{-9} \Delta T^3$$

This shows that the measured shift is insignificant with respect to the error bars below 500 K and only starts to rise slowly above this temperature. Extension of these measurements to low temperatures revealed no detectable shift form 8–300 K (Datchi *et al.*, 2007).

4 Experimental conditions used in this study

4.1 Different types of DACs used

For the experiments described below three different DACs designs were used: (i) Boehler-Almax-DAC (Boehler, 2006) for XRD and Raman analysis, for which a manual of operation has been given by Maier (2010); (ii) μ Scope-RT(G) from easyLab Diacell® for Raman spectroscopy described by Welsch (2009); and (iii) for in situ high pressure experiments at elevated temperatures a μ ScopeDAC-HT(G) easyLab Diacell® was used. A detailed manual for the μ ScopeDAC-HT(G) can be found in the Appendix A.

4.2 Raman spectroscopy

Raman spectra were collected using a Horiba Jobin-Yvon T64000 triple-grating spectrometer equipped with an Olympus BH41 microscope and a 50x long-working distance objective. The measurements were conducted in backscattering geometry using the 514.5 nm line of an Ar⁺ laser and a spectral resolution of 2 cm⁻¹.

4.2.1 Temperature-dependent measurements at ambient pressure

The in-situ temperature-dependent experiments at ambient pressure were conducted in a LINKAM heating/cooling stage ensuring a temperature stability of ± 0.1 K. Polarized spectra were collected on cooling from 850–100 K with a relatively small temperature step in $\bar{Z}(XX)Z$ and $\bar{Z}(XY)Z$ scattering geometries (Porto notation). For selected temperatures $\bar{Z}(X'X')Z$ and $\bar{Z}(X'Y')Z$ spectra were additionally measured, where X' and Y' denote the cubic [110] and $[\bar{1}10]$ crystallographic directions, respectively. Pure PZN-xPT was measured with an acquisition time of 15 s, and averaging over 10 loops. The corresponding experimental conditions for the Ru-doped sample were 30 s and 10 loops; a lower laser power had to be used for the Ru-doped compound in order to avoid sample overheating under laser irradiation due to the difference in the optical properties.

4.2.2 Pressure-dependent measurements at ambient temperature

The in-situ high-pressure Raman spectroscopic experiments at ambient temperature were conducted in gas-membrane-driven easyLab Diacell® μ ScopeDAC-RT(G) and DACs of the Boehler-Almax design. Stainless steel gaskets and 4:1 methanol-ethanol or 16:3:1 methanol-ethanol-water mixtures (Angel *et al.*, 2007) as pressure-transmitting media were

4 Experimental conditions used in this study

used for the experiments up to 9.8 GPa, which is the hydrostatic limit of alcohol mixtures. To obtain hydrostatic conditions above 9.8 GPa and better stability of the sample chamber formed by the drilled gasket, He was used as a pressure medium and rhenium was used for the gasket. The measurements were conducted on plates oriented parallel to the cubic 100 planes. Pure PZN-0.1PT was measured with an acquisition time of 15 s or 20 s, whereas the acquisition time for the Ru-doped compound was 30 s. The pressure values in Raman scattering experiments were determined by the ruby-fluorescence method with an accuracy of 0.1 GPa (Munro *et al.*, 1985).

4.2.3 In-situ high temperature high pressure dependent measurements

In-situ high-pressure high-temperature experiments were carried out using an easyLab Diacell® μ ScopeDAC-HT(G) gas-membrane-driven diamond anvil cell (DAC). The cell is equipped with a resistance gasket heater, ensuring temperature stability of ± 10 K. The temperature was measured by a K-type thermocouple attached to the metal gasket.

The pressure was determined from the shift of the 7D_0 - 5F_0 photoluminescence line of $\text{SrB}_4\text{O}_7\text{:Sm}^{2+}$ which has been shown to have negligible temperature dependence by contrast to the ruby R1 luminescence (Datchi *et al.*, 2007). The uncertainty in pressure determination was ~ 0.1 GPa. Rhenium gaskets were prepared for all experiments to ensure the stability of the sample chamber at elevated temperatures.

Sodium chloride was used as a pressure medium. As each solid medium, NaCl develops a certain uniaxial strain upon mechanical load (Kinsland & Bassett, 1977), which perturbs the hydrostaticity of the experiment. However, at high temperatures the uniaxial strain is considerably reduced (Gallardo *et al.*, 2000), ensuring quasi-hydrostaticity up to 9 GPa, which was the highest pressure achieved at elevated temperatures with our set-up. The constant width of the photoluminescence peak of $\text{SrB}_4\text{O}_7\text{:Sm}^{2+}$ used as a pressure indicator during the pressure run confirmed that quasi-hydrostatic conditions were maintained within the experimental error. Prior the sample loading NaCl was grained to a fine powder using a vibration mill and dried at 500 °C for 24 h, in order to reduce the noise level during the Raman scattering experiments.

The samples were placed in the sample chamber assuring that they were surrounded by NaCl on all sides not touching the diamonds or the gasket. To prevent oxidation of the Re-gasket the DAC was purged with N_2 gas.

In-situ high temperature high pressure experiments were carried out on the model compounds PSN and PST. Both compounds were measured at constant temperatures, below and above T^* , at 400 K and 600 K and different pressures. PSN was measured at 400 K with an acquisition time of 30 s and 20 loops, at 600 K an acquisition time was 30 s with 20 loops and 60 s with 20 loops. PST was measured with an acquisition time of 15 s and 10 loops for 400 K and 30 s with 10 loops for 600 K.

4.3 X-ray diffraction

4.3.1 Temperature-dependent measurements at ambient pressure

Powder XRD measurements were performed with a Philips X'Pert diffractometer (Bragg-Brentano geometry), using an Anton Paar high-temperature cell. The experiments were conducted on heating in the range 300–850 K. The XRD patterns were collected with CuK α radiation in a 2θ -range from 20–80°, with a step size of 0.02° and an accumulation time of 10 s per step.

Synchrotron single-crystal XRD was performed at the F1 beamline at HASYLAB/DESY using a MarCCD 165 detector. Data were collected with a radiation wavelength of $\lambda = 0.4000 \text{ \AA}$, a sample-to-detector distance of 100 mm, a stepwidth of 0.5° per frame and an exposure time of 220 s. For both PZN-0.1PT and PZN-0.1PT:Ru experiments were carried out at $T = 300 \text{ K}$ and 150 K with an open-flow liquid-N₂ cryostat (Oxford Cryosystems, Series 600). Reciprocal lattice sections were reconstructed using the in-house developed software RASTM (Paulmann & Malcherek, 2006).

4.3.2 Pressure-dependent measurements at ambient temperature

In-situ high-pressure x-ray diffraction (XRD) experiments were conducted in diamond anvil cells (DACs) of the Boehler-Almax design. Stainless steel gaskets and 4:1 methanol-ethanol or 16:3:1 methanol-ethanol-water mixtures (Angel *et al.*, 2007) as pressure-transmitting media were used for the experiments up to 9.8 GPa, which is the hydrostatic limit of alcohol mixtures. To obtain hydrostatic conditions above 9.8 GPa and better stability of the sample chamber formed by the drilled gasket, He was used as a pressure medium and rhenium was used for the gasket. The measurements were conducted on plates oriented parallel to the cubic {100} planes.

Synchrotron single-crystal XRD was performed at the F1 beamline at HASYLAB/DESY using a MarCCD 165 detector. Data were collected with a radiation wavelength of $\lambda = 0.5000 \text{ \AA}$, a sample-to-detector distance of 100 mm, a step width of 0.5° between frames, 80 frames per measurement and an exposure time of 10 s per frame. Reciprocal-space sections were reconstructed from the raw data frames using the CRYMALISTM Oxford Diffraction software. The pressure values in the synchrotron XRD experiments were determined by the ruby-fluorescence method with an accuracy of 0.1 GPa (Munro *et al.*, 1985). The pressure dependence of the pseudo-cubic unit-cell parameters was measured with a Huber four-circle single-crystal diffractometer (in the Crystallography Lab of Virginia Tech, headed by Prof. Ross Angel), using the method of eight-position diffraction beam centering, which ensures a precision in the relative volume $V(p)/V_0 \sim 0.0001$ (Angel & Finger, 2011). In these experiments the pressure values were determined with a precision of 0.01 GPa from the measured volume and the previously-determined equation of state of a quartz crystal loaded next to the sample (Angel *et al.*, 1997).

5 Results and Discussion

5.1 Pressure-induced structural changes at room temperature up to 30 GPa

This section is partly based on the papers Maier, B. J., **Waeselmann, N.**, Mihailova, B., Angel, R. J., Ederer, C., Paulmann, C., Gospodinov, M., Friedrich, A. and Bismayer, U. (2011b). *The structural state of relaxor ferroelectrics $\text{PbSc}_{0.5}\text{Ta}_{0.5}\text{O}_3$ and $\text{PbSc}_{0.5}\text{Nb}_{0.5}\text{O}_3$ at high pressures up to 30 GPa. Phys. Rev. B 84, 174104.*

and

Mihailova, B., **Waeselmann, N.**, Maier, B. J., Angel, R.J., Prüßmann, T., Paulmann, C., Gospodinov, M. and Bismayer, U. (2012). *Chemically induced renormalization phenomena in doped Pb-based relaxors under high pressure.*

5.1.1 Pure PST

As described in Section 1.3.3 PST undergoes a pressure-induced phase transition from a relaxor to a non-polar rhombohedral state preceded by a suppression of the mesoscopic-scale polar ordering between the off-centered Pb and B-site cations subsequent enhancement of the B-cation off-centered displacement. The synchrotron single-crystal XRD pattern (indexed in $Fm\bar{3}m$) shown in Figure 5.1 shows that at 5.0 GPa the odd-odd-odd (ooo) superstructure reflections arising from anti-phase BO_6 tilts are superimposed on the broad ooo reflections arising from the long-range chemical B-site ordering. Thus, the crystal is in the rhombohedral phase formed at $p_{C1} = 1.9$ GPa exhibiting $a^-a^-a^-$ tilt pattern which was verified by neutron powder diffraction (Maier *et al.*, 2010a).

Under further pressure increase two new classes of superstructure reflections appear at 7.7 GPa indicating a second pressure induced phase transition between 5.0 and 7.7 GPa. The first class of additional Bragg reflections has Miller indices of type h, k, l with one odd and two even (oeo), while the second class has Miller indices of type h, k, l with two odd and one even (ooo). In terms of symmetry-adapted phonon modes in the Brillouin zone of the aristotype structure (primitive cubic single-perovskite $Pm\bar{3}m$), the oeo reflections are associated with distortions driven by X -point $(0, 1/2, 0)$ phonon modes of the cubic single-perovskite structure, whereas the ooo reflections are associated with activation of phonon modes on the M point $(1/2, 1/2, 0)$.

The occurrence of a phase comprising only in-phase tilts would give rise to ooo (M -point) reflections (Howard *et al.*, 2003). The simultaneous observation of ooo (R -point)

5 Results and Discussion

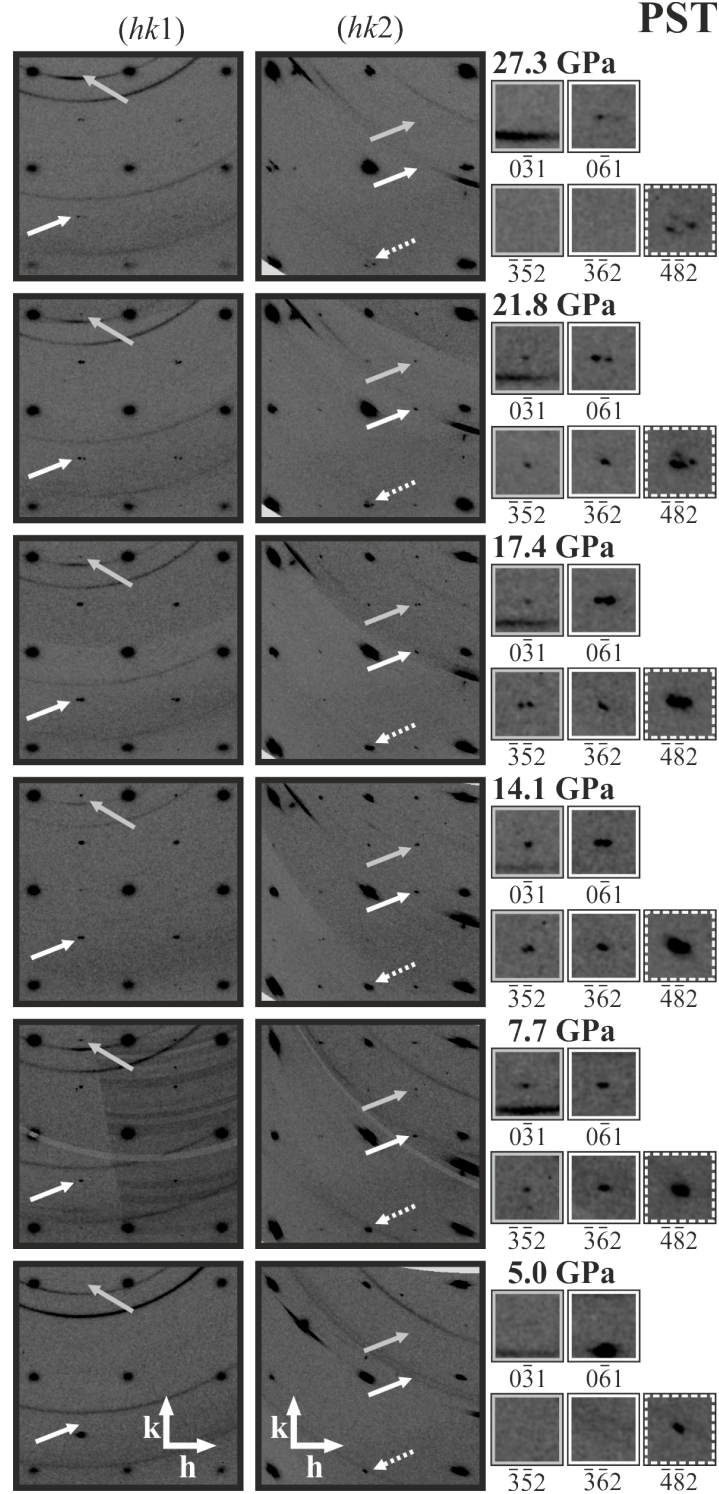


Figure 5.1: Reciprocal-space layer sections of PST reconstructed in $Fm\bar{3}m$ from single-crystal synchrotron XRD data. The reflection in the upper-left and lower-right corner are $\bar{1}\bar{3}1$ and $3\bar{7}1$ for the $(hk1)$ layer and $\bar{6}42$ and $\bar{2}82$ for the $(hk2)$ layer, respectively. The gray and white arrows mark examples of the pressure-induced *odd-odd-even* and *even-odd-even* reflections whereas the white dashed arrows mark an example *even-even-even* reflection. The marked reflections are magnified on the right-hand side of the figure.

5 Results and Discussion

and *ooe* (*M*-point) Bragg reflections can be explained by a coexistence of two phases possessing respectively pure anti-phase tilting (corresponding to a mode at the *R* point ($1/2, 1/2, 1/2$) in the primitive cubic cell) and pure in-phase tilting. However, this cannot explain the appearance of *X*-point Bragg peaks. Therefore, the simultaneous appearance of *M*-point and *X*-point reflections along with the existing *R*-point reflections could arise from three main types of transformation mechanism: (i) a change in the type of tilting from anti-phase tilts only to mixed tilts (e.g. $a^+b^-b^-$), which would contribute to the *R*-point Bragg peaks and would give rise to both *M*- and *X*-point Bragg peaks (Woodward & Reaney, 2005); (ii) development of a pattern of anti-polar A-cation shifts consistent with an *X*-point mode (Campbell *et al.*, 2006), which along with the preexisting anti-phase tilts (associated with *R*-point modes) further lowers the symmetry and allows additional distortions (in-phase tilting along at least one direction or octahedral distortion) that would produce weak *M*-point reflections; (iii) simultaneous development of a tilt pattern involving in-phase tilting along at least one direction as well as an *X*-point pattern of A-cation shifts, which are consistent with each other.

The integrated intensities of the *ooe* (*X*-point) reflections are systematically stronger than the intensities of the *ooe* (*M*-point) reflections. This unambiguously reveals the presence of long-range anti-polar order of the A-site Pb atoms corresponding to an *X*-point distortion mode. A careful analysis of the diffraction patterns reveals that all *X*-point reflections of type *o00* are absent. This indicates that the Pb cations must be displaced in opposite directions in consecutive (001) layers of the cubic structure, where the displacements within the (001) layers can be along any cubic $[uv0]$ direction. Examination of the symmetry of the possible displacement patterns with the program *ISODISTORT* (Campbell *et al.*, 2006) suggests that the X^{5+} mode (Miller-Love notation) provides the most physically reasonable arrangement of anti-ferrodistortive Pb displacements. Such a pattern of Pb displacements is inconsistent with pure in-phase tilt configurations (Howard *et al.*, 2003) but it may coexist with a mixed octahedral tilt pattern. However, it is not possible either to confirm or to rule out a possible change in the type of tilting by structure refinements to the XRD datasets because of the oversaturation of the strongest Bragg peaks under experimental conditions necessary for the detection of the weak *X*- and *M*-point peaks.

From a pure-symmetry point of view, it is possible that the *M*-point Bragg peaks arise from A-site or B-site cation displacements (Campbell *et al.*, 2006). However, the former would mean a coexistence of *X*-point and *M*-point Pb-displacement patterns, which is irrational, while the latter is inconsistent with the Raman scattering data (see Figure 5.2), showing that the peak near 235 cm^{-1} , which results from off-centered B-site cations (Mihailova *et al.*, 2002; Welsch *et al.*, 2011), is strongly suppressed at high pressures.

Raman spectroscopy (see Figure 5.2) also indicates that the most pronounced structural change above p_{C2} is a rearrangement of the Pb system. The major spectral changes above 6 GPa are in the band near 55 cm^{-1} , which is generated by Pb-localized phonon

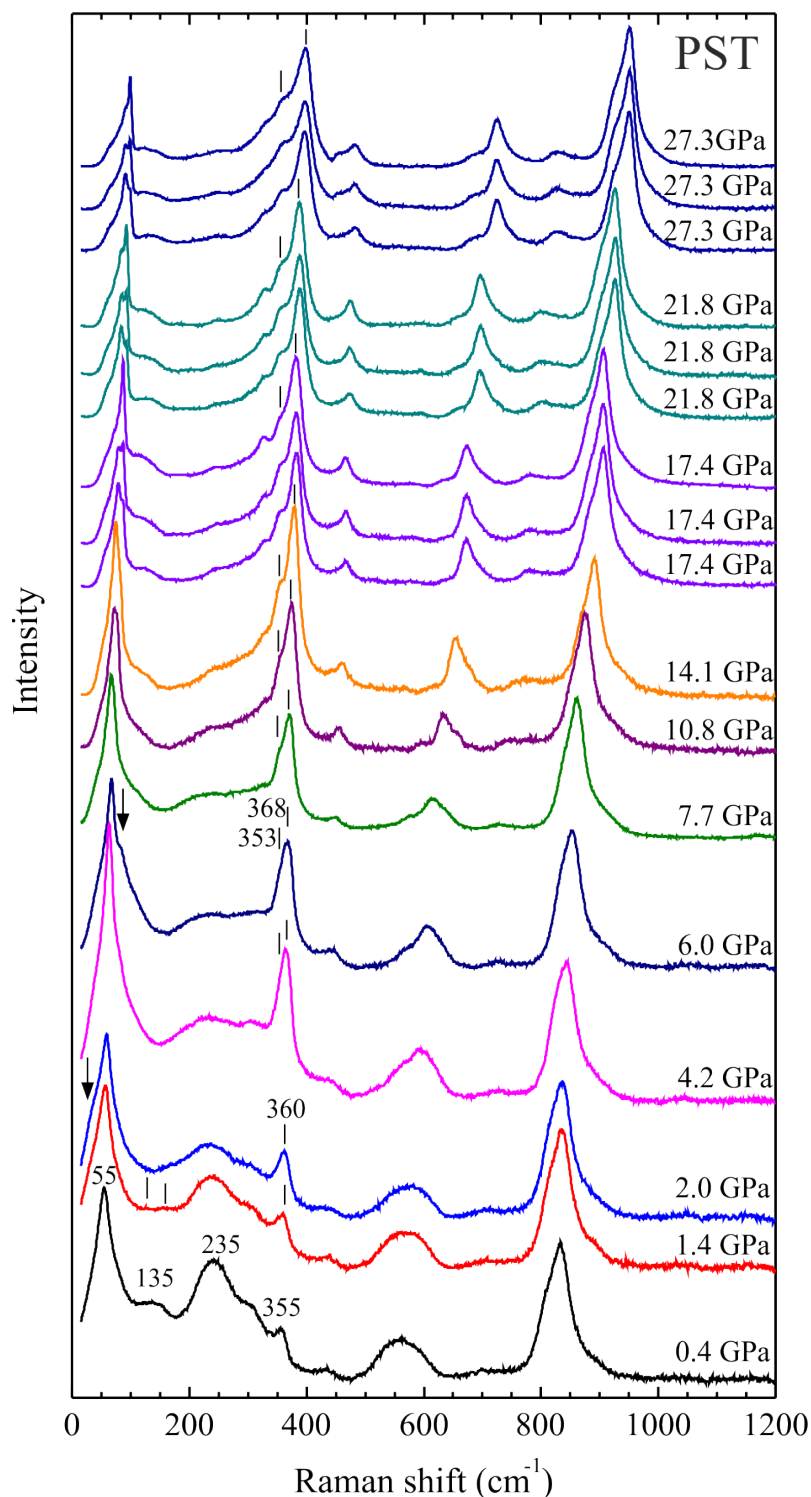


Figure 5.2: Raman spectra of PST at different pressures. The peak near 135 cm^{-1} is split above $p^*_1 = 1.2 \text{ GPa}$; a soft mode near 35 cm^{-1} appears at $p_{C1} = 1.9 \text{ GPa}$ (Mihailova *et al.*, 2008a). Spectra measured at the same pressure are from different spatial areas of the sample. The fitting of all spectra measured above 3.0 GPa requires an additional peak at $\sim 355 \text{ cm}^{-1}$.

5 Results and Discussion

modes. At 6 GPa a new, sharp, higher-wavenumber component appears to the main signal. At very high pressures (17.4 GPa and above) the Raman band arising from Pb vibrations is composed of several sharp signals and the intensity of the highest-wavenumber component varies across the sample (see Figure 5.2 and 5.3), while the Raman scattering above 110 cm^{-1} collected at the same pressure from different areas is almost the same (see Figure 5.2). The structural variations in the intensity ratio of the Raman signals related to Pb vibrations, when measured at the same pressure, is attributed to the coexistence of at least two configurations of Pb atoms, i.e., coexistence of two phases in the sample: the ferroic phase developed above p_{C1} and the ferroic phase developed above p_{C2} .

The presence of a cubic phase ($Fm\bar{3}m$) along with the ferroic phases is also plausible, but definitely it is not the dominant phase at very high pressures because many more Raman peaks than the four peaks ($A_{1g} + E_g + 2F_{2g}$) allowed by symmetry in $Fm\bar{3}m$ are observed at 27.3 GPa. The observation unambiguously rules out the earlier assumptions fixed on dielectric measurements and model calculations, that the high-pressure state of relaxor ferroelectrics should be cubic paraelectric (Samara *et al.*, 2000; Tinte *et al.*, 2006).

The *oeo* (*X*-point) and *ooo* (*M*-point) Bragg reflections are very weak or even disappear at 27.3 GPa (see Figure 5.1). This might be an artificial effect due to the fact that the (*hkl*) layers have been reconstructed in a cubic metric while the ferroic distortion is very strong at this pressure, or it may indicate that the symmetry of the structure indeed becomes higher. The latter is however ruled out by the Raman data. Raman mapping (Figure 5.3a) based on the ratio between the integrated intensities of the higher- and lower-wavenumber major components generated by Pb vibrations (the peaks labeled in Figure 5.3c as P2 and P1) reveal that with pressure increase the fraction of the ferroic phase developed above p_{C2} gradually increases and it is the dominant phase at 27.3 GPa.

Previously it was shown that the Raman peak near 355 cm^{-1} split in two at 3 GPa (Mihailova *et al.*, 2008a). The Raman data up to 30 GPa show that the splitting increases with pressure (see Figure 5.2 and 5.4a). This Raman signal is related to the F_{2u} mode of the aristotype cubic structure and is generated by Pb-O bond stretching within the cubic $\{111\}$ planes. This type of vibration can also be considered as octahedral tilting (Mihailova *et al.*, 2002; Welsch *et al.*, 2011) and hence the peak is strongly enhanced above p_{C1} . The splitting of the peak above 3 GPa indicates a lowering of symmetry of the oxygen cavity surrounding Pb and suggests that the BO_6 tilting around the cubic *x*-, *y*-, and *z*-axes is no longer the same. The tilts may differ from each other in magnitude and/or type. The pressure evolution of the wavenumber of the BO_6 symmetrical stretching giving rise to the peak at 830 cm^{-1} (see Figure 5.4b), also shows that the local structure is changed already at 3 GPa, i.e., below p_{C2} .

The appearance of a higher-wavenumber component to the main Raman signal generated by Pb vibrations at 6 GPa indicates that p_{C2} is most probably between 5.0 and 6.0 GPa. This value corresponds well to our previous neutron powder diffraction data (Maier *et al.*, 2010a), which at 5.5 GPa showed broadening of all diffraction peaks

5 Results and Discussion

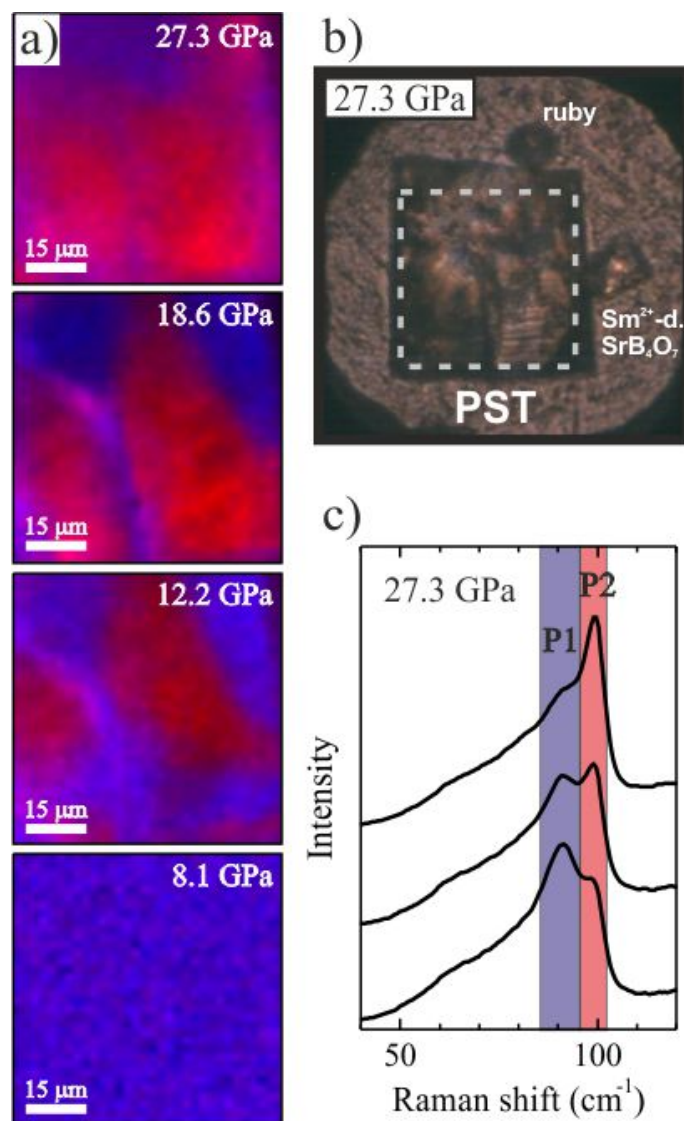


Figure 5.3: Raman mappings (a) of single-crystal PST at different pressures based on the integrated intensity ratio between the signals P2 and P1(c); red corresponds to large ratio $I(P2)/I(P1)$, blue to a smaller ratio. The mapping area is marked by the white dashed square in the crystal image (b). Development of domain pattern associated with the second pressure-induced ferroic phase can be seen in the right-bottom corner of the crystal (b).

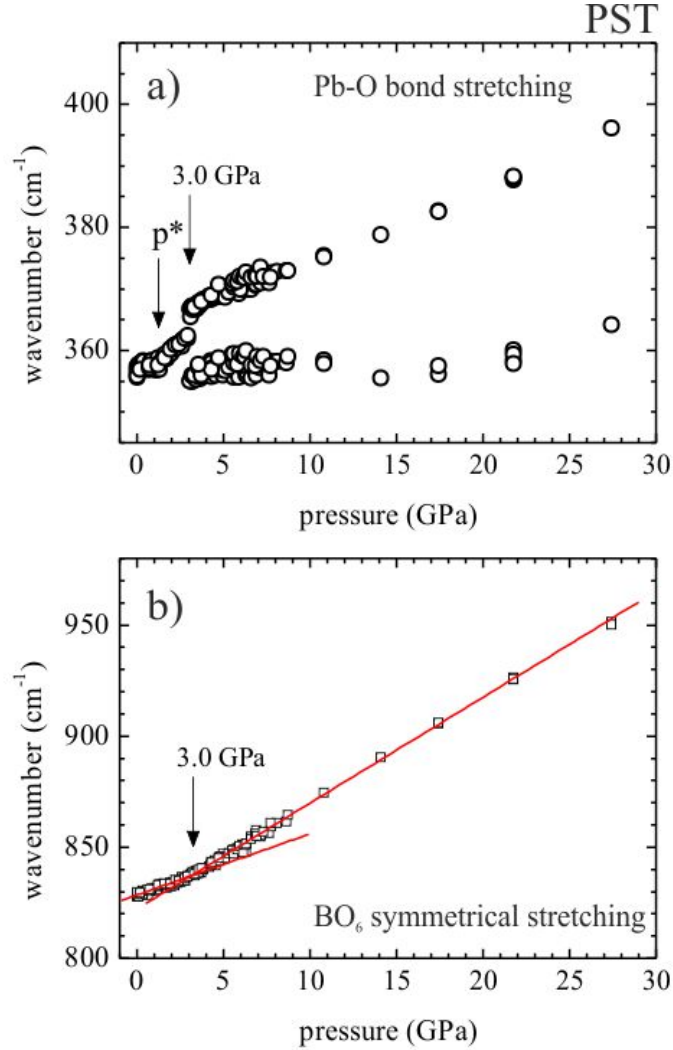


Figure 5.4: Pressure dependence of the wavenumber ω of the peak near 355 cm^{-1} (a) and 830 cm^{-1} (b) for PST; the uncertainties are within the symbols. The low-pressure data are after (Mihailova *et al.*, 2008a). The lines in the bottom plot are linear fits to the data points below p_{C1} and above p_{C2} , correspondingly.

as well as a decrease in the magnitude of the anisotropic displacement ellipsoids refined in $R\bar{3}c$. The former should be due to unresolved splitting resulting from the lowering of the symmetry, while the latter is consistent with ordering of anti-parallel Pb off-center displacements along the cubic $[uv0]$ directions. Neither oeo (X -point) nor ooe (M -point) superstructure Bragg reflections could be observed in the neutron powder patterns up to 7.35 GPa. However, with regard to the intensity ratio $I(oeo)/I(ooo) \sim 1/6$ in the XRD patterns at 7.7 GPa as well as to the smaller Pb atomic form factors for neutrons, we would not expect to be able to detect these peaks above the background. The fact that ooe (M -point) superstructure Bragg peaks are not seen by neutron diffraction underlines that a change of the tilt system from anti-phase to mixed is not the driving structural mechanism that leads to the second pressure-induced phase transition in PST.

5 Results and Discussion

At pressures of 14.1 GPa and above all classes of Bragg reflections observed by single-crystal synchrotron XRD (see Figure 5.1) appear split. The splitting is due to a combination of the presence of multiple domains and an enhancement of the ferroic distortion arising from the phase transition at $p_{C2} \sim 5.5$ GPa. The splitting is only resolved at high pressures and its appearance does not imply the presence of a third pressure-induced phase transition.

Thus, a possible scenario for the structural transformations occurring in PST up to 30 GPa is as follows. At $p^*_1 = 1.2$ GPa the mesoscopic polar order is violated on the account of the development of local anti-polar order of Pb cations and quasi-dynamical long-range order of anti-phase BO_6 tilts of equal magnitude. At $p_{C1} = 1.9$ GPa a static $a^-a^-a^-$ tilt order is developed that leads to the occurrence of a continuous phase transition from cubic to non-polar rhombohedral symmetry. At a second intermediate pressure $p^*_2 = 3.0$ GPa unequal octahedral tilts are locally developed. At $p_{C2} \sim 5.5$ GPa a second phase transition from rhombohedral to monoclinic or triclinic symmetry occurs, which involves a long-range order of Pb anti-polar displacements along cubic $[uv0]$ directions and compatible rearrangements of the O atoms. Above p_{C2} the lower-symmetry phase coexists with the non-polar rhombohedral phase, as its fraction increases with increasing pressure.

5.1.2 Pure PSN

The reciprocal-space layer sections of PSN reconstructed in $Fm\bar{3}m$ from synchrotron single-crystal XRD are shown in Figure 5.5. Since the PSN compound studied here possesses heavily frustrated chemical B-site order, the observed ooo (R -point) Bragg peaks result entirely from anti-phase ($a^-a^-a^-$) tilts characteristic of the phase developed above $p_{C1} = 4.1$ GPa. New classes of pressure-induced Bragg peaks were not detected for PSN over the entire pressure range studied. Therefore, neither long-range order of A-cation anti-polar shifts corresponding to X -point phonon modes nor in-phase octahedral tilts are developed in PSN up to 28.9 GPa.

The Raman spectra of PSN (see Figure 5.6) also do not show any evidence for the development of long-range order of anti-polar Pb off-center shifts. At 24.9 and 28.9 GPa, the Raman band near 50 cm^{-1} can be rationally fitted with three components, but these components are very broad as compared to the corresponding Raman signals for PST, indicating that the structural changes that occur are only local. Spectra collected at the same pressure from different spatial areas of the PSN sample reveal that the sample remained structurally homogeneous in the entire pressure range studied. A splitting of the peak near 350 cm^{-1} unambiguously appears at 10.1 GPa (Figure 5.6 and 5.7a) but the spectrum profiles from data collected between 7.6–10.0 GPa can be equally well fitted by one or two components at $\sim 355 \text{ cm}^{-1}$. This suggests that on the local scale the octahedral tilts around the cubic $[100]$, $[010]$, and $[001]$ become different at pressures above 7 GPa. The position of the peak near 815 cm^{-1} , which arises from the BO_6 symmetrical stretching,

5 Results and Discussion

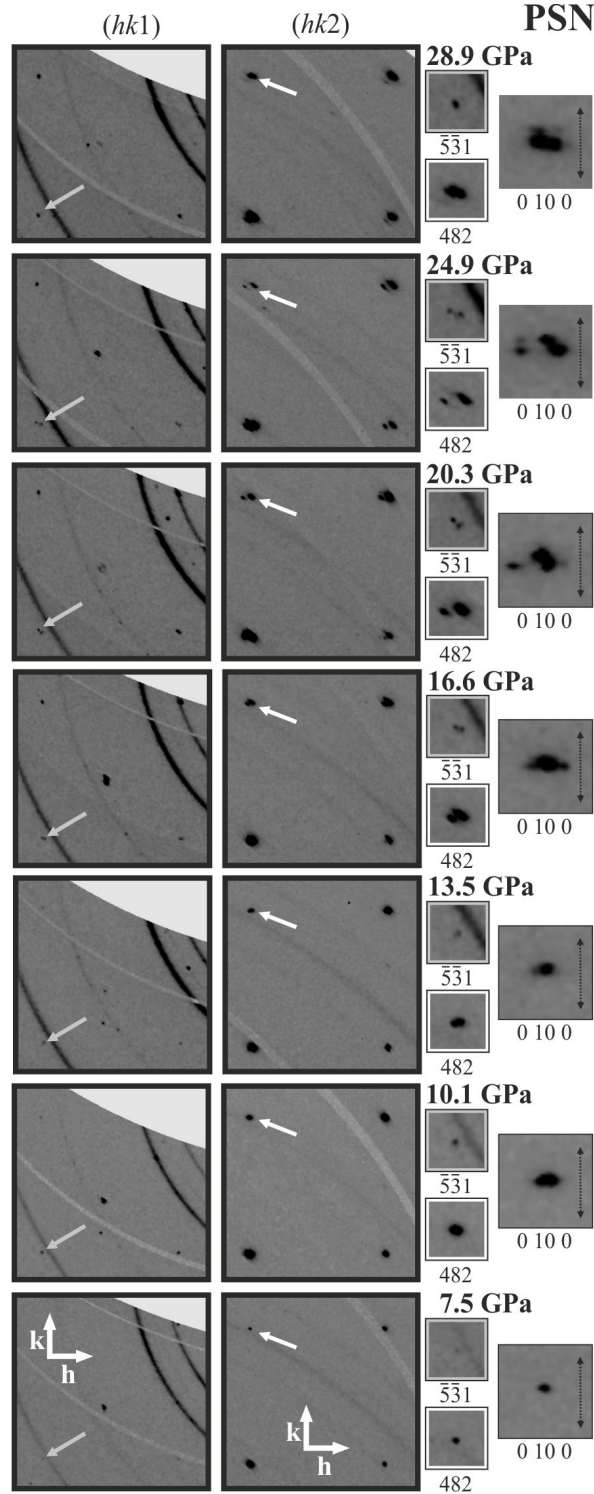


Figure 5.5: Reciprocal-space layer sections of PSN reconstructed in $Fm\bar{3}m$ from single-crystal synchrotron XRD data at different pressures. The reflection in the lower-left and upper-right corner are $\bar{5}\bar{1}1$ and $\bar{3}\bar{3}1$ for the $(hk1)$ layer and 482 and 662 for the $(hk2)$ layer, respectively. The gray and white arrows mark examples of the pressure-induced *odd-odd-odd* and *even-even-even* reflections, which are shown on an enlarged scale. The 0 10 0 reflection is also shown; the black vertical arrows in the 0 10 0-layer sections mark the direction to the coordinate origin.

5 Results and Discussion

has a kink as a function of pressure at 7.1 GPa (see Figure 5.7b), which also indicates local structural changes. Therefore, the Raman data reveals structural transformations in the mesoscopic scale in the vicinity of $p^*_2 \sim 7.5$ GPa, which involve a lowering of the symmetry of the octahedral tilt patterns and might precede a phase transition.

At 13.5 GPa and above all Bragg reflections split (see Figure 5.5), which however could result solely from the increasing rhombohedral distortion of the unit cell and the development of the multidomain rhombohedral structure. In the case of single-crystal diffraction only splitting along the direction to the coordinate origin corresponds to different d -spacings, i.e., to lowering of the crystal symmetry. Splitting along the perpendicular directions is due to twinning. Therefore, splitting of diffraction peaks of type $h00$ would indicate a deviation of the symmetry of the average structure from rhombohedral, because it would solely represent d -space splitting. As an example of an $h00$ -type reflection, Figure 5.5 displays the 0100 Bragg reflection: at 16.6 GPa the diffraction spot looks asymmetric along the direction to the coordinate axis, whereas at higher pressure a splitting corresponding to different d -spacings is noticeable. This indicates that the symmetry of the average structure is lowered from rhombohedral with a tilt system $a^-a^-a^-$ to monoclinic or triclinic, consistent with a tilt system $a^-b^-b^-$ or $a^-b^-c^-$, respectively.

Thus, at p^*_1 and p_{C1} PSN undergoes the same structural transformations as PST. At a second intermediate pressure p^*_2 on the mesoscopic scale both PST and PSN develop a tilt pattern with unequal tilts, which however can be different for PST and PSN. The second phase transition of PSN at $p_{C2} \sim 16.6$ GPa differs from that of PST, as clearly revealed by XRD, and it consists only of lowering of the anti phase-tilt pattern symmetry. The difference between the structural states of PST and PSN above p_{C2} is most probably related to the degree of local Pb displacive order developed at p^*_1 , which in turn should be related to the degree of frustrated chemical B-site order. The phase transitions observed for PSN up to 30 GPa are consistent with the first two pressure-induced phase transitions in PZN proposed by (Janolin *et al.*, 2006).

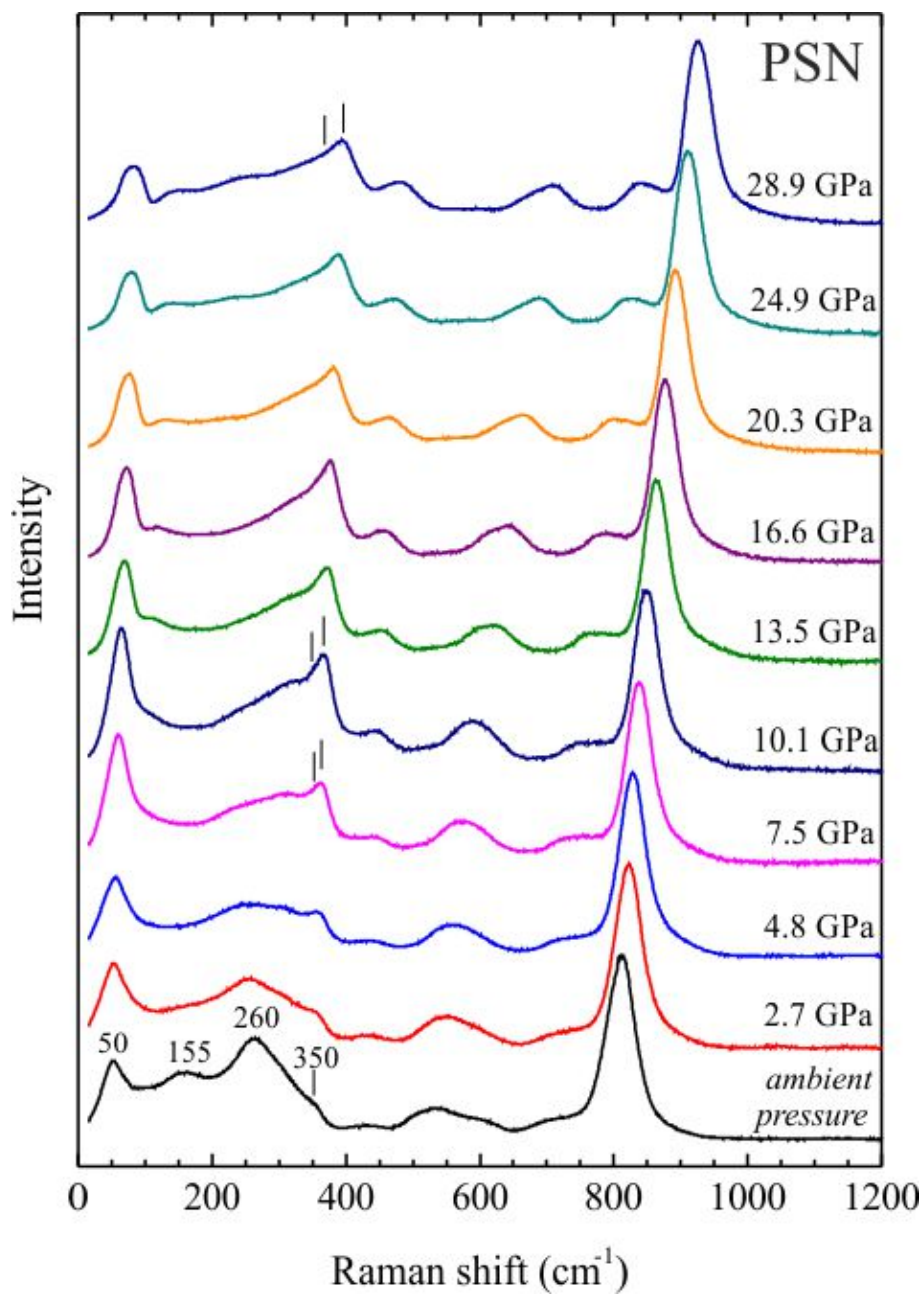


Figure 5.6: Raman spectra of PSN at different pressures.

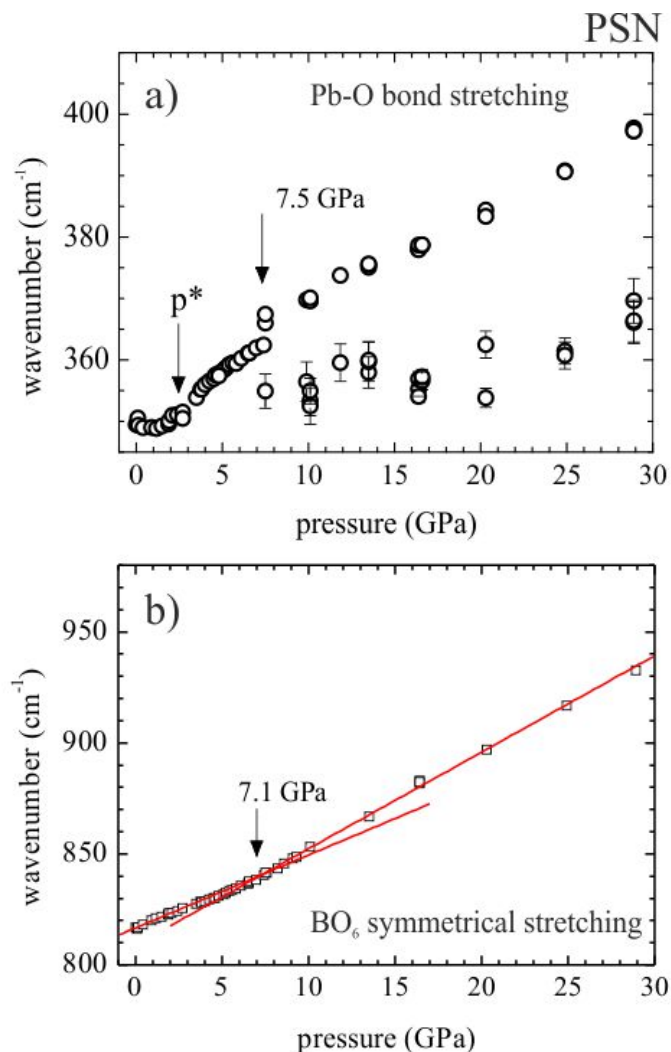


Figure 5.7: Pressure dependence of the wavenumber ω of the peak near 355 cm⁻¹ (a) and 830 cm⁻¹ (b) for PSN; the uncertainties are within the symbols. The low-pressure data are after (Welsch *et al.*, 2009b). The lines in the bottom plot are linear fits to the data points below p_{C1} and above p_{C2} , respectively.

5.1.3 A- and B-site doped PST and PSN

In order to analyze the effect of chemical variations on the second pressure-induced phase transition doped PST and PSN were subjected to in situ high-pressure single-crystal XRD and Raman spectroscopy up to 25 GPa. The Raman spectra and reconstructed reciprocal-space layers collected under different pressures for PBST, PLST, PLSN, PSSN, PSNT and PSTS are shown in Figure 5.9 - 5.14. The Raman data show the same trends as those observed for PST and PSN. The strong enhancement and the splitting of the peak at ~ 350 cm⁻¹ associated with the cubic F_{2u} mode indicates the development of octahedral tilt pattern, with unequal tilts around the cubic [100], [010], and [001] directions. It should be noted that previous high-pressure studies on the same compounds up to 6–9 GPa

5 Results and Discussion

revealed that the soft mode associated with the first pressure-induced phase transition at p_{C1} was detected only when the fraction of the pressure-induced phase was above a certain level. This is due to the fact that above p_{C1} there is still a relaxor cubic state coexisting with the new pressure-induced phase. On the other hand it is known that the integrated area of the soft mode is indicative of the amount of matter undergoing a phase transition. If the relaxor state still persists the soft mode could hardly be resolved because it would be overlapped by the strong peak near 50 cm^{-1} related to the cubic F_{2g} mode, which is present in both phases and is very strong for the cubic phase. For example for pure PSN and PBST a soft mode was not resolved at p_{C1} . The new Raman data presented here show that the soft mode could be resolved at 7.5 GPa for PSN ($\sim 3 \text{ GPa}$ above p_{C1}) and at 13.4 GPa for PBST ($\sim 9.4 \text{ GPa}$ above p_{C1}). The wavenumber of the soft mode (ω_{SM}) as a function of pressure for all compounds clearly shows non-linear behavior (see Figure 5.8). The attempt to fit the $\omega_{SM}(p)$ data points with a power functions of the type $\omega = \omega_0(p - p_0)^n$, with ω_0 , p_0 , n variable without any constraints gave unrealistic values for p_0 , which should correspond to the critical pressure p_{C1} . Fixing p_0 to the value of p_{C1} as detected from single-crystal XRD analysis (Mihailova *et al.*, 2011), lead to satisfactory power-function fit only for PSN and PBST ($n = 0.25$ and 0.32). The failure to apply the classical power function to $\omega_{SM}(p)$ underlines the complexity of structural transformations that occur in relaxors under pressure. On the other hand, for all compounds $\omega_{SM}(p)$ data sets can be fitted with two lines corresponding to the lower- and higher-pressure range (see Figure 5.8). For pure PST and PSN the crossing of the two lines perfectly coincides with the critical pressure p_{C2} of the second phase transition. Therefore, one can assume that for all relaxors the kink on the slope of $\omega_{SM}(p)$ dependence should be indicative of the occurrence of phase transition, since a change of $\frac{\partial \omega}{\partial p}$ for the soft mode reveals a change in the compressibility of the whole system. Indeed, the synchrotron XRD data on all tested relaxor compounds reveal the same critical pressure p_{C2} as determined here (see Table 5.1). The XRD analysis also clarified the structural changes occurring at p_{C2} , in particular if anti-polar long-range order of Pb^{2+} is developed or not.

The solid solution of PST and PSN (PSTN) shows that the dilution of the Ta-system with Nb atoms shifts p_{C1} to higher pressures $\sim 2.5 \text{ GPa}$ which is between the critical pressure of the end members. Also the fraction transformed at p_{C1} is large enough to generate a soft mode at the phase transition pressure. By contrast, the substitution of Sn^{4+} for pairs of Sc^{3+} and Ta^{5+} slightly decreases p_{C1} to 1.3 GPa (Welsch *et al.*, 2011). The latter is related to the disturbance of the intermediate-range order of B-cation off-center displacements in the polar nanoregions induced by the Sn-incorporation, which facilitates the development of anti-phase BO_6 tilt order. A second pressure-induced phase transition occurs in both PSTN and PSTS and similar to PST involving anti-polar ordering of the Pb^{2+} cations and the development of a mixed $a^+b^-b^-$ octahedral-tilt system. According to the XRD data, the critical pressure p_{C2} is between 10.5 and 12.3 GPa for PSTN and between 8.1 and 11.3 GPa for PSTS (see Table 5.1). However, for PSTN even at 19.6 GPa instead of

5 Results and Discussion

sharp *even – even – odd* Bragg peaks as in the case of PSTS (Figure 5.14) and PST, only streak-like diffuse diffraction features parallel to $\langle 100 \rangle^*$ are observed. This indicates that regardless of the fine-scale length of coherence of B-site chemical order, the correlation length of ordered Pb anti-polar shifts for PSTN is shorter than that for PSTS and it is most probably related to the preexisting ferroic species at ambient conditions. Therefore, the delicate balance between the fine-scale polar and anti-ferrodistortive order can be chemically tuned even by doping which does not change the tolerance factor.

Using a dopant for the A-site with a smaller ionic radius than Pb^{2+} reduces the tolerance factor which favors octahedral tilting and thus shifts p_{C1} towards ambient pressure. This is the case for PLST and PSSN. the doping-induced reduction of the tolerance factor and the consequence promotion of octahedral tilting also influences the second pressure-induced phase transition (Mihailova *et al.*, 2011).

For PLSN no sharp *X*-point and *M*-point peaks were detected in the entire pressure range but at 12.0 GPa diffuse streak-like *X*-point diffraction features appeared in the (hkl) layers with l even (see Figure 5.11). The substitution of Sr^{2+} for Pb^{2+} in PSN leads to the development of Pb anti-polar long-range order at $p_{C2} = 7.4$ GPa (see Figure 5.12) and a detectable mixed tilt pattern $a^+b^-b^-$ at 9.6 GPa. Above 14.5 GPa the *X*-point diffraction peaks become as strong as the *R*-point peaks. For PLST the second pressure-induced phase transition involves the same structural changes as in pure PST but the critical pressure p_{C2} is shifted from 5.5 GPa to 8.1 GPa (see Figure 5.10) and a mixed tilt pattern was detected only at 15.6 GPa.

PST doped with Ba^{2+} (PBST) is a canonical relaxor (Mihailova *et al.*, 2008b), i.e., its average structure remains cubic even at temperatures well below T_m . This is due to the local elastic fields induced by the larger ionic radius of the Ba-cations and the violation of the electron lone pairs of the Pb^{2+} cation as Ba^{2+} has an isotropic outer electron shell. Thus, the induced local strains in the vicinity of the Ba^{2+} cations smear out the first pressure-induced phase transition over a pressure range from 2–4 GPa (Mihailova *et al.*, 2011). The ferroic distortion as well as the phase fraction produced at p_{C1} is smaller than for the pure compound.

The new experiments up to 22.4 GPa revealed no additional sets of Bragg peaks over the entire pressure range studied. Hence, doping with Ba suppresses the anti-polar long-range order of Pb^{2+} cations and consequently the BO_6 -tilt pattern does not change to a mixed system. The length of coherence of B-site chemical order in PBST is approximately 5 times larger than that in PST, which would facilitate the anti-polar Pb^{2+} cation ordering. Thus, the local elastic fields induced by the incorporation of Ba have much stronger impact on the second pressure-induced phase transition than the B-site chemical order. The 0 10 0 reflection is shown in Figure 5.9 at 19.8 and 22.4 GPa showing that a resolved d-spacing splitting is observed at the last pressure. This unambiguously reveals that the symmetry is lower than rhombohedral. Hence, similar to PSN, the phase transition in PBST that occurs at p_{C2} involves only a change in the tilt pattern to $a^0b^-b^-$ or $a^-b^-b^-$ with $a < b$.

5 Results and Discussion

Table 5.1: Characteristic pressures of doped PST and PSN

	PC2	Mixed tilt system
PBST	~ 19.8 GPa	no change to a mixed tilt system
PLST	8.1 GPa	15.6 GPa
PLSN		12 GPa diffuse streaks
PSSN	7.4 GPa	9.6 GPa
PSTN	10.5–12.3 GPa	< 19.6 GPa only streaks
PSTS	8.1–11.3 GPa	16.1 GPa

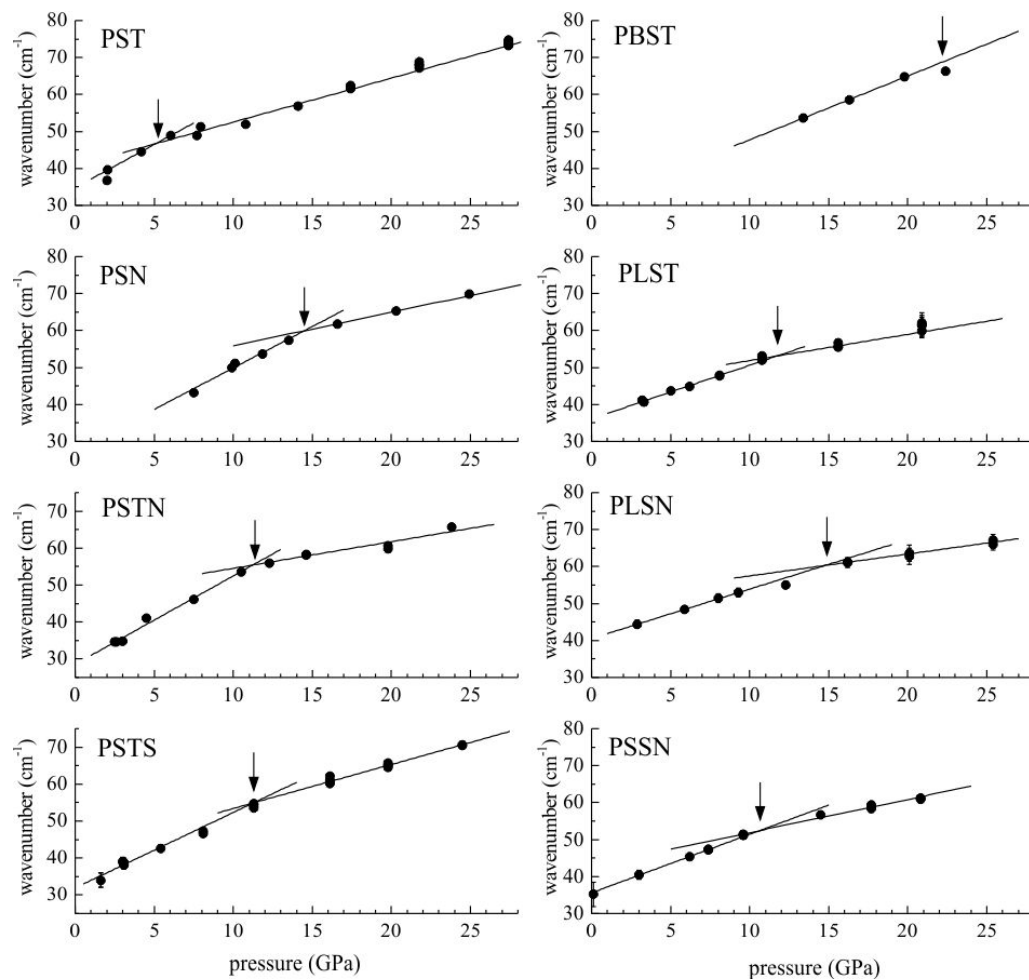


Figure 5.8: Deviation from linear of the pressure induced soft mode at high pressures. The kink marks the second pressure induced phase transition.

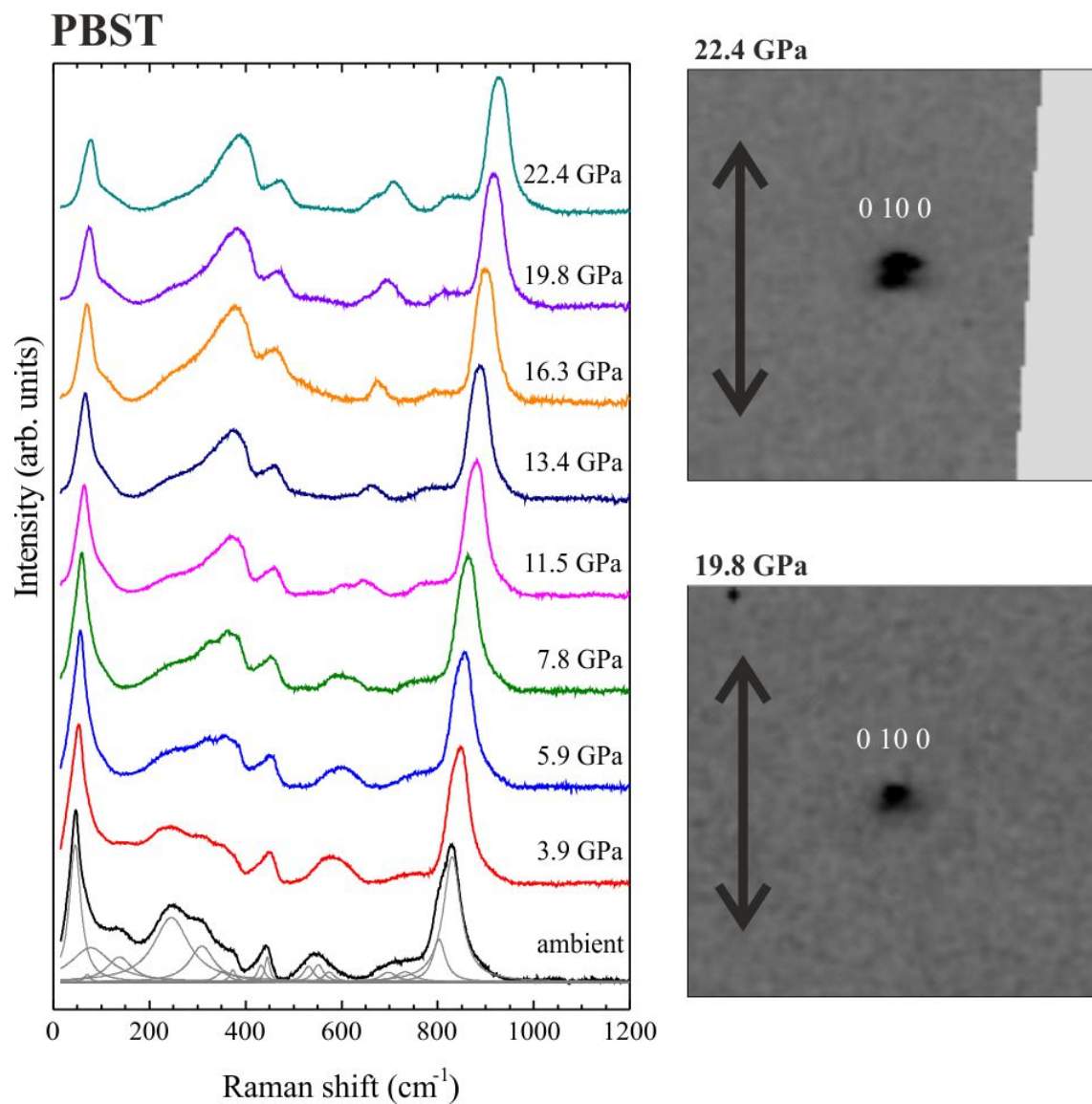


Figure 5.9: Raman spectra of PST doped with Ba at different pressures showing the enhancement of the peak at $\sim 350 \text{ cm}^{-1}$ associated the the cubic F_{2u} mode. The $0\ 10\ 0$ Bragg reflection in the reciprocal space layer at 19.8–22.4 GPa shows the d -space splitting, the arrow marks the direction to the origin.

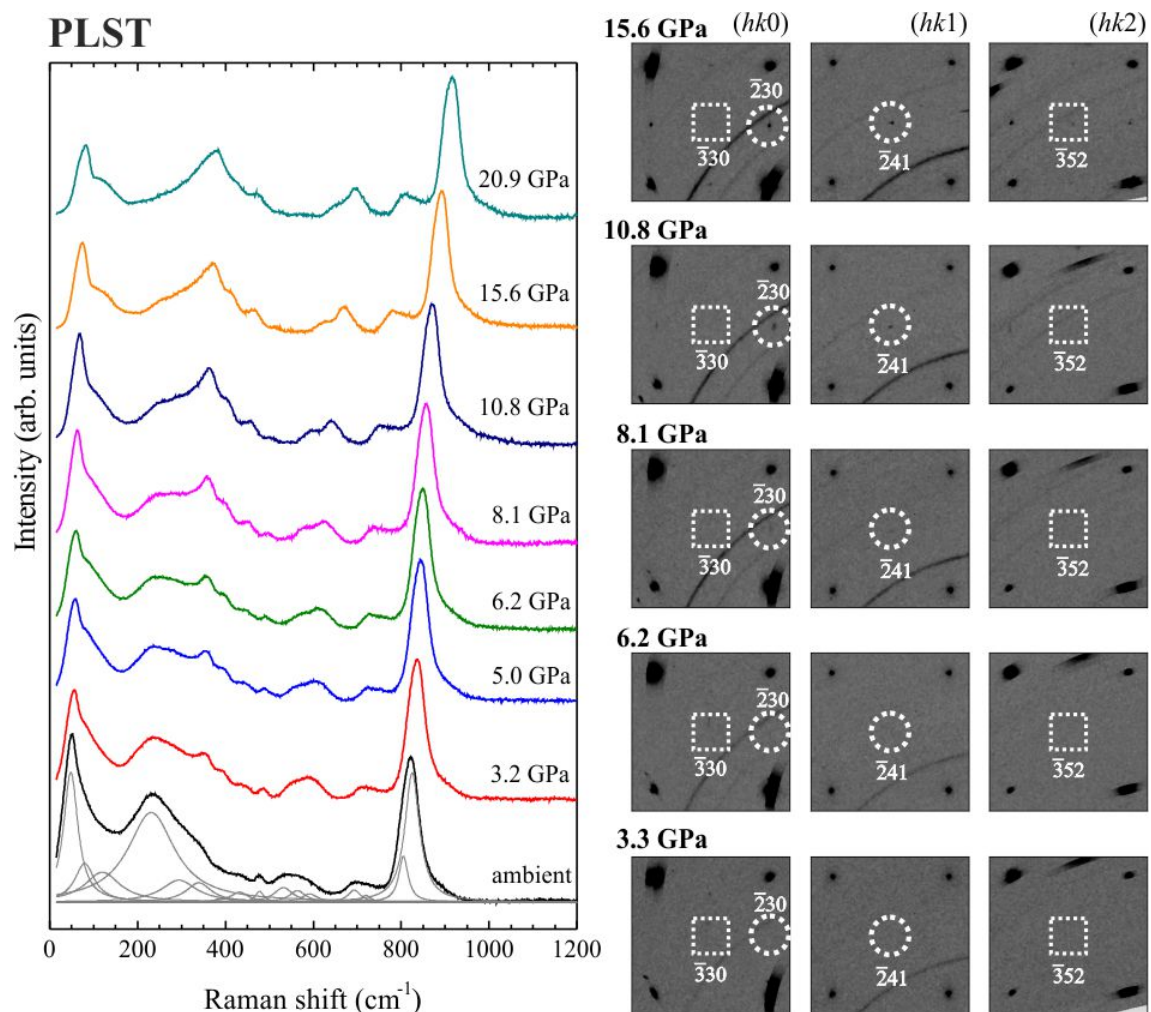


Figure 5.10: Raman scattering and Reciprocal space layers of PLST at different pressures. White dashed circles mark the positions of $h, k = 2n, l = 2n+1$ (eeo) X -point reflections, while white dashed squares mark the position of $h = 2n, k, l = 2n+1$ (ooo) M -point reflections.

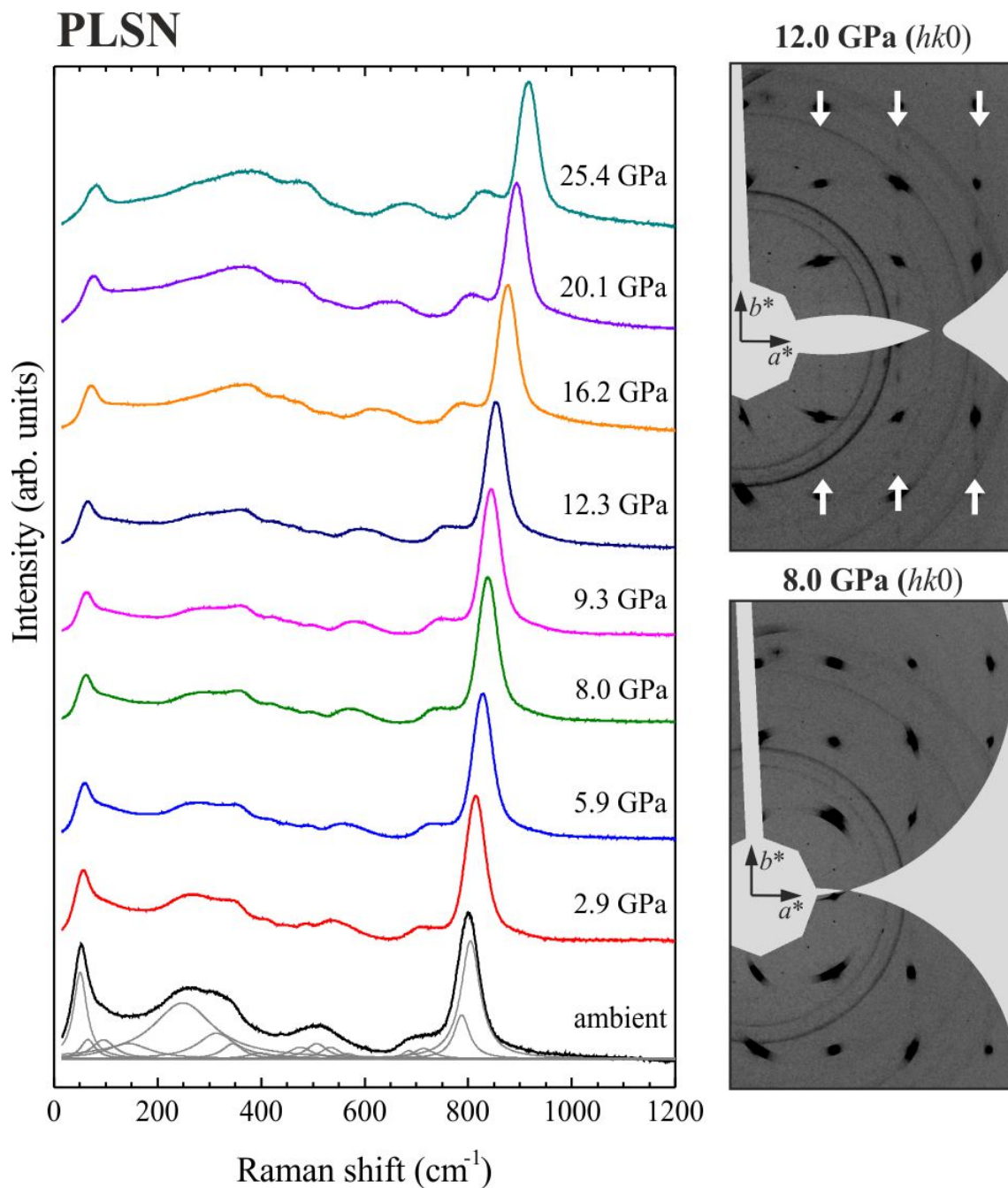


Figure 5.11: Raman scattering and Reciprocal space layers of PLSN at different pressures. The white arrows mark the appearance of diffuse streaks in the $hk0$ layer.

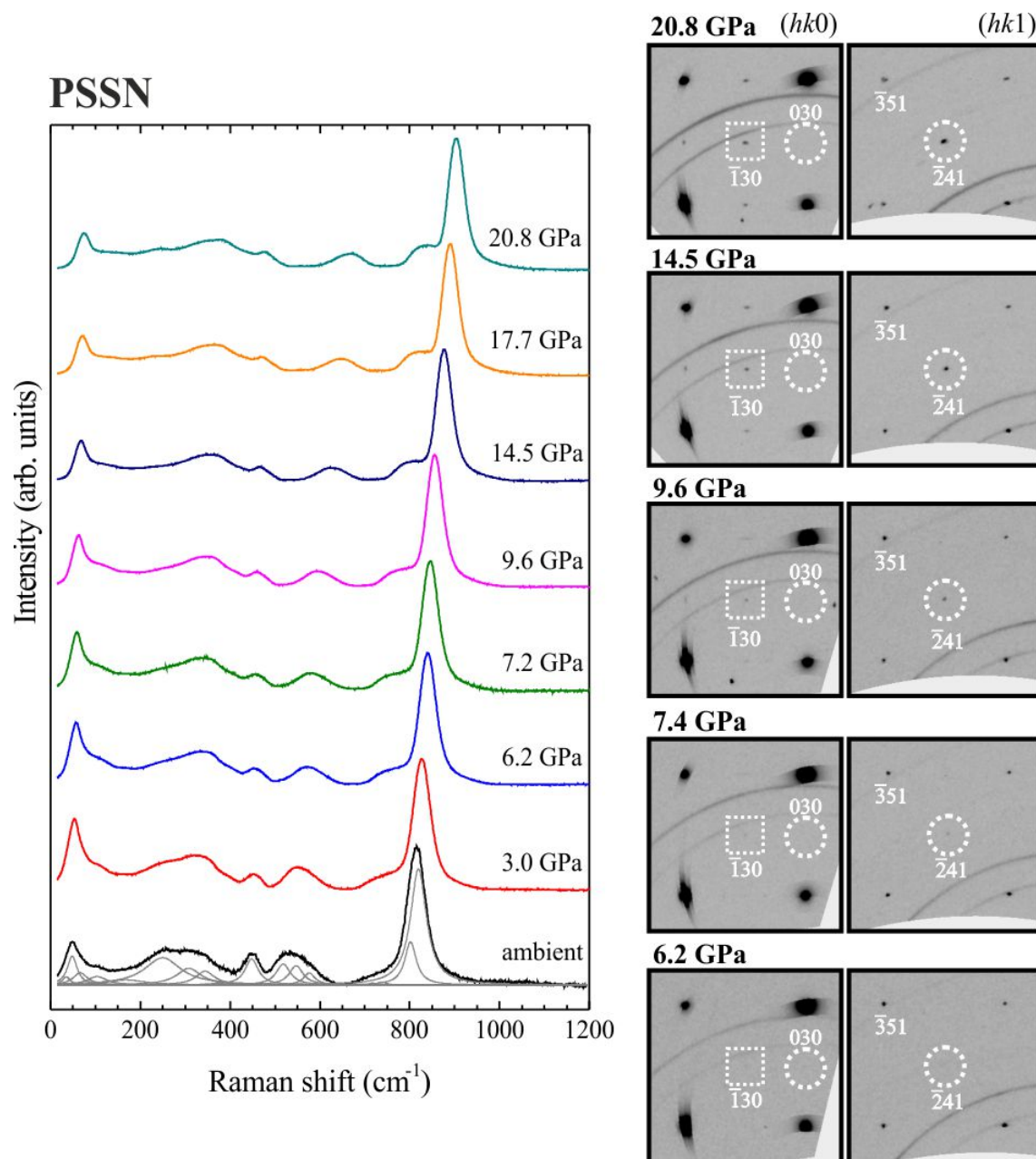


Figure 5.12: Raman scattering and Reciprocal space layers of PLST at different pressures. White dashed circles mark the positions of $h, k = 2n, l = 2n+1$ (*eeo*) X-point reflections, while white dashed squares mark the position of $h = 2n, k, l = 2n+1$ (*eeo*) M-point reflections.

5 Results and Discussion

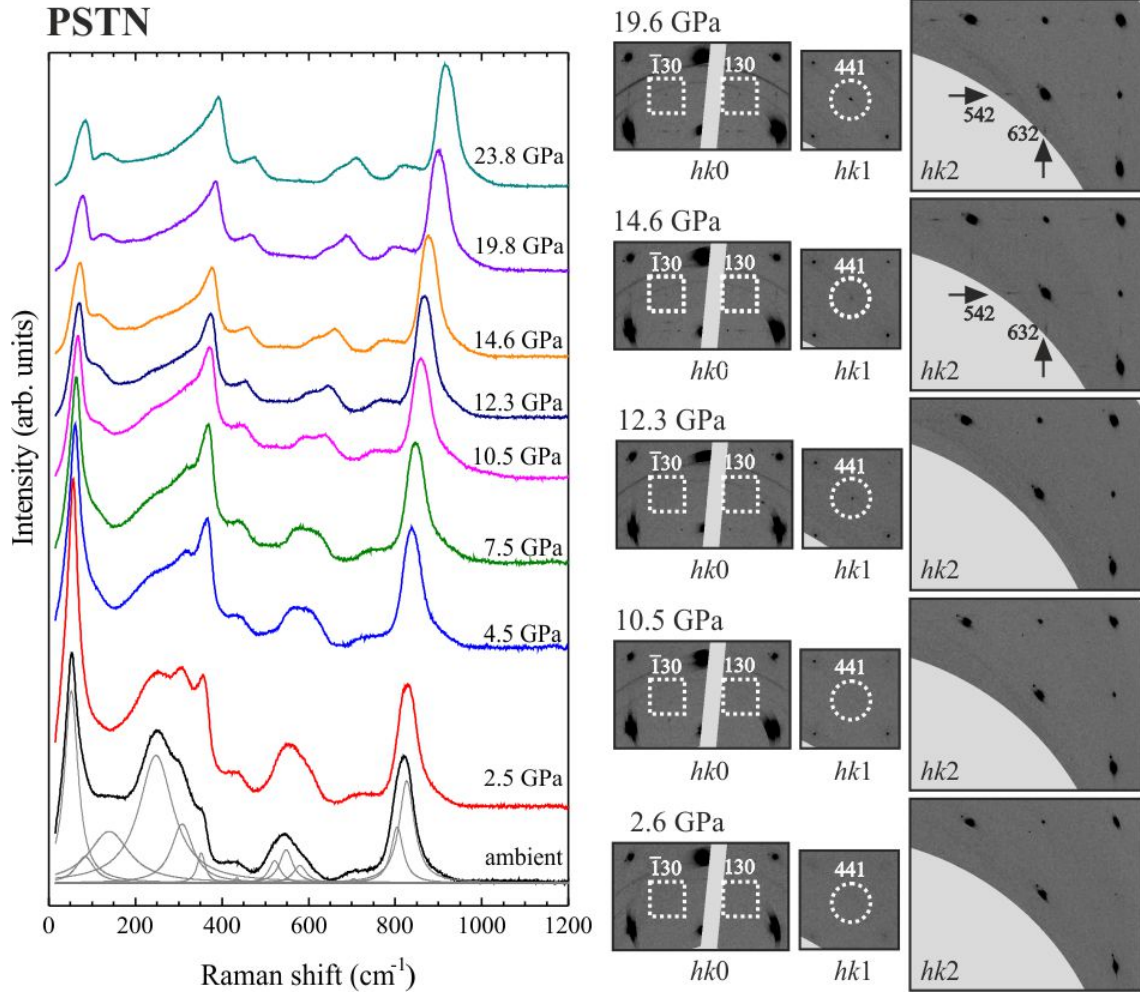


Figure 5.13: Raman scattering and Reciprocal space layers of PSTN at different pressures. White dashed circles mark the positions of $h, k = 2n, l = 2n+1$ (*eeo*) X-point reflections, while white dashed squares mark the position of $h = 2n, k, l = 2n+1$ (*eo*) M-point reflections. The arrows in the $hk2$ layer point to streak-like diffraction features corresponding to X-point reflections.

5 Results and Discussion

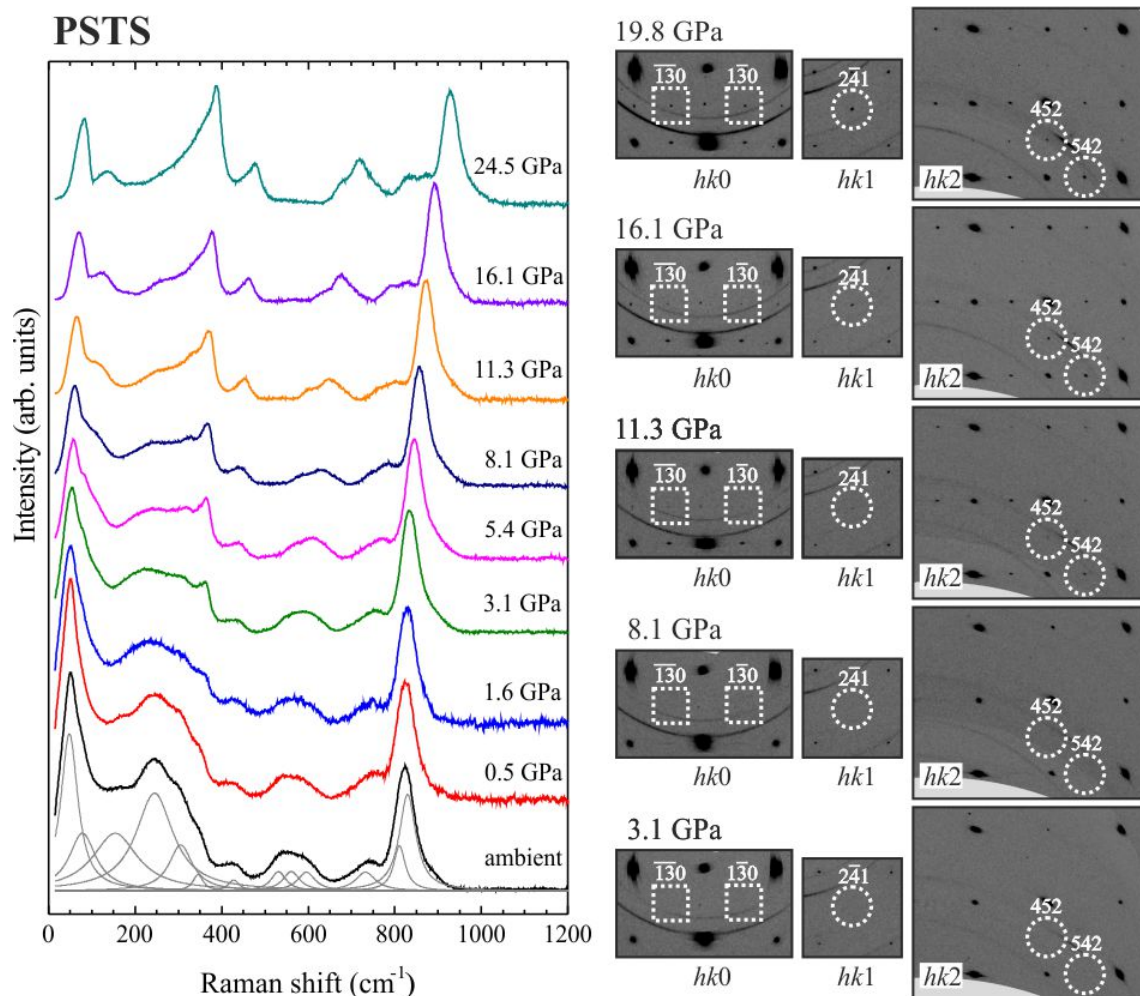


Figure 5.14: Raman scattering and Reciprocal space layers of PSTS at different pressures. White dashed circles mark the positions of $h, k = 2n, l = 2n+1$ (eeo) X -point reflections, while white dashed squares mark the position of $h = 2n, k, l = 2n+1$ (eeo) M -point reflections. The arrows in the $hk2$ layer point to streak-like diffraction features corresponding to X -point reflections.

5.2 The high-pressure structural state of relaxors at elevated temperatures

This section is based on the paper *Waeselmann, N., Mihailova, B., Gospodinov, M., Petrova, D. and Bismayer, U. In-situ high-temperature high-pressure Raman spectroscopy on single-crystal relaxor ferroelectrics $\text{PbSc}_{1/2}\text{Ta}_{1/2}\text{O}_3$ and $\text{PbSc}_{1/2}\text{Nb}_{1/2}\text{O}_3$ Phys. Rev. B, submitted*

The effect of temperature on the Raman spectra of PST and PSN collected in DAC can be seen from the spectra collected at the same low pressure 0.4 ± 0.1 GPa and three different temperatures: room temperature, 400 K and 600 K (Figure 5.15). The development of PNRs with temperature decrease is apparent from the enhancement of the anomalous Raman scattering near 140, 250, 430 and 700 cm^{-1} related to the cubic F_{1u} modes (Welsch *et al.*, 2011; Mihailova *et al.*, 2002). The characteristic temperatures T^* and T_B can be deduced from the temperature dependences of the Raman peaks near 140 and 250 cm^{-1} , resulting from Pb- BO_3 translations and vibrations of off-centered B-site cations, respectively (Welsch *et al.*, 2011; Mihailova *et al.*, 2008b; Dul'kin *et al.*, 2010b). In particular at T^* the FWHM of the peak near 250 cm^{-1} considerably decreases due to the strong enlargement of the correlation length of coupled B-cation polar shifts. The peak near 350 cm^{-1} is related to the cubic silent F_{2u} mode which consists of Pb-O bond stretching within cubic $\{111\}$ planes and can also be thought as anti-phase BO_6 rotation (Welsch *et al.*, 2011; Mihailova *et al.*, 2011, 2002). The anomalous Raman activity of this mode results from coupled deformed Pb-O species. At ambient pressure the peak near 350 cm^{-1} is more pronounced for PST than for PSN due to the longer correlation length between the ferroic Pb-O species.

The Raman spectra of PST and PSN collected at different pressures at 400 K and 100 K are shown in Figure 5.16. Previous in-situ high-pressure experiments at room temperature demonstrated that (i) pressure leads to the suppression of both Raman peaks at 140 and 250 cm^{-1} , indicating decoupling of the Pb and B-cation polar shifts and subsequent reduction of the B-cation off-centered displacements, i.e., suppression of the polar order; (ii) the pressure-induced phase transition at p_{C1} from relaxor to non-polar rhombohedral state containing long-range ordered anti-phase BO_6 tilts is accompanied by the appearance of a soft mode near 37 cm^{-1} ; (iii) the development of the octahedral tilting with pressure increase is mirrored by the strong enhancement of the anomalous Raman scattering near 350 cm^{-1} (Mihailova *et al.*, 2008a, 2011; Waeselmann *et al.*, 2012; Kreisel *et al.*, 2002; Janolin *et al.*, 2006). As can be seen in Figure 5.16, the same pressure-induced structural changes are observed at elevated temperatures. The peak near 350 cm^{-1} is apparently enhanced by pressure for all temperatures, indicating the development of the octahedral tilting. At low pressures the Raman scattering near 250 cm^{-1} is well pronounced at 400 K but suppressed and broadened at 600 K, because the former temperature is still below T^* , whereas the latter temperature is well above T^* (see Table 1.2). The same is valid for the

5 Results and Discussion

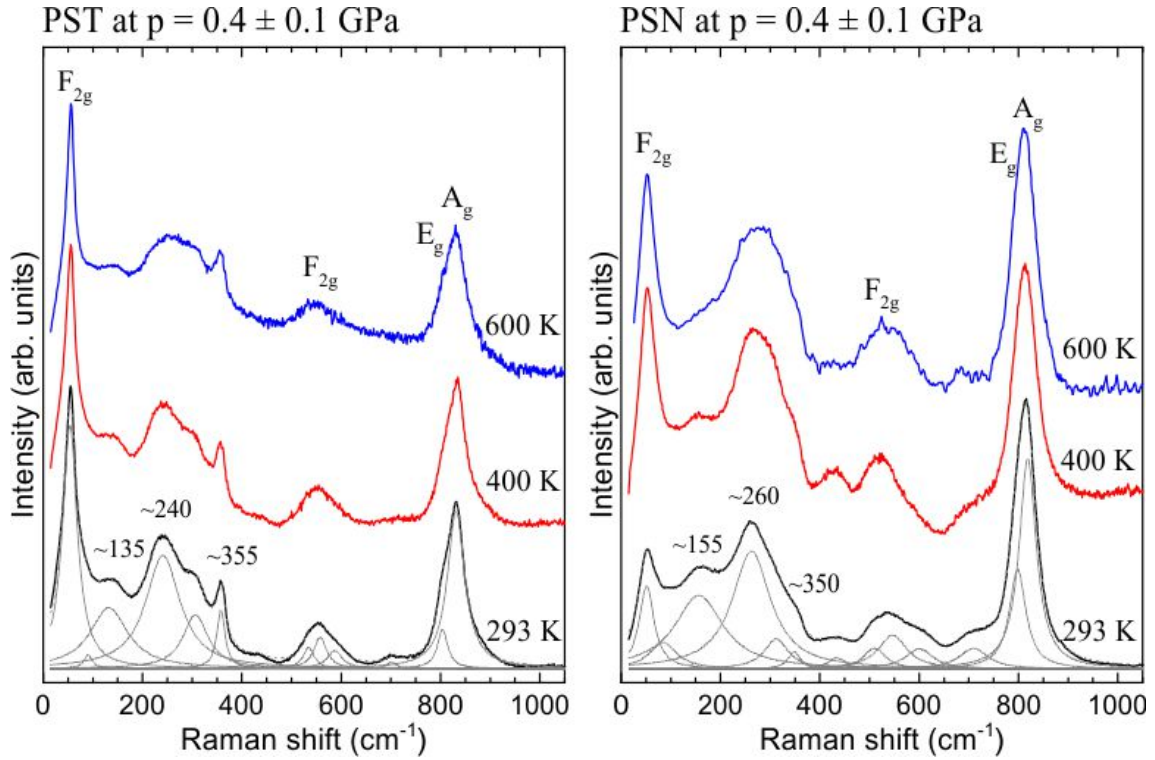


Figure 5.15: Raman scattering of PST and PSN measured in DAC at the same low pressure and different temperatures. The measured pressure was 0.4 GPa in all cases, except for PST at 600 K, for which the actual pressure was determined to be 0.3 GPa, i.e., within the experimental uncertainty all spectra were collected at ~ 0.4 GPa.

peak near 140 cm^{-1} . At 400 K both peaks are suppressed with pressure increase, indicating a suppression of the polar order, similar to the high-pressure state at room temperature.

With increasing temperature the appearance of the soft mode associated with the first phase-transition pressure drops to lower pressure (Figure 5.16 and Figure 5.17. At room temperature p_{C1} is 1.9 GPa for PST. The increase of temperature to 400 K which is 50 K below T^* , reduces p_{C1} to 1.5 GPa. On further temperature increase up to 600 K the soft mode was detected already at 0.3 GPa. For PSN the first phase-transition pressure also decreases at elevated temperatures. At room temperature the soft mode could not be resolved due to the small fraction of substance that undergoes a phase transition and the critical pressure p_{C1} was deduced from the Raman spectra by the maximum of the FWHM of the Pb-localized low-wavenumber mode near 50 cm^{-1} (Welsch *et al.*, 2009a). At $T = 400 \text{ K}$, which is 150 K below T^* , a soft mode was observed at 3.8 GPa, whereas at 600 K the soft mode appeared at 1.8 GPa.

The fact that for PSN the soft mode can be resolved from the strong peak near 50 cm^{-1} at high temperatures suggests that the integrated intensity of the soft mode and consequently, the fraction of the high-pressure phase at 400 K as well as at 600 K is larger than that at room temperature. It should be noted that the temperature-driven paraelectric-

5 Results and Discussion

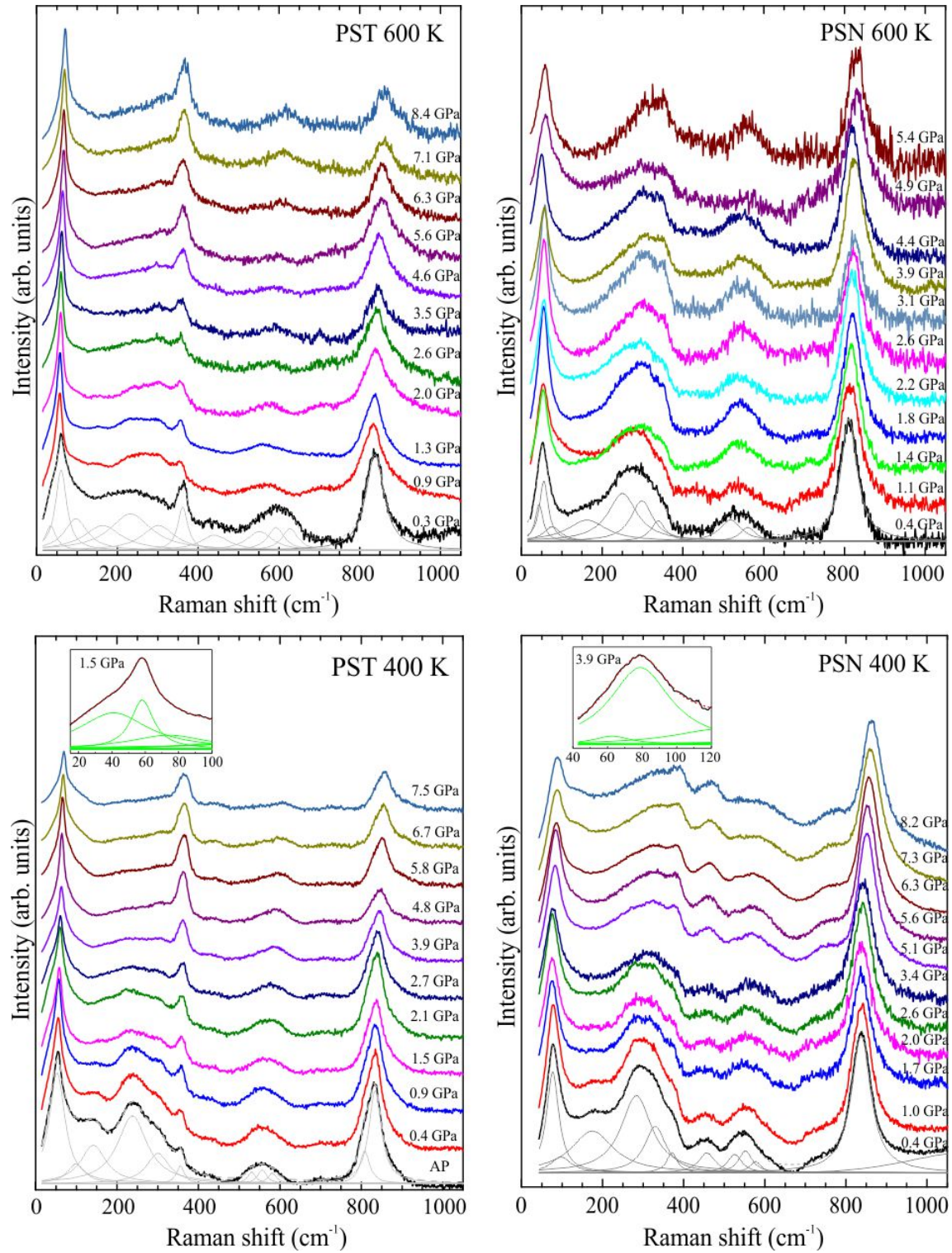


Figure 5.16: High-pressure Raman spectra of PST and PSN at 600 K and 400 K. The insets in the 400 K spectra show the first pressure where the soft mode appears.

5 Results and Discussion

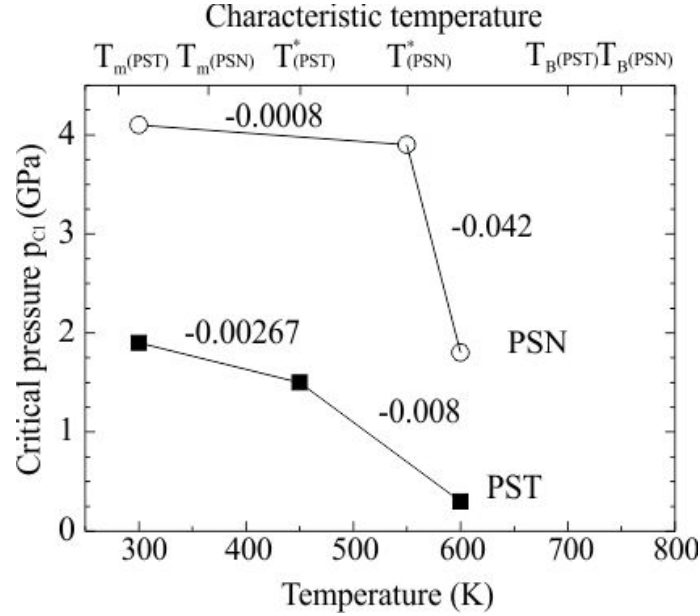


Figure 5.17: Critical pressure p_{C1} versus temperature for PST (filled squares) and PSN (open circles). The values $\Delta p_{C1} / \Delta T$ in different temperature ranges are given above the corresponding lines.

ferroelectric phase transition in PSN has been detected by neutron diffraction at ~ 370 K (Perrin *et al.*, 2000), although at room temperature PSN is still in a relaxor state, i.e., there are abundant PNRs and the predominant structural component is cubic (Maier *et al.*, 2009). The coupling between polar cation displacements in both PNRs and ferroelectric domains is unflavored by the temperature increase. This in turn facilitates the anti-ferrodistortive coupling and hence decreases the critical pressure and may lead to a larger fraction of the material that transforms under pressure into non-polar rhombohedral phase with anti-phase octahedral tilt order. The latter is supported by the fact that for PST the intensity of the soft mode at elevated temperatures is larger than the soft-mode intensity at room temperature. The co-existence of two types of ferroic coupling at ambient conditions: polar and anti-ferrodistortive, explains why for relaxors the high-temperature state is different from the high-pressure state, although the negative dp_{C1} / dT for both PST and PSN, which in general would suggest that the high-symmetry phase is preferred at high temperature as well as at high pressure. Our results about the negative $p_C(T)$ slope are also constant with the observed decrease in T_m with pressure increase (Venturini *et al.*, 2006; Hilczer & Szafranski, 2008), which is due to the suppression of the polar coupling on the account of the pressure-enhanced anti-ferrodistortive coupling.

Figure 5.18 shows the pressure dependences of the positions ω of the peaks near 250 cm^{-1} and 350 cm^{-1} measured at room temperature, 400 K, and 600 K for PST and PSN, respectively. As mentioned above, for all temperatures the peak near 250 cm^{-1} , which is generated by vibrations of off-centered B-site cations, is strongly suppressed with pressure increase. For room temperature the peak softens up to p_{C1} and then starts hardening as

5 Results and Discussion

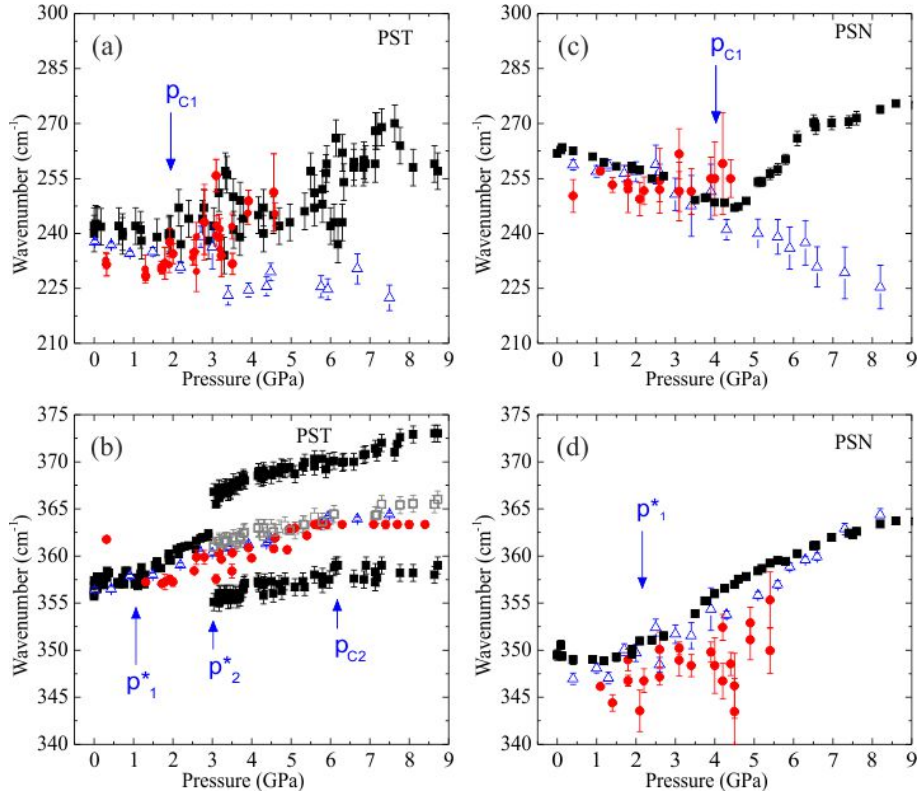


Figure 5.18: Pressure dependence of the positions of different Raman peaks for PST and PSN: the peak near 260 cm^{-1} associated with the B-localized cubic F_{1u} mode (a, c); the peak near 350 cm^{-1} , associated with the cubic F_{2u} consisting of Pb-O bond stretching (b, d). Black filled squares represent the data at room temperature; open blue triangles at 400 K, red filled circles for 600 K. The open gray squares are the calculated mean wavenumber for room temperature above p_2^* from the two split peaks.

the effect is more pronounced for PSN. The observed minimum of $\omega(p)$ near the phase transition is related to the instability of the whole system when approaching the phase transition from both low- and high pressures and the corresponding broadening of the crystal potential.⁴⁹ However, when the crystal is heated to 400 K, which is still below but close to T^* , the peak near 250 cm^{-1} softens in the entire pressure range studied. We suggest that this is related to the combined effects of temperature and pressure on the local multiwell potential of the off-centered B-site cations. For PNRs the intermediate temperature T^* can be considered as a "local phase-transition temperature" and therefore, when a system is approaching T^* from below, the potential barrier of the multiwell potential becomes lower and the shape of the individual wells deviates from parabolic, leading to broader potential wells close to the minima. On the other hand, high pressure triggers the B-cations to move toward the octahedral centers and hence decreases the distance between the potential well minima. This, combined with the broader wells and lower potential barrier, increases the probability of tunneling of B-site cations through the barrier between the separate wells of the multiwell potential instead of freezing the

5 Results and Discussion

B-cations in a one single well. The tunneling probability should increase with pressure and therefore the resultant effective potential that the B-site cations experience at higher pressure should be broader, hence the mode softens. For $600\text{ K} \in (T^*, T_B)$ the peak near 250 cm^{-1} is weak and broad already at ambient pressure due to the suppression of the off-centered displacements of the B-site cations and the reduced polar coupling by the sole temperature effect. The uncertainties in determining the peak positions from the fitting are considerable but nevertheless, $\omega(p)$ seems to have a slightly positive slope in the entire pressure range studied. Such a behavior is expected because the B-site cations at $600\text{ K} > T^*$ should be in a pseudo single-well potential and the hardening of the mode is simply due to the shrinking of the crystal volume under high pressure.

At room temperature the pressure dependence of the O-localized Pb-O bond stretching mode near 350 cm^{-1} (see Figs. 4b and d) is sensitive to the intermediate pressures p_1^* and p_2^* (Maier *et al.*, 2011b). At p_1^* (1.2 GPa for PST and 2.4 GPa for PSN at room temperature) the mesoscopic polar order is violated and a local anti-polar order of Pb atoms as well as quasi-dynamic long-range anti-phase BO_6 -tilt order is developed, whereas at p_2^* ($\sim 3\text{ GPa}$ for PST and $\sim 7 - 10\text{ GPa}$ for PSN at room temperature) the octahedral tilt pattern is changed on the mesoscopic scale (Maier *et al.*, 2011b). Up to p_1^* the wavenumber of the Pb-O bond stretching mode is nearly constant and then begins to strongly increase, whilst at p_2^* the mode splits. For PSN the splitting was observed at 10 GPa (Maier *et al.*, 2011b), i.e., above the pressure achievable at high temperatures with our experimental set-up. At 400 K and 600 K no kink in the $\omega(p)$ -dependence of the Pb-O bond stretching mode was detected below p_{C1} for both PST and PSN, which is most probably due to the fact at elevated temperatures p_1^* approaches ambient pressure. Neither splitting of the peak near 350 cm^{-1} in the pressure range (p_{C1} , p_{C2}) was resolved but this may result from the temperature-induced broadening and subsequent overlapping of the peaks as well as the overall worse signal-to-noise ratio for the high-pressure spectra collected at 400 and 600 K as compared to the spectra measured at room temperature. Therefore, we cannot draw any conclusions about the temperature renormalization of the second intermediate pressure p_2^* . However, for PST the $\omega(p)$ -dependences measured at 400 and 600 K exhibit a steady increase up to $\sim 5.5\text{ GPa}$, which is p_{C2} at room temperature, and then become almost constant (see Figure 5.18b). To compare this trend with the room-temperature data, the mean peak position of the splitted components was also plotted against pressure (open squares in Figure 5.18b) and it showed a similar kink near 5.5 GPa. This indicates that the second pressure-induced phase transition is not affected by the temperature increase, i.e., it is independent of the degree of polar order at ambient pressure. Indeed, at p_{C2} the long-range octahedral tilt pattern is changed to better adopt the shrinking of the unit-cell volume under pressure increase and this process is solely related to the initial mesoscopic anti-ferrodistortive order. The plateau-like $\omega(p)$ for the Pb-O bond stretching mode above p_{C2} suggests that the average Pb-O bond length remains more or less the same and the pressure-induced deformation of the PbO_{12} species is mainly related to change in the

O-Pb-O bond angles, as a consequence of the unequal BO_6 rotation about the cubic [100], [010], and [001] directions.

5.3 Structural changes in relaxor-based solid solutions with giant piezoelectric effect

5.3.1 Temperature-driven structural transformations at ambient pressure

This section is based on the paper *Waeselmann, N., Maier, B. J., Mihailova, B., Angel, R. J., Zhao, J., Gospodinov, M., Paulmann, C., Ross, N. and Bismayer, U. (2012). Pressure-induced structural transformations in pure and Ru-doped $0.9\text{PbZn}_{1/3}\text{Nb}_{2/3}\text{O}_3$ - 0.1PbTiO_3 near the morphotropic phase boundary. Phys. Rev. B 85, 014106.*

XRD and Raman scattering of PZN-0.1PT

Powder XRD patterns of pure and Ru-doped PZN-0.1PT in the 2θ -range that corresponds to the 100 Bragg peak indexed in $Pm\bar{3}m$ (or 200 Bragg peak in $Fm\bar{3}m$) show that the cubic to tetragonal phase transition takes place between 475 and 450 K Figure 5.19. Below T_{C1} an additional shoulder near $2\theta = 21.8^\circ$ appears, due to the splitting of the cubic Bragg peak. Below 375 K, where the tetragonal to monoclinic phase transition is expected the diffraction peak profile is somehow changed, but the strong signal overlapping and insufficient resolution of in-house diffraction experiments hindered the precise phase determination. At 300 K the diffraction peak seems to consist of more than two components, indicating the co-existence of a phase (or phases) with symmetry different from tetragonal. This is in accordance with piezoresponse force microscopy experiments demonstrating the co-existence of at least two types of domains at room temperature (Scholz *et al.*, 2009) and confirms that the compounds studied here are at the MPB.

To check if in both pure and Ru-doped PZN-0.1PT PNRs persist at low temperatures, we have conducted synchrotron single-crystal XRD at $T = 300$ and 150 K, i.e., below T_{C2} . The $(hk0)$ and $(hk1)$ layers (indexation given in $Fm\bar{3}m$) of the reciprocal space reconstructed from synchrotron single-crystal XRD data collected on PZN-0.1PT and PZN-0.1PT:Ru are presented in Figure 5.20. X-ray diffuse scattering streaks along the directions are clearly visible in the $(hk0)$ layers, revealing the existence of PNRs well below the T-M phase transition temperature. These streaks originate from off-center cation displacements which correlate within $\{110\}$ planes of the real space and are typical of Pb-based relaxors (Welberry & Goossens, 2008), (Pasciak *et al.*, 2007). The weak diffuse spots in the $(hk1)$ layers are also due to PNRs. Monte-Carlo simulations show that the observed $\langle 110 \rangle^*$ diffuse scattering can be reproduced fairly well using Pb displacements along each of the cubic $\langle 111 \rangle$, $\langle 110 \rangle$, and $\langle 100 \rangle$ directions (Welberry & Goossens, 2008), (Pasciak *et al.*, 2007), but detailed experimental studies of the neutron diffuse scattering around the 110

5 Results and Discussion

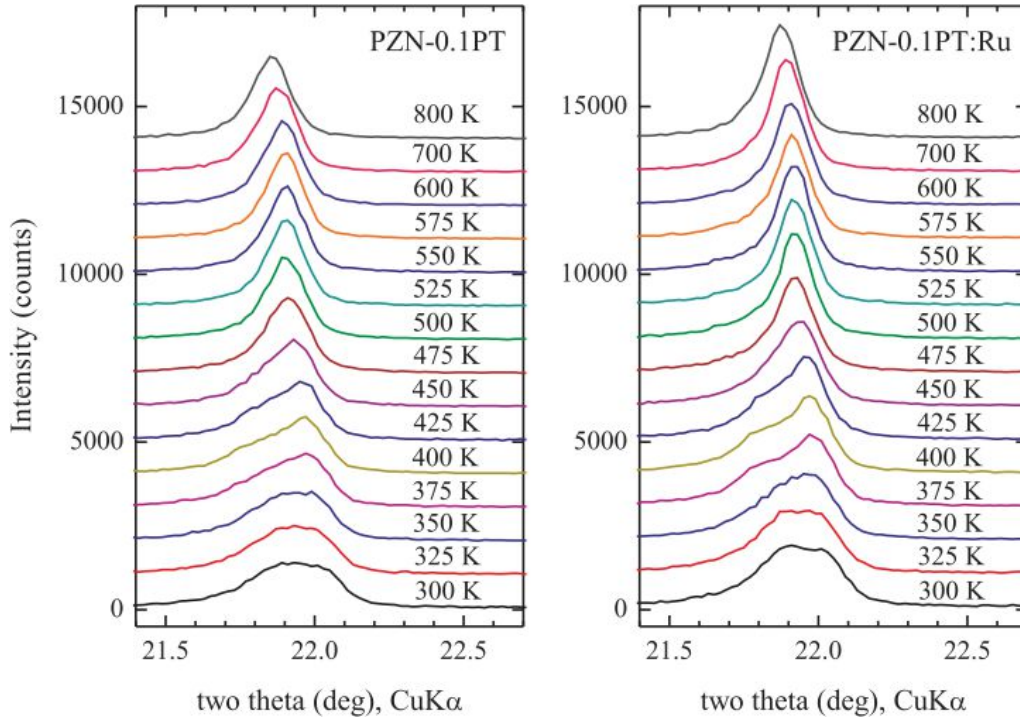


Figure 5.19: Powder XRD patterns of pure and Ru-doped PZN-0.1PT; the 2θ range corresponds to the 100 Bragg peak indexed in $Pm\bar{3}m$, which is equivalent to the 200 Bragg peak in $Fm\bar{3}m$.

reciprocal lattice point suggest the PNRs in PZN- x PT have an inherent rhombohedral distortion (La-Orauttapong *et al.*, 2001), (La-Orauttapong *et al.*, 2003). The fraction of PNRs seems to be slightly larger in the Ru-doped compound than that in the undoped compound as evident by the slightly stronger x-ray diffuse scattering intensity. For both pure and Ru-doped PZN-0.1PT the x-ray diffuse scattering intensity increases when temperature decreases from 300 K to 150 K, indicating that the PNRs further develop in a competing coexistence with the long-range polar order of M_C -type.

The absence of any sharp Bragg peaks with $h, k, l = \text{all odd}$ (see the $hk1$ layers in Figure 5.20) indicates that there is no long-range chemical B-site 1:1 order that would lead to a doubling of the unit cell within spatial regions large enough to be detected by synchrotron single-crystal XRD.

Polarized Raman spectra of PZN-0.1PT collected at different temperatures in $\bar{Z}(XX)Z$ and $\bar{Z}(XY)Z$ geometries are shown in Figure 5.21. A moderate addition of PT to PZN or PMN does not disturb the doubling of the perovskite structure (Svitelskiy *et al.*, 2005), (Iwata *et al.*, 2009), (Cheng *et al.*, 2009). Thus, we observe the allowed Raman active peaks in the prototype cubic double-perovskite structure ($Fm\bar{3}m$): the A_{1g} and E_g modes are active in $\bar{Z}(XX)Z$ geometry while the two F_{2g} modes are active in $\bar{Z}(XY)Z$ geometry. The additional peaks are caused by the distortion of the cubic structure due to PNRs. It has been previously demonstrated that the Raman scattering near 50 and 260 cm^{-1} is

5 Results and Discussion

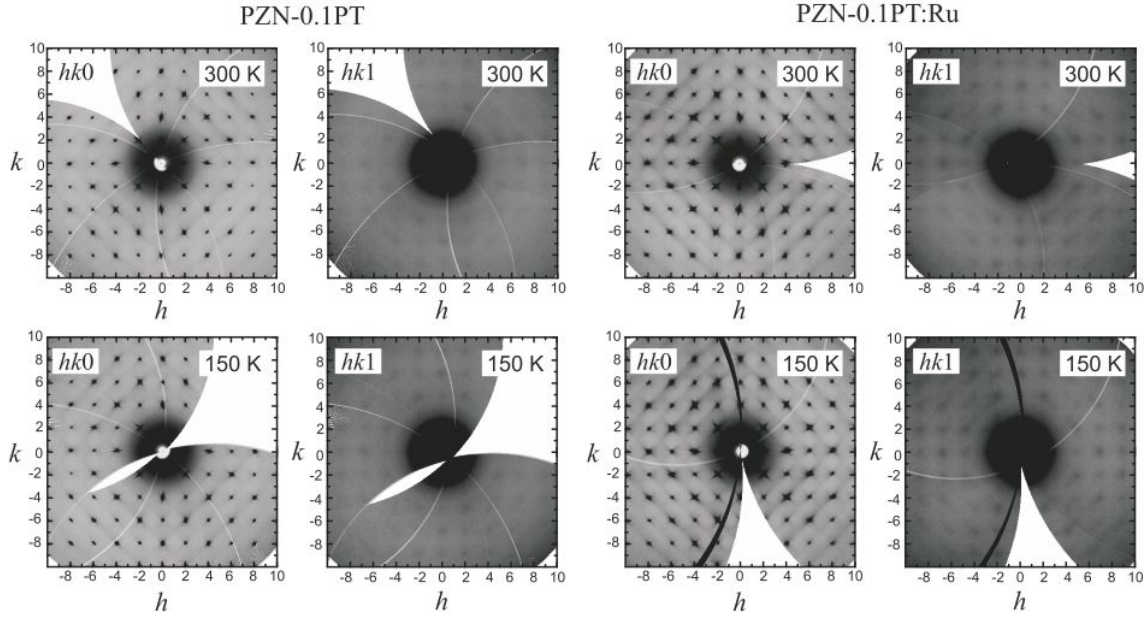


Figure 5.20: Reciprocal-lattice layers reconstructed from synchrotron single-crystal XRD on pure and Ru-doped PZN-0.1PT. The Miller indices refer to a cubic double-perovskite $Fm\bar{3}m$ unit cell.

very sensitive to structural transformations in Pb-based relaxors (Mihailova *et al.*, 2008b), (Welsch *et al.*, 2011), (Maier *et al.*, 2009) and thus, we analyzed in more detail the temperature dependence of the corresponding peaks in the Raman spectra of PZN-0.1PT.

The band near 50 cm^{-1} arises from the Pb-localized F_{2g} mode and at $T > T_{C1}$ one peak should be observed in the $\bar{Z}(XY)Z$ spectrum. However, even at 850 K two peaks are well resolved in the $\bar{Z}(XY)Z$ spectrum of PZN-0.1PT (see Figure 5.21). For relaxors of the type $\text{PbB}'_{1/2}\text{B}''_{1/2}\text{O}_3$ and $\text{Pb}(\text{B}'_{1/2}\text{B}'''_{1/2})_{1-x}\text{B}'''_x\text{O}_3$, one strong peak coming from the cubic F_{2g} mode is observed at high temperatures in geometry, in accordance with the group-theory analysis; a corresponding weak "forbidden" peak is observed in $\bar{Z}(XX)Z$ geometry, due to the presence of Pb off-centered displacements (Mihailova *et al.*, 2008b), (Welsch *et al.*, 2011), (Maier *et al.*, 2009). Therefore, if the second peak in the $\bar{Z}(XY)Z$ spectrum of PZN-0.1PT is caused by additional ferroic distortions, a corresponding component should exist in the $\bar{Z}(XY)Z$ spectrum. However, at high temperatures there is only one "forbidden" $\bar{Z}(XX)Z$ peak instead of two, suggesting that the two peaks in the $\bar{Z}(XY)Z$ spectra of PZN-0.1PT are related to two different cubic vibrational states of Pb atoms. This assumption is strongly supported by the fact that when the polarization of the incident light is along the cubic face diagonal, both peaks near 50 cm^{-1} are suppressed in the cross-polarized $\bar{Z}(X'Z')Z$ spectrum and enhanced in the parallel polarized $\bar{Z}(X'X')Z$ spectrum (see Figure 5.22), following the transformation rules of the Raman polarizability tensor for cubic F_{2g} modes (Mihailova *et al.*, 2002). Two peaks near 50 cm^{-1} in the $\bar{Z}(XY)Z$

5 Results and Discussion

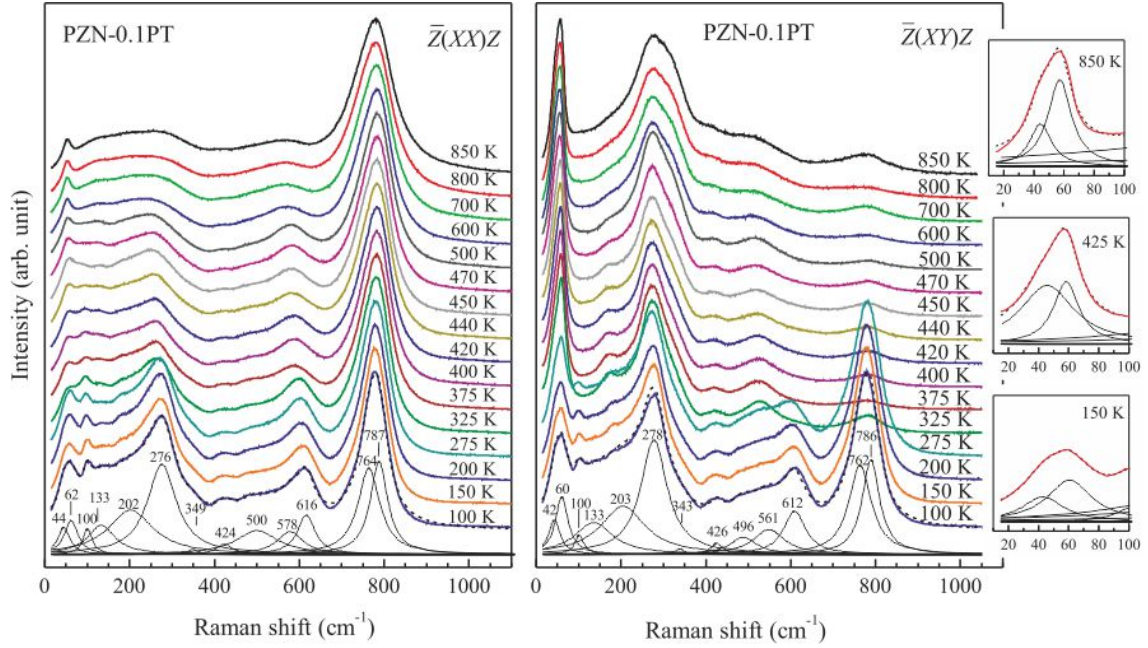


Figure 5.21: Parallel- $\bar{Z}(XX)Z$ and cross- $\bar{Z}(XY)Z$ polarized Raman scattering of PZN-0.1PT collected at different temperatures in the range 100–850 K; thin lines represent the fitting Lorentzians used for 100 K. Insets on right show on an enlarged scale the band near 50 cm^{-1} measured in $\bar{Z}(XY)Z$ geometry (red bold curves), the corresponding fitting Lorentzians (thin curves), and resultant spectrum profiles (black dashed curves).

spectra and only one peak near 50 cm^{-1} in the $\bar{Z}(XX)Z$ spectra are also observed for PMN, PZN and PZN- x PT for $x = 0.045, 0.08$, but not for $x = 0.20$ (Svitelskiy *et al.*, 2005), (Iwata *et al.*, 2009), (Taniguchi *et al.*, 2011), (Svitelskiy *et al.*, 2003).

These findings indicate that the discussed vibrational states of Pb are not due to possible chemical separation of PZN-rich and PT-rich regions, but they are exclusively typical of $\text{PbB}'_{1/3}\text{B}''_{2/3}\text{O}_3$ systems. On the local scale, $\text{PbB}'_{1/3}\text{B}''_{2/3}\text{O}_3$ compounds also exhibit chemically 1:1 B-site ordered regions as in the case of $\text{PbB}'_{1/2}\text{B}''_{1/2}\text{O}_3$ compounds, but due to the different stoichiometry, the ordered regions are of the type $\text{Pb}(\text{B}^{2+}_{2/3}\text{B}^{5+}_{1/3})_{1/2}\text{B}^{5+}_{1/2}\text{O}_3$ (Yan & Pennycook, 1998). Therefore, in $\text{PbB}'_{1/3}\text{B}''_{2/3}\text{O}_3$ systems with a doubled unit cell, there is a high probability to have Pb ions surrounded entirely by the higher-valence B'' cations (see the sketch in Figure 5.23) as well as by both B' and B'' cations, as in the case of $\text{PbB}'_{1/2}\text{B}''_{1/2}\text{O}_3$ systems. Hence, there are two cubic vibrational states of Pb ions: Pb1, surrounded only by B^{5+} , and Pb2, surrounded by both B^{2+} and B^{5+} .

The former state is more constrained because Pb^{2+} experiences strong repulsive interactions from all surrounding B-cations, which should oppose the intrinsic affinity of Pb^{2+} to form a lone pair and hence to displace off the center of the cubooctahedral cavity. By contrast, the second state allows for more flexibility and Pb2 ions may easily displace away from the octahedral center, for example along $\langle 110 \rangle$ to compensate the underbonded oxygen ions (Burton *et al.*, 2006) shared between B^{2+} and B^{5+} cations in

5 Results and Discussion

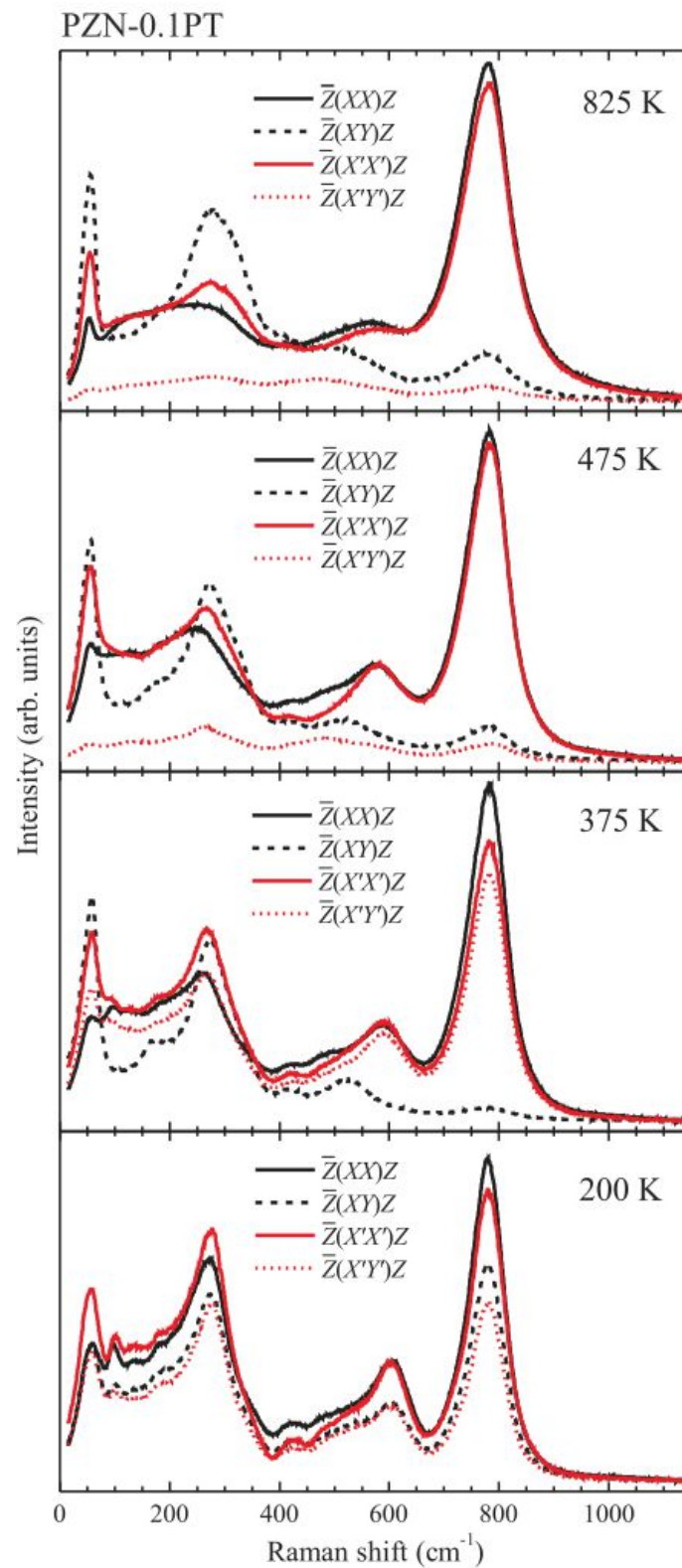


Figure 5.22: Parallel- and cross-polarized Raman spectra of PZN-0.1PT collected at selected temperatures with the incident light polarization parallel to the cubic edge [$\bar{Z}(XX)Z$ and $\bar{Z}(XY)Z$] and parallel to the cubic face diagonal [$\bar{Z}(X'X')Z$ and $\bar{Z}(X'Y')Z$].

5 Results and Discussion

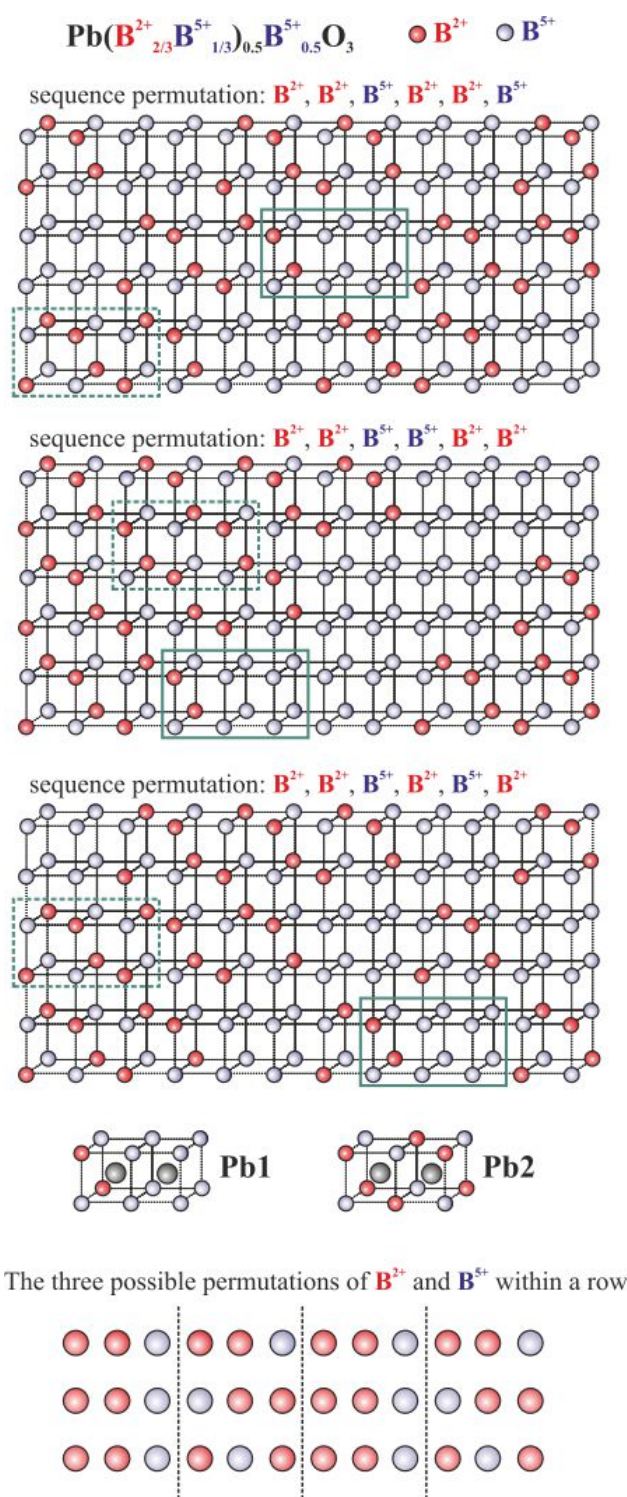


Figure 5.23: Examples of ordered B-cation configurations of type $\text{Pb B}'_{1/2}\text{B}''_{1/2}\text{O}_3$, where B' is randomly occupied by $2/3 \text{ B}^{2+}$ and $1/3 \text{ B}^{5+}$ cations, while B'' is exclusively occupied by B^{5+} . As a result, $\text{Pb}(\text{B}^{2+}_{2/3}\text{B}^{5+}_{1/3})_{1/2}\text{B}^{5+}_{1/2}\text{O}_3$ regions are formed with two Pb states distinguished by the surrounding B cations. The solid bold rectangles mark structural units that comprise Pb1 ions; the dashed bold rectangles mark structural units that comprise Pb2 ions. The sequence permutations refer to the B^{2+} and B^{5+} cations occupying the B' site.

5 Results and Discussion

locally ordered regions of $\text{PbB}'_{1/3}\text{B}''_{2/3}\text{O}_3$ systems or along $\langle 111 \rangle$ between two B-cations with different valence (Chen *et al.*, 1996). The latter structural distortion can be realized also in $\text{PbB}'_{1/2}\text{B}''_{1/2}\text{O}_3$ systems and is in agreement with the proposed rhombohedral-type structure of PNRs (La-Orautapong *et al.*, 2001), (La-Orautapong *et al.*, 2003). As a result, at high temperatures the vibrations of Pb1 ions should contribute to one peak in the spectrum and to none in the $\bar{Z}(XY)Z$ spectrum, Pb2 ions should contribute to one peak in the $\bar{Z}(XX)Z$ spectrum and a part of Pb2 ions, which are off-center displaced, should give rise to a peak in the $\bar{Z}(XX)Z$ spectrum. Statistically, Pb1 states are expected to be twice less than Pb2 states. We assign the lower-wavenumber ($\sim 45 \text{ cm}^{-1}$) and higher-wavenumber peak ($\sim 57 \text{ cm}^{-1}$) in the $\bar{Z}(XY)Z$ spectra to vibrational states of Pb1 and Pb2 ions, respectively, because of two reasons: (i) the lower-wavenumber peak is suppressed when diluting PZN with PT (Iwata *et al.*, 2009), indicating that this peak is related to the less abundant Pb states in the $\text{Pb}(\text{B}^{2+}_{2/3}\text{B}^{5+}_{1/3})_{1/2}\text{B}^{5+}_{1/2}\text{O}_3$ regions; (ii) for $\text{PbB}^{3+}_{1/2}\text{B}^{5+}_{1/2}\text{O}_3$ relaxors the "allowed" $\bar{Z}(XY)Z$ peak is always positioned at a higher wavenumber than the "forbidden" $\bar{Z}(XX)Z$ peak (Mihailova *et al.*, 2008b), (Welsch *et al.*, 2011), (Maier *et al.*, 2009). Based on the comparison to the frequencies of phonon modes measured by inelastic neutron scattering, the peak near 45 cm^{-1} has been previously assigned to disorder-induced scattering from $\text{Pm}\bar{3}\text{m}$ zone-boundary transverse acoustic modes (Svitelskiy *et al.*, 2003). Transferring vibrational energy from acoustic to optical phonon branches when the structure is doubled is highly plausible and coupling between acoustic and optical phonons may occur, but this process should be related with the Pb1 state characteristic of $\text{PbB}'_{1/3}\text{B}''_{2/3}\text{O}_3$ systems because, as mentioned above, a doublet in the $\bar{Z}(XY)Z$ spectrum is not observed for the high-temperature state of $\text{PbB}'_{1/2}\text{B}''_{1/2}\text{O}_3$ relaxors. Taniguchi *et al.* (Taniguchi *et al.*, 2011) have ascribed the peak observed at 45 cm^{-1} as stemming from the F_{2g} mode due to the orientational dependence of the intensity of this peak, without discussing the second peak near 57 cm^{-1} , although both peaks show exactly the same orientational dependence typical of cubic F_{2g} modes (Taniguchi *et al.*, 2011). Actually, the high-quality polarized Raman data presented in Ref. (Taniguchi *et al.*, 2011) clearly support our suggestion that the doublet $45\text{--}57 \text{ cm}^{-1}$ observed at high temperatures in $\bar{Z}(XY)Z$ spectra of $\text{PbB}'_{1/3}\text{B}''_{2/3}\text{O}_3\text{-}x\text{PT}$ arises from two vibrational states of Pb atoms in a cubic double-perovskite $\text{Fm}\bar{3}\text{m}$ structure related to the $\text{PbB}'_{1/3}\text{B}''_{2/3}\text{O}_3$ component.

The temperature dependences of the positions, FWHMs and integrated-intensity ratio $I_{45\text{cm}^{-1}}/I_{45\text{cm}^{-1}} + I_{57\text{cm}^{-1}}$ of the Raman signals near 50 cm^{-1} for PZN-0.1PT are shown in Figure 5.24. For this compound the Pb1-type ions are surrounded predominantly by Nb^{5+} , while Pb2-type ions are surrounded by both Zn^{2+} and Nb^{5+} . Titanium is expected to be randomly distributed in the cationic environments of both Pb1 and Pb2 ions, i.e., its presence is insufficient for the distinction of the two states of Pb ions. As can be seen in Figure 5.24, all characteristic temperatures can be determined from the temperature evolution of the "forbidden" $\bar{Z}(XX)Z$ Raman signal: the Burns temperature $T_B = 730 \text{ K}$ and the intermediate temperature $T^* = 525 \text{ K}$ are revealed by the local maxima in the FWHM as

5 Results and Discussion

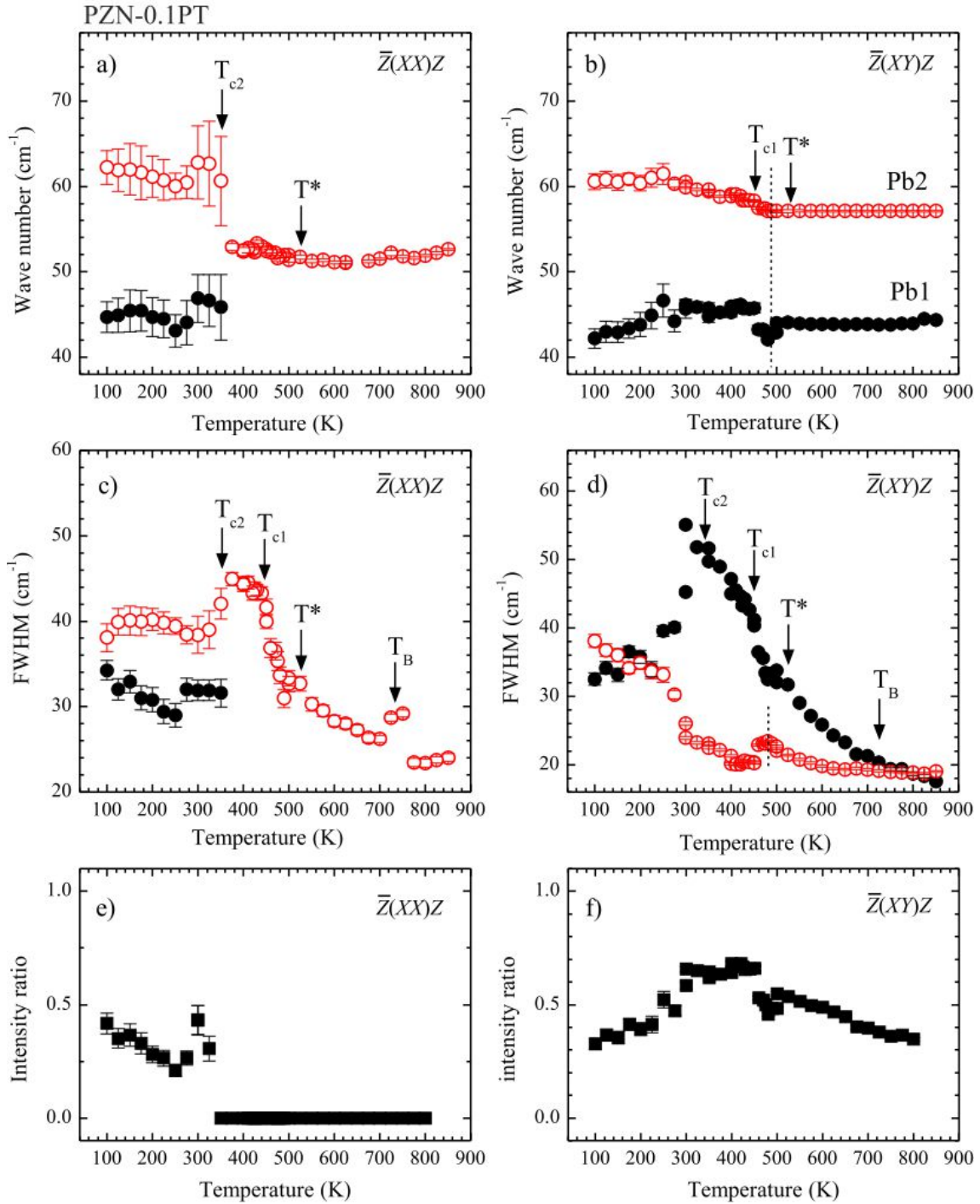


Figure 5.24: Temperature dependence of the positions, FWHMs, and intensity ratio $I_{45\text{cm}^{-1}}/I_{45\text{cm}^{-1}} + I_{57\text{cm}^{-1}}$ of the Raman peaks of PZN-0.1PT related to the Pb-localized F_{2g} mode of the prototype doubled structure ($Fm\bar{3}m$). At high temperatures (above T_{C2}) the solid and open circles correspond to the two vibrational Pb states: Pb1 surrounded predominantly by Nb and Pb2 surrounded by both Zn and Nb; Ti can be in the surroundings of both Pb1 and Pb2 atoms. Below T_{C2} two peaks are observed in both $\bar{Z}(XX)Z$ and $\bar{Z}(XY)Z$ due to the lowering of the point symmetry of the average structure.

5 Results and Discussion

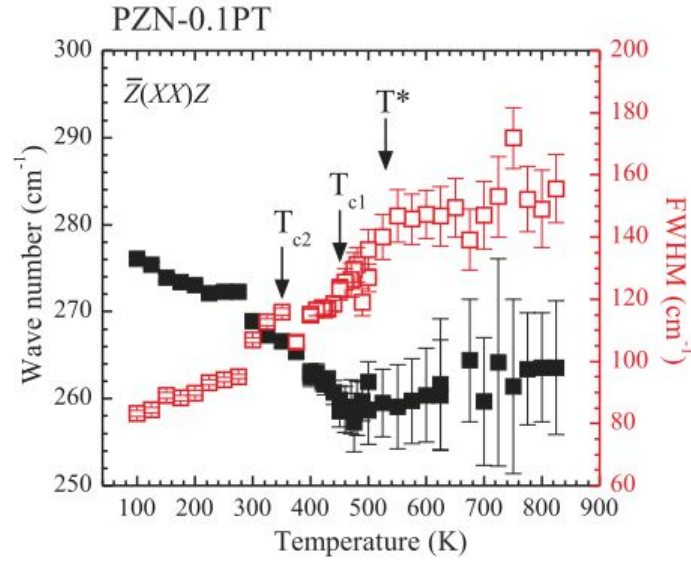


Figure 5.25: Temperature dependence of the position (solid squares) and FWHM (open squares) of the $\bar{Z}(XX)Z$ peak of PZN-0.1PT related to the B-cation-localized F_{1u} mode of the prototype $Fm\bar{3}m$ structure.

a function of temperature (Figure 5.24c), $T_{C1} = 450$ K is marked by the kink in the FWHM (Figure 5.24c) and $T_{C2} = 350$ K is indicated by the splitting of this peak (Figure 5.21, 5.24a, 5.24c and 5.24e) due to lowering of the point symmetry. The values determined from the Raman data are in excellent agreement with the characteristic temperatures measured by acoustic emission (Dul'kin *et al.*, 2006). In the temperature range from 850 K to $T_{C2} = 350$ K the frequency of the $\bar{Z}(XX)Z$ peak changes very slightly, but seemingly the peak hardens below T^* (Figure 5.24a).

The intermediate temperature $T^* = 525$ K is much better shown by the drop in the temperature dependence of the FWHM of the peak near 260 cm^{-1} (Figure 5.25). This peak is related to the infrared-active B-cation localized F_{1u} mode of the prototype $Fm\bar{3}m$ structure, whose Raman activity results from the presence of off-centered B-cation displacements (Mihailova *et al.*, 2002), (Welsch *et al.*, 2011). It should be underlined that so far a sharp decrease in the width of the Raman peak near 260 cm^{-1} at T^* has been reported for relaxors of type $(\text{Pb,A})\text{B}'_{1/2}\text{B}''_{1/2}\text{O}_3$, $\text{PbB}'_{1/2}(\text{B}''_{1-x}\text{B}'''_x)_{1/2}\text{O}_3$ and $\text{Pb}(\text{B}'_{1/2}\text{B}''_{1/2})_{1-x}\text{B}'''_x\text{O}_3$ (Mihailova *et al.*, 2008b), (Welsch *et al.*, 2011), (Maier *et al.*, 2009). The fact that the same is observed for a compound of type $\text{PbB}'_{1/3}\text{B}''_{2/3}\text{O}_3$ -xPT emphasizes on the universal character of the transformation processes occurring at T^* , namely, strongly enhanced coherence between off-centered displacements of B-site cations (regardless of their multiple type), leading to stable PNRs with a mean size and lifetime considerably larger than the mean size and lifetime of polar clusters that appear at T_B .

All characteristic temperatures can also be deduced by comparing the temperature dependence of the FWHM of the peaks near 45 and 57 cm^{-1} in the $\bar{Z}(XY)Z$ spectra (Figure 5.24d). Above T_B the two "cubic" peaks related to Pb1 and Pb2 states have nearly the

5 Results and Discussion

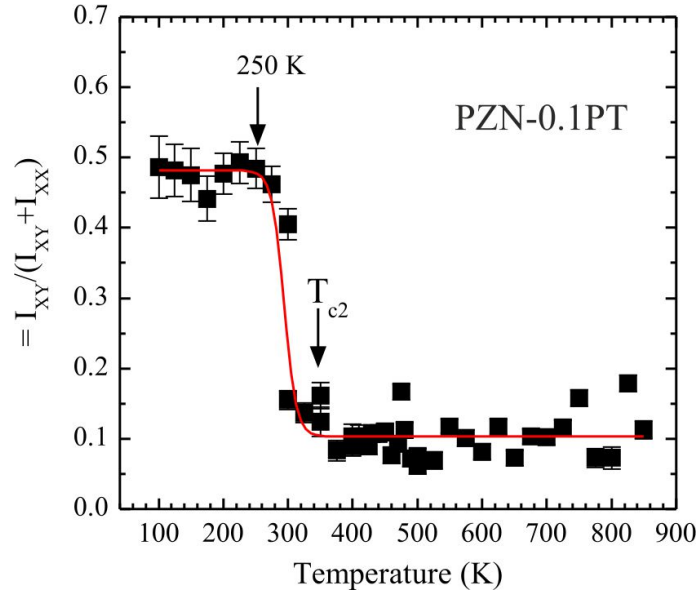


Figure 5.26: Depolarization ratio $\eta = I_{XY}/(I_{XY} + I_{XX})$ of the Raman band between 700 and 900 cm^{-1} for PZN-0.1PT, where I_{XY} and I_{XX} are the integrated intensities of the corresponding peaks in $\bar{Z}(XY)Z$ and $\bar{Z}(XX)Z$ geometry; the curve represents a Boltzmann fit to the experimental points with a midpoint of the slope $x_0 = 293 \pm 5 \text{ K}$.

same widths, but at T_B the Raman peak at 45 cm^{-1} associated with Pb1 ions (surrounded predominantly by Nb^{5+}) begins to broaden much stronger than the $\bar{Z}(XY)Z$ peak near 57 cm^{-1} . On further cooling the peak near 45 cm^{-1} continues to broaden until T_{C2} is reached, but the rate of broadening changes at T^* and at T_{C1} . Below 250 K the widths of the peaks near 45 and 57 cm^{-1} observed in $\bar{Z}(XY)Z$ geometry are similar, indicating that the two Pb states (distinguished by chemical environment) are in coherence concerning local structural distortions. At 250 K the depolarization of the parallel and cross polarized spectra measured when the incident light polarization is parallel to the cubic edge reaches a constant value (see Figure 5.26), indicating a saturation of structural transformations.

Interestingly, the FWHM of the peak near 57 cm^{-1} , related to Pb2 atoms (surrounded by both Zn^{2+} and Nb^{5+}), has a local maximum at 485 K, which is between T_{C1} and T^* (Figure 5.24d). At the same temperature the frequency of this peak begins to harden and the frequency of the peak related to Pb1 has a slight minimum (see Figure 5.24b). These features further emphasize on the fact that the formation of ferroelectric long-range order in PZN-0.1PT is a multistep process. At $T > T_B$ the intensity ratio $I_{45\text{cm}^{-1}}/I_{45\text{cm}^{-1}} + I_{57\text{cm}^{-1}}$ observed in $\bar{Z}(XY)Z$ geometry is ~ 0.35 (see Figure 5.24e). This value matches very well the fraction of cation pairs $\text{B}^{5+}\text{-B}^{5+}$, as deduced from the general formula $\text{Pb}(\text{B}^{2+}_{2/3}\text{B}^{5+}_{1/3})_{1/2}\text{B}^{5+}_{1/2}\text{O}_3$. The intensities of the $\bar{Z}(XY)Z$ peaks near 45 and 57 cm^{-1} change with temperature due to the development of ferroic order. It is well known that near a phase transition the integrated intensities of the low-energy hard phonon modes have a maximum due to the structural instability and their coupling with the flip mode representing the fluctuations

5 Results and Discussion

of the structure between instantaneous configurations (Salje *et al.*, 1983), (Husson, 1998). Indeed, the intensity ratio $I_{45\text{cm}^{-1}}/I_{45\text{cm}^{-1}} + I_{57\text{cm}^{-1}}$ measured in $\bar{Z}(XY)Z$ geometry increases with on cooling, has a broad maximum in the temperature range between T_{C1} and T_{C2} , and then decreases on further cooling.

The assignment of the Raman scattering in the spectral range 100–200 cm^{-1} is hampered by the multiple chemical and structural inhomogeneity existing in PZN-0.1PT. By analogy with other relaxor systems the peaks near 100 and 130 cm^{-1} might be related to the infrared Pb-BO₃ translation F_{1u} mode characteristic of both single ($Pm\bar{3}m$) and double ($Fm\bar{3}m$) perovskite structure (Ref. (Welsch *et al.*, 2011) and references therein), which is activated in the Raman spectra due to polar cation shifts. Hence, these peaks might account for the dynamical coupling between off-centered displacements of Pb and B-cations in PNRs. The two peaks harden in frequency close to the C-T phase transition (see Figure 5.27), similarly to the peak near 260 cm^{-1} (Figure 5.25). Also, both peaks sharpen below T_{C1} as the FWHM of the peak near 100 cm^{-1} has a wide maximum centered at T^* , while the peak at 130 cm^{-1} is broadened in a wider temperature range between T_B and above T_{C1} (Figure 5.27).

Based on the observed spectral changes, one can propose the following scenario for the transformation processes that occur on cooling in PZN-0.1PT. Due to the affinity of Pb²⁺ to form lone pair electrons, the structure possesses intrinsic off-centered displacements of Pb ions which are surrounded by locally ordered Zn and Nb. At $T_B = 730$ K the off-center shifted Pb ions drive the surrounding B-cations to coherently shift away from the octahedral center, which results in a nucleation of small polar clusters. The ferroelectrically active Nb⁵⁺ cations are expected to be more involved in this process as compared to Zn²⁺, thus leading to a significant distortion of the B-site cation shell of the Pb cations surrounded predominantly by Nb⁵⁺. Consequently, below T_B Pb1 cations can have some room for tiny off-center shifts though the strong electrostatic repulsive interactions. This causes a displacive disorder of Pb1 as revealed by the strong increase in the FWHM of the peak at 45 cm^{-1} (see Figure 5.24d). On cooling, the width of this peak further increases due to the increasing distortion in the Nb⁵⁺ shells of Pb1 ions. Hence, the rate of the width increase follows the enlargement of the fraction of polar clusters comprising off-centered Nb atoms. The small plateau near T^* of the FWHM for the 45 cm^{-1} peak (Figure 5.24d) reveals that at this characteristic temperature the dominant transformation process is coupling between polar clusters rather than further nucleation of polar species. Titanium is also ferroelectrically active; Ti⁴⁺ cations can displace along the cubic $\langle 111 \rangle$ direction, following the displacement direction of the major cations in the solid solution (Frenkel *et al.*, 2004) or they can shift along the cubic $\langle 001 \rangle$ to stabilize the second-order Jahn-Teller off-centering of Ti in the presence of stereochemically active lone pair on the Pb ion (Cohen, 1992). Direct evidence for the state of Ti cations cannot be gained from the Raman data presented here, since peaks solely arising from Ti vibrations cannot be distinguished. This however suggests one-mode behaviour for the B-site system and hence one can

5 Results and Discussion

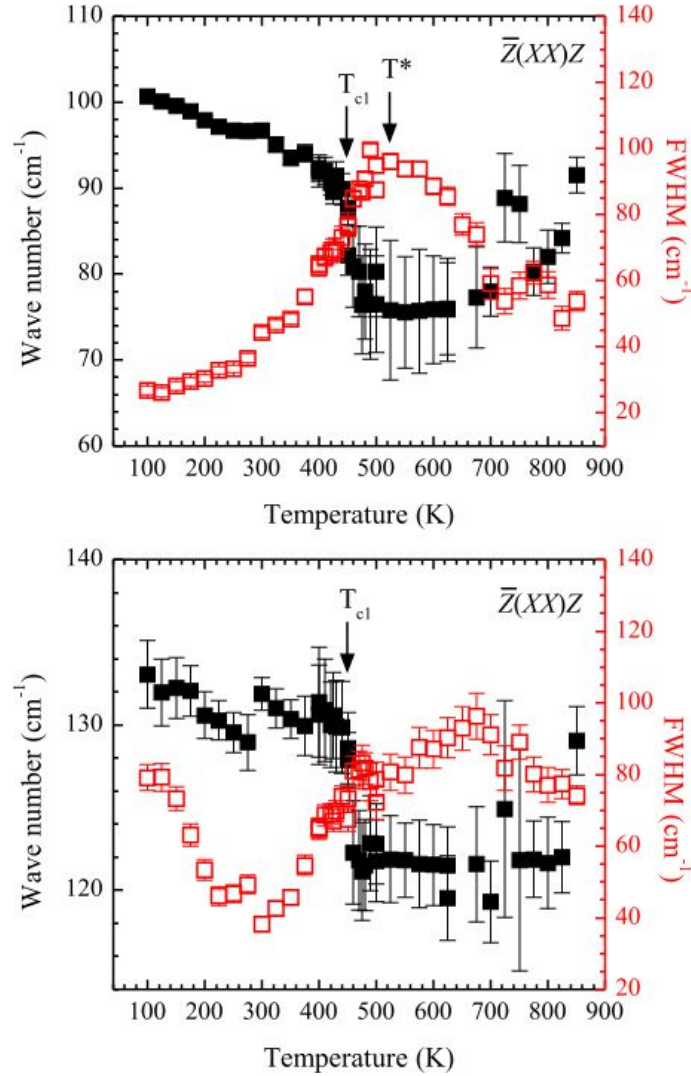


Figure 5.27: Temperature dependence of the position (solid squares) and FWHM (open squares) of the $\bar{Z}(XX)Z$ peaks of PZN-0.1PT near 100 cm^{-1} (upper plot) and 130 cm^{-1} (bottom plot).

speculate that initially Ti cations follow the rhombohedral distortion typical of PNRs (La-Orauttapong *et al.*, 2001), (La-Orauttapong *et al.*, 2003). Probably, between T^* and T_{C1} where the peak at 57 cm^{-1} has a maximum of the width (Figure 5.24d) and starts to harden (Figure 5.24b), tetragonal-type polar atomic arrangements prevail over rhombohedral polar clusters and begin to merge to evolve in long-range ordered tetragonal domains at T_{C1} .

It is worth noting that the development of tetragonal domains does not influence the depolarization ratio of the parallel and cross polarized spectra measured when the incident light polarization is along the cubic edge ($\bar{Z}(XX)Z$ and $\bar{Z}(XY)Z$ spectra) because the tetragonal axes are along the cubic axes and do not incline to the directions of the polarization of the incident and scattering light. However, as can be seen in Figure 5.22, the

5 Results and Discussion

occurrence of tetragonal domains is clearly revealed by the depolarization of the spectra measured when the incident light polarization is along the cubic face diagonal ($\bar{Z}(X'X')Z$ and $\bar{Z}(X'Y')Z$ spectra) because in this case the tetragonal domains are oriented at 45° with respect to the polarization of the incident and scattered light and hence, contribute equally to the parallel and cross polarized spectra. The $\bar{Z}(XX)Z$ and $\bar{Z}(XY)Z$ spectra would depolarize if rhombohedral, orthorhombic (with a unit cell rotated by 45° with respect to the cubic cell) or monoclinic (triclinic) domains are formed. By this reason the $\bar{Z}(XX)Z$ and $\bar{Z}(XY)Z$ are depolarized below T_{C2} . An attempt was made to determine the predominant type of ferroelectric domains in the structure by measuring the angular dependence of the depolarization of the Raman band near $700\text{--}900\text{ cm}^{-1}$ at RT. Since no extrema at every 45° were detected, one can argue that the structural distortion is monoclinic (or triclinic) rather than orthorhombic or rhombohedral. At temperatures below 250 K the spectra measured in all four scattering geometries become almost the same (see Figure 5.22). This indicates that regardless of the chemical inhomogeneity, the structure becomes homogenous with respect to the ferroic distortion developed on the length scale of sensitivity of Raman spectroscopy, i.e., within a few unit cells.

Raman scattering of Ru-doped PZN-0.1PT

Ruthenium is a mixed-valence 4d transition element with the ability to exhibit different oxidation states, e.g. Ru^{3+} , Ru^{4+} , and Ru^{5+} Figure 5.28. The 4d transition ions are known

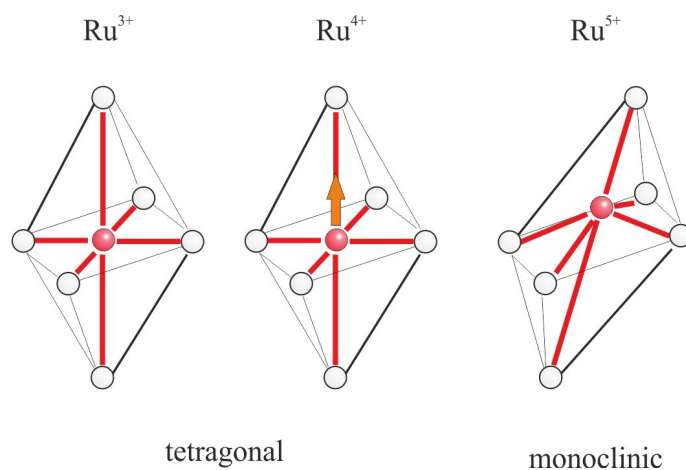


Figure 5.28: Different oxidation states of ruthenium showing the octahedral distortion.

to be more covalently bound to oxygen than 3d transition ions (like Ti^{4+}) and give rise to a strong octahedral crystal field (Clem *et al.*, 1995). Besides, Ru^{4+} can be in a low-spin magnetic or in a high-spin non-magnetic state (Kumaresavanji *et al.*, 2010), (Itoh *et al.*, 1995). Thus, the incorporation of Ru even in small concentrations may considerably influence the structural transformations. It has been previously shown that in PZN-0.1PT Ru ions predominantly replace Ti ions with a mean valence of Ru slightly below 4+

5 Results and Discussion

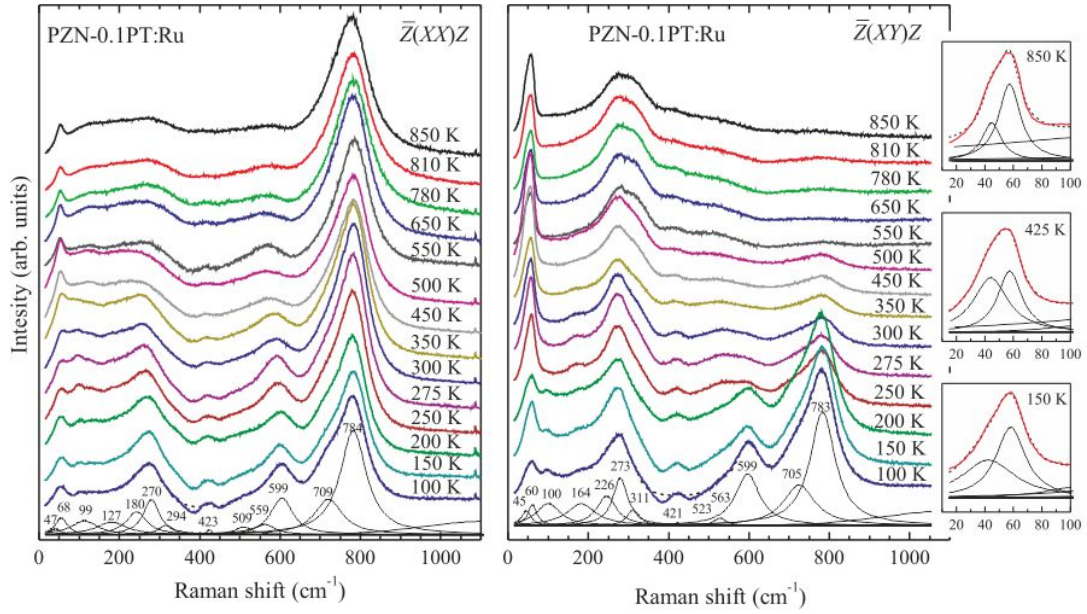


Figure 5.29: Parallel- $\bar{Z}(XX)Z$ and cross- $\bar{Z}(XY)Z$ polarized Raman scattering of Ru-doped PZN-0.1PT collected at different temperatures in the range 100–850 K; thin lines represent the fitting Lorentzians used for 100 K. An additional Gaussian centered near 1150 cm^{-1} was used for this compound to account for the continuum photoluminescence background. Insets on right show on an enlarged scale the band near 50 cm^{-1} measured in $\bar{Z}(XY)Z$ geometry (red bold curves), the corresponding fitting Lorentzians (thin curves), and resultant spectrum profiles (black dashed curves).

(Scholz *et al.*, 2009). Electron paramagnetic resonance spectroscopy revealed two types of paramagnetically active Ru centers in the structure of PZN-0.1PT: Ru^{3+} and Ru^{5+} (Scholz *et al.*, 2009). At room temperature Ru^{3+} prevails over Ru^{5+} , leading to immobilization of the domain walls and hardening of the hysteresis loops; cooling from 300 to 100 K leads to $\text{Ru}^{3+} \rightarrow \text{Ru}^{5+}$ transformation (Scholz *et al.*, 2009).

The $\bar{Z}(XX)Z$ and $\bar{Z}(XY)Z$ Raman spectra of PZN-0.1PT:Ru collected between 850 and 100 K are shown in Figure 5.29. The Raman spectra exhibit the same general features observed for the pure compound. As in the case of the undoped compound, at high temperatures there are two peaks near 50 cm^{-1} in the $\bar{Z}(XY)Z$ spectra and only one peak in the $\bar{Z}(XX)Z$ spectra. Therefore, the addition of Ru does not interfere the two "cubic" states Pb. On cooling, the peaks related to polar distortions enhance and sharpen. The depolarization of the spectra is clearly seen below 200 K, at which temperature a splitting of the peak near 50 cm^{-1} is also resolved. These observations demonstrate the development of M_C -type domains, indicating that Ru doping does not move the compound away from the MPB. The temperature dependence of the depolarization ratio (Figure 5.30) shows that the depolarization of the spectra of PZN-0.1PT:Ru takes place over a temperature range from approximately 300 K to 150 K, which is larger than the corresponding temperature range 350–250 K for pure PZN-0.1PT.

5 Results and Discussion

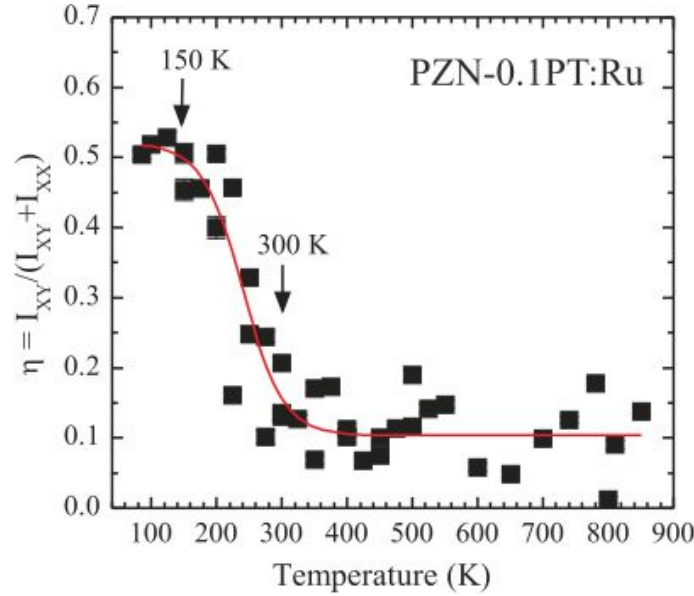


Figure 5.30: Depolarization ratio $\eta = I_{XY}/(I_{XY} + I_{XX})$ of the Raman band between 700 and 900 cm^{-1} for Ru-doped PZN-0.1PT, where I_{XY} and I_{XX} are the integrated intensities of the corresponding peaks in $\bar{Z}(XY)Z$ and $\bar{Z}(XX)Z$ geometry; the curve represents a Boltzmann fit to the experimental points with a midpoint of the slope $x_0 = 240 \pm 11 \text{ K}$.

Ru doping decreases T_{C2} with approximately 50 K, as indicated by the beginning of the stepwise increase in the depolarization ratio (compare Figure 5.26 and 5.30). In addition, the temperature dependence of the depolarization ratio for PZN-0.1PT:Ru does not have such a steep inclination as for pure PZN-0.1PT, revealing a more diffuse development of MC-type domains as compared to the pure compound. The incorporation of a fourth type of cation on the B-site resulted in an additional broadening of the Raman signals and this unfortunately hindered the rational fitting of the spectra above 600 K. Because of the obtained large uncertainties in the fitting parameters for the Raman signals between 100–400 cm^{-1} , we restricted the analysis to the Raman signals related to the Pb-localized F_{2g} mode of the prototype structure (see Figure 5.31).

As in the case of pure PZN-0.1PT, the Burns temperature can be determined from the change in the FWHM of the peaks seen in $\bar{Z}(XY)Z$ geometry (Figure 5.31d). According to these data, T_B for PZN-0.1PT:Ru is just below 700 K, i.e., with $\sim 30 \text{ K}$ lower than for PZN-0.1PT. This is most probably due to the presence of local structural distortions associated with Ru-doping centers, which interferes the coupling of polar displacements of the host-matrix cations. By contrast to the pure compound, T_B is not clearly marked in the temperature dependence of the width of the $\bar{Z}(XX)Z$ peak (Figure 5.31c), suggesting that doping smears out the transformation process. The same is valid for the intermediate temperature T^* , which can be deduced to be $\sim 525 \text{ K}$ by the broad local maximum in the FWHM and the subtle hardening of the $\bar{Z}(XX)Z$ peak (Figure 5.31c and 5.31a) as well as the kink in the FWHM of the $\bar{Z}(XY)Z$ peak at 45 cm^{-1} (Figure 5.31d). Above 500 K

5 Results and Discussion

the B-cation localized mode near 260 cm^{-1} is very broad and hardly resolvable from the nearest overlapping Raman signals, which also indicates that T^* is near 500–525 K. The C-T phase transition temperature T_{C1} can be found from the kink in the temperature dependence of the FWHM of the $\bar{Z}(XX)Z$ peaks (Figure 5.31c), in the same manner as for pure PZN-0.1PT. The T-M phase transition temperature T_{C2} is however more difficult to be determined. According to the depolarization ratio (Figure 5.26), T_{C2} is approximately 300 K; however the maximum in the FWHM of the peak near 45 cm^{-1} (Figure 5.31d) is $\sim 280\text{ K}$, whereas the splitting in the peak arising from Pb-localized vibrations is resolved only at 200 K. This underlines the diffuseness of the structural transformation from tetragonal to monoclinic. Interestingly, that even a very small substitution of Ru for Ti (Ru/Ti ratio = 0.02) considerably influences the development of ferroelectric long-range order in the overall structure. It appears that Ru favors the tetragonal distortion over a wider temperature range. As mentioned above, in PZN-0.1PT Ru is in third-, fourth- and fifth-valence substitutes for Ti^{4+} and at room temperature there is a surplus of Ru^{3+} (Scholz *et al.*, 2009). Octahedra deformed along one of the BO_6 4-fold axis are energetically favorable for Ru^{4+} (Itoh *et al.*, 1995; Ropka *et al.*, 2003). Ru^{3+} cations are also associated with tetragonally elongated octahedra, without off-centering of the cation, whereas Ru^{5+} cations form with the nearest oxygen ions strongly off-centered axially perturbed octahedral (Clem *et al.*, 1995). Seemingly, the predominance of Ru-doping centers related to local tetragonal distortions holds down the formation of monoclinic domains and thus shifts the T-M transition of the whole system to lower temperatures. However, on cooling the host perovskite structure eventually develops a monoclinic-type ferroelectric order and, in turn, forces the Ru doping ions to change the valence from 3+ to 5+ because strongly off-centered axially perturbed BO_6 octahedra better match Ru^{5+} as compared to Ru^{3+} .

5 Results and Discussion

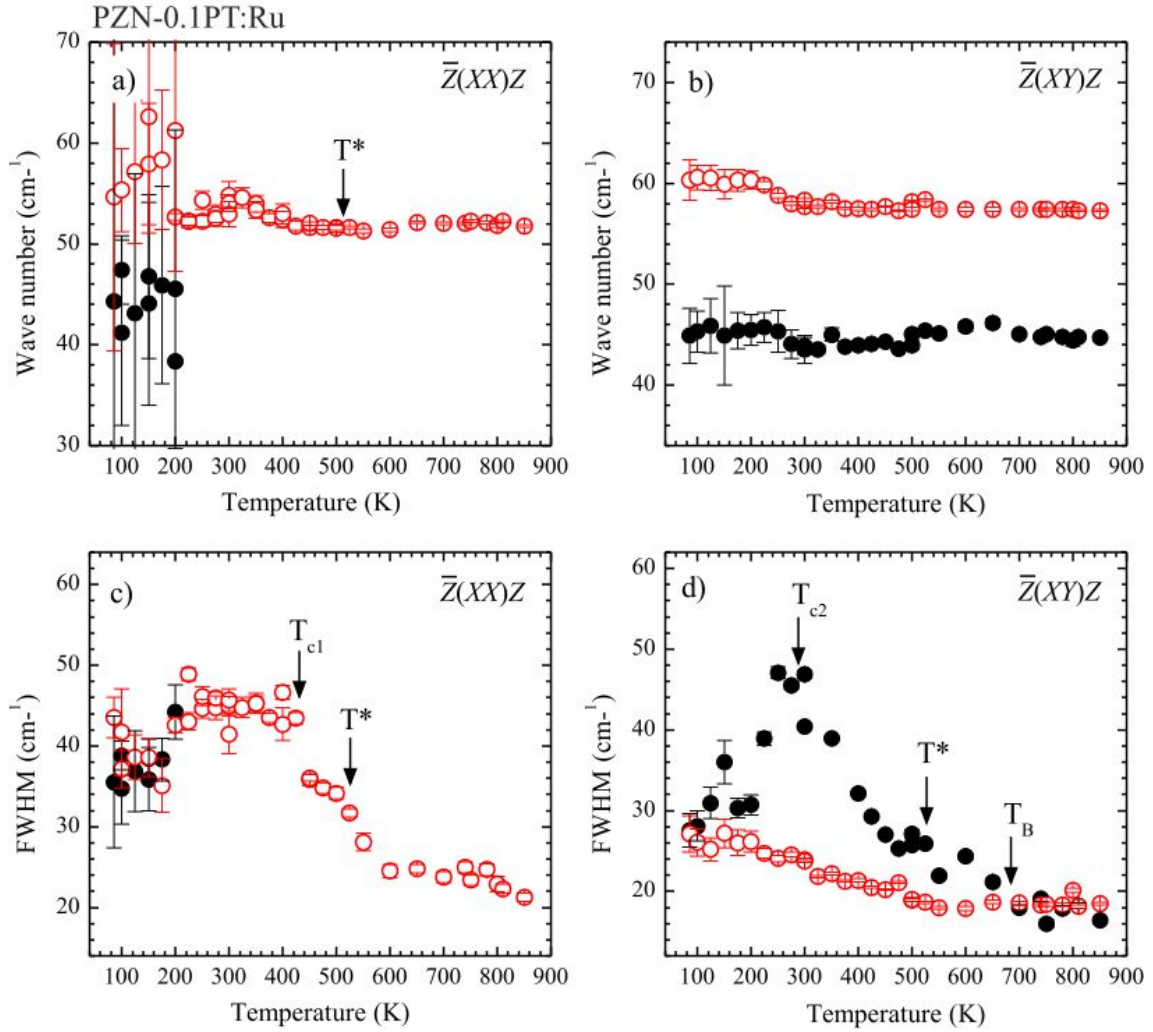


Figure 5.31: Temperature dependence of the positions and FWHMs of the Raman peaks of Ru-doped PZN-0.1PT related to the Pb-localized F_{2g} mode of the prototype doubled structure ($Fm\bar{3}m$). At high temperatures (above T_{C2}) the solid and open circles correspond to the two vibrational Pb states: Pb1 surrounded predominantly by Nb and Pb2 surrounded by both Zn and Nb; Ti can be in the surroundings of both Pb1 and Pb2 atoms. Below T_{C2} two peaks are observed in both $\bar{Z}(XX)Z$ and $\bar{Z}(XY)Z$ due to the lowering of the point symmetry of the average structure.

5.3.2 Pressure-driven structural transformations at room temperature

This section is based on the paper *Waesermann, N., Mihailova, B., Maier, B. J., Paulmann, C., Gospodinov, M., Marinova, V. and Bismayer, U. (2011). Local structural phenomena in pure and Ru-doped $0.9\text{PbZn}_{1/3}\text{Nb}_{2/3}\text{O}_3$ - 0.1PbTiO_3 near the morphotropic phase boundary as revealed by Raman spectroscopy. Phys. Rev. B 83, 214104.*

As has been shown in Section 5.3.1 the structure of pure and Ru-doped PZN-0.1PT at ambient conditions consist of different types of ferroelectric domains, with a predominance of monoclinic domains. This is supported by piezoresponse force microscopy which reveals a coexisting tetragonal and non-tetragonal ferroelectric domains at ambient conditions (Scholz *et al.*, 2009) as well as the majority of diffraction studies indicating a dominance of monoclinic domain in the vicinity of the MPB (Noheda *et al.*, 2001; Xu, 2010).

XRD analysis of PZN-0.1 PT

The FWHM of representative Bragg peaks recorded in high-precision in-house single-crystal XRD experiments as well as the unit-cell parameters and interaxial angles obtained from symmetry-unconstrained unit-cell refinements to the diffracted beam positions are shown in Figure 5.32. Due to the small structural deviation of the ferroelectric phases from the cubic phase, an apparent splitting of the cubic Bragg peaks was not resolved at ambient pressure, only a slight broadening of these peaks.

In Figure 5.32 we show the FWHMs from the rocking curves (resulting from the mutual misorientation of the domains (Gorfman & Thomas, 2010)) of the corresponding Bragg reflections and therefore the pressure dependences of these FWHMs represent purely the pressure-induced change in the degree of domain misorientation. At the same time, the deviation of unit-cell parameters from cubic is sensitive to the overall ferroic distortion of the atomic structure, regardless of the degree of ferroic twinning. For PZN-0.1PT the measured unit-cell parameters at ambient conditions correspond to a monoclinic metric but this fact does not mean that other types of ferroic domains are absent from the structure. The pressure dependences of the Bragg-peak widths and the unit cell parameters (Figure 5.32) reveal four distinguishable ranges of pressure-induced structural states. Between ambient pressure and 1.0 GPa the ferroelectric distortion of the atomic structure is reduced because the unit-cell parameters evolve towards cubic, but the distribution of domain orientations is enhanced, as seen from the strong broadening of the diffraction peaks. This is not the usual pattern of behavior for a ferroic multidomain sample in which one would expect a decrease in the mutual misorientation between domains when the ferroic distortion of the atomic structure is reduced. Hence, the pressure evolution of both the unit cell parameters and FWHMs indicates an enhancement of the ferroic twinning (more and smaller domains with smaller ferroic distortion) in the pressure range up to 1 GPa. We suggest that this process occurs due to the competitive coexistence of different types of

5 Results and Discussion

ferroelectric domains as one of these phases is being suppressed as pressure increases to 1.0 GPa. This is consistent with the abrupt change in the pressure dependencies of the diffraction-peak widths and unit-cell parameters at 1 GPa. On further pressure increase up to 2.1 GPa the peak broadening strongly decreases and the deviation of the unit-cell parameters from cubic decreases, consistent with the evolution of a ferroic single-phase multidomain sample towards cubic symmetry. Between 2.1 and 5.2 GPa, neither broadening of the diffraction peaks nor deviation of the unit-cell parameters from cubic were detected, indicating that the average structure is cubic. Above 5.2 GPa the Bragg peaks again start broadening with pressure increase and the unit-cell parameters slightly deviate from cubic, which indicates the development of a new ferroic state. The dependence of the normalized pressure $F = p/3f(1 + 2f)^{5/2}$ on the Eulerian strain calculated from the measured dependence of the unit-cell volume V on the pressure p (see Figure 5.33) also indicates the existence of three pressure-induced structural $f = (V_0 - V)^{2/3} - 1/2$ transformations near 1.0, 2.1 and 5.9 GPa.

To shed light on the structural state above 2.1 GPa we have conducted synchrotron single-crystal XRD. Figure 5.34 shows representative sections of $(hk0)$ and $(hk1)$ reciprocal-space layers of PZN-0.1PT under pressure. Weak x-ray diffuse scattering along $\langle 110 \rangle^*$ (indexed in $Fm\bar{3}m$ in the whole section) can be seen up to 4.0 GPa, revealing the existence of polar nanoregions. Therefore, at 2.1 GPa PZN-0.1PT reaches a relaxor cubic state with no ferroelectric long-range order, which is consistent with dielectric experiments indicating a ferroelectric-relaxor crossover at moderate pressures (Samara *et al.*, 2000), (Bokov *et al.*, 2007). X-ray diffuse streaks were not observed at 5.0 GPa and above, indicating that the relaxor state of PZN-0.1PT persists up to 4 GPa, but at 5 GPa the polar order is destroyed even on the mesoscopic scale. At 5.9 GPa a new class of sharp Bragg peaks with h, k, l , all odd, appear (see Figure 5.34) associated with the development of anti-phase octahedral tilts of type $a^-a^-a^-$ (Glazer's notation (Glazer, 1972)) (Maier *et al.*, 2010a,b, 2011a,c).

This results in a change from primitive cubic $Pm\bar{3}m$ to rhombohedral $R\bar{3}c$, in the case of absence of long-range chemical B-site order of NaCl type, or from face-centered cubic $Fm\bar{3}m$ to rhombohedral $R\bar{3}$, if a long-range chemical B-site order is presented (see Table 1.1). At ambient pressure PZN-0.1PT does not exhibit any superlattice Bragg peaks indicative of long-range chemical B-site order (see Section 5.3.1). Hence, the synchrotron XRD data in PZN-0.1PT clearly reveal the occurrence of a continuous phase transition from primitive cubic to rhombohedral $R\bar{3}c$ symmetry comprising a long-range order of anti-phase tilts of equal magnitude typical of Pb-based perovskite-type relaxors (Chaabane *et al.*, 2003; Janolin *et al.*, 2006; Mihailova *et al.*, 2011). No other pressure-induced Bragg peaks or d -space-splitting of the existing diffraction peaks were detected up to 18.1 GPa, indicating that no further phase transitions occur in this pressure range.

Figure 5.35 depicts the pressure dependences of the integrated intensities of representative Bragg peaks with $h+k+l = 4n+2$ and h,k,l all equal to $2n+1$ calculated from the synchrotron XRD data. The third class of observed Bragg peaks, having $h+k+l = 4n$, were

5 Results and Discussion

over saturated in the whole pressure range. As can be seen in Figure 5.35, the intensities of the pressure-induced *odd – odd – odd* peaks generated from anti-phase octahedral tilts increase from 5.9 to ~ 11 GPa and then become saturated. The intensities of the peaks with $h+k+l = 4n+2$ initially decrease with the pressure increase, then remain nearly constant in the range 3–5 GPa and above 5.9 GPa show the same trend as the *odd – odd – odd* Bragg peaks. All atoms of the perovskite structure contribute to the Bragg peaks with $h+k+l = 4n+2$, with the more heavily-scattering A- and B-site cations contributing to the scattering factor with opposite signs. Thus the pressure evolution of the intensities of these peaks reflects the suppression of long-range polar order of the cations at moderate pressures and the subsequent development of anti-ferrodistortive order of the oxygen atoms above 5.9 GPa. The saturation in the intensities above 11 GPa indicates that the fraction of ferroic domains with long-range octahedral tilting as well as the octahedral tilt angle then becomes essentially constant at higher pressures.

5 Results and Discussion

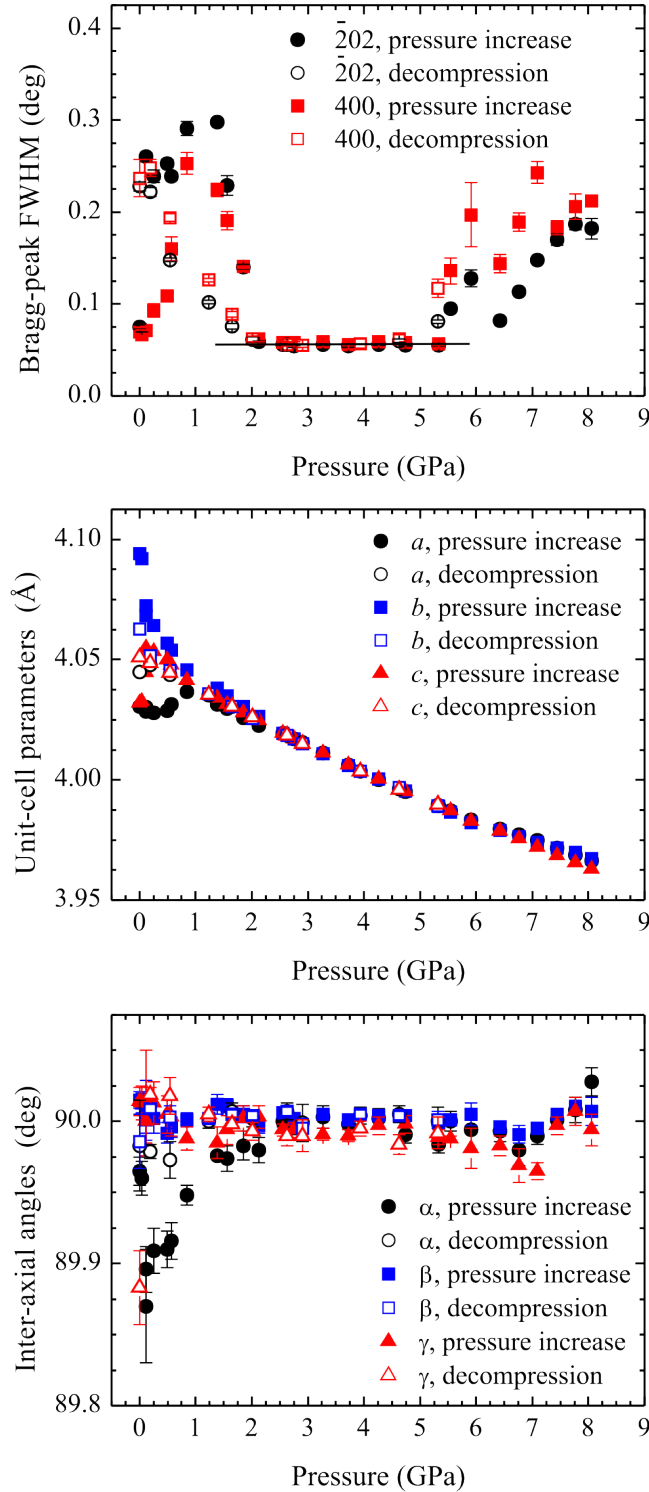


Figure 5.32: Pressure dependence of the FWHM of two representative Bragg peaks (Miller indices refer to $Fm\bar{3}m$) (upper plot), unit-cell parameters (middle plot), and angles (bottom plot) obtained from symmetry-unconstrained unit-cell refinements to single-crystal XRD data. The filled and open symbols correspond to data collected on pressure increase and on decompression, respectively. The error bars for the unit-cell parameters are within the size of the symbols. The horizontal line in the upper plot marks the instrumental resolution.

5 Results and Discussion

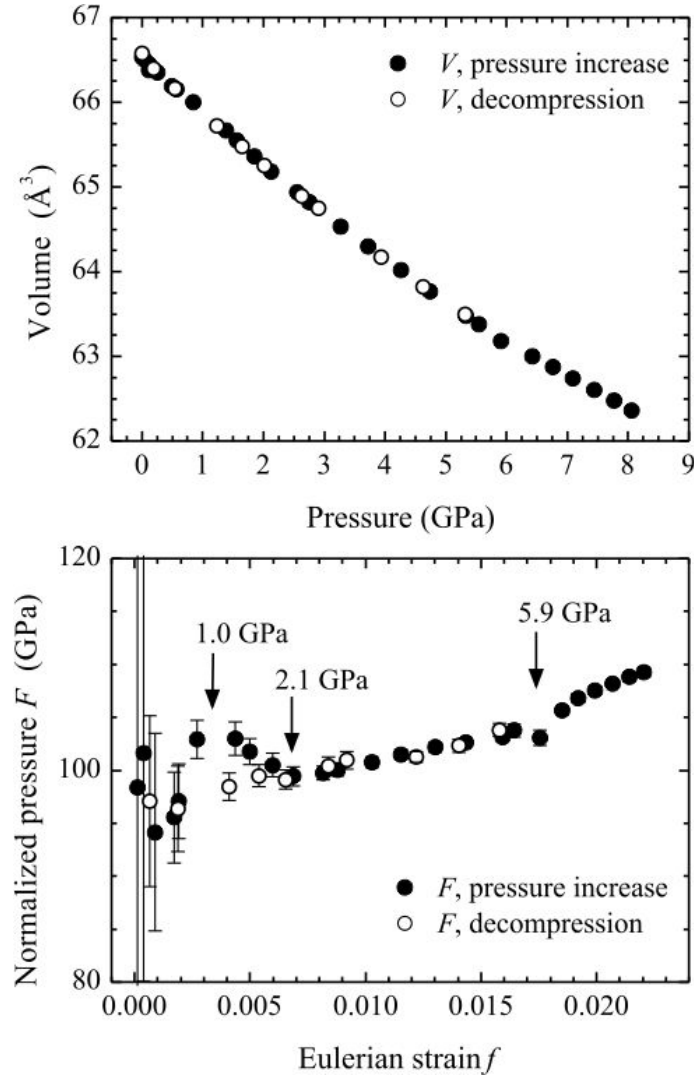


Figure 5.33: Unit-cell volume V vs pressure p measured in high-precision single-crystal XRD experiments (upper plot), and corresponding $F(f)$ dependence (bottom plot), where F is the normalized pressure $F = p/3f(1 + 2f)^{5/2}$ and f is the Eulerian strain $f = (V_0 - V)^{2/3} - 1/2$. The filled and open symbols correspond to data collected on pressure increase and on decompression, respectively. The error bars for the unit cell volume are within the size of the symbols.

5 Results and Discussion

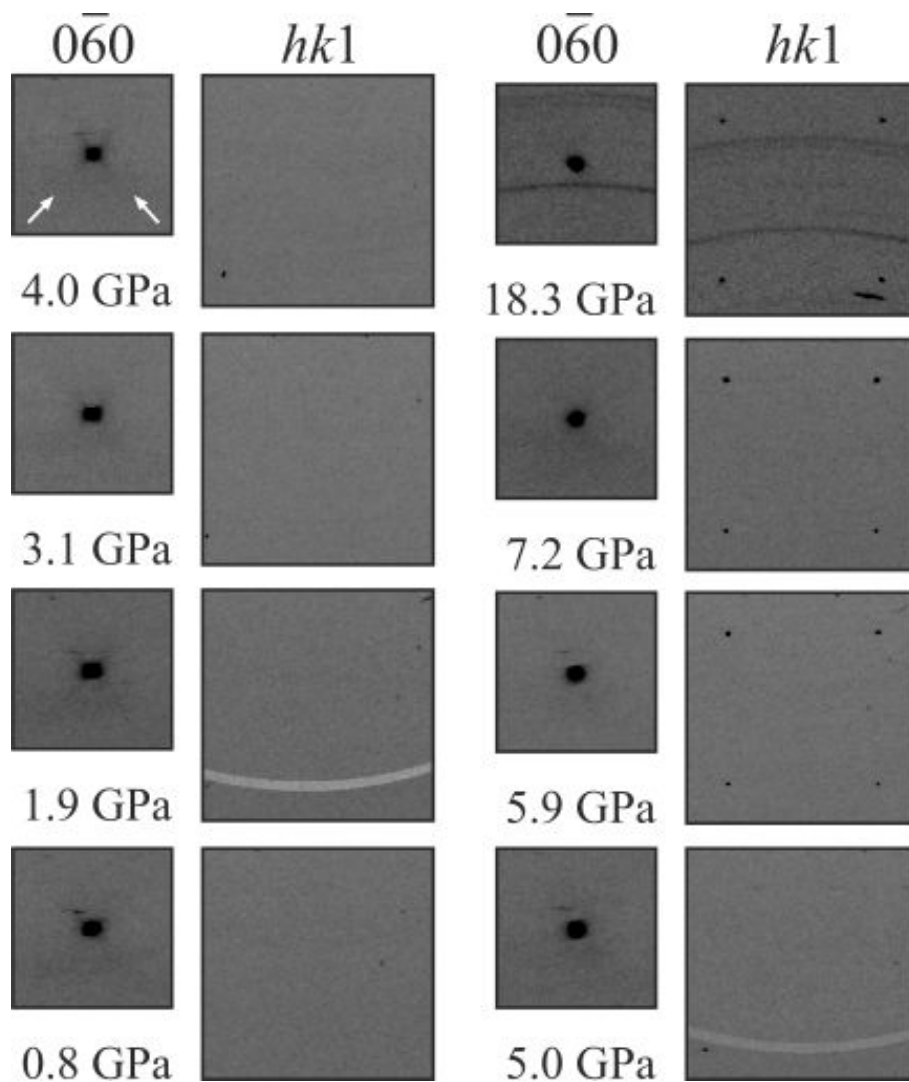


Figure 5.34: Reciprocal-space layers reconstructed from synchrotron single-crystal XRD on PZN-0.1PT. The Miller indices refer to a cubic double-perovskite $Fm\bar{3}m$ unit cell. The arrows in the sector around the $0\bar{6}0$ Bragg peak mark the diffuse scattering along $\langle 110 \rangle^*$. The sectors of $(hk1)$ layers demonstrate that pressure-induced odd-odd-odd Bragg peaks appear at 5.9 GPa; the reflections in the upper-left and bottom-right corner are $\bar{1}\bar{3}1$ and $1\bar{5}1$, respectively.

5 Results and Discussion

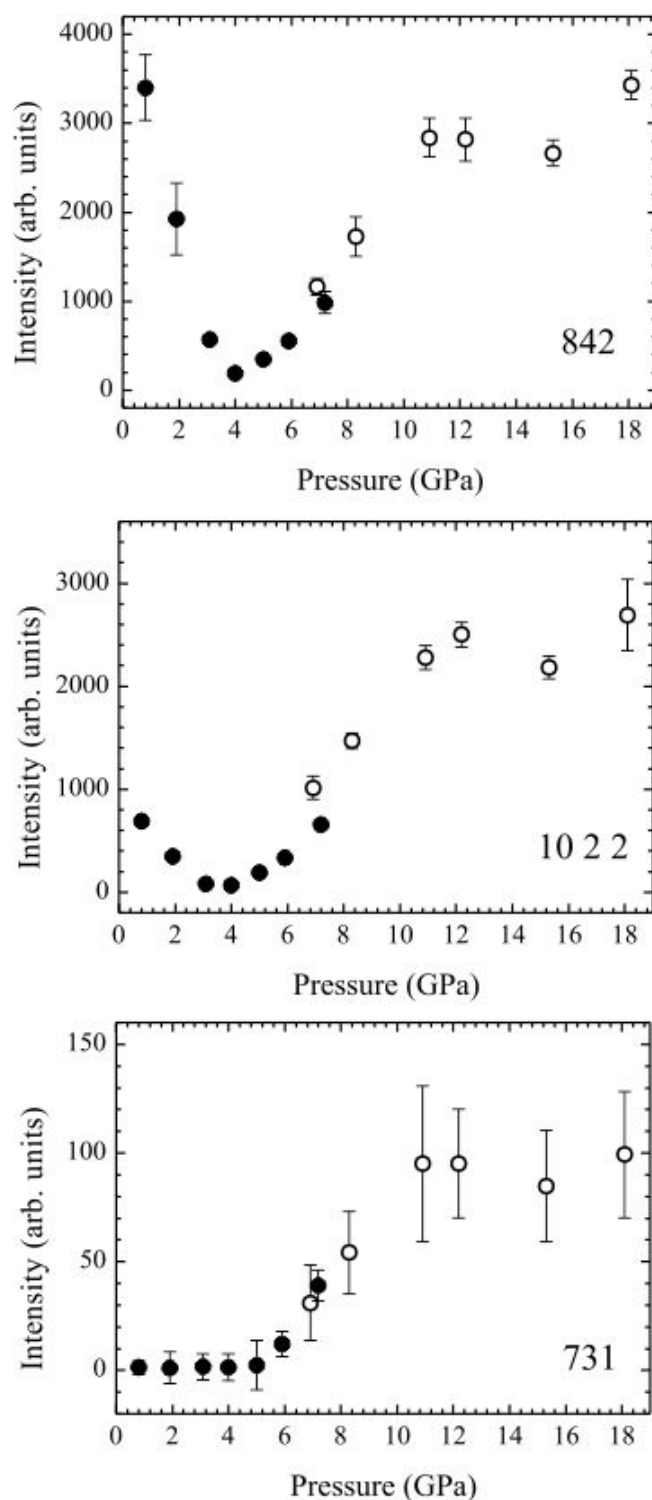


Figure 5.35: Integrated intensities of Bragg peaks measured in single-crystal synchrotron experiments. The intensities are averaged over the peaks which are symmetry-equivalent in the prototype cubic structure. The filled and open symbols correspond to measurements in methanol-ethanol and in He as pressure-transmitting media, respectively; the intensities were normalized to volume of the corresponding sample. Miller indices refer to $Fm\bar{3}m$.

Raman scattering of PZN-0.1PT

Raman spectra of PZN-0.1PT collected at different pressures up to 18.1 GPa are shown in Figure 5.36 showing the typical peak profile of the double perovskite structure $Fm\bar{3}m$. We have analyzed in detail the Raman scattering near 55, 260 and 350 cm^{-1} , which has been proven to be highly sensitive to pressure-induced structural transformations in other Pb-based relaxor materials (Chaabane *et al.*, 2004; Kreisel *et al.*, 2002; Janolin *et al.*, 2006; Mihailova *et al.*, 2008a; Maier *et al.*, 2010a, 2011b,c; Welsch *et al.*, 2011).

The band near 55 cm^{-1} originates from Pb-localized modes related to a Raman-active F_{2g} mode of the prototype structure. For compounds of the type $\text{PbB}'_{1/3}\text{B}''_{2/3}\text{O}_{3-x}\text{PT}$ with x varying between zero and the value corresponding to the MPB, this band is a doublet at high temperatures due to the existence of two cubic local states of the Pb ions having distinct local chemical environments formed by the nearest B-site cations (see Section 5.3.1). However, at temperatures below the para-to-ferroelectric phase transition, the two Pb states related to the chemical environment become dynamically indistinguishable and hence the doubling of the peak near 55 cm^{-1} results from the lowering of the symmetry of the average structure (see Section 5.3.1). Our in-situ high-pressure experiments on PZN-0.1PT were conducted at room temperature, which is below T_{C2} (Dul'kin *et al.*, 2006), (see Section 5.3.1) and therefore the lower-wavenumber component at $\sim 45 \text{ cm}^{-1}$ reflects the presence of ferroelectric long-range order. This Raman signal considerably softens and broadens when pressure is increased from ambient to $\sim 4.5 \text{ GPa}$ (see Figure 5.37) due to the pressure-induced suppression of the polar order.

At the critical pressure $p_C = 5.9 \text{ GPa}$ of the cubic-to-rhombohedral phase transition, the lower-wavenumber component of the band at 55 cm^{-1} starts hardening and narrowing (see Figure 5.37), following the behavior of a soft mode. Indeed, for Pb-based relaxors the occurrence of a pressure-induced cubic-to-rhombohedral phase transition is accompanied by the appearance of a soft mode (Mihailova *et al.*, 2008a; Maier *et al.*, 2010a; Welsch *et al.*, 2011). Thus, the origin of the Raman scattering near 45 cm^{-1} above 5.9 GPa is different from that below 4.5 GPa, i.e., two different phonon modes generate the lowest-wavenumber Raman signal at low pressures and at high pressures. While at low pressures this Raman signal arises from the long-range ferroelectric order, above 5.9 GPa it is associated with the development of long-range anti-ferrodistortive order, namely anti-phase octahedral tilting. Between 4.5 and 5.9 GPa the lowest-wavenumber Raman signal does not disappear (see Figure 5.37), meaning that the corresponding vibrational modes are still underdamped. This indicates that order-disorder structural processes contribute considerably to the pressure-induced structural transformations in PZN-0.1PT, which is most probably related to the complex chemistry on the B-site.

The Raman scattering near 260 cm^{-1} arises from off-center-displaced B-site cations (Welsch *et al.*, 2011; Mihailova *et al.*, 2002) and at ambient pressure it is sensitive to the development of polar order, in particular to the coupling processes at T^* , where large

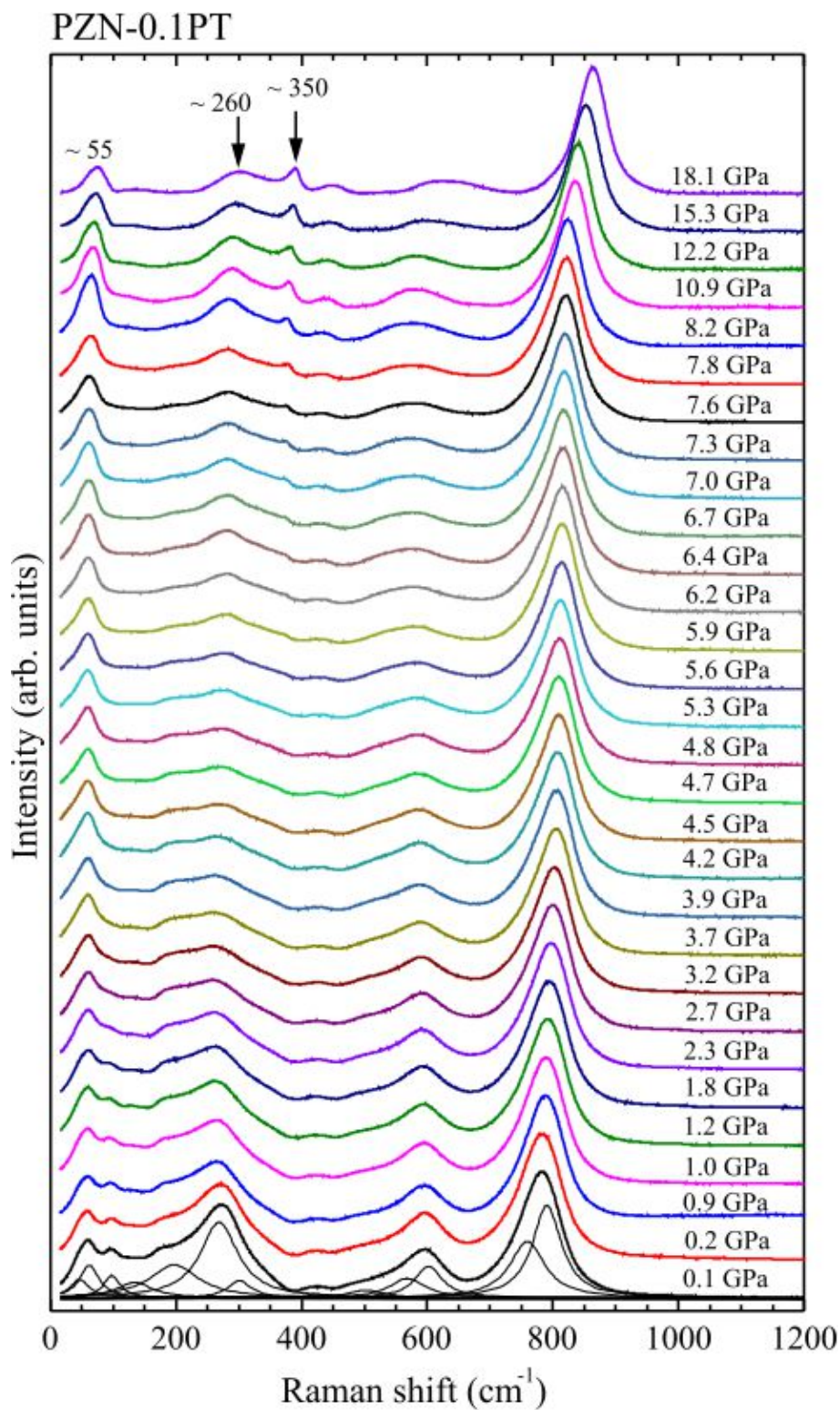


Figure 5.36: Raman spectra of PSN-0.1PT measured up to 18.1 GPa.

polar nanoregions with slower dynamics are formed (see Section 5.3.1), (Welsch *et al.*, 2011; Mihailova *et al.*, 2008b). Similar to other relaxor and relaxor-related materials (Ahart

5 Results and Discussion

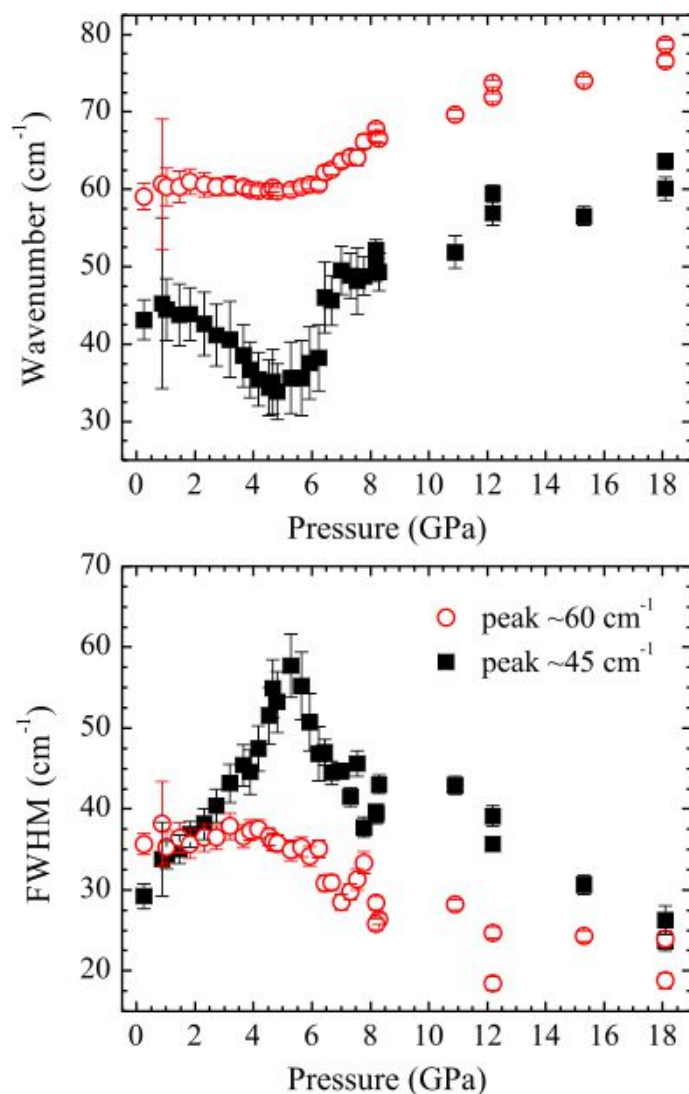


Figure 5.37: Pressure dependence of the wave number and FWHM of the two components of the Raman-scattering band near 55 cm^{-1} observed for PZN-0.1PT, which arises from Pb-localized modes.

et al., 2005; Chaabane *et al.*, 2004; Kreisel *et al.*, 2002; Janolin *et al.*, 2006; Mihailova *et al.*, 2008a, 2011; Sani *et al.*, 2004), pressure reduces the intensity of the Raman scattering at 260 cm^{-1} observed for PZN-0.1PT (see Figure 5.36), indicating a reduction of the polar shifts of the B-site cations. However, the effect is less pronounced for $\text{PbB}'_{1/3}\text{B}''_{2/3}\text{O}_3$ -type systems (Ahart *et al.*, 2005; Chaabane *et al.*, 2004; Kreisel *et al.*, 2002; Janolin *et al.*, 2006) as compared to $\text{PbB}'_{1/2}\text{B}''_{1/2}\text{O}_3$ -type relaxors (Mihailova *et al.*, 2008a; Welberry & Goossens, 2008) and relaxor-related materials with homovalent ions on the B-site (Kreisel *et al.*, 2002; Sani *et al.*, 2004), and PZN-0.1PT shows the same trend. Aliovalent A-site doping of $\text{PbB}'_{1/2}\text{B}''_{1/2}\text{O}_3$ relaxors also results in the persistence of the Raman signal near 260 cm^{-1} under pressure (Maier *et al.*, 2011c). These findings indicate that local electric fields associated with charge imbalance on the A- or B-site of the perovskite

5 Results and Discussion

structure oppose the tendency of external pressure to move the off-centered B-site-cations back to the corresponding octahedral centers. For PZN-0.1PT the wavenumber of the 260 cm^{-1} -peak rapidly increases at 4.5 GPa and the FWHM versus pressure shows a broad maximum in the range 4.5–8 GPa. Synchrotron XRD data indicates that the polar nanoregions vanish above 4.0 GPa (see Figure 5.34). Therefore, the polar B-cation shifts existing above 4.0 GPa are uncorrelated even on the mesoscopic scale. However, their existence apparently opposes the formation of long-range anti-ferrodistortive octahedral-tilt order and enhances the order-disorder structural phenomena in the pressure-induced phase transition at 5.9 GPa.

The Raman peak at 350 cm^{-1} (see Figure 5.36) is related to the silent F_{2u} mode of the prototype cubic structure and is generated by Pb-O bond stretching within the cubic $\{111\}$ planes (Welsch *et al.*, 2011), (Mihailova *et al.*, 2002). This type of vibration can also be considered as anti-phase octahedral tilting (Mihailova *et al.*, 2011; Aroyo *et al.*, 2006; Mihailova *et al.*, 2002) as it changes the Pb-O bond lengths and hence the peak is enhanced with pressure due to the development of static long-range ordered tilts. This peak is resolved in the cross-polarized Raman spectra of PZN-0.1PT measured at ambient pressure in air but in the unpolarized spectra collected in the DAC it was resolved only above 1.8 GPa. The position of the peak near 350 cm^{-1} strongly increases between 4.5 and ~ 7.0 GPa, while the FWHM strongly decreases and become nearly constant above 7 GPa (see Figure 5.38). Similar pressure dependence has been observed for PMN- x PT (Chaabane *et al.*, 2004). Also, similar to other $\text{PbB}'_{1/3}\text{B}''_{2/3}\text{O}_3$ -based materials (Ahart *et al.*, 2005; Chaabane *et al.*, 2004; Janolin *et al.*, 2006) the peak at 350 cm^{-1} of PZN-0.1PT is less enhanced with pressure as compared to Pb-based perovskites with a B-site stoichiometry equal or approximately equal to 1:1 (Mihailova *et al.*, 2008a; Welberry & Goossens, 2008), (Sani *et al.*, 2004). This again indicates a competition between uncoupled B-site off-centered displacements and anti phase tilt order in the vicinity of the pressure-induced phase transition at 5.9 GPa. The nearly constant FWHM above 7 GPa and the absence of any pressure-induced splitting of the peak at 350 cm^{-1} , as previously observed for other relaxors (Mihailova *et al.*, 2008a; Maier *et al.*, 2011b), shows that between 7 and 18.1 GPa the oxygen environment of the Pb^{2+} cations remain the same even on the local scale.

It should be emphasized that according to Raman spectroscopy, after decompression the atomic structure is fully recovered at ambient pressure. The increase in the FWHMs of the Bragg peaks (see Figure 5.32) also indicates that the long-range ferroelectric order reappears below 2.1 GPa. However, the peak widths are different in detail from those measured prior to compression, and the deviation of the unit-cell parameters from cubic is considerably less than that of the initial structure. This indicates that the domain texture is different and the overall ferroic distortion of the average structure is smaller as compared to the initial state. From this point of view the phase transition at 1 GPa might be thought as being irreversible. However, the complete reversibility of the Raman scattering indicates

5 Results and Discussion

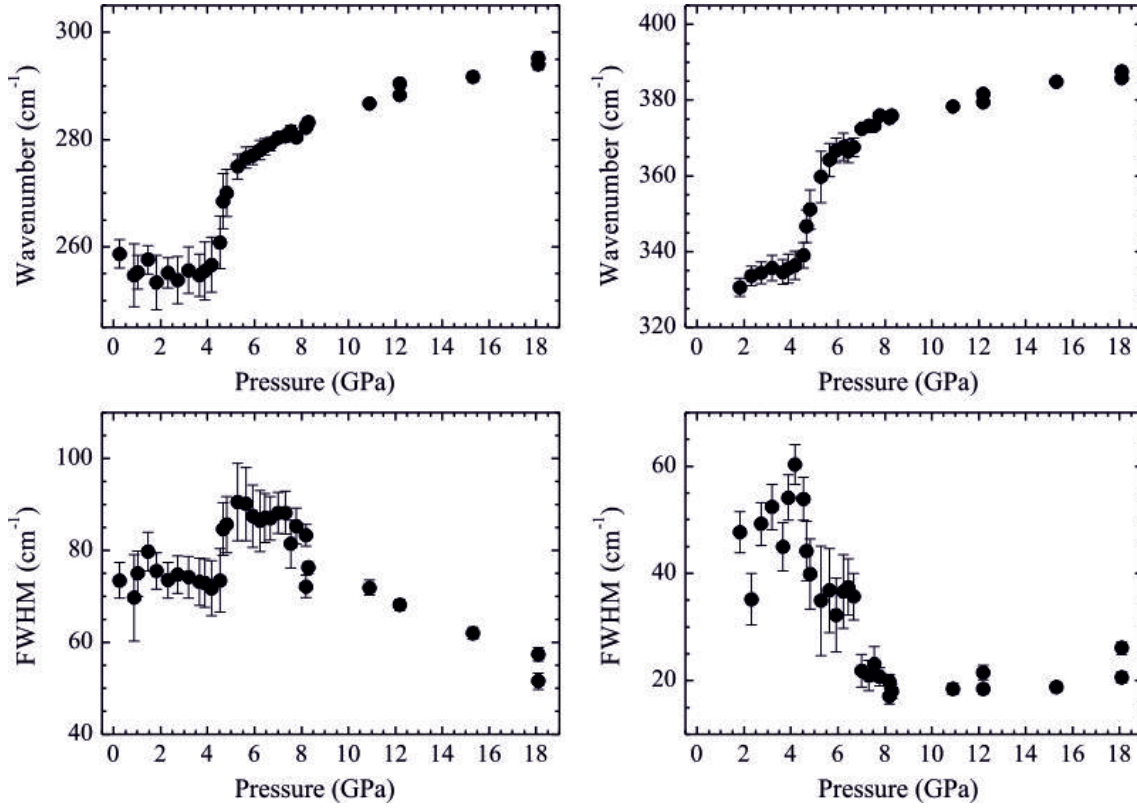


Figure 5.38: Pressure dependence observed in PXN-0.1PT of the wavenumber and FWHM of the Raman peak near 260 cm^{-1} which arises from vibrations of off-centered B-site cations (left) and near 350 cm^{-1} which arises from Pb-O bond stretching within the cubic $\{111\}$ planes and can be considered as octahedral tilting.

that the predominant monoclinic atomic arrangements are recovered on decompression. Most probably, the correlation length of ferroic distortion in the final state is shorter than in the initial state, which results in smaller domains and a smaller deviation of the measured unit-cell parameters from the cubic values. It should be mentioned that based only on the data presented here, one cannot state whether a second type of ferroelectric domains reappears or not on decompression.

Raman scattering of Ru-doped PZN-0.1PT

At ambient pressure, the addition even of a small amount of Ru ($\text{Ru}/(\text{Zn}+\text{Nb}+\text{Ti}) \sim 0.002$) leads to a substantial hardening of the polarization-field and strain-field hysteresis loops of PZN-0.1PT (Scholz *et al.*, 2009) and favors the tetragonal state in a wider temperature range compared to the undoped compound (see Section 5.3.1). These effects are attributed to the fact that Ru substitutes for Ti and at room temperature the average valence of the ruthenium cations is between 4+ and 3+ (Scholz *et al.*, 2009). To check whether Ru doping influences the structural state at high pressures, we have conducted Raman scattering in the pressure range up to 8.4 GPa. According to the Raman spectra (see Figure 5.39

5 *Results and Discussion*

Ru-doped PZN-0.1PT exhibits the same structural changes with pressure that have been observed for the pure compound (compare Figure 5.36 and 5.39). The Raman scattering near 260 cm^{-1} is moderately suppressed with pressure increase, while that near 350 cm^{-1} is enhanced. The ratio between the integrated intensities of the peaks at 350 and 260 cm^{-1} (not shown) for pure and Ru-doped PZN-0.1PT is the same. This indicates that Ru doping does not influence the pressure-induced local structural changes, although at ambient pressure Ru-doping decreases the characteristic and critical temperatures (see Section 5.3.1). Ru-doping leads to overall broadening and larger overlaps of the Raman peaks, which results in larger uncertainties in the peak parameters derived from the fitting of the spectral profiles. The pressure dependencies of the two components of the band near 55 cm^{-1} for Ru-doped PZN-0.1PT are shown in Figure 5.40. Similar to the pure compound, the FWHM of the peak near 45 cm^{-1} observed for Ru-doped PZN-0.1PT exhibits a maximum between 4.5 and 5.9 GPa. This peak also softens when pressure approaches 4.5 GPa and hardens at higher pressures, indicating the occurrence of the same cubic-to-rhombohedral phase transition as for pure PZN-0.1PT. Due to the large uncertainties, the exact value of the critical pressure cannot be determined from the pressure dependence of the position of the peak near 45 cm^{-1} . However, for both undoped and Ru-doped PZN-0.1PT the wavenumber of the peak near 60 cm^{-1} is constant until 5.9 GPa and then begins to harden. This indicates that Ru-doping does not change the critical pressure, which is in accordance with the pressure dependence of the FWHM of the peak at 45 cm^{-1} .

5 Results and Discussion

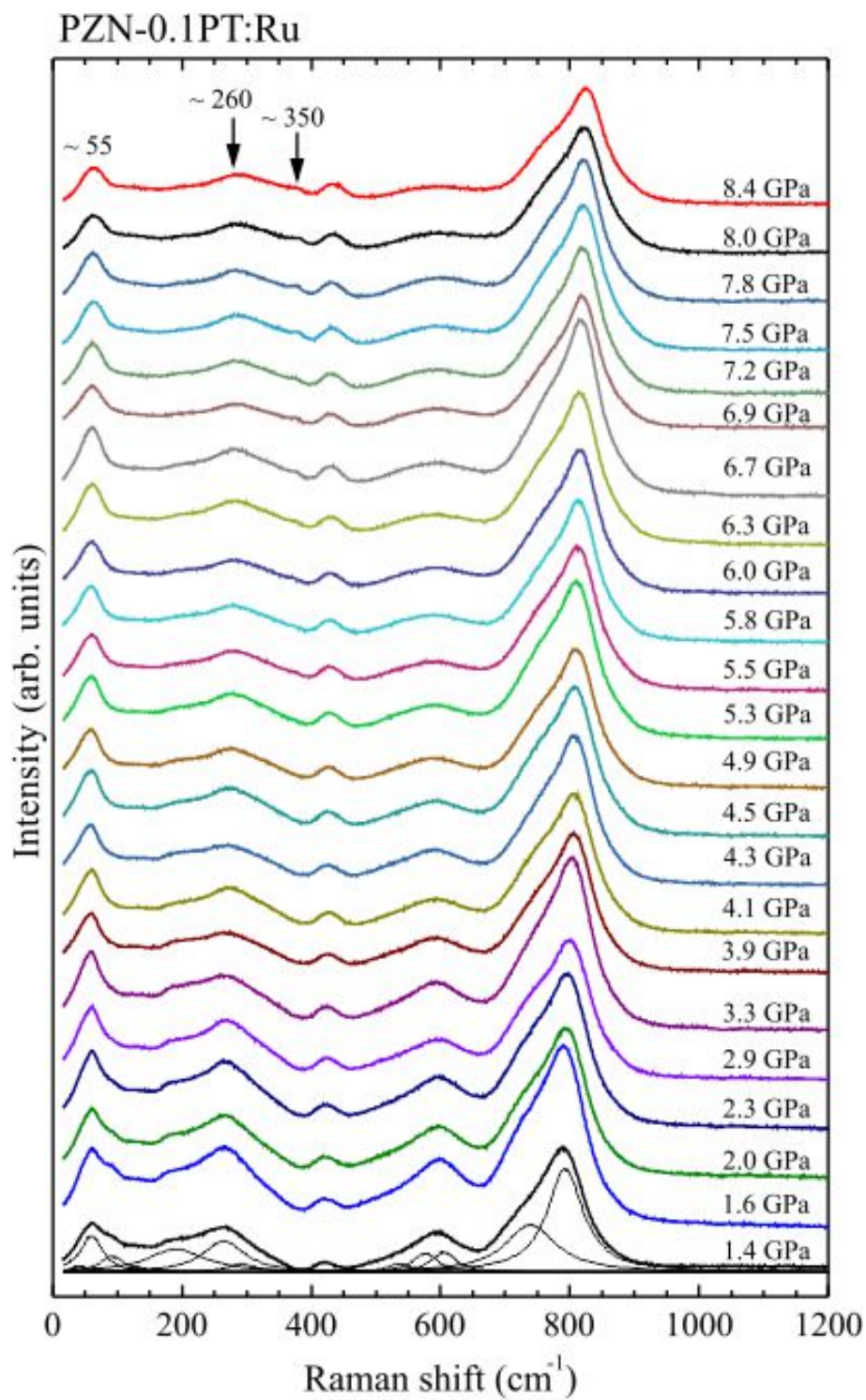


Figure 5.39: Raman spectra of Ru-doped PSN-0.1PT measured up to 8.4 GPa.

5 Results and Discussion

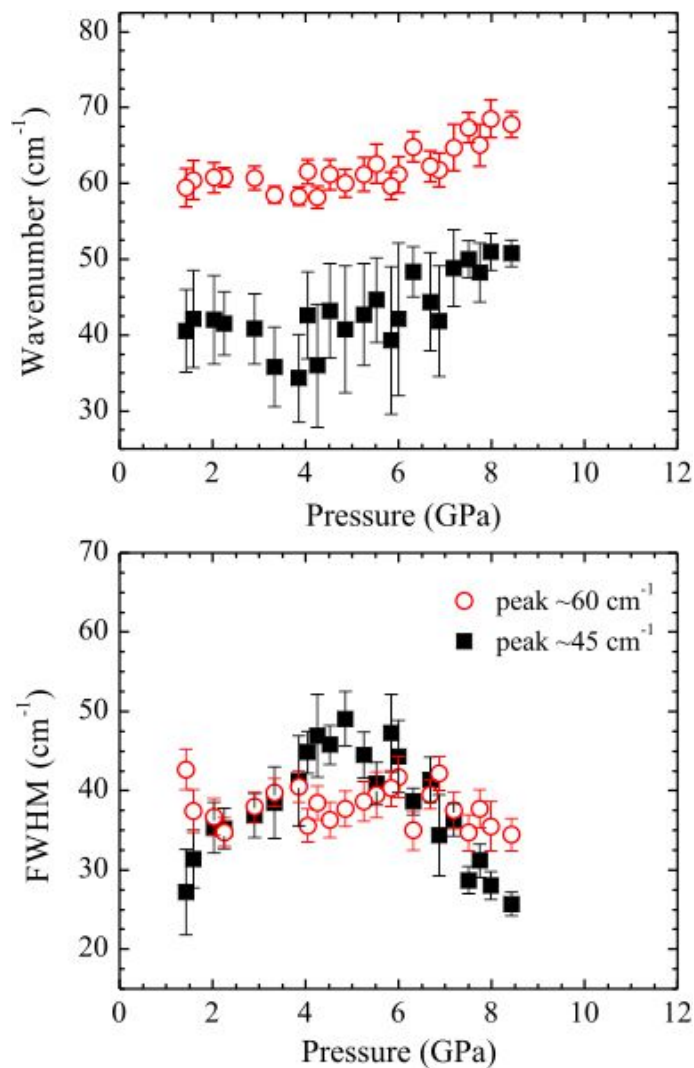


Figure 5.40: Pressure dependence of the wave number and FWHM of the two components of the Raman-scattering band near 55 cm^{-1} observed for Ru-doped PZN-0.1PT, which arises from Pb-localized modes. Note the difference between the X-axis scales in this figure and in Figure 5.37.

6 Conclusions

6.1 Structural changes in Pb-based relaxors under pressure

In the pressure range up to 30 GPa, two phase transitions are observed in both PST and PSN. The phase transitions are preceded by characteristic pressures at which the local symmetry is changed. Thus, one can propose four important pressure points typical of Pb-based perovskite-type relaxors (see Figure 6.1, 2nd column): (i) the characteristic pressure p^*_1 , at which the off-centered Pb and B-cations in PNRs decouple, while local anti-polar order of Pb cations as well as quasi-dynamical long-range order of anti-phase BO_6 tilts of equal magnitude are developed; (ii) the critical pressure p_{C1} at which a continuous phase transition from a relaxor-cubic to a non-polar rhombohedral state occurs, as the primary order parameter is anti-phase $a^-a^-a^-$ tilt order; (iii) the characteristic pressure p^*_2 at which the octahedral tilts around the cubic [100], [010] and [001] directions become different from each other on the local scale; (iv) the critical pressure p_{C2} at which a second phase transition from non-polar rhombohedral to non-polar monoclinic or triclinic symmetry occurs. The latter phase transition involves long-range ordered anti-phase tilts with unequal magnitudes ($a^0b^-b^-$) without Pb displacement ordering or a long-range order of Pb anti-polar displacements along cubic $[uv0]$ directions and a compatible mixed tilt system ($a^+b^-b^-$). The characteristic and critical pressures for the tantalate compound are lower than the corresponding values for the niobate compound, similarly to the critical temperatures of the paraelectric-to-ferroelectric phase transition (Lines & Glass, 1977).

Although PST and PSN have the same stoichiometry and tolerance factor, the degree of frustrated chemical B-site order in PST is slightly higher than in PSN, i.e., PST exhibits a longer coherence length between B'-O-B'' linkages. This is most probably the reason why the intrinsic coherence of ferroic Pb-O species existing at ambient pressure is more pronounced in PST than in PSN. The degree of frustrated chemical B-site order and coherent ferroic Pb-O species strongly influences the structural state at p^*_1 and consequently the nature of the structural transformations at p_{C2} .

Up to 30 GPa, no experimental evidence for the occurrence of a polar state involving nucleus ferroic order was detected. The pressure-induced decoupling between off-centered shifts of Pb and B cations in polar nanoregions that occur at p^*_1 triggers the development of anti-ferrodistortive long-range order. This suggests that at ambient pressure and room temperature the polar and anti-ferrodistortive order coexist on the mesoscopic scale and this might be the reason for the relaxor state.

6 Conclusions

Both solid solutions PSTN and PSTS undergo a second pressure-induced phase transition involving anti-polar ordering of Pb^{2+} cations and development of a mixed octahedral tilt system $a^+b^-b^-$. However, even at the highest pressure measured (19.6 GPa) PSTN does not show even-even-odd Bragg reflections but only diffuse streaks parallel to the $\langle 100 \rangle^*$ direction. This is most probably related to the preexisting ferroic species at ambient conditions leading to shorter correlation length of ordered Pb anti-polar shifts for PSTN than for PSTS regardless of the fine-scale B-site chemical ordering.

Due to the disturbance of coherent Pb-O ferroic species existing at ambient pressure and the induced local electric field, Ba doping substantially shifts the second critical pressure p_{C2} from ~ 5.5 GPa to 22 GPa and hinders the development of long-range anti-polar order of Pb^{2+} cations, thus restricting the structural transformation only to an alteration in the magnitudes of the octahedral tilts.

A-site doping with homo- or heterovalent cations having an ionic radius smaller than the ionic radius of Pb^{2+} , results in a reduction of the tolerance factor, which promotes anti-phase BO_6 tilting driven by an X -point phonon mode. However, the local electric fields induced by the heterovalent A-site substitution oppose the development of Pb anti polar ordering and the compatible mixed tilt system. Complementary off-beam Raman scattering experiments suggest that this is related to the fact that the A-doping-induced local electric fields pull back the pressure-induced suppression of off-centered B-cations observed for pure PST and PSN, as well as homovalent doped PSN (the case of Sr^{2+} for PSN). Thus the substitution of La^{3+} for Pb^{2+} has two competitive effects on the second pressure-induced phase transition and depending on the degree of the aliovalent substitution on the A-site (i) the overall anti polar Pb ordering may be enhanced at least on the mesoscopic scale as in the case of PSN-La ($x = 0.23$) or slightly disturbed as in the case of PST-La ($x = 0.08$), leading to a shift of p_{C2} to higher pressures. Thus, the difference in the high temperature state can be attributed to the small variations of the fine-scale degree of chemical 1:1 B-site ordering and dominantly the correlation length of intrinsic Pb-O ferroic species at ambient conditions.

6.2 The evolution of Pb-based relaxors under elevated temperatures and pressures

The in-situ high-pressure high-temperature Raman scattering data presented here unambiguously confirm the coexistence of mesoscopic polar and anti-ferrodistortive order in perovskite-type relaxors (Welsch *et al.*, 2011; Maier *et al.*, 2011c; Baba-Kishi & Pasciak, 2010; Takesue *et al.*, 1999; Dul'kin *et al.*, 2011) and the proposed ferrielectric nature of the relaxor state (see Section 5.3.1 and 6.4). Using temperature and pressure as two separate tuning mechanisms, one can select a structural state with a certain degree of polar order (by changing temperature) or of anti-ferrodistortive order (by applying pressure). At

6 Conclusions

elevated temperatures the first pressure-induced phase transition drops to lower pressures as the polar coupling is suppressed, which in turn facilitates the development of the mesoscopic anti-ferrodistortive order existing at ambient pressure into a long-range ordered anti-ferrodistortive state at high pressure.

Figure 6.1 shows a sketch indicating the changes under temperature and pressure for Pb-based perovskite-type relaxors undergoing a phase transition. On the x-axis the evolution of dynamic PNRs (ellipsoids with single black arrow) with temperature is shown. Room-temperature high-pressure structural studies on PSN with $T_C \sim 370$ K and on PST with $T_C \sim 270$ K as well as doped PSN and PST with canonical relaxor behavior have revealed the suppression of the polar order with pressure (Mihailova *et al.*, 2011; Maier *et al.*, 2011b). The first two columns in Figure 6.1 shows the sequence of structural changes with pressure at temperatures close to T_m : At the first intermediate pressure p_1^* the large PNRs are reduced due to the decoupling between the polar shifts of the A- and B-site cations and the correlation length of the mesoscopic anti-ferrodistortive order which for ambient pressure exists at all temperatures (light gray ellipsoids with paired arrows) starts to enlarge. The first phase transition is associated with a static long-range order of anti-phase octahedral tilts $a^- a^- a^-$ and the formation of non-polar rhombohedral domains (dark gray rectangles with paired arrows). At higher pressures a second phase transition occurs, which is also preceded by an intermediate pressure (not shown in sketch) and involves the occurrence of triclinic or monoclinic domains comprising long-range order of different BO_6 -tilt pattern and matching anti-ferroelectric order of Pb^{2+} cations. At elevated temperatures (3rd column in Figure 6.1) the PNRs are suppressed while the anti-ferrodistortive coupling is not significantly affected and hence, the development of anti-ferrodistortive long-range order is less hindered by the competitive mesoscopic polar order, which leads to a considerable decrease in the first critical pressure. We could not performed in-situ high-pressure experiments at temperatures above T_B but the results obtained at 600 K suggest that p_{C1} should be just above ambient pressure (4th column in Figure 6.1). The second pressure-induced phase transition involving a change in the type of the anti-ferrodistortive long-range order seems to be negligibly affected by temperature.

6 Conclusions

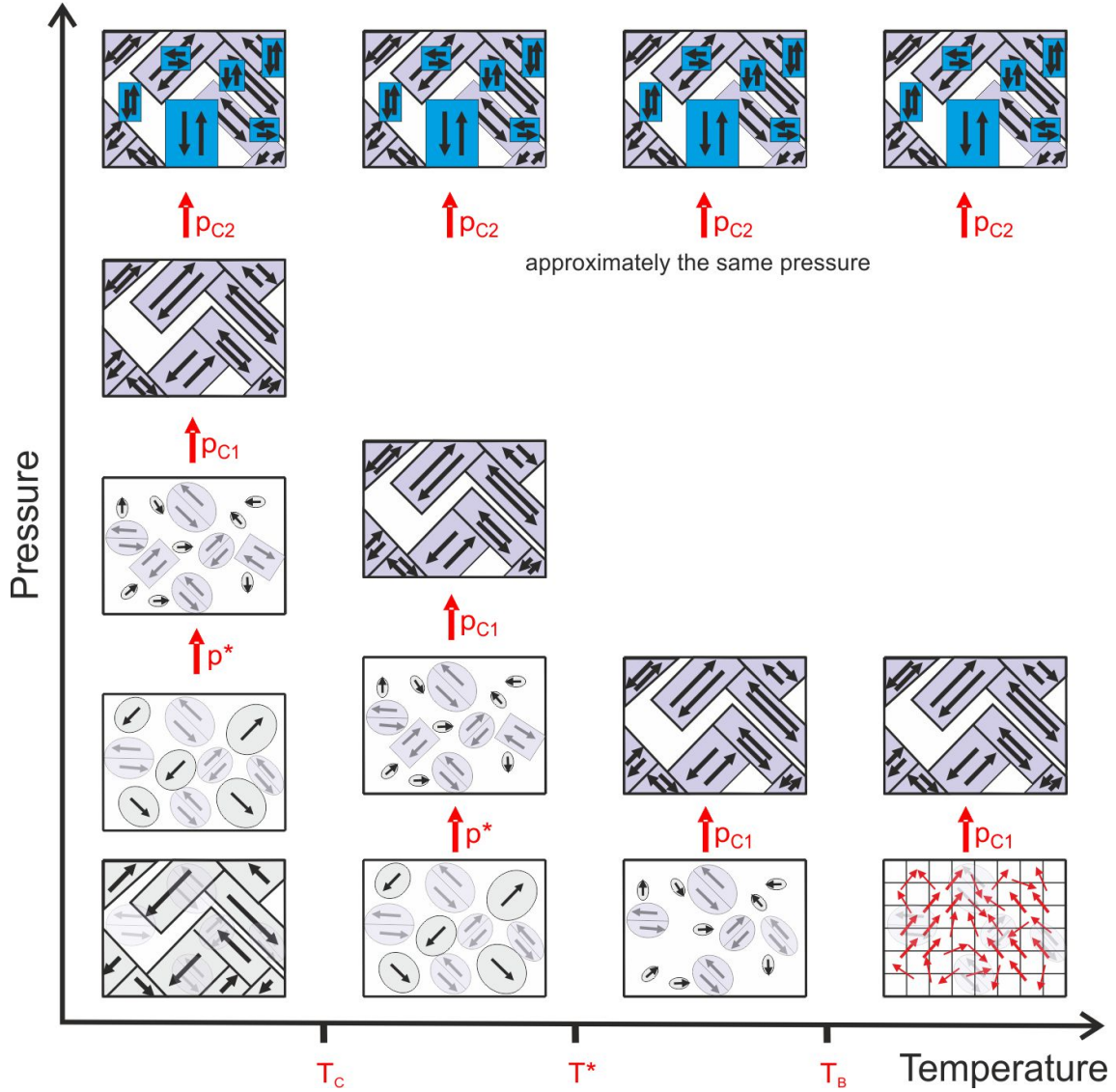


Figure 6.1: Schematic presentation of the structural changes taking place in relaxors under temperature and pressure. Ellipsoids and rectangles with a single arrow denote polar nanoregions and long-range ordered ferroelectric domains, respectively, whereas ellipsoids and rectangles with a pair of opposite arrows represent anti-ferrodistortive nanoregions and long-range ordered anti-ferrodistortive domains, respectively. The red arrows designate uncoupled cation off-centered shifts. Differently colored rectangles with a pair of opposite arrows designate the high-pressure long-range order below and above p_{C2} .

6.3 Structural changes in the solid solution PZN-0.1PT

6.3.1 Temperature-induced structural changes

The Raman peaks related to the cubic Pb-localized F_{2g} mode, which exists only in a doubled perovskite structure, are highly sensitive to the nucleation and development of polar order. By following the temperature evolution of the spectral parameters of these peaks, one can identify all characteristic temperatures typical of PZN-0.1PT. The two peaks near 50 cm^{-1} observed in the high-temperature $\bar{Z}(XY)Z$ spectra of PZN- x PT are attributed to two distinct cubic states of Pb ions in regions with a local chemical order of the type $\text{Pb}(\text{B}^{2+}_{2/3}\text{B}^{5+}_{1/3})_{1/2}\text{B}^{5+}_{1/2}\text{O}_3$ (see Figure 5.23): (i) less abundant Pb1 ions surrounded by Nb^{5+} and (ii) more abundant Pb2 ions surrounded by both Zn^{2+} and Nb^{5+} . The temperature dependence of the Raman spectra of PZN-0.1PT indicates that off-centered Pb2 ions induce coherent polar shifts of ferroelectrically active B-cations, which in turn facilitates the off-centering of Pb1 ions. Also, Raman data suggest the predominance of monoclinic-type ferroelectric domains in the room temperature structure of as-synthesized (unpoled) crystals.

A low degree of B-site doping with mixed-valence elements like Ru can substantially influence the development of ferroelectric long-range order in PZN- x PT solid solutions close to the MPB. This phenomenon is most probably due to the different preferred types of local octahedral distortion associated with the different valent states of the doping cations (see Figure 5.28). The incorporation of Ru into the structure of PZN-0.1PT slightly decreases T_B , smears the transformation processes near T^* and favors the long-range tetragonal order over a wide temperature range, shifting the T-M transition to lower temperatures.

6.3.2 Pressure-induced structural changes

Under pressure increase from ambient to 1 GPa, the ferroelectric structural distortion in PZN-0.1PT is reduced but the twinning is enhanced (the number of domains increases and the average domain size decreases), which increases in the overall strain of the average structure. This process induces a structural transformation near 1 GPa, involving a change of the preexisting multiphase (monoclinic + tetragonal) multidomain state to another, most probably, single-phase multidomain state. As a result, between 1 and 2 GPa the ferroic structural distortion continues to be reduced and the overall strain also decreases. Near 2 GPa the system reaches a cubic relaxor state, in which the polar order exists only on the mesoscopic scale, as polar nanoregions. The polar nanoregions persist up to 4 GPa, whereas uncoupled polar displacements of B-site cations are abundant even at 18.1 GPa. At 5.9 GPa PZN-0.1PT undergoes a reversible pressure-induced phase transition from a cubic to an anti-ferrodistortive phase comprising long-range ordered anti-phase octahedral tilts. Such a phase transition is typical of Pb-based perovskite-type relaxors. The contribution

6 Conclusions

of order-disorder structural phenomena involved in this phase transition of PZN-0.1PT is considerable due to the persistence of uncoupled B-site-cation off-centered shifts, which in turn is a result of the complex chemistry on the B-site and the associated local electric fields. At 11 GPa the average structure reaches a saturation in the pressure-induced ferroic distortion. Up to 18.1 GPa no further change in the tilt pattern was detected even on the local scale. The predominant polar atomic arrangements recover on decompression but the correlation length of ferroic distortion in the final state is shorter than in the initial state.

Low levels of Ru doping on the B-site ($\text{Ru}/(\text{Zn}+\text{Nb}+\text{Ti}) \sim 0.002$) does not influence the reversible phase transition near 5.9 GPa, although the same level of doping affects the temperature-driven structural transformations at ambient pressure. The comparison between the pressure dependence of the structure and properties up to 1 GPa suggests that the remarkable piezoelectric and electromechanical responses in PZN- x PT result from intrinsic ferroic structural inhomogeneities on the mesoscopic scale rather than from the complex multidomain texture.

6.3.3 A note about the structure-property relation in $\text{PbB}'_{1/3}\text{B}''_{2/3}\text{O}_3\text{-PbTiO}_3$ binary systems

The origin of the giant piezoelectric effect in ferroelectric solid solutions is still obscure (Glazer, 2011). In general, it can be related to the chemically-induced complex domain structure in the vicinity of the MPB or to intrinsic structural inhomogeneities on the mesoscopic scale. The former case can be further subdivided into two cases: (i) coexistence of ferroelectric domains of different symmetry, i.e., competition between different types of long-range polar order, or (ii) existence of one type of low-symmetry domains, e.g., monoclinic or triclinic, which allows for a high density of domain walls. In both cases the domain texture should play an important role for the giant response functions in this class of materials and we should expect higher piezoelectric and electromechanical coefficients if the ferroelectric twinning is enhanced, i.e., the number of domains increases and the mean domain size of the domains decreases. Our results indicate that in the low pressure range (from ambient pressure to 1.0 GPa) the twinning is strongly enhanced, while the ferroic deviation of the atomic structure is reduced. On the other hand, it has been shown that the application of pressure up to 0.5 GPa decreases the piezoelectric and electromechanical coefficients of PZN-0.09PT and the effect is particularly strong for the shear coefficients d_{31} and k_{31} (Yasuda *et al.*, 2005). Pressure has the same effect on the shear coefficients of PMN-0.32PT (Yasuda *et al.*, 2006). This suggests that at least the large shear piezoelectric and electromechanical responses are related to the intrinsic structural complexity on the local scale, rather than to the domain texture. This result is in full agreement with model calculations on single-domain and multidomain states of

PNM-0.33PT (Damjanovic *et al.*, 2003), demonstrating that the multidomain configuration has minor effect on both the uniaxial and shear piezoelectric responses.

6.4 A plausible structural state of Pb-based B-site complex perovskite-type relaxors

The formation of PNRs is usually considered in terms of chemically B-site ordered and disordered regions as seen by x-ray, neutron or electron diffraction. The predominant opinion is still that dynamical polar nanoregions are associated exclusively with chemically B-site disordered regions, although Raman scattering clearly indicates that all Pb-based B-site complex perovskite-type relaxor systems have lattice dynamics typical of a doubled structure, i.e., typical of B-site ordered regions. Modes existing only in a doubled perovskite structure are strongly influenced by the formation of polar order as demonstrated for relaxors (ABO₃ type) as well as for relaxor-based solid solutions (this study) (Mihailova *et al.*, 2008b; Welsch *et al.*, 2011; Maier *et al.*, 2009), regardless of the stoichiometry on the B-site. This suggests that on the mesoscopic scale one can hardly discriminate chemically ordered from chemically disordered regions and polar regions simply penetrate through the structure. Putting in another way, fine-scale atomic arrangements that are chemically 1:1 ordered exist also in that fraction of the material seen by diffraction as chemically disordered and therefore, regions exhibiting polarization should always possess local chemical 1:1 B-site order. This statement is supported by x-ray absorption spectroscopic data revealing a surprisingly high degree of local 1:1 ordering of the B-site cations (on the length scale of ~ 5 Å) in relaxor-based solid solutions (Frenkel *et al.*, 2004) exhibiting no long-range chemical B-site order.

However, chemical 1:1 B-site order favors anti-ferroelectric off-center displacements of the nearest Pb and O ions (Chen, 2000), meaning that there should be anti-ferroelectric-type coupling inside polar regions. This, on a first glance, incongruous statement actually has a very simple and elegant explanation: ferrielectricity, due to the coexistence of ferroelectric and anti-ferroelectric coupling in ferroic regions. Local chemical 1:1 B-site cation order favors anti-polar shifts of the Pb atoms. On the other hand, off-centering of Pb cations favors polar displacements of the corresponding nearest ferroelectrically active B-cations and hence, small polar BO₃-Pb species are formed in the structure. The faults of the chemical B-site order modulate the off-center shifts of the Pb cations and, consequently the dipoles associated with polar BO₃-Pb atomic species, which on the mesoscopic scale leads to frustrated ferrielectric order. These arguments are not valid for Ba-based systems, because Ba does not form stereochemically active lone pairs, i.e., has no affinity to displace off-center and therefore anti-ferroelectric coupling inside PNRs is very unlikely. This principle difference between the nature of ferroic order in PNRs might

6 Conclusions

be the key reason to explain why Pb-based relaxors systems have considerably stronger response functions as compared to Ba-based relaxor systems.

The assumption that polar nanoregions in Pb-based perovskite-type relaxor ferroelectrics might be ferrielectric in nature rather than ferroelectric is supported by the fact that pressure suppresses the coupling between off-centered Pb and B-site cations and the polar B-cation shifts, thus favoring the establishment of anti-ferrodistortive long-range order, which is developed from ferroic species already existing at ambient conditions (Welsch *et al.*, 2011; Mihailova *et al.*, 2008a; Maier *et al.*, 2010b). In addition, for chemically disordered $\text{PbSc}_{1/2}\text{Ta}_{1/2}\text{O}_3$ a phase transformation attributed to the development of modulated anti-ferrodistortive order slightly above the temperature of the dielectric-permittivity maximum was observed by acoustic emission (Dul'kin *et al.*, 2010a). Incommensurate modulated anti-ferrodistortive order was observed by transmission electron microscopy in $\text{PbSc}_{1/2}\text{Ta}_{1/2}\text{O}_3$ single crystals with high-degree of chemical B-site order (Baba-Kishi & Pasciak, 2010). Local anti-ferroelectric order was also deduced from x-ray diffuse scattering data on $\text{PbSc}_{1/2}\text{Nb}_{1/2}\text{O}_3$ (Takesue *et al.*, 1999). A ferrielectric type of the nano-scale polar order in relaxors is also an alternative plausible explanation for the V-type dependence of the dielectric-permittivity maximum temperature on an external electric field observed for PMN-0.33PT by acoustic emission (Dul'kin *et al.*, 2009), which is typical of anti-ferroelectric order. The T_C for PMN-0.33PT as detected by XRD shows the expected gradual increase with increasing the electric field (Dul'kin *et al.*, 2009), but XRD probes the ferroic long range order, i.e., indicates the temperature at which normal ferroelectric domains appear, whereas acoustic emission measures the response of the whole system, i.e., it is sensitive also to structural transformations related to PNRs.

Bibliography

- Adar, F., Delhay, M. & DaSilva, E. (2003). Evolution of instrumentation for detection of the Raman effect as driven by available technologies and by developing applications. At the *Waters Symposium, Pittcon*.
- Ahert, M., Cohen, R. E., Struzhkin, V., Gregoryanz, E., Rytz, D., Prosandeev, S. A., Mao, H.-K. & J. Hemley, R. (2005). High-pressure Raman scattering and x-ray diffraction of the relaxor ferroelectric $0.96\text{Pb}(\text{Zn}_{1/3}\text{Nb}_{2/3})\text{O}_3$ - 0.04PbTiO_3 . *Phys. Rev. B* **71**, 144102.
- Angel, R. J., Allan, D. R., Miletich, R. & Finger, L. W. (1997). The use of quartz as an internal pressure standard in high-pressure crystallography. *J. Appl. Cryst.* **30**, 461.
- Angel, R. J., Bujak, M., Zhao, J., Gatta, G. D. & Jacobsen, S. D. (2007). Effective hydrostatic limits of pressure media for high-pressure crystallographic studies. *J. Appl. Cryst.* **40**, 26.
- Angel, R. J. & Finger, L. W. (2011). SINGLE: a program to control single-crystal diffractometers. *J. Appl. Cryst.* **44**, 247.
- Aroyo, A., M. I. and Kirov, Capillas, C., Perez-Mato, J. & Wondratschek, H. (2006). Bilbao Crystallographic Server: II. Representations of crystallographic point groups and space groups. *Acta Crystallogr.* **A62**, 115.
- Baba-Kishi, K. Z. & Pasciak, M. (2010). An electron diffraction and Monte Carlo simulation study of an incommensurate antiferroelectric state in the relaxor ferroelectric $\text{Pb}_2\text{ScTaO}_6$. *J. Appl. Cryst.* **43**, 140.
- Barnett, J. D., Block, S. & Piermarini, G. J. (1973). An Optical Fluorescence System for Quantitative Pressure Measurement in the Diamond-Anvil Cell. *Rev. Sci. Instr.* **44**, 1.
- Bhalla, A., Guo, R. & Roy, R. (2000). The perovskite structure - a review of its role in ceramic science and technology. *Mat. Res. Innovat.* **4**, 3.
- Blin, R. (2011). *Advanced Ferroelectricity*, volume 151 of *International Series of Monographs on Physics*. Oxford Scientific Publications.
- Boehler, R. (2006). New diamond cell for single-crystal x-ray diffraction. *Rev. Sci. Instrum.* **77**, 115103.
- Bokov, A. A. (1997). Influence of disorder in crystal structure on ferroelectric phase transitions. *J. Exp. Theor. Phys.* **84**, 994.

Bibliography

- Bokov, A. A., Hilczer, A., Szafranski, M. & Ye, Z.-G. (2007). Impossibility of pressure-induced crossover from ferroelectric to nonergodic relaxor state in a $\text{Pb}(\text{Mg}_{1/3}\text{Nb}_{2/3})_{0.7}\text{Ti}_{0.3}\text{O}_3$ crystal: Dielectric spectroscopic study. *Phys. Rev. B* **76**, 184116.
- Bokov, A. A. & Ye, Z.-G. (2006). Recent progress in relaxor ferroelectrics with perovskite structure. *J. Mater. Sci.* **41**, 31.
- Burns, G. & Dacol, F. H. (1983). Crystalline ferroelectrics with glassy polarization behavior. *Phys. Rev. B* **28**, 2527.
- Burton, B. P., Cockayne, E., Tinte, S. & Waghmare, U. V. (2006). First-principles-based simulations of relaxor ferroelectrics. *Phase Transitions: A Multinational Journal* **79**, 91.
- Campbell, B. J., Stokes, H. T., Tanner, D. E. & Hatch, D. M. (2006). ISODISPLACE: a web-based tool for exploring structural distortions. *J. Appl. Cryst.* **39**, 607.
- Chaabane, B., Kreisel, J., Bouvier, P., Lucazeau, G. & Dkhil, B. (2004). Effect of high pressure on the $\text{Pb}(\text{Mg}_{1/3}\text{Nb}_{2/3})\text{O}_3$ - PbTiO_3 solid solution: A Raman scattering investigation. *Phys. Rev. B* **70**, 134114.
- Chaabane, B., Kreisel, J., Dkhil, B., Bouvier, P. & Mezouar, M. (2003). Pressure-induced suppression of the diffuse scattering in the model relaxor ferroelectric $\text{PbMg}_{1/3}\text{Nb}_{2/3}\text{O}_3$. *Phys. Rev. Lett.* **90**, 257601.
- Chang, W. S., Lim, L. C., Yang, P., Wang, F.-T., Hsieh, C.-M. & Tu, C.-S. (2008). Structural phase transformations and nanotwin domains in $0.93\text{Pb}(\text{Zn}_{1/3}\text{Nb}_{2/3})\text{O}_3$ - 0.07PbTiO_3 . *J. Phys: Condens. Matter* **20**, 395229.
- Chen, I. W. (2000). Structural origin of relaxor ferroelectrics – revisited. *J. Phys. Chem. Solids* **61**, 197.
- Chen, I.-W., Li, P. & Wang, Y. (1996). Structural origin of relaxor perovskites. *J. Phys. Chem. Solids* **57**, 1525.
- Cheng, J., Yang, Y., Tong, Y.-H., Lu, S.-B., Sun, J.-Y., Zhu, K., Liu, Y.-L., Siu, G. G. & Xu, Z. K. (2009). Study of monoclinic-tetragonal-cubic phase transition in $\text{Pb}(\text{Zn}_{1/3}\text{Nb}_{2/3})\text{O}_3$ - 0.08PbTiO_3 single crystals by micro-Raman spectroscopy. *J. Appl. Phys.* **105**, 053519.
- Clem, P. G., Payne, D. A. & Warren, W. L. (1995). Observation of two charge states of ruthenium in PbTiO_3 single crystals. *J. Appl. Phys.* **77**, 5865.
- Cohen, R. E. (1992). Origin of ferroelectricity in perovskite oxides. *Nature* **358**, 136.
- Cross, L. E. (1987). Relaxor Ferroelectrics. *Ferroelectrics* **76**, 241.
- Cross, L. E. (2008). *Piezoelectricity*, volume 114 of *Springer Series in Material Science*, chapter Relaxor Ferroelectrics. Springer, pp. 131–156.

Bibliography

- Damen, T. C., Porto, S. P. S. & Tell, B. (1966). Raman Effect in Zinc Oxide. *Phys. Rev.* **142**, 570.
- Damjanovic, D., Budimir, M., Davis, M. & Setter, N. (2003). Monodomain versus polydomain piezoelectric response of $0.67\text{Pb}(\text{Mg}_{1/3}\text{Nb}_{2/3})\text{O}_3$ – 0.33PbTiO_3 single crystals along nonpolar directions. *Appl. Phys. Lett.* **83**, 527.
- Datchi, F., Dewaele, A., Loubeyre, P., Letoullec, R., Godec, Y. L. & Canny, B. (2007). Optical pressure sensors for high-pressure-high-temperature studies in a diamond anvil cell. *High Pressure Research* **27**, 447.
- Datchi, F., LeToullec, R. & Loubeyre, P. (1997). Improved calibration of the $\text{SrB}_4\text{O}_7\text{:Sm}^{2+}$ optical pressure gauge: Advantages at very high pressures and high temperatures. *J. Appl. Phys.* **81**, 3333.
- Datchi, F., Loubeyre, P. & LeToullec, R. (2000). Extended and accurate determination of the melting curves of argon, helium, ice (H_2O), and hydrogen (H_2). *Phys. Rev. B* **61**, 6535.
- Dkhil, B., Gemeiner, P., Al-Barakaty, A., Bellaiche, L., Dul'kin, E., Mojaev, E. & Roth, M. (2009). Intermediate temperature scale T^* in lead-based relaxor systems. *Phys. Rev. B* **80**, 064103.
- Dul'kin, E., Mihailova, B., Catalan, G., Gospodinov, M. & Roth, M. (2010a). Phase transformation above T_m in $\text{PbSc}_{0.5}\text{Ta}_{0.5}\text{O}_3$ relaxor as seen via acoustic emission. *Phys. Rev. B* **82**, 180101(R).
- Dul'kin, E., Mihailova, B., Gospodinov, M., Mojaev, E. & Roth, M. (2010b). Evidence of local anisotropic strains in relaxor ferroelectrics below intermediate temperature T^* detected by acoustic emission. *Journal of Physics: Condensed Matter* **22**, 222201.
- Dul'kin, E., Mihailova, B., Gospodinov, M. & Roth, M. (2011). Electric field dependence of characteristic temperatures in $\text{PbSc}_{0.5}\text{Ta}_{0.5}\text{O}_3$ and $\text{Pb}_{0.78}\text{Ba}_{0.22}\text{Sc}_{0.5}\text{Ta}_{0.5}\text{O}_3$ relaxors studied via acoustic emission. *Europhys. Lett.* **94**, 57002.
- Dul'kin, E., Mojaev, E., Roth, M., Raevski, I. P. & Prosandeev, S. A. (2009). Nature of thermally stimulated acoustic emission from $\text{PbMg}_{1/3}\text{Nb}_{2/3}\text{O}_3$ – PbTiO_3 solid solutions. *Appl. Phys. Lett.* **94**, 252904.
- Dul'kin, E., Roth, M., Janolin, P.-E. & Dkhil, B. (2006). Acoustic emission study of phase transitions and polar nanoregions in relaxor-based systems: Application to the $\text{PbZn}_{1/3}\text{Nb}_{2/3}\text{O}_3$ family of single crystals. *Phys. Rev. B* **73**, 012102.
- Dunstan, D. J. & Spain, I. L. (1989). Technology of diamond anvil high-pressure cells: I. Principles, design and construction. *Journal of Physics E: Scientific Instruments* **22**, 913.

Bibliography

- Eremets, M. I. (1996). *High Pressure Experimental Methods*, chapter Diamond Anvils. Oxford Science Publications, p. 54.
- Frenkel, A., Pease, D., Giniewicz, J., Stern, E., Brewe, D., Daniel, M. & Budnick, J. (2004). Concentration-dependent short-range order in the relaxor ferroelectric $(1 - x)\text{Pb}(\text{Sc,Ta})\text{O}_3\text{-}x\text{PbTiO}_3$. *Phys. Rev. B* **70**, 014106.
- Gallardo, P., Besson, J., Itie, J., Gauthier, M., Mezouar, M., Klotz, S., Hausermann, D. & Hanfland, M. (2000). Uniaxial stress component in WC toroidal anvils under high pressure and temperature. *Physica Status Solidi A: Applications and Materials Science* **180**, 427.
- Geiger, C. A. (2004). *EMU Notes in Mineralogy*, volume 6, chapter An introduction to spectroscopic methods in the mineral science and geochemistry. European Mineralogical Union, pp. 1–42.
- Glazer, A. M. (1972). The Classification of Tilted Octahedra in Perovskites. *Acta Crystallogr.* **B28**, 3384.
- Glazer, A. M. (2011). Proceedings of the European Meeting on Ferroelectricity (Abstract). 11th European Meeting on Ferroelectricity Bordeaux, France.
- Glinchuk, M. D. & Farhi, R. (1996). A random field theory based model for ferroelectric relaxors. *J. Phys.: Condens. Matter* **8**, 6985.
- Goldschmidt, V. M. (1927). *Geochemische Verteilungsgesetze der Elemente*. Norske Videnskap, Oslo.
- Gorfman, S. & Thomas, P. A. (2010). Evidence for a non-rhombohedral average structure in the lead-free piezoelectric material $\text{Na}_{0.5}\text{Bi}_{0.5}\text{TiO}_3$. *J. Appl. Cryst.* **43**, 1409.
- Guo, R., Cross, L. E., Park, S.-E., Noheda, B., Cox, D. E. & Shirane, G. (2000). Origin of the High Piezoelectric Response in $\text{PbZr}_{1-x}\text{Ti}_x\text{O}_3$. *Phys. Rev. Lett.* **84**, 5423.
- Hilczer, A. & Szafranski, M. (2008). Dielectric response of disordered $\text{Pb}(\text{Sc}_{1/2}\text{Ta}_{1/2})\text{O}_3$ single crystal under hydrostatic pressure. *Phase Transitions: A Multinational Journal* **81**, 987.
- Hirota, K., Wakimoto, S. & Cox, D. E. (2006). Neutron and X-ray Scattering Studies of Relaxors. *J. Phys. Soc. Jpn.* **75**, 111006.
- Howard, C. J., Kennedy, B. J. & Woodward, P. M. (2003). Ordered double perovskites – a group-theoretical analysis. *Acta Crystallogr.* **B59**, 463.
- Husson, E. (1998). Raman Spectroscopy Applied to the Study of Phase Transitions. *Key Engineering Materials* **155-156**, 1.

Bibliography

- Imry, Y. & Ma, S.-K. (1975). Random-Field Instability of the Ordered State of Continuous Symmetry. *Phys. Rev. Lett.* **35**, 1399.
- Isupov, V. A., Pronin, I. P. & Sizykh, V. I. (1989). Investigation of the diffuse ferroelectric phase transition in leadmagnesium niobate. *Ferroelectrics* **90**, 147.
- Itoh, M., Shikano, M. & Shimura, T. (1995). High- and low-spin transition of Ru^{4+} in the perovskite-related layered system $\text{Sr}_{n+1}\text{Ru}_n\text{O}_{3n+1}$ ($n=1, 2$, and ∞) with the change in n . *Phys. Rev. B* **51**, 16432.
- Iwata, Makoto, Hasegawa, Yusuke, Aoyagi, Rintaro, Maeda, Masaki, Wakiya, Naoki, Suzuki, Hisao, Ishibashi & Yoshihiro (2009). Low-Frequency Raman Spectroscopy in $\text{Pb}(\text{Zn}_{1/3}\text{Nb}_{2/3})\text{O}_3$ - PbTiO_3 Mixed Crystals. *Ferroelectrics* **378**, 84.
- Janolin, P. E., Bouvier, P., Kreisel, J., Thomas, P. A., Kornev, I. A., Bellaiche, L., Crichton, W., Hanfland, M. & Dkhil, B. (2008). High-Pressure Effect on PbTiO_3 : An Investigation by Raman and X-Ray Scattering up to 63 GPa. *Phys. Rev. Lett.* **101**, 237601.
- Janolin, P. E., Dkhil, B., Bouvier, P., Kreisel, J. & Thomas, P. A. (2006). Pressure instabilities up to 46 GPa in the relaxor ferroelectric $\text{PbZn}_{1/3}\text{Nb}_{2/3}\text{O}_3$. *Phys. Rev. B* **73**, 094128.
- Jeong, I.-K. & Lee, J. K. (2006). Local structure and medium-range ordering in relaxor ferroelectric $\text{Pb}(\text{Zn}_{1/3}\text{Nb}_{2/3})\text{O}_3$ studied using neutron pair distribution function analysis. *Appl. Phys. Lett.* **88**, 262905.
- Kinsland, G. L. & Bassett, W. A. (1977). Strength of MgO and NaCl polycrystals to confining pressures of 250 kbar at 25°C. *J. Appl. Phys.* **48**, 978.
- Kleemann, W. (1993). Random-Field Induced Antiferromagnetic, Ferroelectric And Structural Domain States. *Int. J. Mod. Phys. B* **7**, 2469.
- Klotz, S., Chervin, J.-C., Munsch, P. & Le Marchand, G. (2009). Hydrostatic limits of 11 pressure transmitting media. *J. Phys. D: Appl. Phys.* **42**, 075413.
- Kornev, I. A., Bellaiche, L., Bouvier, P., Janolin, P.-E., Dkhil, B. & Kreisel, J. (2005). Ferroelectricity of Perovskites under Pressure. *Phys. Rev. Lett.* **95**, 196804.
- Kreisel, J., Bouvier, P., Dkhil, B., Thomas, P. A., Glazer, A. M., Welberry, T. R., Chaabane, B. & Mezouar, M. (2003). High-pressure x-ray scattering of oxides with a nanoscale local structure: Application to $\text{Na}_{1/2}\text{Bi}_{1/2}\text{TiO}_3$. *Phys. Rev. B* **68**, 014113.
- Kreisel, J., Dkhil, B., Bouvier, P. & Kiat, J. M. (2002). Effect of high pressure on relaxor ferroelectrics. *Phys. Rev. B* **65**, 172101.
- Kroumova, E., Aroyo, M., Perez-Mato, J., Kirov, A., Capillas, C., Ivantchev, S. & Wondratschek, H. (2003). Bilbao Crystallographic Server : Useful Databases and Tools for Phase-Transition Studies. *Phase Transitions: A Multinational Journal* **76**, 155.

Bibliography

- Kumaresavanji, M., Sousa, L. L. L., Machado, F. L. A., Adriano, C., Pagliuso, P. G., Saitovitch, E. M. B. & Fontes, M. B. (2010). Effects of Ru doping on the transport and magnetic properties of a $\text{La}_{1.32}\text{Sr}_{1.68}\text{Mn}_{2-y}\text{Ru}_y\text{O}_7$ layered manganite system. *J. Phys: Condens. Matter* **22**, 236003.
- Kuwata, J., Uchino, K. & Nomura, S. (1981). Phase-Transition in the $\text{Pb}(\text{Zn}_{1/3}\text{Nb}_{2/3})\text{O}_3$ - PbTiO_3 system. *Ferroelectrics* **37**, 579.
- La-Orautapong, D., Noheda, B., Ye, Z.-G., Gehring, P. M., Toulouse, J., Cox, D. E. & Shirane, G. (2002). Phase diagram of the relaxor ferroelectric $(1-x)\text{Pb}(\text{Zn}_{1/3}\text{Nb}_{2/3})\text{O}_3-x\text{PbTiO}_3$. *Phys. Rev. B* **65**, 144101.
- La-Orautapong, D., Toulouse, J., Robertson, J. L. & Ye, Z. G. (2001). Diffuse neutron scattering study of a disordered complex perovskite $\text{Pb}(\text{Zn}_{1/3}\text{Nb}_{2/3})\text{O}_3$ crystal. *Phys. Rev. B* **64**, 212101.
- La-Orautapong, D., Toulouse, J., Ye, Z. G., Chen, W., Erwin, R. & Robertson, J. L. (2003). Neutron scattering study of the relaxor ferroelectric $(1-x)\text{Pb}(\text{Zn}_{1/3}\text{Nb}_{2/3})\text{O}_3-x\text{PbTiO}_3$. *Phys. Rev. B* **67**, 134110.
- Landsberg, G. S. & Mandelstam, L. I. (1928). Über die Lichtzerstreuung in Kristallen. *Zeitschrift für Physik* **50**, 769.
- Lines, M. E. & Glass, A. M. (1977). *Principles And Applications of Ferroelectrics and Related Materials*. Clarendon Press, Oxford.
- Madeswaran, S., Rajasekaran, S., Jayavel, R., Ganesamoorthy, S. & Behr, G. (2005). Domain structure studies on $\text{Pb}(\text{Zn}_{1/3}\text{Nb}_{2/3})\text{O}_3$ - PbTiO_3 mixed crystal system. *Materials Science and Engineering: B* **120**, 32. The 8th International Symposium on Ferroic Domains (ISFD-8, 2004).
- Maier, B. J. (2010). Phase transitions in advanced relaxor-ferroelectric materials with a perovskite-type structure. Ph.D. thesis, Universität Hamburg.
- Maier, B. J., Angel, R. J., Marshall, W. G., Mihailova, B., Paulmann, C., Engel, J. M., Gospodinov, M., Welsch, A.-M., Petrova, D. & Bismayer, U. (2010a). Octahedral tilting in Pb-based relaxor ferroelectrics at high pressure. *Acta Crystallogr. B* **66**, 280.
- Maier, B. J., Angel, R. J., Mihailova, B., Marshall, W. G., Gospodinov, M. & Bismayer, U. (2011a). High-pressure powder neutron diffraction study on lead scandium niobate. *J. Phys.: Condens. Matter* **23**, 035902.
- Maier, B. J., Mihailova, B., Paulmann, C., Ihringer, J., Gospodinov, M., Stosch, R., Güttler, B. & Bismayer, U. (2009). Effect of local elastic strain on the structure of Pb-based relaxors. A comparative study of pure, Ba- and Bi-doped $\text{PbSc}_{0.5}\text{Nb}_{0.5}\text{O}_3$. *Phys. Rev. B* **79**, 224108.

Bibliography

- Maier, B. J., Waesermann, N., Mihailova, B., Angel, R. J., Ederer, C., Paulmann, C., Gospodinov, M., Friedrich, A. & Bismayer, U. (2011b). The structural state of relaxor ferroelectrics $\text{PbSc}_{0.5}\text{Ta}_{0.5}\text{O}_3$ and $\text{PbSc}_{0.5}\text{Nb}_{0.5}\text{O}_3$ at high pressures up to 30 GPa. *Phys. Rev. B* **84**, 174104.
- Maier, B. J., Welsch, A.-M., Angel, R. J., Mihailova, B., Zhao, J., Engel, J. M., Schmitt, L. A., Paulmann, C., Gospodinov, M., Friedrich, A. & Bismayer, U. (2010b). A-site Doping Induced Renormalization of Structural Transformations in $\text{PbSc}_{0.5}\text{Nb}_{0.5}\text{O}_3$ Relaxor Ferroelectric under High Pressure. *Phys. Rev. B* **81**, 174116.
- Maier, B. J., Welsch, A.-M., Mihailova, B., Angel, R. J., Zhao, J., Paulmann, C., Engel, J. M., Marshall, W. G., Gospodinov, M., Petrova, D. & Bismayer, U. (2011c). Effect of La doping on the ferroic order in Pb-based perovskite-type relaxor ferroelectrics. *Phys. Rev. B* **83**, 134106.
- Mao, H. K., Xu, J. & Bell, P. M. (1986). Calibration Of The Ruby Pressure Gauge To 800-kbar Under Quasi-Hydrostatic Conditions. *J. Geophys. Res.* **91**, 4673.
- Megaw, H. D. (1946). Crystal structure of double oxides of the perovskite type. *Proceedings of the Physical Society* **58**, 133.
- Merkel, S., Hemley, R. J. & kwang Mao, H. (1999). Finite-element modeling of diamond deformation at multimegabar pressures. *Appl. Phys. Lett.* **74**, 656.
- Mihailova, B., Angel, R., Maier, B. J., Welsch, A.-M., Zhao, J., Gospodinov, M. & Bismayer, U. (2011). The Structural State of Lead-Based Relaxor Ferroelectrics Under Pressure. *IEEE Trans. Ultrason., Ferroelectr., Freq. Control* **58**, 1905.
- Mihailova, B., Angel, R. J., Welsch, A.-M., Zhao, J., Engel, J., Paulmann, C., Gospodinov, M., Ahsbahs, H., Stosch, R., Güttler, B. & Bismayer, U. (2008a). Pressure-induced phase transition in $\text{PbSc}_{0.5}\text{Ta}_{0.5}\text{O}_3$ as a model Pb-based perovskite relaxor ferroelectric. *Phys. Rev. Lett.* **101**, 017602.
- Mihailova, B., Bismayer, U., Güttler, B., Boris, M. G. A., Berndhard, C. & Aroyo, M. (2005). Nanoscale phase transformations in relaxor-ferroelectric lead scandium tantalate and lead scandium niobate. *Z. Kristallogr.* **220**, 740.
- Mihailova, B., Bismayer, U., Güttler, B., Gospodinov, M. & Konstantinov, L. (2002). Local structure and dynamics in relaxor-ferroelectric $\text{PbSc}_{1/2}\text{Nb}_{1/2}\text{O}_3$ and $\text{PbSc}_{1/2}\text{Ta}_{1/2}\text{O}_3$ single crystals. *J. Phys.: Condens. Matter* **14**, 1091.
- Mihailova, B., Gospodinov, M., Güttler, B., Petrova, D., Stosch, R. & Bismayer, U. (2007). Ferroic nanoclusters in relaxors: the effect of oxygen vacancies. *J. Phys.: Condens. Matter* **19**, 246220.

Bibliography

- Mihailova, B., Maier, B., Paulmann, C., Malcherek, T., Ihringer, J., Gospodinov, M., Stosch, R., Güttler, B. & Bismayer, U. (2008b). High-temperature structural transformations in relaxor-ferroelectric $\text{PbSc}_{0.5}\text{Ta}_{0.5}\text{O}_3$ and $\text{Pb}_{0.78}\text{Ba}_{0.22}\text{Sc}_{0.5}\text{Ta}_{0.5}\text{O}_3$. *Phys. Rev. B* **77**, 174106.
- Mulvihill, M., Park, S., Risch, G., Li, Z., Uchino, K. & Shrout, T. (1996). The role of processing variables in the flux growth of lead zinc niobate-lead titanate relaxor ferroelectric single crystals. *Japanese Journal of Applied Physics, Part 1: Regular Papers, Brief Communications & Review Papers* **35**, 3984.
- Munro, R. G., Piermarini, G. J., Block, S. & Holzapfel, W. B. (1985). Model line-shape analysis for the ruby R lines used for pressure measurement. *J. Appl. Phys.* **57**, 165.
- Nasdala, L., Smith, D. C., Kaindl, R. & Ziemann, M. A. (2004). *Spectroscopic Methods in Mineralogy*, volume 6 of *EMU Notes in Mineralogy*, chapter Raman spectroscopy: Analytical perspectives in mineralogical research. European Mineralogical Union, pp. 281–343.
- Noheda, B., Cox, D., Shirane, G., Park, S., Cross, L. & Zhong, Z. (2001). Polarization rotation via a monoclinic phase in the piezoelectric 92% $\text{PbZn}_{1/3}\text{Nb}_{2/3}\text{O}_3$ –8% PbTiO_3 . *Phys. Rev. Lett.* **86**, 3891.
- Park, S. & Shrout, T. (1997). Ultrahigh strain and piezoelectric behavior in relaxor based ferroelectric single crystals. *J. Appl. Phys.* **82**, 1804.
- Pasciak, M., Wolcyrz, M. & Pietraszko, A. (2007). Interpretation of the diffuse scattering in Pb-based relaxor ferroelectrics in terms of three-dimensional nanodomains of the $\langle 110 \rangle$ -directed relative interdomain atomic shifts. *Phys. Rev. B* **76**, 014117.
- Paulmann, C. & Malcherek, T. (2006). Software development for studies of disorder-induced diffuse scattering using CCD-detectors. *Hasylab Annual Report Part I*, 1399.
- Perrin, C., Menguy, N., Suard, E., Mueller, C., Caranoni, C. & Stepanov, A. (2000). Neutron diffraction study of the relaxor ferroelectric phase transition in disordered $\text{Pb}(\text{Sc}_{1/2}, \text{Nb}_{1/2})\text{O}_3$. *J. Phys.: Condens. Matter* **12**, 7523.
- Raman, C. V. & Krishnan, K. S. (1928). A New Type of Secondary Radiation. *Nature* **121**, 501.
- Repelin, Y., Husson, E., Bennani, F. & Proust, C. (1999). Raman spectroscopy of lithium niobate and lithium tantalate. Force field calculations. *Journal of Physics and Chemistry of Solids* **60**, 819.
- Ropka, Z., Radwański, R. & Baran, A. (2003). Electronic structure and magnetism of Sr_2RuO_4 . *Physica C: Superconductivity* **387**, 262 . Proceedings of the 3rd Polish-US Workshop on Superconductivity and Magnetism of Advanced Materials.

Bibliography

- Salje, E., Devarajan, V., Bismayer, U. & Guimaraes, D. M. C. (1983). Phase transitions in $\text{Pb}_3(\text{P}_{1-x}\text{As}_x\text{O}_4)_2$: influence of the central peak and flip mode on the Raman scattering of hard modes. *Journal of Physics C: Solid State Physics* **16**, 5233.
- Samara, G. A. (2003). The relaxational properties of compositionally disordered ABO_3 perovskites. *J. Phys.: Condens. Matter* **15**, R367.
- Samara, G. A. & Venturini, E. L. (2006). Ferroelectric/relaxor crossover in compositionally disordered perovskites. *Phase Transitions: A Multinational Journal* **79**, 21.
- Samara, G. A., Venturini, E. L. & Boatner, L. A. (2006). Dielectric properties and phase transitions of $\text{Cd}_{2/3}\text{Nb}_{2/3}\text{O}_7$: Effects of pressure and temperature. *Journal of Applied Physics* **100**, 074112.
- Samara, G. A., Venturini, E. L. & Schmidt, V. H. (2000). Pressure-induced crossover from long-to-short-range order in $[\text{Pb}(\text{Zn}_{1/3}\text{Nb}_{2/3})\text{O}_3]_{0.905}(\text{PbTiO}_3)_{0.095}$ single crystal. *Appl Phys Lett* **76**, 1327.
- Sani, A., Noheda, B., Kornev, I. A., Bellaiche, L., Bouvier, P. & Kreisel, J. (2004). High-pressure phases in highly piezoelectric $\text{PbZr}_{0.52}\text{Ti}_{0.48}\text{O}_3$. *Phys. Rev. B* **69**, 020105.
- Scholz, T., Mihailova, B., Schneider, G. A., Pagels, N., Heck, J., Malcherek, T., Fernandes, R. P., Marinova, V., Gospodinov, M. & Bismayer, U. (2009). Ferroelectric properties of ruthenium-doped lead zinc niobate-lead titanate single crystal. *J. Appl. Phys.* **106**, 074108.
- Scott, J. F. (2007). Applications of Modern Ferroelectrics. *Science* **315**, 954.
- Setter, N. & Cross, L. E. (1980). The role of B-site cation disorder in diffuse phase transition behavior of perovskite ferroelectrics. *J. Appl. Phys.* **51**, 4356.
- Shannon, R. D. (1976). Revised effective ionic radii and systematic studies of interatomic distances in halides and chalcogenides. *Acta Crystallogr.* **A32**, 751.
- Smekal, A. (1923). Zur Quantentheorie der Dispersion. *Naturwissenschaften* **11**, 873. 10.1007/BF01576902.
- Smolenskii, G., Isupov, V., Agranovskaya, A. & Popov, S. (1961). Ferroelectrics with diffuse phase transitions. *Soviet Physics Solid State* **2**, 2584.
- Spain, I. & Dunstan, D. (1989). Technology of diamond anvil high-pressure cells: II Operation and Use. *Journal of Physics E: Scientific Instruments* **22**, 923.
- Stenger, C. G. F. & Burggraaf, A. J. (1980). Order-disorder reactions in the ferroelectric perovskites $\text{Pb}(\text{Sc}_{1/2}\text{Nb}_{1/2})\text{O}_3$ and $\text{Pb}(\text{Sc}_{1/2}\text{Ta}_{1/2})\text{O}_3$. I. Kinetics of the ordering process. *Physica Status Solidi A: Applications and Materials Science* **61**, 275.

Bibliography

- Svitelskiy, O., La-Orauttapong, D., Toulouse, J., Chen, W. & Ye, Z. G. (2005). PbTiO₃ addition and internal dynamics in Pb(Zn_{1/3}Nb_{2/3})O₃ crystal studied by Raman spectroscopy. *Phys. Rev. B* **72**, 172106.
- Svitelskiy, O., Toulouse, J., Yong, G. & Ye, Z. G. (2003). Polarized Raman study of the phonon dynamics in Pb(Mg_{1/3}Nb_{2/3})O₃ crystal. *Phys. Rev. B* **68**, 104107.
- Syassen, K. (2008). Ruby under pressure. *High Pressure Research* **28**, 75.
- Takemura, K. & Dewaele, A. (2008). Isothermal equation of state for gold with a He-pressure medium. *Phys. Rev. B* **78**, 104119.
- Takesue, N., Fujii, Y., Ichihara, M. & Chen, H. (1999). Self-Accommodation of Ionic Size-Effect Atomic Displacements in Antiferroelectric Order in Relaxor Lead Scandium Niobate. *Phys. Rev. Lett.* **82**, 3709.
- Taniguchi, H., Itoh, M. & Fu, D. (2011). Raman scattering study of the soft mode in Pb(Mg_{1/3}Nb_{2/3})O₃. *Journal of Raman Spectroscopy* **42**, 706.
- Tinte, S., Burton, B. P., Cockayne, E. & Waghmare, U. V. (2006). Origin of the Relaxor State in $PbB_xB_{1-x}O_3$ Perovskites. *Phys. Rev. Lett.* **97**, 137601.
- Toulouse, J., Jiang, F., Svitselskiy, O., Chen, W. & Ye, Z. G. (2005). Temperature evolution of the relaxor dynamics in Pb(Zn_{1/3}Nb_{2/3})O₃: A critical Raman analysis. *Phys. Rev. B* **72**, 184106.
- Uesu, Y., Matsuda, M., Yamada, Y., Fujishiro, K., Cox, D., Noheda, B. & Shirane, G. (2002). Symmetry of high-piezoelectric Pb-based complex perovskites at the morphotropic phase boundary: I. Neutron diffraction study on Pb(Zn_{1/3}Nb_{2/3})O₃-9%PbTiO₃. *Journal of the Physical Society of Japan* **71**, 960.
- Valasek, J. (1921). Piezo-Electric and Allied Phenomena in Rochelle Salt. *Phys. Rev.* **17**, 475.
- Vanderbilt, D. & Cohen, M. (2001). Monoclinic and triclinic phases in higher-order Devonshire theory. *Phys. Rev. B* **63**.
- Venturini, E. L., Grubbs, R. K., Samara, G. A., Bing, Y. & Ye, Z.-G. (2006). Ferroelectric and relaxor properties of Pb(Sc_{0.5}Nb_{0.5})O₃: Influence of pressure and biasing electric field. *Phys. Rev. B* **74**.
- Waeselmann, N., Maier, B. J., Mihailova, B., Angel, R. J., Zhao, J., Gospodinov, M., Paulmann, C., Ross, N. & Bismayer, U. (2012). Pressure-induced structural transformations in pure and Ru-doped 0.9PbZn_{1/3}Nb_{2/3}O₃-0.1PbTiO₃ near the morphotropic phase boundary. *Phys. Rev. B* **85**, 014106.
- Welberry, T. R. & Goossens, D. J. (2008). Different models for the polar nanodomain structure of PZN and other relaxor ferroelectrics. *J. Appl. Cryst.* **41**, 606.

Bibliography

- Welsch, A.-M. (2009). High-pressure Raman scattering of pure and doped $\text{PbSc}_{0.5}\text{Ta}_{0.5}\text{O}_3$ and $\text{PbSc}_{0.5}\text{Nb}_{0.5}\text{O}_3$ single crystals. Ph.D. thesis, University of Hamburg.
- Welsch, A.-M., Maier, B. J., Engel, J., Mihailova, B., Angel, R. J., Paulmann, C., Gospodinov, M., Friedrich, A., Stosch, R., Güttler, B. & Bismayer, U. (2009a). Effect of Ba on pressure-induced structural changes in the relaxor ferroelectric $\text{PbSc}_{0.5}\text{Ta}_{0.5}\text{O}_3$. *Phys. Rev. B* **80**, 104118.
- Welsch, A.-M., Maier, B. J., Mihailova, B., Angel, R. J., Zhao, J., Paulmann, C., Engel, J. M., Gospodinov, M., Marinova, V. & U., B. (2011). Transformation processes in relaxor ferroelectric $\text{PbSc}_{0.5}\text{Ta}_{0.5}\text{O}_3$ heavily doped with Nb and Sn. *Z. Kristallogr.* **226**, 126. Accepted.
- Welsch, A.-M., Mihailova, B., Gospodinov, M., Stosch, R., Güttler, B. & Bismayer, U. (2009b). High pressure Raman spectroscopic study on the relaxor ferroelectric $\text{PbSc}_{0.5}\text{Nb}_{0.5}\text{O}_3$. *J. Phys.: Condens. Matter* **21**, 235901.
- Woodward, D. I. & Reaney, I. M. (2005). Electron diffraction of tilted perovskites. *Acta Crystallogr. B* **61**, 387.
- Woodward, P. M. & Baba-Kishi, K. Z. (2002). Crystal structures of the relaxor oxide $\text{Pb}_2(\text{ScTa})\text{O}_6$ in the paraelectric and ferroelectric states. *J. Appl. Cryst.* **35**, 233.
- Xu, G. (2010). Competing Orders in $\text{PZN}-x\text{PT}$ and $\text{PMN}-x\text{PT}$ Relaxor Ferroelectrics. *J. Phys. Soc. Jpn.* **79**, 011011.
- Xu, G., Zhong, Z., Bing, Y., Ye, Z.-G., Stock, C. & Shirane, G. (2004). Anomalous phase in the relaxor ferroelectric $\text{Pb}(\text{Zn}_{1/3}\text{Nb}_{2/3})\text{O}_3$. *Phys. Rev. B* **70**, 064107.
- Yan, Y. & Pennycook, S. J. (1998). Determination of the ordered structures of $\text{Pb}(\text{Mg}_{1/3}\text{Nb}_{2/3})\text{O}_3$ and $\text{Ba}(\text{Mg}_{1/3}\text{Nb}_{2/3})\text{O}_3$ by atomic-resolution Z-contrast imaging. *Appl. Phys. Lett.* **72**, 3145.
- Yasuda, N., Fujita, K., Ohwa, H., Matsushita, M., Yamashita, Y., Iwata, M. & Ishibashi, Y. (2006). Effect of Pressure on Piezoelectric Properties of Relaxor Ferroelectric Solid-Solution $\text{Pb}[(\text{Mg}_{1/3}\text{Nb}_{2/3})_{0.68}\text{Ti}_{0.32}\text{O}_3]$ Single Crystal. *Japanese Journal of Applied Physics* **45**, 7413.
- Yasuda, N., Itoh, Y., Ohwa, H., Matsushita, M., Yamashita, Y., Iwata, M. & Ishibashi, Y. (2005). Piezoelectric Properties of $\text{Pb}[(\text{Zn}_{1/3}\text{Nb}_{2/3})_{0.91}\text{Ti}_{0.09}\text{O}_3]$ Single Crystal under Pressure. *J. Korean Phys. Soc.* **45**, 7413.
- Ye, Z.-G. (1998). Relaxor ferroelectric complex perovskites: Structure, Properties and Phase Transition. *Key Engineering Materials* **155-156**, 81.

Bibliography

Zha, C., Mao, H. & Hemley, R. (2000). Elasticity of MgO and a primary pressure scale to 55 GPa. *Proceeding of the National Academy of Science of the United States of America* **97**, 13494.

A High-temperature high-pressure DAC easyLab Diacell® μ ScopeDAC-HT(G)

This manual describes the handling of our easyLab Diacell® μ ScopeDAC-HT(G) gas-membrane-driven diamond anvil cell (HPHT-DAC). The cell has been bought from Diacell before easyLab took over the company. Afterwards the HPHT-DAC was improved by easyLab and later modified by our workshop to handle the cell easier. Thus, none of the official manuals describes our actual cell but the improved version of the HPHT-DAC from easyLab. The screw numbering in the figures is according to the Diacell® μ ScopeDAC-HT(G) user guide P00389 (April 2008).

The Diacell® μ ScopeDAC-HT(G) is a gas-membrane-driven consisting of four main parts:

- Outer clamping ring
- The gas-membrane
- Inner piston cylinder DAC
- The gasket heater

The assembly of the HTHP-DAC is shown in the user guide from easyLab as well as a description of the parts and their numbers. In the official instructions the parts are labeled by letters. Here the numbers from the user guide are used to label the parts, if available, otherwise the letters from the official instructions are used, holes for associated screws are marked by an asterisk (*) (Note: before ordering new screws always check the actual size as they may vary for our cell, as in the case of part number 37). To mount the diamond anvils in the upper cylinder (#18) place the anvil (mounted on the anvil ring #2) on the clean carbide plate. Place the whole assembly in the triangular holder (#14) and fix it to the hemisphere (#16), tighten the three screws fully (see Figure A.2. Mount the diamond anvil (fixed to the anvil ring #3) of the lower piston (#17) on the clean carbide plate. Place the whole assembly on the support plate (#27) and the insulator (#11) before fixing it to the lower piston with the holder (#15) using the four screws(K) (do not tighten the screws all the way till the cell is aligned).

Now the heater (#1) has to be placed in piston and connected to the lower screwing ring (#19) as follows (Note: the cell can also be operated without the heater if only pressure is needed for the experiment): Take the assembled heater (#1) attach the ceramic tubes H2 and place the assembly into the lower piston in such a way that lead with the ceramic

A High-temperature high-pressure DAC easyLab Diacell® μ ScopeDAC-HT(G)

tubes (H2) pass through H2*. Place the small ceramic tubes H3 (see Figure A.1) into the holes in the lower screwing ring (#19) as marked in Figure A.3. From below the lower screwing ring insert the screws #31 and place the spacers (they are unique to our cell) as well as the vertical leads H3. Now the heater-piston assembly has to be placed in such a way that the heater connects to the vertical leads while resting on the spacers. If this is achieved slightly tighten the screws #31 and screw the heater leads into the vertical leads using the tool H6. If the assembly is complete the ceramic tubes #34 are placed over the leads #23 and the screws #31 can be tightened all the way.

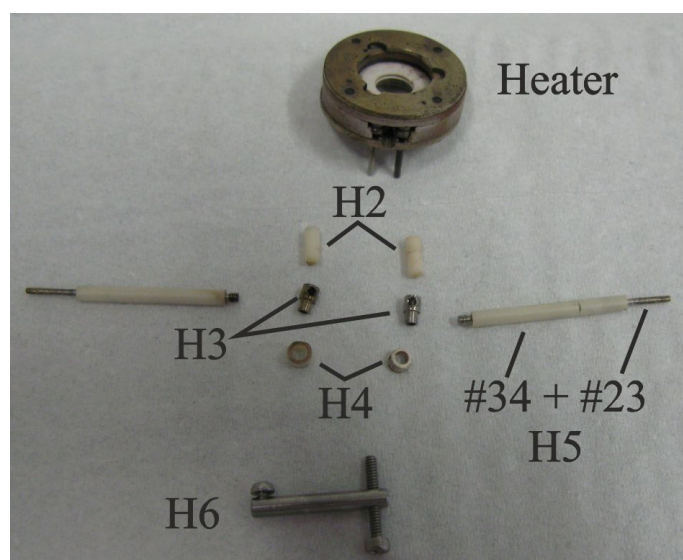


Figure A.1: Heater assembly to the lower piston.

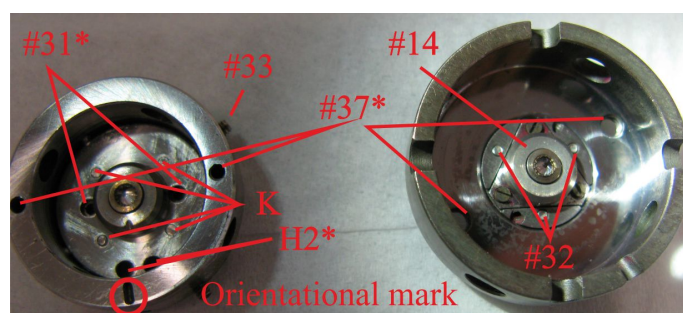


Figure A.2: HTHP-DAC top view of the closed cell.

The general alignment procedure is explained in Appendix B. The HTHP-DAC can be aligned when fully assembled with the gas-membrane (#25) and the upper screwing ring (#12, #20) but it is much more convenient to detach the upper cylinder (#18) by opening the screws #30. The upper cylinder is placed over the lower piston in such a way that the orientational marks are aligned to each other and the diamond anvil are brought close to each other by very gently pushing down on the cylinder. The horizontal off-set is aligned using the screws #33 (0.9 allen key) which can be accessed through the holes #33*

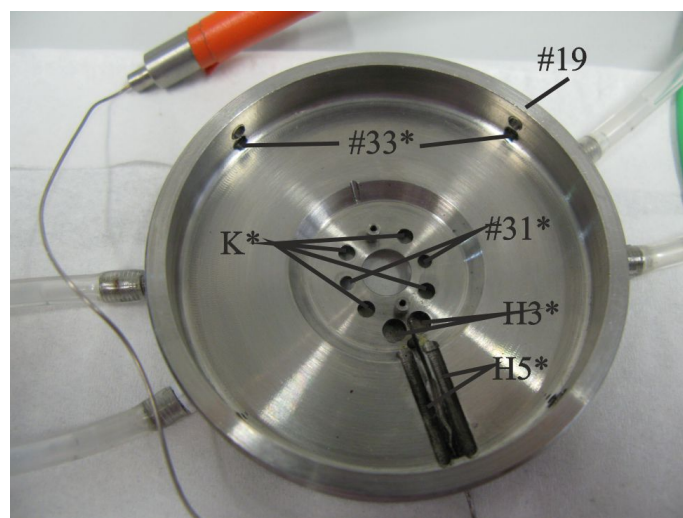


Figure A.3: HTHP-DAC top view of the closed cell.

(Figure A.3) in the lower screwing ring. The vertical tilt alignment is achieved by using the screws #32 (Figure A.2, A.4) hold the hemisphere (#16). Once the cell is aligned, tighten the screws K all the way (Figure A.2).

To apply pressure for an experiment or to indent a gasket place the gasket (the gasket should be marked with a mechanical scratch to be able to orient it always in the same manner) according to the orientational mark into the piston and place the cylinder on top (mind the orientation). Place the spacers on the cylinder (unique for our cell) in such a way that the screws #30 will pass through them when you place the outer cell (#12, 25, 20) on top, slightly tighten the screws. Place the screws #37 (for stainless steel gaskets A2 quality (stainless steel) can be used for rhenium gaskets quality 12.9 (black screw) has to be used) and gently tighten the screws on a rotational basis with the membrane ring until the cell is closed and both culet surfaces touch the gasket. The thickness of the indented area in the cell can be estimated if the distance between the outer diamond surfaces is measured once the cell is all the way closed and the initial thickness of the gasket is known. The decrease in the distance is linear to the indentation of the gasket thus if the distance decreases by $5\text{ }\mu\text{m}$ so does the thickness of the gasket between the culets. Once it is no longer possible to apply more pressure by tightening the screws and the membrane ring the gas-membrane may be used to apply further pressure (Note: never inflate the gas-membrane if the membrane ring is not all the way tightened).

To apply temperature the heater terminal (#24) has to be connected (thoughtfully tighten the screws) to the cell and the water cooling has to be installed. First start the water cooling and make sure that there are no leakages. Then program the temperature control unit according to the original manual. Note that with this device the change in temperature can only be controlled on increase, not on decrease.

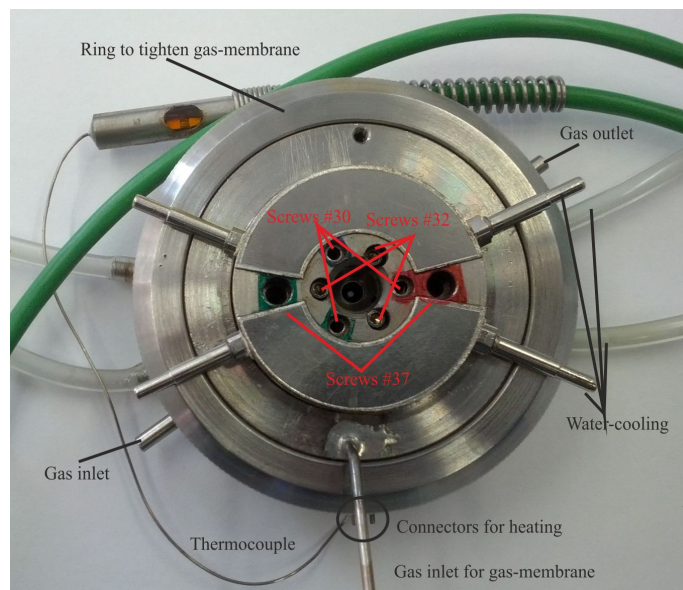


Figure A.4: HTHP-DAC top view of the closed cell.

To open the cell after the experiment unscrew the screws #37 and insert the opening tool (see Figure A.6) into the holes. On a rotational basis unscrew the membrane ring and tighten the screws of the opening tool until the cell is open.

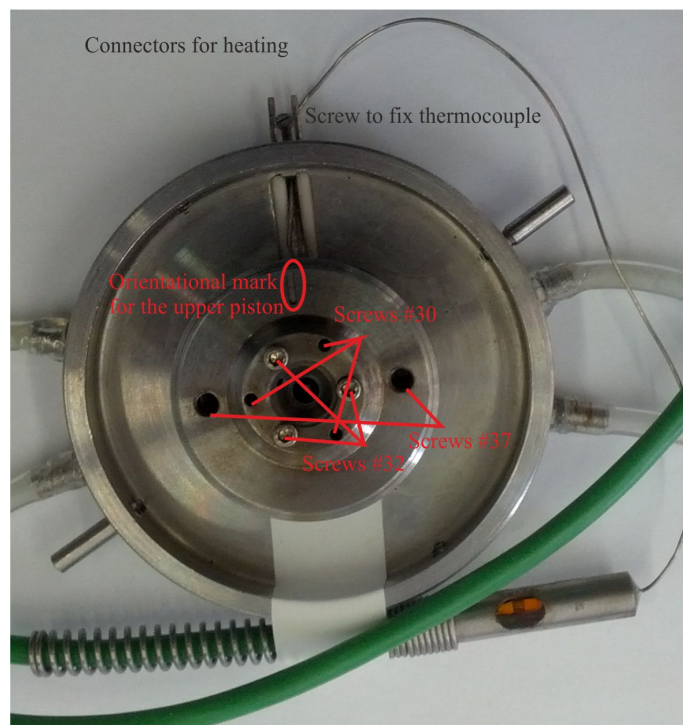


Figure A.5: HTHP-DAC top view showing the lower half of the outer cell and the closed inner piston.



Figure A.6: Tool to open the HTHP-DAC after the experiment.

B Alignment of the diamond anvils

The culets of the diamond anvils have to be perfectly aligned to prevent failure of the diamonds during the experiment. The culets have to be aligned in such a way that they are parallel to each other (vertical tilt alignment) and directly on top of each other (horizontal alignment). During the alignment the diamonds have to be brought into direct contact. This is extremely critical as the direct contact between diamonds can easily lead to failure, especially if the diamonds are tilted. Thus, the whole alignment procedure has to be done with great care and self-evidently, after carefully cleaning the culets (e.g. with acetone).

Depending on the DAC used, the alignment may vary slightly but the general approach is the same. One diamond anvil (upper or lower) is fixed to the cell in such a way that it can not be moved, while the other diamond anvil is mounted in such a way that it can be aligned to the fixed diamond anvil.

First the anvil is moved horizontally in such a way that the two culets are very close to each other but not touching. Use a microscope with transmission light to observe the two culets (Figure B.1 upper row). If the culets are perfectly on top of each other the edges of the culets can be seen depending on the microscope. In transmission light the horizontally misaligned culets produce an elliptical shape. The anvils have to be moved in such a way that they show a perfect circle which indicates that they are directly on top of each other. This alignment might have to be repeated after the vertical tilt alignment.

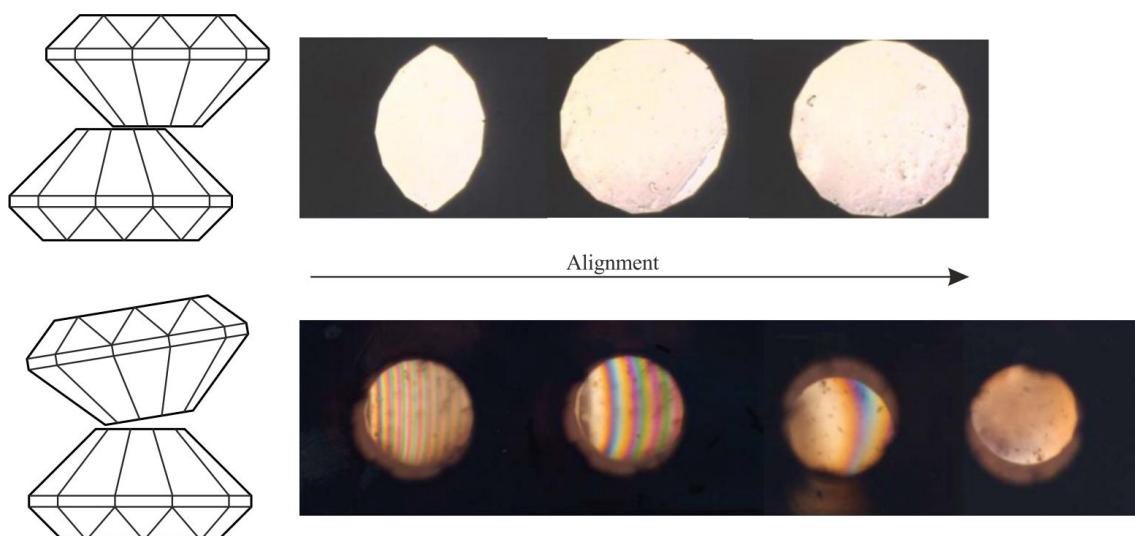


Figure B.1: Horizontal (upper row) and tilt alignment (bottom row) of diamond anvils.

B Alignment of the diamond anvils

The vertical tilt alignment is done by observing the disappearance of the Newton fringe lines (see Figure B.1 bottom row). The Newton fringes appear when a culet area is exposed to a higher pressure load. Thus, the Newton fringes result from the fact that tilted anvil is touching the fixed anvil. The closer the fringes are, the more the anvils are tilted to each other (Note! Newton fringes are commonly colored rings, if you only see black and white fringes that means the anvils are strongly tilted against each other). The flexible diamond anvil is normally mounted to half-sphere which is controlled by three screws. Using these screws the vertical tilt has to be adjusted in such a way that the Newton fringes become broader until they disappear. Note: Using a droplet of isopropane on the culet and observing the change in the droplet shape helps observing the distance and the tilt of the culet surfaces to each other. The droplet will show the contact between the two surfaces before they are actually touching and it will acquire a perfectly round shape in the center of the culet once the tilt alignment is done (but always use the Newton fringes as reference for alignment, the droplet is just an addition). If the cell is newly aligned the alignment has to be checked after indenting the gasket to make sure that the alignment was done properly and will withstand the pressure of the experiment.

A note on cleaning the culets: The culets are best cleaned with a q-tip and acetone or isopropane (isopropane takes longer to evaporate). A chemist would say "once for the bad stuff, twice for the dirt, and a third time to make it clean". Thus, once all the gasket remnant is gone and your next step is to start loading the cell you have to clean the culet surface three times (using the air gun after each step). The same cleaning procedure holds true for cleaning the gasket before loading (after drilling). The gasket should be put in the ultra-sonic bath for ~ 10 min 3 times, always with fresh acetone and blow dried after each run. If you have very bad dirt on the culet surface, like it always happens after using rhenium gaskets, you first try to get it off with the scalpel, carefully scraping it off. If that does not work you can use diamond polish paste. Tip a toothpick into the paste and rub it on the culet surface, then take the scalpel to scratch off the remnant of the gasket. After using the diamond paste you have to clean very thoughtfully as this paste causes luminescence if not removed all the way. You have to make sure that all the cleaning liquid is evaporated (use air gun) before proceeding with the loading of the cell.

C Manual for the spark eroder available at the Institute of Mineralogy and Petrology

After successfully indenting the gasket, a hole has to be drilled into the center of the indented part. To drill the hole three different methods can be used:

- a spark eroder (Figure C.1)
- mechanical microdrill
- laser drilling

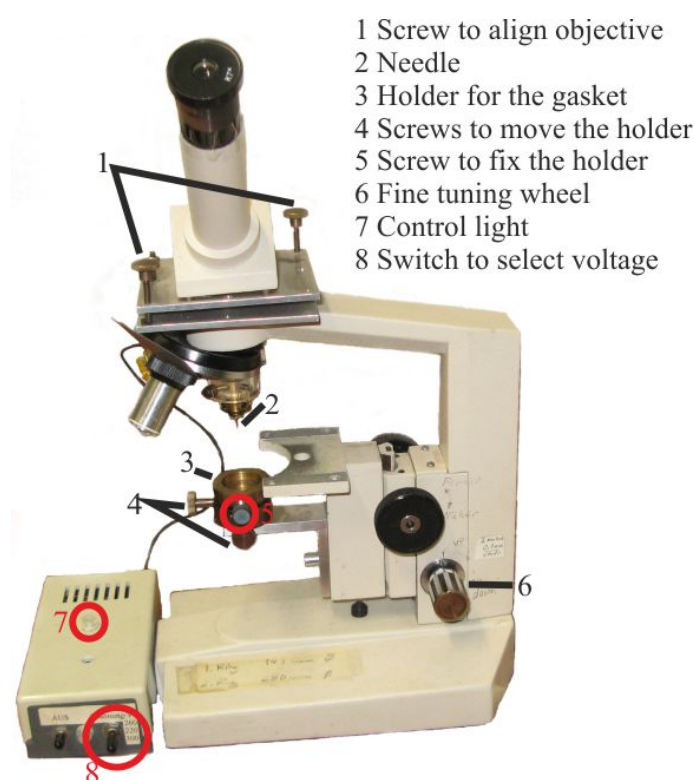


Figure C.1: Manual spark eroder.

The spark eroder is build up of an optical microscope equipped with a holder for the gasket and a power supply (see Figure C.1). An electric charge is used to melt and evaporate the gasket close to the tip of the needle, which operates as an electrode and is usually made of tungsten. The diameter of the hole is mainly influenced by the applied voltage between the gasket and the electrode but it also depends on the material used. Generally it can be

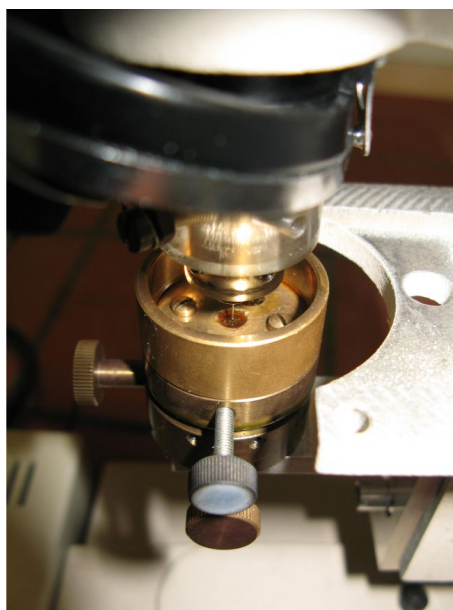


Figure C.2: Gasket holder with gasket mounted to the spark eroder in the process of drilling a hole.

estimated that the hole has a diameter greater or equal than the diameter of the tungsten wire (note: the tip of the wire has to be round in order to drill a round hole).

First a test drill has to be performed to check if the selected needle is perfectly aligned with the cross in the objective of the microscope as follows:

- place the gasket into the holder and fix the holder to the spark eroder using screw 5
- adjust the holder so that the cross form the objective is where the hole should be (some place outside the indented area)
- select a needle (e.g. diameter $200\text{ }\mu\text{m}$) switch to the needle and drill a scratch (a small hole which does not go through for adjustment of the position)
 - to drill the gasket, the holder has to be filled with a cooling liquid. **Note:** Usually oil is used due to its thermal conductivity and viscosity. However, during this study it was figured out that remnants of oil may stay on the rim of the gasket hole even after cleaning the gasket with acetone in ultrasonic bath. Then, when an alcohol mixture is used as a pressure medium, these oil remnants dissolve in the pressure medium, thus contamination the sample chamber and may lead to high-level photoluminescence background during Raman experiments, depending on the excitation wavelength used. From this point of view it is much better to use water or simple alcohols such as ethanol, methanol, isopropane or the mixture used as a pressure medium.
 - carefully move the needle close to the surface of the gasket (Figure C.2). You are close enough to the gasket when you can hear and see the spark (sometimes

before this you can already see bubbles rising from the needle tip). Also the little light on the power supply goes off once the needle is too close (touching; be careful not to bend the needle) the gasket. If that happens the spark can not be generated any more between the needle and the gasket.

- remove the cooling liquid on top of the gasket
- switch back to the objective and check the position of the scratch
 - if the scratch is not under the cross of the objective, adjust the objective to the scratch using screws labeled 1
 - reposition the cross of the objective to the middle of the indented gasket
 - add cooling liquid
 - drill the hole by carefully turning the fine tuning wheel. If you turn the wheel too fast, the control light on the power supply will switch off because you are too close to the gasket and no spark can be generated (be careful not to bend the needle while drilling). On the other hand if you are too far away you will not hear and see the spark. 360° rotation of the fine-tuning wheel are $\sim 100 \mu\text{m}$ with our current spark eroder. If the thickness of the indented area is known, you can estimate how far you have to turn to drill all the way through.
 - check if the hole has the same diameter on both sides of the gasket, i.e., if the hole is cylindrical. If the hole is conical rather than cylindrical, drill again from the other side.

Curriculum vitae

Personal

Name	Naëmi Waesermann
Birth	25. Januar 1983, Hamburg, Germany
Office address	Universität Hamburg Mineralogisch-Petrographisches Institut Grindelallee48 D-20146 Hamburg Fax: +49 (0)4042838-2422 Phone: +49 (0)40 42838-2076 e-mail: naemi.waesermann@mineralogie.uni-hamburg.de

Education

2000–2004	Apprenticeship as a chemical-technical assistant, graduation: 30.01.2004 Hamburg, Germany.
10/2004–09/2009	Studies of Mineralogy with focus geochemistry, petrology, and crystallography at the University of Hamburg, Germany. Diploma thesis: <i>Compositional zoning of the Los Chocoyos tephra, Atitlán Caldera, Guatemala.</i>
03/2006	Participation at the course <i>Physical Volcanology</i> from the University of Kiel, Melling, Germany.
09/2006	Participation at the course <i>X-ray methods for structural science</i> , University of Dresden, Germany.
02/2007	Participation at the course <i>Rheology of Rocks</i> , GeoForschungsZentrum Potsdam, Germany.
09/2007	Participation at the course <i>Gran Canary island field petrology</i> from the University of Mainz, Gran Canaria, Spain.
11/2008	Participation at the course <i>International Short Course Pyroclastic Rocks</i> , Bozen, Italy.
01/2007–12/2007	Student assistant at multi-anvil press DESY/HASYLAB, GeoForschungsZentrum Potsdam, Germany.
07/2008–09/2008	Student assistant for the volcanological excursion to Italy, University of Hamburg, Germany.

Curriculum vitae

- 10/2009–10/2012 Doctorate studies at the University of Hamburg, Germany. Research on relaxor ferroelectrics using temperature, pressure and in situ high-temperature high-pressure dependent Raman spectroscopy.
- 11/2010 Participance at the course *Synchrotron X-ray and IR Methods in the Geosciences*, Synchrotron Radiation Source ANKA, Karlsruhe Institute of Technology, Germany.
- 01/2011 Participance at the course *Vibrational spectroscopy at high pressures*, GeoForschungsZentrum Potsdam, Germany.
- 02/2011 Participance at the course *High-pressure experimental techniques and applications to the Earth's interior*, Bayerisches Geoinstitut, University of Bayreuth, Germany.
- 11/2011 Participance at the course *Advanced Archeometry*, University of Fribourg, Swiss.
- 05/2012 Participance at the course *Applied solid state NMR spectroscopy in mineral and geoscience*, University of Bochum, Germany.
- 06/2012 Participance at the international school *Raman spectroscopy applied to earth science and cultural heritage*, University of Nancy, France.

Teaching activities

- 2009–2012 Assistance to Dr. Mihaylova for the BSc course *Mineralogical practicum*, University of Hamburg.

List of publications

- **Waeselmann, N.**, Mihailova, B., Maier, B. J., Paulmann, C., Gospodinov, M., Marinova, V. and Bismayer, U. Local structural phenomena in pure and Ru-doped $0.9\text{PbZn}_{1/3}\text{Nb}_{2/3}\text{O}_3$ - 0.1PbTiO_3 near the morphotropic phase boundary as revealed by Raman spectroscopy, *Phys. Rev. B*, 2011, 83, 214104
- **Waeselmann, N.**, Maier, B. J., Mihailova, B., Angel, R. J., Zhao, J., Gospodinov, M., Paulmann, C., Ross, N. and Bismayer, U. Pressure-induced structural transformations in pure and Ru-doped $0.9\text{PbZn}_{1/3}\text{Nb}_{2/3}\text{O}_3$ - 0.1PbTiO_3 near the morphotropic phase boundary *Phys. Rev. B*, 2012, 85, 014106
- Maier, B. J., **Waeselmann, N.**, Mihailova, B., Angel, R. J., Ederer, C., Paulmann, C., Gospodinov, M., Friedrich, A. and Bismayer, U. Structural state of relaxor ferroelectrics $\text{PbSc}_{0.5}\text{Ta}_{0.5}\text{O}_3$ and $\text{PbSc}_{0.5}\text{Nb}_{0.5}\text{O}_3$ at high pressures up to 30 GPa *Phys. Rev. B*, 2011, 84, 174104
- **Waeselmann, N.**, Mihailova, B., Gospodinov, M., Petrova, D. and Bismayer, U. In-situ high-temperature high-pressure Raman spectroscopy on single-crystal relaxor ferroelectrics $\text{PbSc}_{1/2}\text{Ta}_{1/2}\text{O}_3$ and $\text{PbSc}_{1/2}\text{Nb}_{1/2}\text{O}_3$ *Phys. Rev. B*, *submitted*
- Mihailova, B., **Waeselmann, N.**, Maier, B. J., Angel, R. J., Prüßmann, T., Paulmann, C., Gospodinov, M. and Bismayer, U. Chemically induced renormalization phenomena in doped Pb-based relaxors under high pressure *in preparation*

Contributions to conferences

- **Waeselmann, N.**, Mihailova, B., Welsch, A.-M., Maier, B. J. and Bismayer, U. Pb-based relaxor ferroelectrics under high pressure and temperature 437. Wilhelm und Else Heraeus Seminar, Bad Homburg, 13.12-16.12.2009
- **Waeselmann, N.**, Mihailova, B., Maier, B. J., Gospodinov, M. and Bismayer, U. The local structure of 0.9PZN - 0.1PT at high temperature and pressure SPP 1236 3rd

List of publications

Berichtskolloquium, Oberursel, 10.03-12.03.2010

- **Waesermann, N.**, Mihailova, B., Maier, B. J., Gospodinov, M. and Bismayer, U. The effect of Ru-doping on the phonon states of $\text{PbZn}_{1/3}\text{Nb}_{2/3}\text{O}_3$ - PbTiO_3 single crystals at the morphotropic phase boundary Deutsche Mineralogische Gesellschaft, Münster, 19.09-21.09.2010
- **Waesermann, N.**, Mihailova, B., Maier, B. J., Gospodinov, M. and Bismayer, U. The local structure of 0.9PZN-0.1PT at high temperature and pressure Deutsche Physikalische Gesellschaft Frühjahrstagung der Sektion Kondensierte Materie, Regensburg, 21.03-26.03.2010
- **Waesermann, N.**, Mihailova, B., Maier, B. J., Gospodinov, M. and Bismayer, U. Temperature/ pressure-induced structural changes in pure and Ru-doped $\text{PbZn}_{1/3}\text{Nb}_{2/3}\text{O}_3$ - PbTiO_3 near the morphotropic phase boundary 3rd International Symposium on Structure-Property Relationships in Solid State Materials, Stuttgart, 27.06-02.07.2010
- **Waesermann, N.**, Maier, B. J., Paulmann, C., Mihailova, B., Bismayer, U., Angel, R. J., Zhao, J. and Gospodinov, M. The structure of lead-based perovskite-type (ABO_3) relaxor ferroelectrics at high pressure and high temperature SPP 1236 4th Bereichskolloquium Huenfeld, 2011
- **Waesermann, N.**, Mihailova, B., Maier, B. J., Paulmann, C., Gospodinov, M. and Bismayer, U. Local structural phenomena in pure and Ru-doped $\text{PbZn}_{1/3}\text{Nb}_{2/3}\text{O}_3$ - PbTiO_3 near the morphotropic phase boundary as revealed by Raman spectroscopy European Meeting on Ferroelectricity, Bordeaux, 26.06-02.07.2011
- **Waesermann, N.**, Mihailova, B., Gospodinov, M. and Bismayer, U. In-situ high-pressure and high-temperature Raman spectroscopy on advanced perovskite-type relaxor ferroelectrics 7th European Conference on Mineralogy and Spectroscopy, Potsdam, 04.09-07.09.2011
- **Waesermann, N.**, Schlüter, J., Bergemann, C., Bersani, D. and Mihailova, B. Raman spectroscopy on garnet and ruby as a non-destructive analytical method in gemmology 7th European Conference on Mineralogy and Spectroscopy, Potsdam, 04.09-07.09.2011

List of publications

- **Waesermann, N.**, Mihailova, B., Gospodinov, M. and Bismayer, U. In-situ high-pressure and high-temperature Raman spectroscopy on advanced perovskite-type relaxor ferroelectrics, GeoRaman 10, Nancy, 11.06-13.06.2012

Annual reports of synchrotron facilities

- Maier, B. J., **Waesermann, N.**, Mihailova, B., Angel, R. J., Paulmann, C., Gospodinov, M. and Bismayer, U. Effect of La and Sr on the pressure-induced phase transitions of $\text{PbSc}_{0.5}\text{Ta}_{0.5}\text{O}_3$ and $\text{PbSc}_{0.5}\text{Nb}_{0.5}\text{O}_3$ Annual report 2010 DESY, 2011
- Maier, B. J., **Waesermann, N.**, Mihailova, B., Angel, R. J., Paulmann, C., Gospodinov, M. and Bismayer, U. Pressure-induced phase transitions in relaxors $\text{PbSc}_{0.5}\text{Ta}_{0.5}\text{O}_3$ and $\text{PbSc}_{0.5}\text{Nb}_{0.5}\text{O}_3$ up to 30 GPa Annual report 2010 DESY, 2011
- Maier, B. J., **Waesermann, N.**, Mihailova, B., Angel, R. J., Paulmann, C., Gospodinov, M. and Bismayer, U. Effect of Ba on the pressure-induced phase transitions of $\text{PbSc}_{0.5}\text{Ta}_{0.5}\text{O}_3$ up to 23 GPa Annual report 2010 DESY, 2011
- Maier, B. J., **Waesermann, N.**, Mihailova, B., Angel, R. J., Paulmann, C., Gospodinov, M. and Bismayer, U. Effect of B-site substitution on the high-pressure structural state of $\text{PbSc}_{0.5}\text{Ta}_{0.5}\text{O}_3$ Annual report 2010 DESY, 2011

Acknowledgments

Last but not least I like to thank all those who helped me throughout my studies.

It would be too much to list them all but I like to express my gratitude to my supervisors Dr. habil. Boriana Mihaylova and Prof. Dr. Ulrich Bismayer for all their patience and support during my PHD studies.

Also this work would not have been possible without the great help of the workshop of the University of Hamburg and the knowledge from the members of the SPP 1236 on high pressure experiments. But also I like to thank my colleges here in our institute for all the discussions and support.

But my greatest thanks goes to those who had to share me with my work, my family and friends.

This work was financially supported by the Deutsche Forschungsgemeinschaft via the Grants No. MI 1127/2-2 (within the the framework of DFG SPP 1236) and No. INST 152/460-1.